

Applying Fluvial Depositional Concepts in Solute Transport Modelling

Dissertation
der Mathematisch-Naturwissenschaftlichen Fakultät
der Eberhard Karls Universität Tübingen
zur Erlangung des Grades eines
Doktors der Naturwissenschaften
(Dr. rer. nat.)

vorgelegt von
Jeremy Paul Bennett M.Sc.
aus Wellington, Neuseeland

Tübingen
2018

Gedruckt mit Genehmigung der Mathematisch-Naturwissenschaftlichen Fakultät der
Eberhard Karls Universität Tübingen.

Tag der mündlichen Qualifikation

Dekan

1. Berichterstatter

2. Berichterstatter

3. Berichterstatter

01.10.2018

Prof. Dr. Wolfgang Rosenstiel

Prof. Dr.-Ing. Olaf A. Cirpka

Dr.-Ing. Claus Haslauer

Dr. Martin Ross

Abstract

The spatial configuration of hydraulic properties in the subsurface controls groundwater flow and solute transport. Exploitable aquifer systems are often found in fluvial sedimentary deposits, which can exhibit predictable stratigraphic characteristics. However, sedimentary concepts are often overlooked when simulating aquifer heterogeneity. This can lead to differences in predictions of groundwater flow and solute transport. Understanding these differences is the central focus of this doctoral thesis. The main hypothesis is that by integrating geological concepts into hydrogeological modelling, we can improve predictions of solute transport. In this thesis, I linked geological concepts to hydrogeological parameters based on extensive site characterisations from the literature. An object-based modelling framework was developed in the Python programming language to facilitate further improvements in using geological conceptual models in numerical flow and transport simulations. By comparing model ensembles generated using object-based, multiple-point geostatistical, and multi-Gaussian simulation methods, I show that hydrogeological models that account for geological processes behave differently to models where such processes are neglected. In particular, transverse solute mixing is strongly affected by sedimentary anisotropy and the juxtaposition of zones of contrasting hydraulic conductivity that have been widely reported in the field. In addition, conditioning simulations to field data is important to constrain prediction of flow and transport to the range that is in accordance with observed data. Therefore, simulation methods that can integrate geological concepts and conditioning information (e.g., multiple-point geostatistical methods) have the greatest potential to improve the accuracy of solute transport predictions. The methods and workflow implemented in this work provide a platform for further investigation of the effects of geological realism on solute transport simulations.

Kurzfassung

Die räumliche Konfiguration der hydraulischen Eigenschaften im Untergrund steuert die Grundwasserströmung und den Stofftransport. Nutzbare Aquifersysteme finden sich häufig in fluvialen Sedimentablagerungen, die vorhersagbare stratigraphische Eigenschaften aufweisen können. Sedimentäre Konzepte bleiben jedoch bei der Simulation der Aquiferheterogenität oft unbeachtet. Dies kann zu Abweichungen in der Vorhersage von Grundwasserströmung und Stofftransport führen. Das Verständnis dieser Abweichungen steht im Mittelpunkt der vorliegenden Dissertation. Die zentrale Hypothese ist, dass wir durch die Integration geologischer Konzepte in die hydrogeologische Modellierung die Vorhersage des Stofftransports verbessern können. In dieser Arbeit habe ich geologische Konzepte mit hydrogeologischen Parametern verknüpft, die auf umfangreichen Standortcharakterisierungen aus der Literatur basieren. In der Programmiersprache Python wurde ein objektbasiertes Modellierungsframework entwickelt, um weitere Verbesserungen bei der Verwendung geologischer konzeptioneller Modelle in numerischen Strömungs- und Transportsimulationen zu ermöglichen. Durch den Vergleich von Modell-Ensembles, die mit objektbasierten, mehrpunktgeostatistischen und multi-Gaußschen Simulationsmethoden erzeugt wurden, zeige ich, dass sich hydrogeologische Modelle, die geologische Prozesse berücksichtigen, anders verhalten als Modelle, bei denen solche Prozesse vernachlässigt werden. Insbesondere die transversale Vermischung von gelösten Stoffen wird stark durch die Sedimentanisotropie und benachbarte Zonen mit kontrastierender hydraulischer Leitfähigkeit beeinflusst, die im Feld oft angetroffen werden. Darüber hinaus ist die Konditionierung von Simulationen auf Felddaten wichtig, um die Vorhersage von Strömung und Transport auf den Bereich einzuschränken, der mit den beobachteten Daten übereinstimmt. Daher haben Simulationsmethoden, die geologische Konzepte und Konditionierungsinformationen integrieren können (z.B. geostatistische Mehrpunktverfahren), das größte Potenzial, die Genauigkeit von Stofftransportvorhersagen zu verbessern. Die in dieser Arbeit implementierten Methoden und Arbeitsabläufe bieten eine Plattform für die weitere Untersuchung der Auswirkungen von geologischer Realitätsnähe auf die Simulation des Stofftransports.

Acknowledgements

Therefore, since we are surrounded by such a great cloud of witnesses, let us throw off everything that hinders and the sin that so easily entangles. And let us run with perseverance the race marked out for us... – Hebrews 12:1

I would like to express my sincere gratitude to the following people:

- My friends, family, and community, including Tyler, Tony, Adrian, the Unterwegs team, and the Kreuzkirche Tübingen.
- The wider research community for their willingness to share their time, ideas, and code: Alessandro Comunian, Graham Fogg, Guillaume Pirot, and Calogero Rizzo. Special thanks to Philippe Renard and Julien Straubhaar (University of Neuchâtel) for their help with multiple-point geostatistical algorithms.
- Martin Ross and colleagues at the University of Waterloo for their warm hospitality during my research stay in Winter/Spring 2017.
- My colleagues at the Centre for Applied Geosciences at the University of Tübingen, particularly within the Hydrogeology workgroup, and other members of the RTG “Integrated Hydrosystem Modelling”. Special thanks to Monika Jekelius for her tireless efforts in administering the research training group.
- Claus Haslauer, of whom I have asked many dumb questions and with whom I have often rung the *Erfolgstischglocke*.
- And, of course, Olaf A. Cirpka, whose commitment to his students, colleagues, and research is indefatigable. It has been an absolute privilege to be trained, tested, and tortured by this fellow.

Finally, I would like to acknowledge the love, patience, and fortitude of my wife Hannah. Twelve years ago we promised to love each other through the crazy times and the gaps – it feels like we have had a lot of both during this dissertation, but I can’t wait to continue the adventure with you and Amelie.

Acknowledgements

Contents

Abstract	i
Kurzfassung	iii
Acknowledgements	v
Contents	vii
List of Figures	ix
1 Introduction	1
1.1 Research Objectives	3
2 Key Concepts and Recent Advances	5
2.1 Fluvial Depositional Environments	5
2.2 Modelling Heterogeneity in Sedimentary Deposits	10
2.3 Quantifying the Effects of Heterogeneity	16
3 Results and Discussion	25
3.1 Sedimentary Anisotropy in Scour Pool Features	25
3.2 A Framework for Generating Fluvial Subsurface Models	31
3.3 Solute Transport in a Synthetic Braided-River Deposit	37
4 Overall Conclusions and Outlook	47
Bibliography	49
A Publications	63
A.1 List of Publications	63
A.2 Bennett et al., <i>Water Resources Research</i> , 2017	65
A.3 Bennett et al., <i>Groundwater</i> , 2018	85
A.4 Bennett et al., <i>Water Resources Research</i> , submitted August 2018	105
B Technical Documentation	153

List of Figures

2.1	Hierarchy of fluvial depositional units	7
2.2	Architectural elements	8
2.3	Conceptual model of the proglacial environment	9
2.4	Outcrop image and hydrofacies distribution of glacial outwash sediments . .	11
2.5	Transverse dispersion in steady-state contaminant plumes	18
3.1	Conceptual model of scour-pool fill development	26
3.2	One realisation of generated trough geometries	27
3.3	Advective streamlines in four test cases	29
3.4	Steady-state concentration distributions in observation planes	30
3.5	Hierarchical modelling framework implemented in HyVR	32
3.6	Hydrofacies assemblage geometries currently implemented in HyVR	32
3.7	Internal structures of truncated ellipsoids generated using HyVR	33
3.8	Geological conceptual model and simulated parameter fields, MADE site . .	35
3.9	Workflow for generating model ensembles	38
3.10	Log-hydraulic conductivity and hydrofacies parameter fields	42
3.11	Probability distribution functions of log-hydraulic conductivity parameter field ensembles	43
3.12	Minimum hydraulic resistance distributions	43
3.13	Advective particle distributions in observation planes	44
3.14	Transverse moments from steady-state concentration distributions	45

I Introduction

The spatial variability of hydraulic conductivity controls how groundwater and solutes move through the subsurface. As groundwater is widely abstracted for many different uses, and because many aquifer systems are vulnerable to contamination from anthropogenic sources, the accurate characterisation of groundwater flow and solute transport is essential. Concepts about, and observations of, sedimentary processes and the corresponding deposits can provide insight into the spatial configuration of hydrogeological parameters. However, such conceptual information can be difficult to incorporate into flow-and-transport simulations and has therefore often been neglected in hydrogeological research. By creating subsurface models that better reflect the depositional environments in which the aquifer materials were deposited, predictions of flow and transport may be improved. The goal of this doctoral thesis is to understand to what extent geological realism influences the accuracy of groundwater flow and solute transport simulations in fluvial deposits.

Fluvial deposits are typically unconsolidated sediments that have been deposited by channel processes. They often form important porous aquifers from which groundwater is extracted. These aquifer systems are attractive for exploitation as they are generally highly permeable and often close to the ground surface, which reduces pumping cost and effort. However, these properties can also make them vulnerable to over-extraction, as well as contamination from diffuse and point sources. Fluvial sedimentary deposits are composed of assemblages of facies at multiple scales and are often formed by cyclical depositional processes (e.g., glacial advance and retreat). Researchers have characterised sedimentary features at different scales using hierarchical approaches (e.g., Aigner et al., 1999); such approaches are also useful when classifying deposits for hydrogeological purposes (e.g., Heinz and Aigner, 2003b). In this thesis, I developed and used hierarchical modelling frameworks to create geologically realistic parameter fields for forward flow-and-transport simulations. This thesis focused on glaciofluvial deposits, as many important aquifer systems are comprised of such depositional features and have therefore been the subject of numerous hydrogeological studies (e.g., Anderson, 1989).

Characterising heterogeneity in sedimentary deposits can be broadly classified into three modelling approaches: descriptive, process-imitating, and structure-imitating (Koltermann and Gorelick, 1996). Often modelling methods will integrate different model approaches at different scales. Stochastic approaches to hydrogeology can often replicate observed data very well. However, such approaches have often been criticised due to the perceived lack of geological realism or plausibility. Many approaches to characterising hydraulic conductivity fields reduce complex sedimentary architectures to geostatistical rules that are a function of distance

(i.e., two-point geostatistics). This can result in sedimentary structures, such as sharp contact surfaces or the connectedness of features, not being adequately represented in subsequent hydrogeological models. Multiple-point geostatistical (MPS) methods (e.g., Mariethoz, Renard, and Straubhaar, 2010) may offer a good trade-off between the integration of geological concepts via training images and conditioning to data. I explored the application of MPS approaches in solute transport modelling in this thesis.

The ultimate goal of characterising heterogeneous subsurface deposits in hydrogeology is the accurate prediction of groundwater flow and solute transport. The spatial distribution of hydraulic conductivity controls the advance, mixing, and spreading of solutes, which are important processes in understanding many contamination problems. Mixing can control reaction rates of solute species, and spreading determines the shape of spatially integrated breakthrough curves. Recent work suggests that non-stationary anisotropy can enhance transverse mixing (Cirpka, Chiogna, et al., 2015), however it is unclear to what extent this enhancement occurs in realistic sedimentary structures. The influence of sedimentary anisotropy in fluvial deposits on solute transport was investigated in this thesis.

Relevance to Integrated Hydrosystem Modelling

Groundwater resources are of utmost importance. Although only 0.76 % of the total water present on earth, groundwater provides a significant proportion (30 %) of the global freshwater supply (Shiklomanov, 1993). Groundwater is extracted for a variety of uses and is estimated to provide 50 % of drinking water, 20 % of irrigation water, and 40 % of industrial water supply globally (Zektser and Everett, 2004). With increasing pressure placed on groundwater resources through population growth and climate-induced variability of recharge, it is essential that groundwater resources are protected and potential threats are understood and mitigated accordingly.

Integrated hydrosystem models offer a holistic framework for understanding the flow of water and contaminants through catchments and assessing groundwater resources. Accurate characterisation of hydraulic parameters in aquifers can be critical in such models. Integrated hydrosystem models that include subsurface hydrological processes can produce inaccurate results if aquifer heterogeneity exerts a key control on hydrology yet has been inadequately described (Refsgaard et al., 2014). Interfaces between hydrosystem model compartments (e.g., groundwater and surface water) are also sensitive to subsurface heterogeneity (e.g., Cardenas et al., 2004).

1.1 Research Objectives

Three research objectives provided a framework for this doctoral thesis:

1. To investigate how variability in geological processes affects solute transport in sedimentary aquifers.
2. To build geologically plausible hierarchical facies models and assess their ability to replicate typically observed solute transport behaviour.
3. To explore how knowledge of geological processes can be used to improve solute transport modelling in practice.

The first objective was to understand what types of variability in fluvial deposits affect solute transport. Typically, such aquifer systems comprise sediments that have been deposited during a range of environmental conditions, often occurring cyclically, but with different spatial and temporal scales. The aim was to link depositional processes and features to the configuration of hydrogeological properties, including dipping parameters, that can induce hydraulic anisotropy.

For the second objective, hierarchical facies models were developed to answer questions about the importance of geological realism in solute transport modelling. By assessing multiple model ensembles with varying characteristics, such as multi-scale heterogeneity and modelling approaches, it may be possible to determine which hydrostratigraphic features have the greatest influence on solute transport.

The final objective was to effectively combine the first two research objectives to provide a practical way forward. The importance of geological information for constraining hydrogeological models was assessed, along with the ability of such information to improve the prediction of solute transport. Practical measures for improving the geological plausibility in current simulation strategies were also developed. This objective also encompassed the evaluation of novel flow and solute transport metrics, such as connectivity, and topological descriptors, and what effect different approaches for modelling heterogeneity in sedimentary deposits have on these metrics.

To achieve these objectives, I simulated a series of realistic, spatially distributed hydraulic parameter fields using various sediment generation tools and constrained by quantitative and qualitative information. I performed forward groundwater flow and solute transport simulations using the generated parameter fields and assessed the simulation results using relevant metrics. I developed a framework for including geological information in hydrogeological modelling studies, including a workflow suitable for practice.

Thesis Structure

This thesis is structured as follows: Chapter 2 describes key concepts in the area of study, as well as recent advances. In Chapter 3, I present the main results of the three work packages that comprise this thesis: Sedimentary anisotropy in scour pool features; a framework for generating fluvial subsurface models; and solute plume behaviour in a synthetic braided-river deposit. I have included the accompanying publications and technical documentation in Appendices A and B, respectively. Chapter 4 summarises the achievements of the thesis and provides an outlook for future research.

2 Key Concepts and Recent Advances

In this chapter, I present key concepts in fluvial depositional environments, review approaches to modelling heterogeneity in sedimentary deposits, and introduce methods for quantifying the effects of heterogeneity on flow and transport, and recent advances thereof.

2.1 Fluvial Depositional Environments

Sediments can be transported by a number of mechanisms, including water, ice, wind, and gravity (Leeder, 1999). Fluvial deposition describes the process of sediments being deposited by water in channel systems and plays a critical role in the formation of porous aquifers. The characteristics of fluvial deposits are determined by the mechanisms of sediment transport and the flow regimes in which they are deposited. Important factors can include the flow regime (e.g., frequency, duration, and magnitude of flood events), the properties of the material (e.g., lithology, weathering, and particle-size distribution), and the morphology of the river (Schumm, 1963). Deposition may not just occur within the channel itself but also adjacent to the channel during high-magnitude flows. These flows can have a wide range of causes, including heavy rainfall in the catchment or hydrological disturbances from glacial melting or volcanic activity.

Sediments can only be transported in streams if there is sufficient flow energy (e.g. Miller et al., 1977); this means that coarse sediments are usually transported in high-energy rivers (or during high-flow events in low-energy environments). Schumm (1963) classified river systems into three modes according to their discharge and sediment load characteristics: suspended load, mixed load, and bedload. Typically, bedload rivers are the most relevant to hydrogeology as these high-energy systems can transport and deposit large volumes of coarse sediments, thus providing the building blocks of productive aquifers. Braided channels can be distinguished by the complex patterns of flow divergence and convergence around barforms (Leeder, 1999). These systems are highly dynamic, which is reflected in the heterogeneous nature of the deposits that they leave behind.

2.1.1 Hierarchical Depositional Concepts

Fluvial deposition occurs over a wide range of spatial and temporal scales, driven by forcing conditions that are often cyclical in nature. The processes affecting deposition may be allo-cyclic, that is, driven by forces that transcend the area of deposition (e.g., subsidence, tectonic uplift, climatic variation) or autocyclic, where variation in sedimentary features occurs due to processes within the depositional basin (Beerbower, 1964).

The cyclicity of sedimentary deposits allows them to be categorised using hierarchical schemes. Sedimentologists have developed hierarchical facies modelling approaches to assist

the characterisation of heterogeneous deposits that vary over wide spatial and temporal scales (e.g., Miall, 1991; Aigner et al., 1999). At spatial scales between 10^1 to 10^2 m, the continental sequences and coastal systems of interest to hydrogeologists are typically controlled by high-frequency climatic cycles. These cycles, such as Milankovitch and annual seasonal cycles, influence many important processes (e.g., stream power, sediment availability) that determine fluvial deposition (e.g., Fischer, 1986). Hierarchical frameworks can be used to model continental deposits such as fluvial sequences, the architectural elements within them, their own internal bedding, and other individual event beds.

Hierarchical sedimentary deposits, where larger forms are composed of smaller units, can be delineated by bounding surfaces (or bedding contacts) that represent features at differing spatial and temporal scales (Allen, 1983), as depicted in Figure 2.1 (Miall, 1996). At the highest hierarchical level, allocyclic processes generally control the depositional environment, creating stratigraphic contacts that may form important hydraulic boundaries between contrasting sedimentary deposits (e.g., macroforms, Jackson, 1975). At lower hierarchical levels, variable sediment transport regimes lead to the development of bedforms and sediment textures with varying orientation that control the distribution and connectivity of hydraulic properties at various internal scales within sedimentary deposits. The smallest features represent processes active over geologically short timescales, e.g., seconds to days (first-order surfaces [Miall, 1996], microforms [Jackson, 1975]). Diagenetic processes occurring during and after deposition, such as compaction and deformation of sediments, can also affect the structure and hydraulic properties of fluvial deposits. Multiple methods for modelling heterogeneity and uncertainty may be applied within one hydrogeological modelling approach, and bounding surface classification is a useful framework for delineating these methods.

Architectural element analyses are methods for describing facies in fluvial deposits systematically by accounting for their complex three-dimensional nature (Bridge and Diemer, 1983; Miall, 1985). The classification system for fluvial deposits proposed by Miall (1985) comprises eight architectural elements that make up larger fluvial features, namely: channels, gravel bars and bedforms, sandy bedforms, foreset macroforms, lateral accretion deposits, sediment gravity flow deposits, laminated sand sheets, and overbank fines (see Figure 2.2). These architectural elements are also highly heterogeneous in nature and “reflect the cumulative effect of many dynamic events over periods of tens to thousands of years” (Miall, 1985, p. 266). They are composed of facies that have differing petrophysical characteristics derived from the flow regime in which they were deposited. This is demonstrated in Figure 2.2, where the abbreviations to the right of each architectural element denote the lithofacies using Miall’s classification system, e.g., Gm denotes crudely bedded gravel and Sh denotes horizontally laminated sand (Miall, 1985). Highly heterogeneous fluvial styles represent a challenge to hydrogeolo-

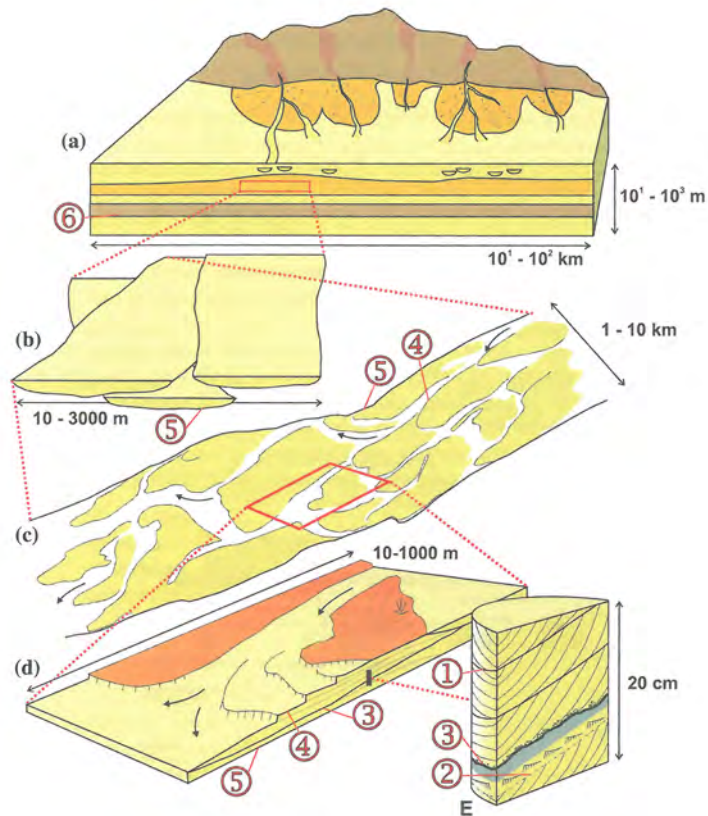


Figure 2.1: Hierarchy of fluvial depositional units (Miall, 2013, Fig. 2.3, p. 12). Numbers in red circles denote the order of the bounding surfaces.

gists wishing to characterise flow and transport through these porous media.

2.1.2 Glaciofluvial Environments

In this thesis, I focus on modelling glaciofluvial depositional features. Glaciofluvial (or glacial outwash) deposits are associated with large ice masses and occur in the proglacial environment, that is, beyond the terminal point of a glacier. Outwash plains, or sandurs, are generally braided-channel systems (Miall, 1977). Typically, the grain-size distribution becomes finer further away from the ice mass as flow energy and channel gradient decreases (Miall, 1977; Brodzikowski and Van Loon, 1987); this is demonstrated in the varying distal, medial, and proximal facies depicted in Figure 2.3. Sediment deposition in the proglacial environment is usually dominated by seasonal meltwater flows (Miall, 1977) but is also influenced by catastrophic flood events, or jökulhlaups, that occur due to the breach of glacial lakes or subglacial volcanic activity (Maizels, 1993).

Siegenthaler and Huggenberger (1993) described the glaciofluvial deposits of the Upper Rhine valley in south western Germany and northern Switzerland as having the following morphological components: (i) interconnected channels, (ii) river bars, (iii) scour pools, and (iv) flood plains. Channels in glaciofluvial deposits are highly variable in space and time. They

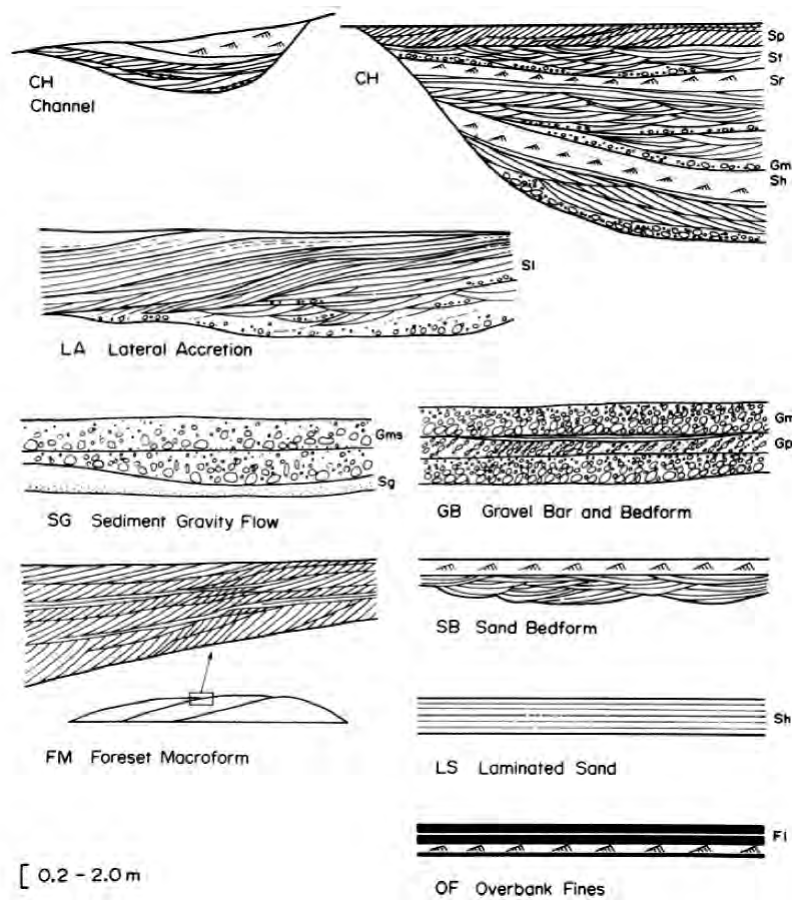


Figure 2.2: Architectural elements (Miall, 1985, Fig. 1, p. 268).

are often paved with clasts that are stacked along the channel bed, sloping in the principal direction of flow (imbrication). Sudden changes in the location and morphology of principal channels (avulsion) can occur during moderate- to high-flow events. Abandoned channels are then gradually filled with sediment – the orientation and texture of deposited sediments is influenced by the flow conditions at the time of deposition. River bars are accumulations of clasts, are widely variable, and are usually elongated along the principal direction of flow. Point bars occur on the inner bank of river bends where flow velocities decrease and lateral accretion occurs. Mid-channel bars are also common, forming between braid channels. Scour pools are localised depressions that occur at the confluences of braided channels (Mosley, 1976). Carling and Glaister (1987) reported separation of coarse and fine clasts downstream of a step in the channel bed morphology (e.g., below the head of a scour pool); such bimodal facies assemblages have been widely observed, including by Siegenthaler and Huggenberger (1993). Flood plains in glaciofluvial systems are generally inactive except during high-flow events; such events may produce sheet-like gravel debris flows that radically alter the morphology of the river system (Siegenthaler and Huggenberger, 1993). High-magnitude flows

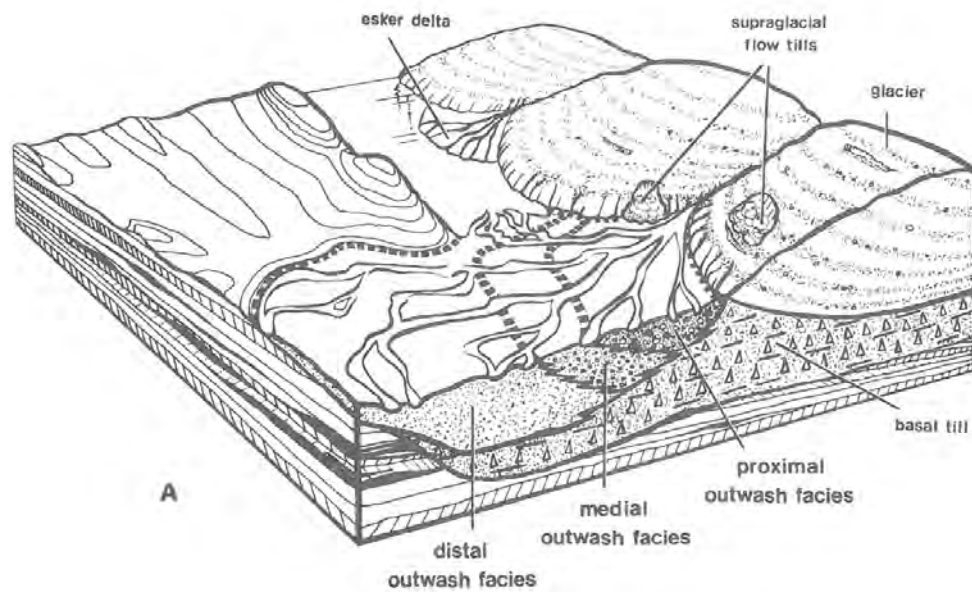


Figure 2.3: Conceptual model of the proglacial environment from Anderson (1989, p. 507), adapted from Brodzikowski and Van Loon (1987).

can also create sandy bedforms (SB in Figure 2.2) in low-velocity zones and deposit overbank fines (OF in Figure 2.2) towards the end of flood events as river stage (water level) decreases and flow velocities reduce (Bierkens and Weerts, 1994).

Scour-pool fills have been of particular interest to sedimentologists as they are thought to be preserved due to their low relative elevation in the stratigraphic sequence (Siegenthaler and Huggenberger, 1993) and can often be delineated in quarry outcrop studies using non-invasive geophysical methods, such as ground-penetrating radar (e.g., Aspiron and Aigner, 1999). They are prevalent in the braided-outwash plains of glacial outwash areas, such as the Upper Rhine valley (e.g., Heinz and Aigner, 2003a).

2.1.3 Implications for Hydrogeology

Whereas sedimentologists who undertake extensive surveys of the geological record are often primarily focused on understanding the environment in which the sediments were deposited, hydrogeologists are interested in how the structure of these deposits affect groundwater flow and solute transport (e.g., Maxey, 1964; Anderson, 1989). Although zones of distinct hydraulic properties (hydrofacies) are generally congruent with lithological units, additional criteria often omitted from geological classifications can be required to adequately characterise an aquifer (Maxey, 1964). Examples of these additional properties include grain size and sorting – characteristics that can have a large effect on hydrogeological properties (e.g., Heinz and Aigner, 2003a, p. 4). Quantification of the hydraulic properties of individual hydrofacies may be performed in the laboratory on disturbed samples, or inferred from easily measured prop-

erties such as grain size and porosity (e.g., Koltermann and Gorelick, 1995). Direct quantification in the field is difficult as the hydraulic tests (e.g., pumping and slug tests) may integrate volumes that cut across hydrofacies boundaries. However, gas pneumatic tests (e.g., Klingbeil et al., 1999) and direct-push injection logging (e.g., Bohling, Liu, Knobbe, et al., 2012) can provide information about the variability of hydraulic conductivity at a smaller scale.

Linking sedimentary features to groundwater flow and solute transport is often difficult, due to inherent uncertainties in the configuration of subsurface hydraulic parameters. Connected features such as buried channels often present preferential pathways for the movement of fluid and transport of solutes (Fogg, 1986). In many fluvial systems, these channels demonstrate a high degree of connectivity between highly permeable units, encouraging flow-focusing (e.g., Werth et al., 2006) and resulting in higher fluid and transport velocities. Alternatively, overbank fines often act as confining layers in aquifer systems due to their low hydraulic conductivity and relatively homogeneous nature. Sedimentary units may also be defined not just in terms of their physical hydrogeological properties, but also geochemical similarities (chemofacies). Correlation between hydraulic conductivity and sorption behaviour (K_D) has been observed in aquifers such as the Borden site, Canada (Allen-King, Halket, et al., 1998), and understanding the spatial distribution of chemofacies in the subsurface is especially applicable in reactive transport modelling (e.g., Loschko et al., 2018).

2.2 Modelling Heterogeneity in Sedimentary Deposits

Modelling heterogeneity in fluvial aquifers is difficult due to the highly dynamic nature of the environments in which sediments were deposited. Methods for modelling heterogeneity in sedimentary deposits can be generally categorised into one or more of the following approaches: (i) descriptive, (ii) process-imitating, and (iii) structure-imitating (Koltermann and Gorelick, 1996). Descriptive modelling approaches are heuristic in nature, making use of intuition or simple and/or empirical relationships between facies within a domain of interest. Process-imitating modelling approaches simulate the major processes that control sedimentary deposition. Structure-imitating approaches focus on replicating the structure of an aquifer by applying known (or assumed) rules of aquifer structures to a model domain. This may include geostatistical methods, where hydraulic conductivity fields are created according to the covariance or higher order measures of dependence observed in actual data, or sedimentation pattern imitation methods, where the characteristic geometries of deposits observed in the field are used to simulate aquifers.

Descriptive Approaches

Descriptive methods combine “site-specific [e.g., borehole data, outcrop and geophysical observations] and regional data [e.g., geological maps] with conceptual depositional models and geologic insight” (Koltermann and Gorelick, 1996, p. 2641). Such methods often rely on the

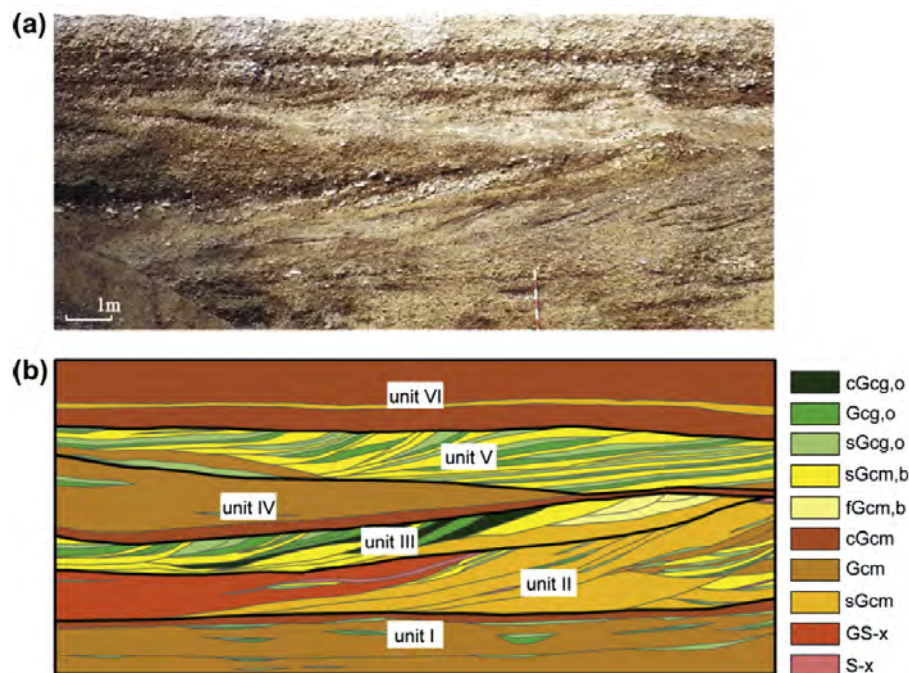


Figure 2.4: Outcrop photograph (a) and hydrofacies distribution (b) of glacial outwash sediments (Bayer et al., 2011, Fig. 4, p. 5).

intuition and expertise of experienced geoscience practitioners. However, descriptive modelling approaches can miss information from more formal characterisation methods (i.e., geostatistics) and cannot account for uncertainty in their interpretation (Johnson and Dreiss, 1989) as they are generally deterministic (i.e., only one realisation is produced). Descriptive methods are most effective where aquifers have undergone significant characterisation. However, with data scarcity, the uncertainty of a descriptive model becomes much higher.

Descriptive approaches are helpful for characterising aquifer analogues – surficial deposits expected to have the same spatial configuration of sedimentary features, and therefore hydraulic properties, as aquifers. Aquifer analogues can provide valuable information that is difficult or impossible to gain from non-invasive characterisation methods or borehole sampling only. The analogues are comprehensively mapped and classified into their constituent facies using ground-penetrating radar (GPR) and/or high-resolution photography of freshly-exposed quarry pit faces. Figure 2.4 shows an example of an aquifer analogue from Bayer et al. (2011), who characterised heterogeneity in the hydrofacies of the Hertten gravel pit in south western Germany. Aquifer analogues have been used in numerous studies on the role of aquifer heterogeneity on solute transport (e.g., Whittaker and Teutsch, 1999; dell’Arciprete et al., 2014; Allen-King, Kalinovich, et al., 2015).

Descriptive methods can be useful for constraining simulations in other sedimentary modelling approaches. For example, Comunian et al. (2011) used the analogues of (Bayer et al., 2011,

see above) to delineate zones in which to apply MPS methods. Descriptive models, such as geological maps, conceptual models (e.g., Lunt et al., 2004), and outcrop maps, can be used as training images in MPS methods (Koltermann and Gorelick, 1996), but should encompass the expected heterogeneity in the deposit to be modelled.

Process-Imitating Approaches

Process-imitating (or genetic) modelling approaches simulate the major depositional, tectonic, hydrological, and climatic processes that control sedimentary deposition (Koltermann and Gorelick, 1996, p. 2636) in a depositional system. The physical processes that generate sedimentary deposits (i.e., fluid flow and sediment transport) are parameterised using the governing equations of sediment transport and deposition. Such models (e.g., Koltermann and Gorelick, 1992; Nicholas et al., 2013) require that the key processes be known and that numerous model parameters and forcing functions are assigned. Process-imitating methods are difficult to condition to data, and can be computationally demanding as the governing equations of fluid flow and sediment transport (or approximations thereof) must be solved at each model time step. Openly available process-based modelling programs, such as FLUMY (MINES ParisTech, 2017) and CAESAR (Coulthard, 2017), are relatively efficient and user-friendly. However, it is not straightforward to apply the outputs of these software in hydrogeological models and therefore I did not implement these methods in this doctoral thesis.

Structure-Imitating Approaches

An important aspect of the implementation of geostatistics in hydrogeology is the idea “that heterogeneity can be described by a ‘structure’, i.e., that the geological processes that created the medium have imposed a pattern on the spatial distribution of the inhomogeneous values” (De Marsily et al., 2005, p. 165). Structure-imitating modelling approaches aim to emulate the geostatistical, probabilistic, or geometric structure of an aquifer.

Two-point geostatistical methods simulate the statistical structure of a deposit based on separation (or lag) distances between two points. These can be grouped into Gaussian and non-Gaussian methods (Koltermann and Gorelick, 1996).

Gaussian methods assume that the underlying distributions of the hydraulic properties are Gaussian. Data (e.g., hydraulic conductivity) may be transformed into log-space and/or with normal scores in order to meet this assumption. Gaussian methods make use of covariance structures, which relate separation distances to how property values vary, derived from field data. Gaussian methods that have been widely implemented in hydrogeological modelling include: the Turning Bands Method (Tompson et al., 1989), spectral methods (e.g., Dietrich and Newsam, 1993), and sequential Gaussian simulation (e.g., Gómez-Hernández and Journel, 1993). These methods generate continuous parameter fields and cannot reproduce the sharp bedding contacts often found in fluvial deposits. For this reason, truncated

Gaussian and pluriGaussian (Armstrong et al., 2011) methods for simulating discrete distributions were developed. These methods apply thresholds to continuous Gaussian fields to produce discrete distributions. Geological information can be used to constrain the threshold values. Alternatively, multiple Gaussian fields with varying geostatistical structures (i.e., ranges, orientation) can be aggregated through “rock type rules” (Armstrong et al., 2011), allowing for the inclusion of geological concepts about the relationship between depositional units. These methods have been implemented in solute transport modelling (e.g. Mariethoz, Renard, Cornaton, et al., 2009), but generally cannot capture the connectivity of natural sedimentary features.

Non-Gaussian (or non-parametric) two-point methods include indicator kriging (Journel, 1983) or transitional probabilities combined with Markov chain models (Carle et al., 1998), as implemented in the geostatistical modelling software T-PROGS (Carle, 1999). T-PROGS has been widely used for simulating heterogeneous porous media in solute transport research (e.g., Engdahl and Weissmann, 2010; Pryshlak et al., 2015; Bianchi and Zheng, 2016) as it has a well-developed interface and can be conditioned to geological data. Another geostatistical approach in hierarchical sedimentary deposits was implemented by Ritzi and coworkers, who developed global spatial correlation functions for cross-stratified sediments. These methods use two-point spatial correlations as well as transitional probabilities between units at different hierarchical scales (Ritzi, Dai, et al., 2004; Ritzi, Huang, et al., 2013). Haslauer et al. (2012) used spatial copula models to simulate non-Gaussian hydraulic conductivity fields based on data from the C.F.B. Borden site, Canada (Sudicky, 1986).

Aquifer model calibration provides parameters that produce an optimal fit to field observations of dependent quantities, such as hydraulic heads or solute arrival times (Anderson et al., 2015). Calibration is often completed in practice through trial-and-error or parameter estimation programs with pre-defined spatial structures (e.g., PEST, Doherty, 2010). The spatial structures can be devised such that they consider geological concepts (e.g., buried channel features). However, these optimisation methods can be sensitive to the parameterisation of the aquifer model, and generally small-scale heterogeneity cannot be uniquely identified. Geostatistical inversion offers a more sophisticated approach to aquifer model calibration methods and combines hydraulic head and other information (e.g., tracer breakthrough curves, borehole flowmeter data) to estimate flow and transport parameters without imposing exact geometries. Conditional simulations provide an ensemble of realisations of a hydraulic conductivity field that meet the data, as opposed to a best estimate of a single smoothed field (Nowak and Cirpka, 2006); these multiple realisations allow for a better estimation of model uncertainty (Zimmerman et al., 1998). Geostatistical inversion methods generally do not account for geological conceptual knowledge, although recent work (Laloy et al., 2018) can integrate

training images that accounts for this.

In this thesis, my aim was to bring more geological information into hydrogeological modelling. I therefore focused on using modelling methods that could explicitly account for features of sedimentary deposits, such as the geometry and configuration of discrete geobodies, sharp erosive surfaces with juxtaposing zones of contrasting hydraulic properties, and bedding structures (i.e., dip and azimuth). Such features can be simulated using object-based and multiple-point geostatistical methods, which I discuss in the next two sections.

2.2.1 Object-Based Modelling Methods

Object-based (or boolean) methods are structure-imitating modelling approaches that simulate the heterogeneity of fluvial deposits by randomly placing geometric objects that represent sedimentary features into the model domain (De Marsily et al., 2005). These methods require an understanding of the characteristic geometries of the depositional system; such methods generally rely on extensive field characterisations (i.e., aquifer-analogue studies) to provide these parameters. Object-based methods originated in reservoir modelling (e.g., Haldorsen and Chang, 1986) but have since been implemented widely in subsurface simulation, as they can preserve the three-dimensional forms of geobodies, are generally computationally efficient, and can be parameterised using probabilistic rules and geometric constraints that are informed by geological observations (Koltermann and Gorelick, 1996). Stochastic simulations are possible by generating ensembles of aquifer models using the same model parameters.

Jussel et al. (1994) used object-based methods to simulate glaciofluvial deposits based on extensive site investigations, including the determination of hydraulic conductivity of hydrofacies and geostatistical characterisation. They generated numerical aquifers using geometric rules for simulating the shape of the sedimentary features and filling these with hydraulic conductivity values randomly drawn from a distribution with mean and variance of that feature type. Scheibe and Freyberg (1995) also used object-based methods to model point bars in a river floodplain. They populated a model domain with sedimentary features at multiple scales, with the geometrical parameters drawn from distributions informed by field observations, and hydraulic conductivity assigned on the basis of the small-scale features. More sophisticated parameterisations of braided-river deposits were developed by Webb and Anderson (1996), Deutsch and Tran (2002), and Ramanathan et al. (2010), among others.

2.2.2 Multiple-Point Geostatistics

Multiple-point geostatistical (MPS) methods simulate aquifer structure and hydraulic parameter fields based on the conditional probabilities of patterns in training images (De Marsily et al., 2005). This approach is becoming increasingly popular, particularly in reservoir modelling applications, and involves analysing training images for spatial patterns. MPS was “born out of a need to address the issue of a lack of physical realism as well as the lack of control in

the simulated fields in traditional modelling” (Mariethoz and Caers, 2015, p. ix). MPS methods are better able to model complex geological features, such as sinuous channels, that cannot be simulated using variograms or other two-point geostatistical methods (Strebelle, 2002; Honarkhah and Caers, 2010).

A key obstacle in the use of MPS methods is that prior knowledge of the variable of interest in the form of training images is required (Linde et al., 2015). This may comprise geological sketches, geophysical data, or aerial imagery (Koltermann and Gorelick, 1996). Data, such as borehole logs or facies proportions, can be used to condition the simulated parameter fields. At each node of a simulation grid the neighbourhood (data within a set distance) is assessed and then compared to the training image. A conditional distribution of values based on node values in matching neighbourhoods in the training image is established and a value is drawn randomly from this and placed at the node in the simulation grid until the grid is completed (Mariethoz and Caers, 2015). The first MPS algorithms could only simulate categorical variables, but recent algorithms, such as DeeSse (Straubhaar, 2017) are also able to simulate multivariate continuous fields.

2.2.3 Combining Modelling Approaches

Methods for modelling heterogeneity in fluvial deposits may combine multiple approaches at different scales of heterogeneity. The method used will depend on the data available and the related uncertainty. Descriptive modelling approaches are appropriate where features can be adequately mapped. This is often possible at larger scales, where contrasts between hydrostratigraphic units can be delineated from borehole information or geophysical measurements. Stochastic modelling approaches can then be used to simulate heterogeneity at a smaller scale than cannot be resolved by these field characterisation methods.

A common approach is to model major stratigraphic contacts using descriptive methods and then model heterogeneity within the major strata (e.g., Weissmann and Fogg, 1999; Comunian et al., 2011). Major stratigraphic contacts may be modelled by manually “connecting the dots” between contacts observed in borehole logs, or with interpolation techniques, such as kriging or implicit modelling using radial basis functions (e.g., LeapFrog Geo, Seequent, 2018). Heterogeneity within the major contacts can then be modelled using stochastic methods. Another approach implemented by Bianchi and Zheng (2016) used facies-based methods (T-PROGS, Carle, 1999) to generate features at scales between 10^0 to 10^2 m and then populate the facies with random values drawn from a hydrofacies-specific distribution.

As discussed in this section, there are numerous methods for simulating heterogeneity in fluvial sedimentary deposits, many of which are openly available. However, the outputs of these methods are often not compatible with standard flow-and-transport modelling packages, or may not account explicitly for sedimentary bedding, which can be used to derive

anisotropy parameters. Therefore, in this thesis I have developed my own simulation method that produces parameter fields, including sedimentary bedding, that can be used in numerical flow-and-transport simulations.

2.3 Quantifying the Effects of Heterogeneity

Heterogeneity in aquifer systems plays a critical role in groundwater flow and solute transport: Freeze and Cherry (1979, p. 397) state that without “the effects of heterogeneities in natural geological materials, the problem of prediction and detection of contaminant behaviour in groundwater flow systems would be easily solved”. This is demonstrated by Darcy’s Law, which can be used to describe flow in porous media, and relates the hydraulic-head field $h(\mathbf{x})$ to the vector of specific discharges \mathbf{q} through hydraulic conductivity \mathbf{K} :

$$\mathbf{q} = -\mathbf{K}\nabla h(\mathbf{x}) \quad (2.1)$$

with the vector of spatial partial derivatives ∇ , and the vector of spatial coordinates \mathbf{x} in the x -, y - and z -directions, respectively. \mathbf{K} is a symmetric, positive-definite, second-order hydraulic-conductivity tensor. Heterogeneity of \mathbf{K} inevitably leads to greater variability in groundwater flow fields.

Heterogeneity is sometimes modelled at a scale much finer than can be practically resolved using flow-and-transport models. Therefore, the resolution of hydrofacies properties must be translated into a coarser resolution suitable for numerical flow analysis. The process of calculating effective hydraulic conductivity is often referred to as upscaling (De Marsily et al., 2005). I did not perform formal upscaling of hydrofacies in this thesis and therefore detailed discussion of upscaling has not been included here. Renard and de Marsily (1997) and Sanchez-Vila, Guadagnini, et al. (2006) provide comprehensive reviews of this topic.

Connectivity

In hydrogeology, connectivity describes the degree to which a porous medium comprises highly conductive pathways through which the preferential movement of water and solutes may occur (Renard and Allard, 2013). These preferential pathways are critical for understanding groundwater flow and solute transport in many porous aquifer systems (e.g., Fogg, 1986; Zheng and Gorelick, 2003). Metrics of connectivity may be static, in that they are derived only from the spatial distribution of hydraulic conductivity, or dynamic, where they are influenced by the processes of interest, such as solute transport (Renard and Allard, 2013, p. 169). The multi-Gaussian fields implemented by many hydrogeologists exhibit a different connectivity (i.e., the intermediate values are connected) to other simulation methods (Zinn and Harvey, 2003). The inability of multi-Gaussian methods to account for the connectivity observed in sedimentary features can lead to significant differences in predictions of flow and transport

(Whittaker and Teutsch, 1999; Kerrou et al., 2008; Bianchi, Zheng, et al., 2011; Zhang and Zhang, 2015).

The minimum hydraulic resistance is a measure of static connectivity in hydraulic conductivity fields that has been implemented by Tyukhova and Willmann (2016) and Rizzo and de Barros (2017). In section 3.3, I analysed the static connectivity of hydraulic conductivity fields by taking line integrals of the hydraulic resistance \mathcal{R} , as defined by Rizzo and de Barros (2017):

$$\mathcal{R}_\Gamma = \int_\Gamma \frac{1}{K} d\gamma. \quad (2.2)$$

where Γ belongs to the set of all possible curves that connect the planes at the model inlet and outlet and K is hydraulic conductivity. The minimum hydraulic resistance for each hydraulic conductivity field is therefore the lowest \mathcal{R} -value in the set and corresponds to the maximum connectivity pathway. Rizzo and de Barros (2017) implemented a graph-theory approach based on Dijkstra's algorithm (Dijkstra, 1959) to efficiently compute the minimum hydraulic resistance. Note that no flow simulation is required to compute the minimum hydraulic resistance. It is thus a property of the hydraulic conductivity field rather than of flow or transport.

2.3.1 Solute Transport

Solute transport and mixing is important in many hydrogeological applications, including the characterisation of groundwater contamination (e.g., the prediction of solute breakthrough curves and delineation of source zones) and associated remediation efforts (e.g., the mixing of reactants). The heterogeneity of hydraulic conductivity has a greater impact on solute transport than groundwater flow as the processes are affected by the variations in fluid flow paths (Gelhar, 1993).

Mixing in the transverse direction is especially important as it can facilitate reactions between electron acceptors present in ambient groundwater (e.g., oxygen) and electron donors (e.g., contaminants), with transverse dispersion coefficients limiting the spatial extent of contamination (Figure 2.5, Cirpka, Frind, et al., 1999). Ham et al. (2004) demonstrated that the length of steady-state plumes undergoing bimolecular reactions was only dependent on transverse dispersivity, and that longitudinal dispersivity is only relevant for transient plume development. Liedl, Yadav, et al. (2011) extended the two-dimensional studies of Cirpka, Frind, et al. (1999), Ham et al. (2004), and Liedl, Valocchi, et al. (2005) into three-dimensional model domains; it was shown numerically that transverse dispersion is also a decisive factor in three dimensions. The importance of transverse mixing in solute transport has been demonstrated by many experimental studies (e.g., Bauer et al., 2009; Ballarini et al., 2014) and field investigations (Anneser2008a; e.g., Tuxen et al., 2006).

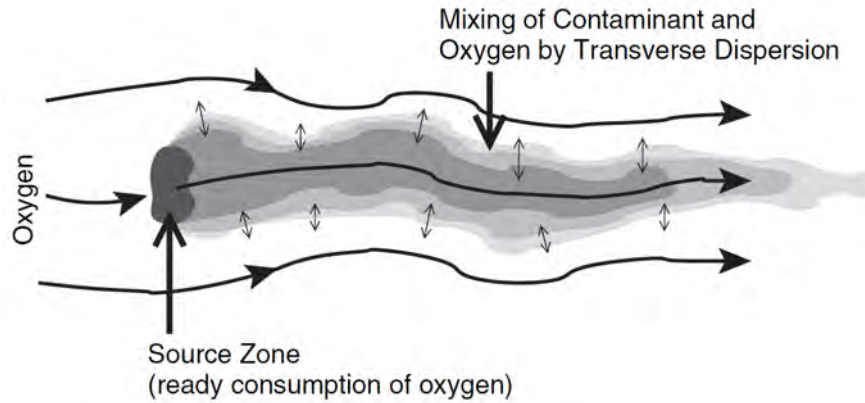


Figure 2.5: Importance of transverse dispersion in steady-state contaminant plumes (from Cirpka, Olsson, et al., 2006, Fig. 1, p. 213).

The movement of a solute through a porous medium is most commonly described using the advection-dispersion equation:

$$\frac{\partial c}{\partial t} + \mathbf{v} \cdot \nabla c - \nabla \cdot (\mathbf{D} \nabla c) = 0 \quad (2.3)$$

with concentration c [$M L^{-3}$], the seepage velocity \mathbf{v} [$L T^{-1}$], and the local hydrodynamic dispersion tensor \mathbf{D} [$L^2 T^{-1}$]. In steady-state transport the first term of Equation 2.3 can be neglected. Heterogeneity of hydraulic conductivity influences solute transport through the seepage velocity $\mathbf{v} = \mathbf{q}/\theta$, with porosity θ [-]. Porosity values do not vary to the same magnitude as hydraulic conductivity, therefore the effect of porosity heterogeneity on solute transport is less than that of hydraulic conductivity (Le Borgne et al., 2015).

Hydrodynamic dispersion describes the spreading of solutes due to velocity variations “caused by spatial heterogeneity of conductivity at a smaller scale than is explicitly modelled” (Zinn and Harvey, 2003, p. 3). It is influenced by the local velocities within the porous medium, which depend on the spatial distribution of hydraulic conductivity and boundary conditions. The hydrodynamic dispersion tensor \mathbf{D} is often parameterised by a linear function of contaminant-specific pore diffusion coefficients and the seepage velocity multiplied by dispersivity values (Scheidegger, 1961), here expressed for the transverse component:

$$D_t = D_p + \alpha_t |\mathbf{v}(\mathbf{x})| \quad (2.4)$$

where D_p [$L^2 T^{-1}$] is the pore diffusion coefficient of the solute and α_t [L] is the transverse dispersivity; again, the seepage velocity \mathbf{v} links solute transport to the groundwater flow field. Local longitudinal dispersion has been demonstrated to have only a minor effect on solute transport in three-dimensional heterogeneous porous media (e.g., Zarlenga and Fiori, 2013),

and can thus be neglected in solute transport modelling. For simplicity, the dispersion tensor \mathbf{D} may be oriented in the direction of the mean groundwater velocity (here the x -direction), instead of the local velocity:

$$\mathbf{D}(\mathbf{x}) = \begin{bmatrix} 0 & 0 & 0 \\ 0 & D_t(\mathbf{v}(\mathbf{x})) & 0 \\ 0 & 0 & D_t(\mathbf{v}(\mathbf{x})) \end{bmatrix} \quad (2.5)$$

Steady-State, Conservative Advective-Dispersive Solute Transport

In this work, I solved steady-state conservative advective-dispersive solute transport using the scheme devised by Cirpka, Chiogna, et al. (2015). The scheme is based on streamlines from particle tracking methods (described below). Concentration distributions are solved at observation planes that are placed at regular distances orthogonal to the mean flow direction. The advective component of transport is based on the particle travel times between observation planes, and transverse dispersion between streamline is solved using a cell-centred Finite Volume method using Voronoi tessellation (see Cirpka, Chiogna, et al., 2015, section 3).

Particle Tracking

Particle tracking has been widely used to quantify solute transport behaviour numerically (e.g., Schwartz, 1977; Zinn and Harvey, 2003; Cirpka, Chiogna, et al., 2015). Advective-dispersive transport (equation (2.3)) can be formulated within the Lagrangian framework of particle tracking with random walk:

$$\mathbf{x}_p(\tau + \Delta\tau) = \mathbf{x}_p(\tau) + \Delta\tau\mathbf{v}\mathbf{x}_p + \boldsymbol{\zeta} \quad (2.6)$$

subject to

$$\mathbf{x}_p(0) = (0, y_{p,0}, z_{p,0}) \quad (2.7)$$

where \mathbf{x}_p is the vector of particle coordinates, τ is the travel time, $\Delta\tau$ is the travel-time increment, $[y_{p,0}, z_{p,0}]$ are the y, z coordinates of the particle at the inlet plane $x = 0$, and the random-walk component $\boldsymbol{\zeta}$, which is a vector of multi-Gaussian random numbers with zero mean and covariance matrix $2\mathbf{D}\Delta\tau$.

Advective particle trajectories can be quantified using stretching and folding metrics – kinematic descriptors that were developed by Falk and Langer (1998) and Kelley and Ouellette (2011). Chiogna, Cirpka, et al. (2015) applied the concept to steady-state advective transport in three-dimensional anisotropic porous media. In that work, stretching and folding were quantified for streamtubes – ensembles of streamlines originally configured as a circle perpendicular to the main direction of flow at the model inlet face. A linear transformation matrix is

fitted to the deformed streamtube at planes throughout the model domain. The stretching metric represents the normalised, squared L_2 -norm of the linear deformation of the original streamtube configuration; folding is the non-linear component of the deformation. As the metrics for each streamtube depend on its starting position, ensembles of streamtubes with different initial positions are used and the metrics are averaged over the model domain. I used this descriptor in the first work package (section 3.1).

To solve advective particle tracking numerically in this thesis, I adopted the semi-analytical method of Pollock (1988), which assumes that the velocity components in each direction vary linearly within the individual model grid cells. The Pollock method was implemented in MATLAB, using the parallel computing capabilities of the graphical processing unit.

Macrodispersion

Macrodispersion can be defined as the spreading of a solute “due to variability in local advective velocity” (Kitanidis, 1992, p. 5) The macrodispersion tensor is commonly characterised by calculating half the rate of change of the normalised second-central spatial moments (e.g., Gelhar, 1993). Longitudinal macrodispersion can be calculated by multiplying half the longitudinal gradient of the normalised second-central temporal moment with the cubed effective velocity. Dentz et al. (2000) distinguished between “ensemble” and “effective” dispersion tensors \mathbf{D}_{ens} and \mathbf{D}_{eff} , respectively, based on concepts introduced by Kitanidis (1988) and Dagan (1989).

$$\mathbf{D}^{ens}(t) = \frac{1}{2} \frac{\partial}{\partial t} \mathbf{M}_{xx}^{2c} (E [(c(\mathbf{x}, t))]) \quad (2.8)$$

$$\mathbf{D}^{eff}(t) = \frac{1}{2} \frac{\partial}{\partial t} E [\mathbf{M}_{xx}^{2c}(t)] \quad (2.9)$$

$$\text{with } \mathbf{M}_{xx}^{2c}(t) = \frac{\int_{V_\infty} (\mathbf{x} - \mathbf{x}_c(t))^2 c(\mathbf{x}, t) d\mathbf{x}}{\int_{V_\infty} c(\mathbf{x}, t) d\mathbf{x}} \quad \text{and} \quad \mathbf{x}_c(t) = \frac{\int_{V_\infty} \mathbf{x} c(\mathbf{x}, t) d\mathbf{x}}{\int_{V_\infty} c(\mathbf{x}, t) d\mathbf{x}} \quad (2.10)$$

in which $E[\cdot]$ denotes the expected-value operator, and the integral $\int_{V_\infty} d\mathbf{x}$ implies integration from $-\infty$ to $+\infty$ over all spatial dimensions. \mathbf{M}_{xx}^{2c} and \mathbf{x}_c are the normalised second central moments and centre of mass of the solute cloud, respectively. The effective (or relative) dispersion is a measure of the average spread of the individual plumes, whereas the ensemble (or absolute) dispersion also includes the uncertainty of locating the plume centre.

Bulk ensemble and effective dispersivities can also be calculated based on two-particle statistics of particle-tracking random-walk (PT-RW) trajectories, with the random displacement $\boldsymbol{\xi}$ in equation (2.6) restricted to the (y, z) directions:

$$\alpha_\ell^{ens} = \frac{1}{2} \frac{d\sigma_\tau^2}{dx} \bar{\sigma}^2, \quad \alpha_\ell^{eff} = \frac{1}{2} \frac{d\gamma_\tau}{dx} \bar{\sigma}^2 \quad (2.11)$$

$$\alpha_y^{ens} = \frac{1}{2} \frac{d\sigma_y^2}{dx}, \quad \alpha_y^{eff} = \frac{1}{2} \frac{d\gamma_y}{dx} \quad (2.12)$$

$$\alpha_z^{ens} = \frac{1}{2} \frac{d\sigma_z^2}{dx}, \quad \alpha_z^{eff} = \frac{1}{2} \frac{d\gamma_z}{dx} \quad (2.13)$$

with the variances σ^2 and semivariograms γ of travel times and displacements in the y - and z -directions (τ , y , and z , respectively) for pairs of particles introduced at the same location at the inlet face.

Transverse Moments of Steady-State Concentration Distributions

Because it can be difficult to quantify the exact distribution of solute plumes in groundwater, the statistical moments of concentration distributions can be helpful in understanding solute transport in steady-state plumes. The zeroth moment $m_0(x)$ and the normalised first $\mathbf{m}_1(x)$ and second central moments $\mathbf{M}_{2c}(x)$ in the transverse directions are defined as:

$$m_0(x) = \int_0^{\ell_y} \int_0^{\ell_z} c(\mathbf{y}, x) q_x^{in}(\mathbf{y}) dydz \quad (2.14)$$

$$\mathbf{m}_1(x) = \int_0^{\ell_y} \int_0^{\ell_z} \mathbf{y} c(\mathbf{y}, x) q_x^{in}(\mathbf{y}) dydz / m_0(x) \quad (2.15)$$

$$\mathbf{M}_{2c}(x) = \int_0^{\ell_y} \int_0^{\ell_z} (\mathbf{y} - \bar{\mathbf{y}}) \otimes (\mathbf{y} - \bar{\mathbf{y}}) c(\mathbf{y}, x) q_x^{in}(\mathbf{y}) dydz / m_0(x) \quad (2.16)$$

where $c(\mathbf{y}, x)$ the concentration of particles at cross section x with the transverse coordinates $\mathbf{y} = (y, z)$ and $q_x^{in}(\mathbf{y})$ is the corresponding initial specific discharge at the model inlet face. The normalised first moment ($\mathbf{m}_1(x)$) is the mean centre of mass of the concentration distribution, and the second central moments (σ_y^2 , σ_z^2 , and the mixed moment C_{yz}) describe the spreading of the plume about the centre of mass. The transverse moments of model ensembles can thus provide predictions of plume centres and spreading.

Plume Dilution

While second-central moments (i.e., macrodispersion) are an adequate metric for the spread of a solute plume, they do not adequately determine the mixing of the plume with the surrounding ambient groundwater. Kitanidis (1994) devised the concept of a (volumetric) dilution index, based on the information entropy metric proposed by Shannon (1948). Rolle et al. (2009) applied this concept to steady-state plumes by introducing the flux-related dilution index $E_Q(x)$ [$L^3 T^{-1}$], providing an Eulerian metric of transverse solute mixing:

$$E_Q(x) = \exp \left[- \int_{-\infty}^{+\infty} \int_{-\infty}^{+\infty} p_Q(x, y, z) \cdot \ln(p_Q(x, y, z)) \cdot q_x(x, y, z) dy dz \right] \quad (2.17)$$

in which $p_Q(x, y, z)$ [$T L^{-3}$] denotes the flux-weighted density of the solute mass within the control plane at distance x :

$$p_Q(x, y, z) = c(x, y, z) \left(\int_{-\infty}^{+\infty} \int_{-\infty}^{+\infty} c(x, y', z') q_x(x, y', z') dy' dz' \right)^{-1} \quad (2.18)$$

and q_x denotes the specific-discharge component in the x -direction. The flux-related dilution index may be interpreted as the effective volumetric flux that is occupied by the mass flux of the solute. The metric corrects for the compression and expansion of the plume cross section in high- and low-velocity zones – something not accounted for in transverse moments. The flux-related dilution index is not directly affected by strictly kinematic plume deformation, whereas it is influenced by indirect effects caused by enhanced transverse-dispersive mass flux transfer across the extended plume surface.

2.3.2 Anisotropy in Flow and Transport

Hydraulically anisotropic porous media can induce complex groundwater flow fields. Bakker and Hemker (2002; 2004) demonstrated this with the groundwater whirls – bundles of spiralling groundwater streamlines – that they modelled in non-stationary anisotropic porous media. Stauffer (2007) reported distortion of flow paths in synthetic porous media with inclined bedding, supporting the findings of Bakker and Hemker. Porous media may be considered anisotropic if the local values of hydraulic conductivity are dependent on the spatial orientation of the applied hydraulic gradient. In three dimensions, \mathbf{K} in equation (2.1) is a 3×3 tensor:

$$\mathbf{K} = \begin{bmatrix} K_{xx} & K_{xy} & K_{xz} \\ K_{yx} & K_{yy} & K_{yz} \\ K_{zx} & K_{zy} & K_{zz} \end{bmatrix}$$

If \mathbf{K} is isotropic, it simplifies to the identity matrix times the scalar hydraulic conductivity. In general, \mathbf{K} is anisotropic, which means that its value varies according to the direction of flow. Horizontal anisotropy in hydraulic conductivity is common in sedimentary systems and is often approximated by dividing the hydraulic conductivity in the horizontal direction ($K_h = K_{xx} = K_{yy}$) with an anisotropy ratio a to obtain the value of hydraulic conductivity in the vertical direction ($K_v = K_{zz} = K_h/a$). However, if the hydraulic conductivity is not oriented in the principal direction of the system of coordinates, the off-diagonal components

of \mathbf{K} cannot be neglected.

Complex flow topologies in anisotropic porous media were investigated by Chiogna, Rolle, et al. (2014) and helicity was found to occur in both homo- and heterogeneous hydraulic conductivity fields. They extended this study of streamline topology in Chiogna, Cirpka, et al. (2015), using stretching and folding (see section 2.3.1) to quantify the topology of the streamlines. Cirpka, Chiogna, et al. (2015) assessed transverse mixing in non-stationary anisotropic heterogeneous media of Chiogna, Cirpka, et al. (2015) using the flux-related dilution index (see *Plume Dilution*, section 2.3.1). The synthetic porous media used in the studies of anisotropic effects mentioned in this paragraph did not resemble fluvial deposits. Fluvial depositional processes can cause phenomena such as cross-bedding, imbrication, depositional layering, upwards (or inverse) fining, and laminations in aquifer systems. These natural phenomena alter the anisotropy of the porous media and should be accounted for in modelling approaches.

In order to explore the effects of realistic anisotropy on solute transport, I developed synthetic porous media with variable anisotropy based on plausible bedding structures. I computed the full anisotropic hydraulic conductivity tensor by rotating the diagonal tensor of the principal values using a rotation matrix. A full 3×3 hydraulic-conductivity tensor \mathbf{K}_i was assigned to each model grid cell i by taking the product of the scalar within-bedding hydraulic conductivity value $K_{\parallel,i}$ (analogous to K_h), a diagonal anisotropy matrix \mathbf{M}_i (expressing the ratio of across-bedding to within-bedding conductivity), and the rotation matrix \mathbf{R}_i , which is derived from dip ψ and azimuth κ of the bedding:

$$\mathbf{K}_i = K_{\parallel,i} \mathbf{R}_i \mathbf{M}_i \mathbf{R}_i^T \quad (2.19)$$

$$\mathbf{R}_i = \begin{bmatrix} \cos(\kappa) \cos(\psi) & \sin(\kappa) & \cos(\kappa) \sin(\psi) \\ -\sin(\kappa) \cos(\psi) & \cos(\kappa) & -\sin(\kappa) \sin(\psi) \\ -\sin(\psi) & 0 & \cos(\psi) \end{bmatrix} \quad (2.20)$$

$$\mathbf{M}_i = \begin{bmatrix} 1 & 0 & 0 \\ 0 & 1 & 0 \\ 0 & 0 & a^{-1} \end{bmatrix} \quad (2.21)$$

where $K_{\parallel,i}$ is the within-bedding hydraulic conductivity in cell i and $a = K_{\parallel}/K_{\perp}$ is the ratio of hydraulic conductivity parallel and perpendicular to the bedding, respectively.

Although there is abundant numerical and experimental evidence to support the effects of heterogeneity on the distribution of contaminants in the subsurface, many studies have used spatial distributions of hydraulic parameters that do not represent observed sedimentary deposits. A lack of geological plausibility is also often missing from stochastic approaches to

hydrogeology. Such approaches may produce parameter fields that adequately replicate large-scale groundwater flow and solute transport data (e.g., hydraulic head fields, solute breakthrough curves). However, as the parameter fields are often not consistent with depositional concepts, small-scale variation in flow and transport may not be captured. Further investigation into the differences between more traditional methods of simulating subsurface heterogeneity and emerging techniques is thus required. In this thesis, I aimed to quantify what role geological realism plays in groundwater flow and solute transport.

3 Results and Discussion

In this chapter, I summarise the three main work packages of my thesis. The accepted publications and submitted manuscript can be found in Appendix A.

3.1 Sedimentary Anisotropy in Scour Pool Features

The traditional stochastic perspectives of flow and transport in heterogeneous porous media (e.g., Dagan, 1989; Rubin, 2003) assume that hydraulic conductivity is multi-Gaussian and locally isotropic. With this assumption, it is the spatial variability of hydraulic-conductivity values that causes fluctuations in velocities, and subsequent spreading and mixing of solute plumes. However, analogues of porous media observed in the field demonstrate spatial variation that suggests that the hydraulic-conductivity tensor \mathbf{K} is anisotropic with spatially variable orientation of the tensor (Jussel et al., 1994). Such anisotropy can induce complex flow topology and chaotic streamline trajectories (Sposito, 2001), and has subsequent effects on transverse mixing in steady-state solute plumes (e.g., Chiogna, Cirpka, et al., 2015; Cirpka, Chiogna, et al., 2015). However, the porous media used in these previous studies were not representative of sedimentary features observed in the field.

The features modelled in this work package mimic scour-pool fills. These sedimentary features have been observed widely in braided-river deposits (e.g., Siegenthaler and Huggenberger, 1993; Heinz, Kleineidam, et al., 2003) and have most likely been preserved due to their low elevation with respect to other depositional elements (Siegenthaler and Huggenberger, 1993). The formation and filling of these features, as summarised in Figure 3.1, creates deposits with spatially variable orientation (i.e., cross-bedding) that causes anisotropy of hydraulic properties. Scour-pool fills are typically elongated in the direction of paleoflow and have the form of truncated ellipsoids, with a concave-upward lower bounding surface. Previous flow-and-transport studies have found that the anisotropy and configuration of internal structures in scour-pool fills can induce helical motion (Stauffer, 2007) and enhance advective mixing and flow deviation (Huber and Huggenberger, 2016).

The aim of this work package was to investigate whether the complex groundwater flow and solute transport dynamics reported previously in model problems (e.g., Bakker and Hemker, 2002; Cirpka, Chiogna, et al., 2015) also occur in sedimentary structures that exhibit external geometries and internal anisotropy that resemble features observed in the field.

3.1.1 Model Setup and Methods

The depositional features simulated in this work package were analogous to stacks of scour-pool fills reported by Heinz, Kleineidam, et al. (2003) in the upper Rhine valley, south western Germany, and Browne and Naish (2003) in the Canterbury Plains of New Zealand. The fea-

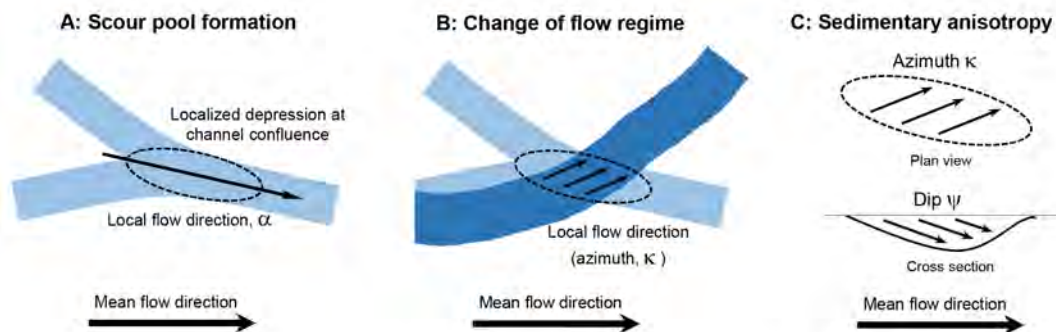


Figure 3.1: Conceptual model of scour-pool fill development after Siegenthaler and Huggenberger (1993). (A) Formation of a scour at the confluence of two stable channels. (B) Anisotropic filling of the scour at a later time, reflecting the later flow direction. (C) Plan view and cross section of a scour fill feature (Bennett, Haslauer, and Cirpka, 2017, Fig. 1, p. 3).

tures were simulated using an object-based modelling approach similar to Jussel et al. (1994), but in three dimensions. Model grid cells at points (x, y, z) were assigned to trough i , provided the following conditions were met:

$$\frac{((x - X_i) \cos(\alpha_i) + (y - Y_i) \sin(\alpha_i))^2}{\ell^2} + \frac{((x - X_i) \sin(\alpha_i) + (y - Y_i) \cos(\alpha_i))^2}{w^2} + \frac{(z - Z_i)^2}{d^2} \leq 1 \wedge z \leq Z_i \quad (3.1)$$

with the central coordinates of trough i , X_i , Y_i , and Z_i , the angle between the major axis of the trough and the mean flow direction α_i , and the half-length, half-width, and depth of the troughs, ℓ , w , and d respectively, set to be identical for all troughs. An ensemble of 100 trough realisations was generated and one realisation thereof is depicted in Figure 3.2.

Five test cases were devised, with either hydraulic anisotropy and/or heterogeneity of isotropic hydraulic conductivity applied (see Table 3.1). I calculated hydraulic anisotropy using equation 2.19 from randomly generated bedding parameters. The trough features were block-wise homogeneous so that all model grid cells within a particular trough had the same hydraulic parameters. The setup of each test case (aside from case 1) was applied to all generated trough fields.

I took geometric model parameters (e.g., trough axes lengths, bedding parameters) from observations of braided river deposits in the Upper Rhine valley where possible (Siegenthaler and Huggenberger, 1993; Beres et al., 1999; Heinz and Aigner, 2003a). Hydraulic parameters were derived from characterisation and/or numerical studies in similar depositional environments (Klingbeil et al., 1999; Janković et al., 2009).

In this work package, I used an infinite periodic model domain and applied a uniform-

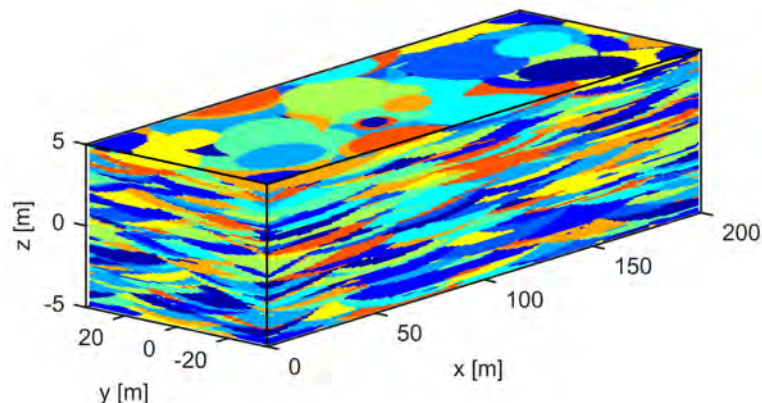


Figure 3.2: One realisation of the generated trough geometries; colours denote individual troughs (from Bennett, Haslauer, and Cirpka, 2017, Fig. 2, p. 9).

Table 3.1: Summary of test cases.

Isotropic hydraulic conductivity K^{iso}	Local \mathbf{K} -tensor	
	Isotropic	Anisotropic, rotated
Homogeneous	Case 1	Case 2
Heterogeneous ($\sigma_{\ln K}^2=1$)	Case 3	Case 4
Heterogeneous ($\sigma_{\ln K}^2=2.3$)	Case 3-high	-

in-the-mean negative hydraulic gradient (e.g., Dykaar and Kitanidis, 1992; Cirpka, Chiogna, et al., 2015). This removed any potential boundary effects in the numerical simulations, and ensured particle tracking was not limited by the model domain. Steady-state groundwater flow was solved using the mixed-hybrid finite element method (e.g., Arnold and Brezzi, 1985) with zero-order Raviart-Thomas elements (Raviart and Thomas, 1977) extended into three dimensions, i.e., cuboids (Nedelec, 1980). This method can handle full three-dimensional \mathbf{K} tensors. Conservative advective-dispersive solute transport was solved using the method of Cirpka, Chiogna, et al. (2015), summarised in 2.3.1.

3.1.2 Results and Discussion

In the ensembles of groundwater flow fields, hydraulic-head distributions in all test cases showed little variation from one another. Ensemble averages of standard deviation of specific discharge showed more variation between test cases. These values for specific discharge in the mean direction of flow q_x seemed to be most affected by the heterogeneity of isotropic hydraulic conductivity. However, rotation of the \mathbf{K} -tensor affected the variability of q_y , with

the anisotropic test cases showing more variance than isotropic test cases with equivalent or lower variance of K^{iso} . Variability of q_y may also have been affected by the geometry of the scour-pool fills.

Advective particle-tracking trajectories better elucidate the differences between the non-trivial test cases (Figure 3.3). In the isotropic test cases, the streamline trajectories fluctuate, and these fluctuations are more pronounced in case 3-high. However, in these isotropic cases, the streamline topology (i.e., their location with respect to neighbouring streamlines) hardly changes. Conversely, the anisotropic test cases demonstrated chaotic streamline trajectories, with interweaving of streamlines and apparent changes in the configuration of streamline neighbours. These configuration changes are supported by the evolution of stretching and folding metrics in the test case ensembles. Stretching (linear deformation of the streamtubes) and folding (non-linear component of streamtube deformation) is by one to two orders of magnitude larger in the anisotropic test cases than in the isotropic ones. In the isotropic, but highly heterogeneous, case 3-high, an early transition from stretching- to folding-dominated behaviour was observed, which suggests that non-linear plume deformation is enhanced by heterogeneity of K^{iso} . Despite this early transition in case 3-high, it is clear that plume deformation is increased in hydraulically anisotropic test cases, creating larger plume surface areas that facilitate the mixing of ambient and plume groundwater.

Advective arrival-time distributions reflect the variability and correlation structure of the longitudinal velocity components, which are primarily influenced by the spatial variability of isotropic hydraulic conductivity. This implies that internal anisotropy is irrelevant for longitudinal spreading, and that the traditional focus on the heterogeneity of isotropic hydraulic conductivity is suitable for studies of longitudinal macrodispersion.

Bulk dispersivities derived from both linear stochastic theory and particle tracking with transverse random-walk components (PT-RW) showed a similar dominance of isotropic hydraulic conductivity on effective and ensemble dispersivities in the longitudinal direction, suggesting that internal anisotropy does not affect longitudinal velocity fluctuations. However, internal anisotropy led to larger dispersivities in the transverse horizontal directions than in isotropic test cases, as particle trajectories move horizontally around lower hydraulic conductivity zones. In general, the agreement between dispersivities derived from linear stochastic theory and PT-RW was worse when even relatively weak heterogeneity ($\sigma_Y^2 = 1$) was introduced.

Steady-state concentration distributions were very different between the test cases, as can be seen in Figure 3.4. The test cases that included internal anisotropy (cases 2 and 4) demonstrate considerable deformation of the initial source distribution, particularly in the transverse horizontal direction. The enlarged surface area and extensive lateral spreading of the plume

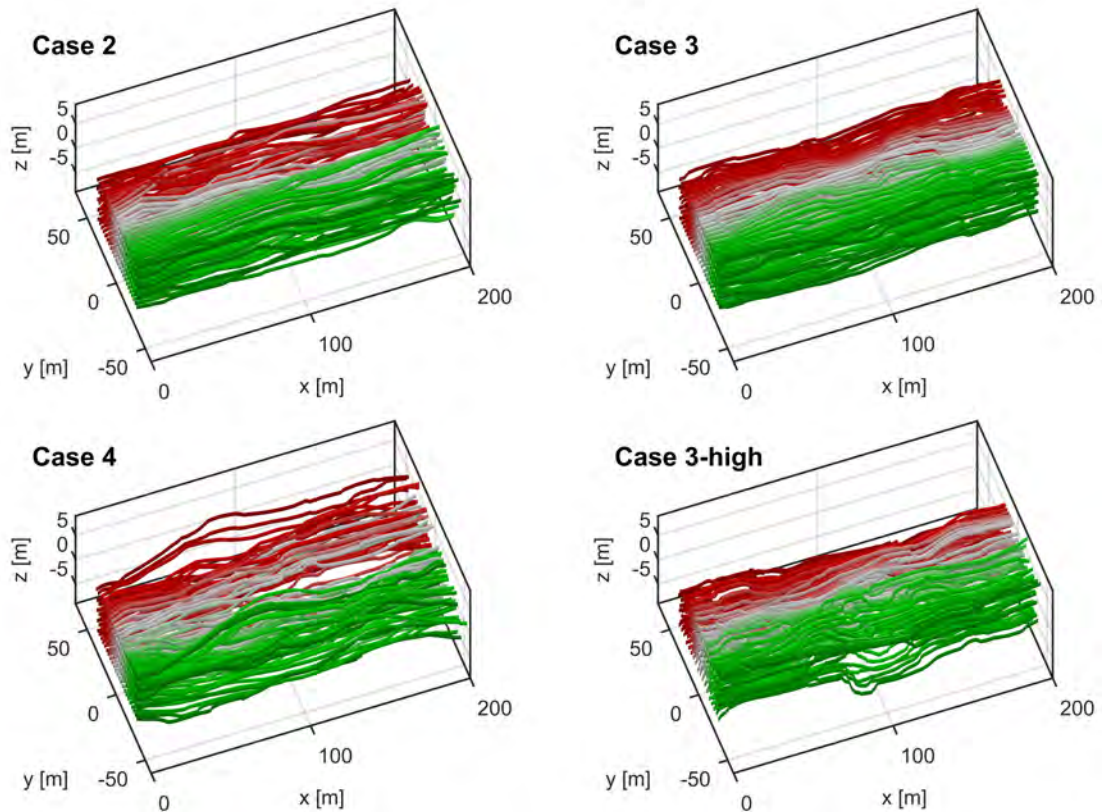


Figure 3.3: Advective streamlines in four of the test cases. Colour of the streamlines denotes the initial y -coordinate value of the streamline. Cases are according to Table 3.1. (from Bennett, Haslauer, and Cirpka, 2017, Fig. 3, p. 12).

enhances mixing between water within the plume and ambient groundwater. In the isotropic test cases (cases 1, 3, and 3-high), the plume remains relatively compact with little lateral spreading and few intermediate concentration values visible.

3.1.3 Conclusions and Implications

The results of this work package suggest that sedimentary anisotropy should be considered when examining the transverse deformation and mixing of steady-state solute plumes. Variation in sedimentary anisotropy causes deformation of material surfaces, which in turn enlarges surface areas over which mass transfer between plume and ambient water can occur.

Heterogeneity of isotropic hydraulic conductivity contributes to the variability of longitudinal groundwater velocity components and therefore longitudinal spreading and mixing. Beaudoin and de Dreuzy (2013) demonstrated that greater variability of isotropic hydraulic conductivity can impact transverse dispersion coefficients. However, the results of the present work package suggest that internal anisotropy is more relevant to transverse mixing than scalar values of hydraulic conductivity, even at relatively low levels of heterogeneity ($\sigma_Y^2 = 1$).

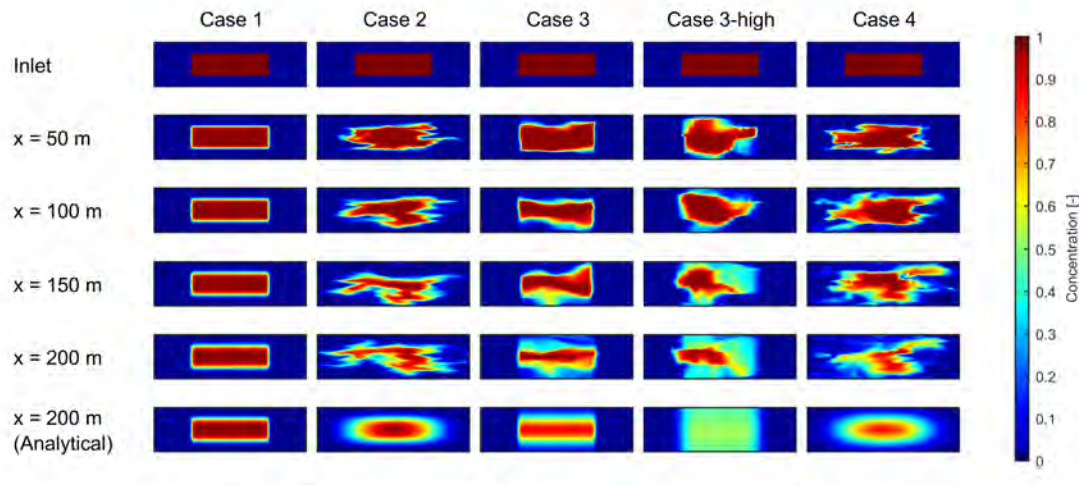


Figure 3.4: Steady-state concentration distributions in observation planes for all test cases for one trough realisation. The bottom row shows the analytical concentration distribution at the model outlet calculated from two-particle semivariograms of transverse displacement of random-walk particle trajectories. The spatial dimensions of the cross sections are $70 \text{ m} \times 10 \text{ m}$ ($20 \times$ vertical exaggeration) and cases are according to Table 3.1. (from Bennett, Haslauer, and Cirpka, 2017, Fig. 7, p. 16).

This work package focused on a single sedimentary feature present in braided-river deposits: scour-pool fills. However, these deposits include a wide range of sedimentary features at varying scales. It is therefore necessary to explore groundwater flow and solute transport in more complex sedimentary models. Currently, the complex groundwater velocity flow fields that are induced by sedimentary anisotropy cannot be measured at the field scale. New field characterisation methods are thus required to further quantify and understand transverse mixing in aquifer systems.

3.2 A Framework for Generating Fluvial Subsurface Models

Geological conceptual models and hierarchical modelling frameworks (e.g., Aigner et al., 1999) are helpful for understanding subsurface heterogeneity in a hydrogeological context (Anderson, 1989). However, it is often difficult to translate field observations and site conceptual models into parameter fields that can be used in numerical flow and transport simulations. Thus, hydrogeological research needs a tool that can be used to assess the effects of different geological conceptual models and parameterisations on groundwater flow and solute transport in a quantitative manner (i.e., coupled with predictive flow-and-transport modelling).


The key goals of the framework development were: (i) The simulation of spatially distributed hydraulic parameter fields (including bedding orientations) that are based on geological concepts; and (ii) the creation of an aquifer simulation package that can be extended by other users. To this end, I developed the Hydrogeological Virtual Realities (HyVR) package, which uses object-based methods to simulate subsurface heterogeneity at a scale relevant for groundwater studies at contaminated sites (10^1 to 10^3 m) and can generate ensembles of parameter fields that can be used to explore the effects of sedimentary structures on groundwater flow and solute transport.

3.2.1 Modelling Concepts

To characterise the sedimentary features in this work package, I defined a hierarchical modelling framework (e.g., Miall, 1991; Aigner et al., 1999) that comprises five hierarchical scales: major strata, architectural elements, hydrofacies assemblages, hydrofacies, and microstructure (summarised in Figure 3.5). Stratigraphic contacts are large-scale features (10^2 to 10^4 m in lateral extent) that represent allocyclic changes to depositional environments controlled by tectonic or climatic forcing. Architectural elements are sedimentary features formed by autocyclic processes (Beerbower, 1964) that occur over periods of tens to thousands of years (Miall, 2013) and range in lateral extent between 10^1 to 10^2 m (Miall, 1985). Hydrofacies assemblages are internal structures within architectural elements that have a coherent spatial arrangement and are hydrogeologically distinct; they may have a lateral extent of 10^0 to 10^2 m. The hydrofacies that make up such assemblages are units of similar hydraulic properties and may be continuous over lateral extents between 10^{-1} and 10^1 m. In this hierarchical classification, variability within hydrofacies has been denoted as microstructure and represents variations of hydraulic properties at scales between 10^{-3} and 10^{-1} m.

3.2.2 Modelling Methods

Large-scale strata and architectural element boundaries are simulated by assigning either flat or two-dimensional random fields at mean contact surface elevations. The user sets the boundary elevations for the major strata as an input parameter. The boundaries and type of architectural elements can either be randomly generated or set by the user.



Hierarchical scale	Example feature	Lateral extent
Major strata/ contacts	<ul style="list-style-type: none"> ◦ Glacial ◦ Fluvial 	10^2 to 10^4 m
Architectural elements	<ul style="list-style-type: none"> ◦ Channels ◦ Scour-pool fills ◦ Gravel and sand bars 	10^1 to 10^2 m
Hydrofacies assemblages	<ul style="list-style-type: none"> ◦ Hydraulically distinct zones 	10^0 to 10^2 m
Hydrofacies	<ul style="list-style-type: none"> ◦ Openwork gravel ◦ Sandy silt ◦ Massive sand 	10^{-1} to 10^1 m
Microstructure	<ul style="list-style-type: none"> ◦ Hydraulic conductivity ◦ Porosity 	10^{-3} to 10^{-1} m

Figure 3.5: Hierarchical modelling framework implemented in HyVR (from Bennett, Haslauer, Ross, et al., 2018, Fig. 1, p. 3).

I applied an object-based approach to simulate hydrofacies assemblages using the following three simplified geometries: extruded parabolas, truncated ellipsoids, and sheets (Figure 3.6). Truncated ellipsoids are identical to those described in section 3.1.1. Extruded parabolas can be generated along arbitrary curves of variable sinuosity to create channel-like features. Sheets are tabular, laterally extensive units that can be used to approximate a variety of such sedimentary features. Using these three geometries, a range of fluvial architectural elements could be simulated, including channels, scour-pool fills, gravel and sand bars, and laminated sand or silty/clay units.

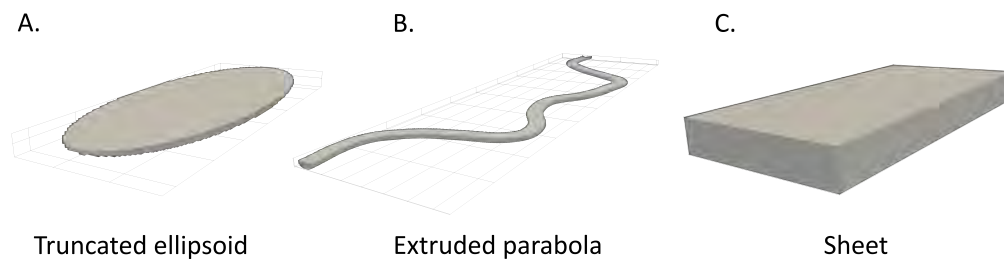


Figure 3.6: Hydrofacies assemblage geometries currently implemented in HyVR (from Bennett, Haslauer, Ross, et al., 2018, Fig. 2, p. 4).

Hydrofacies assemblages can include multiple hydrofacies with varying bedding properties (Figure 3.7). Dip sets are hydrofacies with a set thickness and dip value that can be simulated in all hydrofacies assemblages; the user can control the sequence of repetition. Lag surfaces can be simulated at the base of erosive hydrofacies assemblages (i.e., extruded parabolas and truncated ellipsoids). The thickness of the lag surface and the hydrofacies type are input parameters. Truncated ellipsoids can have an additional internal configuration of nested ellip-

soidal hydrofacies called bulb sets. The dip values in bulb-set truncated ellipsoids are based on the three-dimensional gradient at the ellipsoid boundary (Figure 3.7, Bulb dip). Microstructure is simulated within hydrofacies using Gaussian random fields generated using the spectral method of Dietrich and Newsam (1993), with mean and variance input parameters set for each hydrofacies.

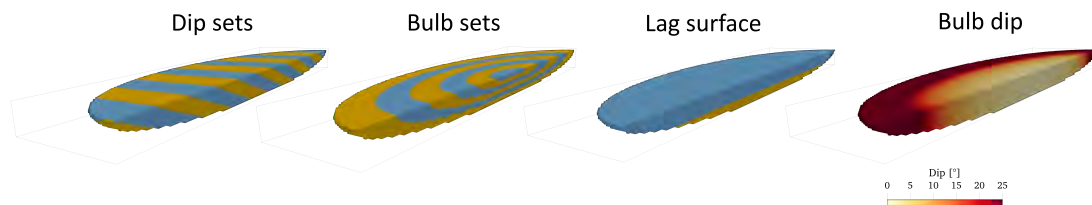


Figure 3.7: Internal structures of truncated ellipsoids generated using HyVR (from Bennett, Haslauer, Ross, et al., 2018, Fig. 4, p. 6).

The Technical Documentation in Appendix B includes further details about the modelling methods implemented in HyVR and how to use the simulation package. The most current version of HyVR can be accessed online at <https://github.com/driftingtides/hyvr>, along with the associated [technical documentation](#).

3.2.3 An Example Simulation: The MADE Site

To demonstrate the use of the HyVR simulation package, I performed an example simulation based on the MacroDispersion Experiment (MADE) site at the Columbus Air Force Base, Mississippi, USA. The input parameters were derived from the numerous characterisations of the site (e.g., Boggs et al., 1990; Bowling, Rodriguez, et al., 2005; Bowling, Harry, et al., 2007). The MADE site can be categorised into four major strata, from ground surface to the lowest elevation: A meandering fluvial stratum; a braided fluvial stratum; a transitional sand stratum; and a marine clay stratum, which acts as a confining layer below. The architectural elements for each major stratum were inferred from borehole logs (Boggs et al., 1990) and geophysical observations (Bowling, Harry, et al., 2007); these, along with their associated hydrofacies assemblage geometries, are summarised in Table 3.2. Hydrofacies were assigned based on those categorised in the braided-river stratum by Rehfeldt et al. (1992), as well as additional hydrofacies based on the characterisation of Bowling, Rodriguez, et al. (2005), with hydraulic parameter values adopted from a range of sources (Mitchell, 1956; Witt and Brauns, 1983; Jussel et al., 1994).

Figure 3.8 depicts a single HyVR realisation of the MADE site (panels B-F), along with the geological conceptual model of Bowling, Rodriguez, et al. (2005) in panel A. The “soft conditioning” to the approximate elevations of the major strata contacts allows for a favourable comparison between the HyVR simulation and the geological conceptual model. Cross-bedded

Table 3.2: Major strata and architectural elements included in the MADE site HyVR example.

Major strata	Mean elevation of contact surfaces [mbgs]*	Architectural elements	Hydrofacies assemblage geometries	Hydrofacies
Meander	0.0 - 3.0	Meander channel	Extruded parabola (with lag surface)	Clay, silty clay, sandy gravel
		Silt sheet	Sheet	Silty clay
Braided fluvial	3.0 - 8.0	Cross-bedded scour	Truncated ellipsoid	Sandy clayey gravel, openwork gravel, sand, sandy gravel
		Sandy gravel	Sheet	Sandy gravel
Transitional sands	8.0 - 9.5	Sand sheet	Sheet	Fine sand
		Clay lens	Truncated ellipsoid	Silty clay, fine sand
Marine clays	9.5 - 11.0	Clay sheet	Sheet	Clay

*metres below ground surface

hydrofacies assemblages are present in the braided fluvial system, consistent with the observations of Bowling, Rodriguez, et al. (2005). Univariate distributions of log-hydraulic conductivity from Bohling, Liu, Dietrich, et al. (2016) also show similarities with the HyVR realisations.

3.2.4 Conclusions and Implications

The HyVR simulation package is a helpful tool that bridges the gap between sedimentological and hydrogeological research. The package produces spatially distributed hydraulic parameter fields using a hierarchical framework and object-based methods; these fields can then be easily transferred to standard flow-and-transport simulation tools (e.g., MODFLOW 6). HyVR allows geological conceptual models to be realised as hydrogeological models for flow-and-transport simulations.

I have developed HyVR specifically to simulate fluvial sedimentary deposits that form aquifer systems. There are, of course, numerous other geometries that could be implemented aside from those already available. Also, combinations of different geometries could be used to form complex features, such as channel complexes with levees, lateral accretions, and crevasse splays. Such geometry combinations have been successfully implemented in event-based models (e.g., Pycrz et al., 2009) and would be a valuable addition to the HyVR package. The main requirement for additional geometry types is that their form can be easily parameterised and applied to a simulation model grid. The derivation of HyVR input parameters from geo-

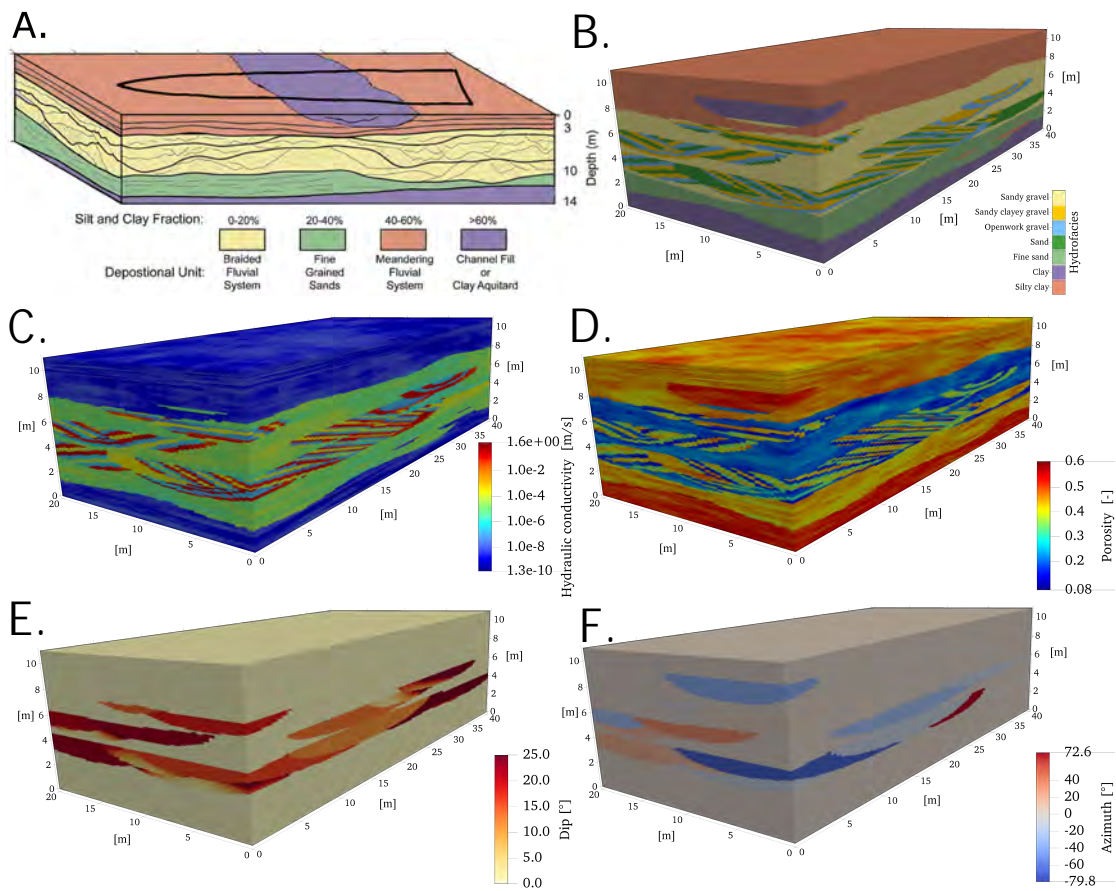


Figure 3.8: (A) Geological conceptual model of the MADE site, amended from Bowling, Rodriguez, et al. (2005). (B)-(F) Distributed parameter fields from a single HyVR realisation using parameters derived from the characterisation of the MADE site. (from Bennett, Haslauer, Ross, et al., 2018, Fig. 5, p. 8).

statistical analysis (e.g., Markov chains, transitional probabilities) of site data would be an interesting avenue for further research. I developed the package with the addition of new simulation features in mind, including extended code commenting and documentation.

A valid critique of the HyVR package is the lack of conditioning to hard data, such as borehole information. In this case, HyVR outputs could be useful for generating three-dimensional training images for multiple-point geostatistical methods (e.g., DeeSse, Mariethoz, Renard, and Straubhaar, 2010). The HyVR parameter fields also cannot be calibrated using inverse methods. Nevertheless, the package is still of practical use for testing hypotheses in hydrogeological research.

3.3 Solute Transport in a Synthetic Braided-River Deposit

In order to deal with the effects of uncertainty about the spatial distribution of hydraulic parameters in the subsurface, stochastic hydrogeologists have employed a range of methods that are often based on simplifying assumptions (e.g., multi-Gaussianity, ergodicity). These assumptions can lead to significant differences in groundwater flow and solute transport simulations between models using differing methods (e.g., Gómez-Hernández and Wen, 1998). The goal of this work package was to assess differences in groundwater flow and solute transport behaviour between ensembles of parameter fields generated using object-based, multiple-point geostatistical (MPS), and multi-Gaussian simulation methods, by comparing the model ensembles with a synthetic virtual reality.

This work package was motivated in part by a 2016 debates series in *Water Resources Research* on the lack of application of stochastic subsurface hydrology by practitioners. My intent was to use openly available tools (cf. Cirpka and Valocchi, 2016) that can incorporate geological structures (cf. Fogg and Zhang, 2016; Sanchez-Vila and Fernández-García, 2016) to see if stochastic concepts could be implemented in a practical application, i.e., predicting the location and extent of a solute plume.

3.3.1 Simulation Methods and Model Setup

In this work package, I generated a single synthetic virtual reality using the object-based HyVR simulation package described in chapter 3.2. This is the base case for subsequent simulations; it is also subject to virtual borehole sampling that is then later used for conditioning MPS and multi-Gaussian simulations. Subsequently, three modelling methods were used to emulate the hydraulic properties of the synthetic virtual reality: the HyVR simulation package (Bennett, Haslauer, Ross, et al., 2018); the MPS Direct Sampling algorithm (Mariethoz, Renard, and Straubhaar, 2010), implemented in the DeeSse program (Straubhaar, 2017); and the sequential Gaussian co-simulation program GCOSIM3D (Gómez-Hernández and Journel, 1993).

Simulation of the Synthetic Virtual Reality

The synthetic virtual reality imitates braided-river deposits observed in the Upper Rhine valley by Siegenthaler and Huggenberger (1993). The main sedimentary features described by these authors were: troughs and scour-pool fills, horizontally bedded gravels, and massive, coarse-grained “brown gravel” beds (Siegenthaler and Huggenberger, 1993). The first two sedimentary features have been classified together as one architectural element: truncated ellipsoids of open framework/bimodal gravel (OW/BM) within a horizontally bedded background gravel (HG). The internal arrangement of the OW/BM hydrofacies could not be resolved explicitly, therefore bulb-type bedding structures (see Figure 3.7), which produce locally anisotropic hydraulic conductivity, were assigned to these features. The HG features were assigned horizontal-to-vertical anisotropy only. The second architectural element simulated

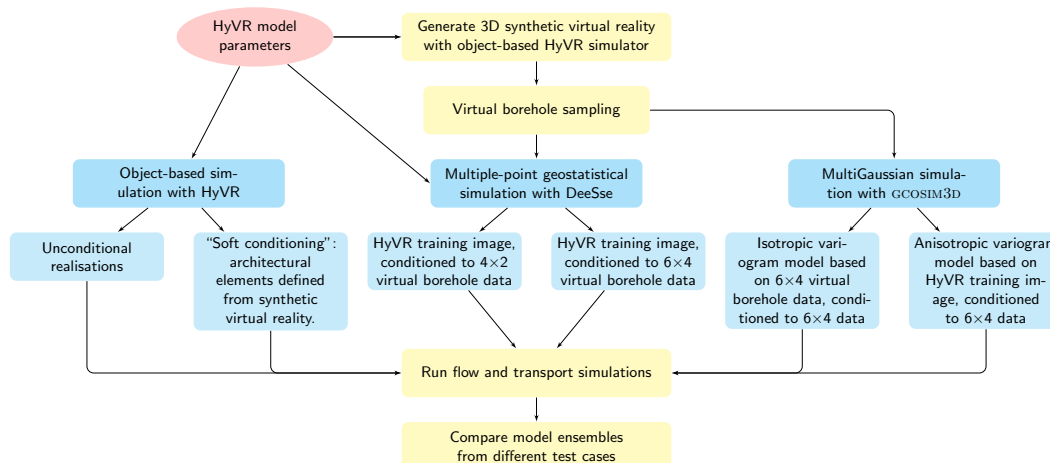


Figure 3.9: Workflow implemented in the third work package for the generation of model ensembles.

was the laterally extensive brown gravel (BG) sheets without internal bedding structure. Parameters for the simulation of the features were adopted from Jussel et al. (1994), Huber and Huggenberger (2016), and Bennett, Haslauer, and Cirpka (2017), and are summarised in Table 3.3.

Table 3.3: Parameters for the object-based simulation of fluvial aquifers.

Parameter	BG	OW/BM	HG
Within-bedding hydraulic conductivity, K_{\parallel} [m s^{-1}] ^a	1×10^{-5}	1×10^{-2}	1×10^{-4}
Anisotropy ratio, K_{\parallel}/K_{\perp} [-]	1	10^{b}	6^{c}
$\sigma_{\ln K}^2$	1	1	1
Porosity, θ [-] ^a	0.1	0.3	0.2
σ_{θ}^2	1×10^{-4}	1×10^{-4}	1×10^{-4}
Paleoflow direction range α [$^{\circ}$]	-	$[-25, +25]^{\text{b}}$	-
Dip range, ψ [$^{\circ}$]	-	$[0, +25]^{\text{c}}$	-

^aJussel et al. (1994)

^bBennett, Haslauer, and Cirpka (2017)

^cHuber and Huggenberger (2016)

Virtual borehole data sets were created by sampling the entire vertical profile of the synthetic virtual reality at selected locations. Two data sets were created with varying numbers of boreholes in the x - and y - directions (4×2 and 6×4). In the x -direction, the virtual boreholes were placed at the model inlet and outlet faces and at regular intervals in between. In the y -direction, the boreholes were placed at regular intervals and offset from the model boundary by one y grid spacing.

Object-Based Ensemble Generation Using HyVR

Two ensembles of realisations were generated using the HyVR simulation package. I generated the first model ensemble using the same input parameters as for the synthetic virtual reality, and thus it is not conditioned. The second object-based model ensemble again uses the same input parameters, however it has the same architectural element configuration (type and mean elevation) as the synthetic virtual reality – this is referred to here as “soft conditioning”.

Multiple-Point Geostatistical Model Ensembles Using DeeSse

I used the MPS program DeeSse (Straubhaar, 2017) to generate two conditional model ensembles in this work package. MPS methods typically require a training image: in this case, the training image was generated using the HyVR simulation package with identical input parameters as the synthetic virtual reality, albeit with a smaller model domain of $\ell_x \times \ell_y \times \ell_z$ of 70 m \times 40 m \times 10 m. The two model ensembles were conditioned to the 4 \times 2 and 6 \times 4 borehole data sets respectively and the following distributed parameters were simulated: hydrofacies, log-hydraulic conductivity, porosity, dip, and azimuth.

Multi-Gaussian Model Ensemble Generation

I simulated conditional multi-Gaussian fields of log-hydraulic conductivity and porosity using the sequential Gaussian co-simulation program GCOSIM3D (Gómez-Hernández and Journel, 1993). To account for anisotropy in the synthetic virtual reality, K_{\parallel} -values from the conditioning data were converted into isotropic hydraulic conductivity K_{iso} by calculating the geometric mean at each model cell $i(x, y, z)$:

$$K_{iso,i} = \frac{K_{\parallel,i}}{\sqrt{a}} \quad (3.2)$$

where a is the anisotropy ratio $K_{\parallel} / K_{\perp}$ for that particular hydrofacies.

The first multi-Gaussian ensemble was generated using an isotropic exponential geostatistical model and conditioned to the 6 \times 4 virtual borehole data. The conditioning data were normally transformed based on the marginal distribution of the data set. An anisotropic variogram model could not be fitted due to large horizontal distances between the boreholes. The model ranges for log-hydraulic conductivity, porosity, and cross-correlation of those two parameters were 1.6 m, 1.1 m, and 2.2 m, respectively. The second multi-Gaussian model ensemble used an anisotropic exponential geostatistical model that was derived from the same object-based training image used in the MPS model ensembles. The training image data was first transformed into normal space using the marginal distribution of the training image; the 6 \times 4 virtual borehole data used for conditioning was also normally transformed using the marginal distribution of the training image. The model ranges in the x -, y -, and z -directions for log-hydraulic conductivity, porosity, and cross-correlation of those two parameters were

[29, 24, 1.5] m, [33, 27, 1.4] m, and [45, 33, 1.5] m, respectively.

I fitted exponential variogram models manually using the AR2GEMS software (AR2Tech, 2017). Following simulation, parameter fields were back-transformed into parameter space using the corresponding marginal distributions.

Table 3.4: Summary of model ensembles generated.

Model ensembles	Simulation tools	Remarks
Synthetic virtual reality	HyVR ^a	-
Object-based, no conditioning	HyVR ^a	No conditioning
Object-based, soft conditioning	HyVR ^a	Soft conditioning to architectural element table from synthetic virtual reality
MPS, 4×2 data	DeeSse ^b	Object-based training image, conditioned to 4×2 borehole data
MPS, 6×4 data	DeeSse ^b	Object-based training image, conditioned to 6×4 borehole data
Multi-Gaussian, isotropic	GCOSIM3D ^c	Isotropic variogram derived from 6×4 borehole data only, conditioned to 6×4 borehole data
Multi-Gaussian, anisotropic	GCOSIM3D ^c	Anisotropic variogram derived from object-based training image, conditioned to 6×4 borehole data

^aObject-based modelling with the HyVR package (Bennett, Haslauer, Ross, et al., 2018)

^bMultiple-point geostatistical (MPS) simulation using DeeSse (Straubhaar, 2017)

^cSimulation of multi-Gaussian fields using GCOSIM3D (Gómez-Hernández and Journel, 1993)

Numerical Methods for Flow and Transport Simulation

Steady-state groundwater flow was solved using the groundwater flow model MODFLOW 6 (Langevin et al., 2017). This model uses a control-volume finite-difference method for the discretisation of groundwater flow (equation 2.1). The XT3D option (Provost et al., 2017) allows for full three-dimensional anisotropy to be accounted for in MODFLOW 6 using a method that estimates the head-gradient vector in a model grid cell using head information from adjacent grid cells. A fixed mean flux \bar{q}_x of 1×10^{-5} m s⁻¹ was applied at the inlet and outlet faces using the MODFLOW 6 well package. I assigned volumetric discharges Q_i [m³ s⁻¹] to each inlet and outlet grid cell i , weighted by the hydraulic conductivity K_i of the grid cell to avoid negative inlet and outlet discharges:

$$Q_i = \bar{q}_x \cdot \ell_y \cdot \ell_z \cdot \frac{K_i}{\sum_{i=1}^n K_i} \quad \forall \quad i(x = 0, nx) \quad (3.3)$$

with ℓ_y and ℓ_z the dimensions of the model domain in the y - and z -directions, respectively. All model boundaries aside from the inlet and outlet faces were no-flow, and a single fixed-head value of 1 m was assigned to one grid cell. Advective particle tracking and steady-state conservative advective-dispersive transport was solved using the methods described in section 2.3.1; the concentration solver was amended to allow for variable porosity. The solute source zone was located at the centre of the model inlet plane and was a rectangle with dimensions $W \times H = 14 \text{ m} \times 2 \text{ m}$. The inflow concentration for streamlines initialised within and outside of the source zone were set to one [-] and zero [-], respectively.

3.3.2 Results and Discussion

Parameter Fields

Figure 3.10 shows log-hydraulic conductivity and hydrofacies fields for the synthetic virtual reality and single realisations from selected model ensembles. The synthetic virtual reality (Figure 3.10, top row) is dominated by the horizontal gravels with highly conductive scour-pool fill features. The laterally extensive brown gravel sheets with low hydraulic conductivity are thin and relatively evenly distributed throughout the profile of the model domain. The unconditional, object-based realisation in Figure 3.10 (second row) has thick brown gravel features, which will be a dominant influence on flow and transport behaviour. The third row of Figure 3.10 depicts an MPS realisation conditioned to the 6×4 data set. The scour-pool fill geometries simulated with DeeSse look similar to those in the synthetic virtual reality, including the distribution of hydraulic conductivity and bedding parameters dip and azimuth. The multi-Gaussian model ensembles (Figure 3.10, bottom two rows) are quite different to the model ensembles that include hydrofacies simulations (i.e., object-based, MPS). The statistically isotropic multi-Gaussian fields vary over short distances; the anisotropic multi-Gaussian fields can reproduce laterally extensive features, but not the juxtaposition of zones of contrasting hydraulic conductivity and porosity.

There was generally a good match between the marginal distributions of log-hydraulic conductivity for the synthetic virtual reality and the ensemble mean distributions of the model ensembles, with all distributions reproducing the bimodal distributions of the synthetic virtual reality. The unconditional object-based model ensemble showed more variability in the proportions of hydrofacies, which resulted in a larger 5th-95th percentile range. In this model ensemble, the random nature of assigning architectural elements also produced realisations without the BG hydrofacies. The MPS ensemble conditioned to 4×2 data had a much higher proportion of higher conductivity model cells – the smaller number of conditioning data in this ensemble meant that the distribution was closer to that of the training image. The distribution of the MPS ensemble with 6×4 data showed a much better fit to the synthetic virtual reality: this suggests that additional conditioning data help to improve predictions

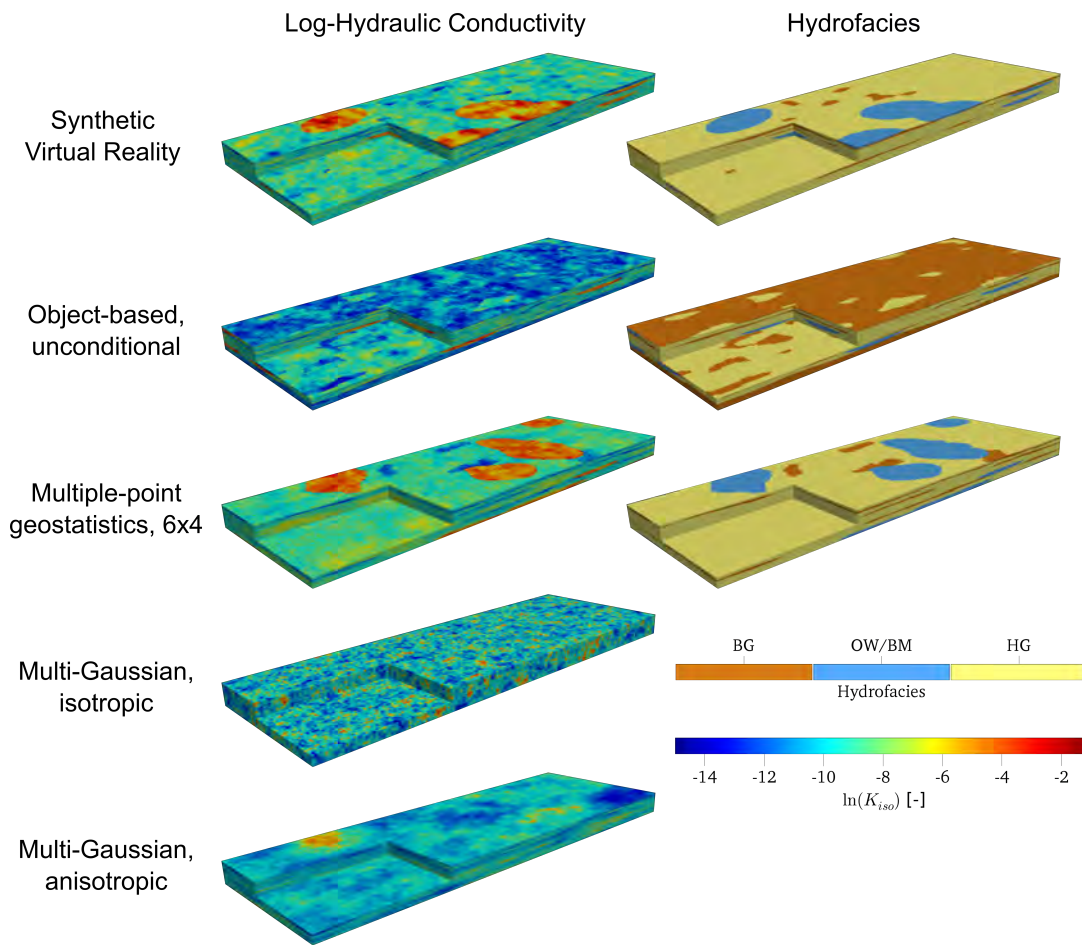


Figure 3.10: Log-hydraulic conductivity and hydrofacies parameter fields for example realisations. The model domain dimensions are $\ell_x \times \ell_y \times \ell_z = 200 \times 70 \times 10$ m.

of hydraulic parameter distributions. The normal-score transformations undertaken for the multi-Gaussian ensembles resulted in ensemble marginal distributions that matched the synthetic virtual reality quite well. The summary statistics of ensemble marginal distributions were similar, although the variances of log-hydraulic conductivity and porosity distributions were lower in the multi-Gaussian ensembles.

I calculated the connectivity between the model inlet and outlet planes based on the minimum hydraulic resistance of Rizzo and de Barros (2017), using isotropic hydraulic conductivity fields geometrically averaged using equation 3.2. The boxplots in Figure 3.12 depict the distribution of \log_{10} -minimum hydraulic resistance for all model ensembles and the virtual reality. The unconditional, object-based ensemble has the greatest range; the soft-conditioned, object-based ensemble has a median value very close to that of the synthetic virtual reality. The MPS model ensemble distributions of minimum hydraulic resistance are the closest to that of the synthetic virtual reality, with only a 4 % difference between the median value of

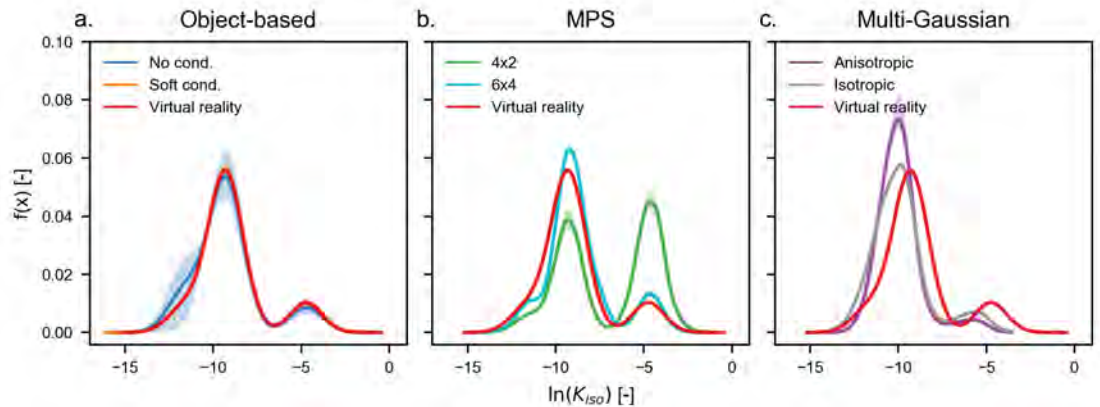


Figure 3.11: Probability distribution functions of log-hydraulic conductivity parameter field ensembles. The solid line represents the mean value and the shading represents the 5th-95th percentiles.

the MPS ensemble conditioned to 6×4 data and the synthetic virtual reality. Conversely, the multi-Gaussian ensembles do not capture the connectivity of the synthetic virtual reality. This suggests that hydrofacies-based approaches should be implemented when investigating connectivity in heterogeneous porous media.

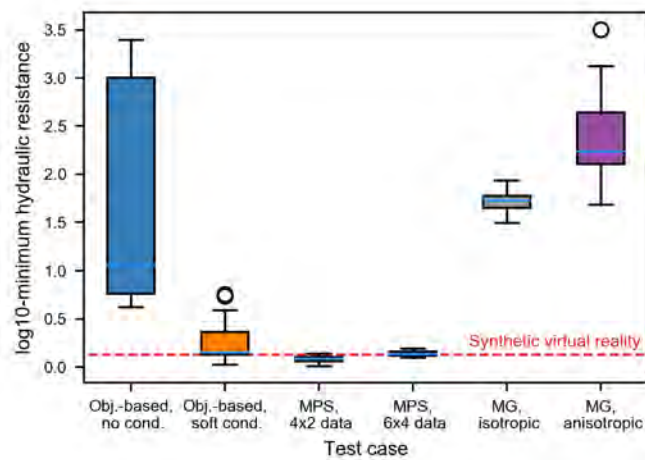


Figure 3.12: Distributions of minimum hydraulic resistance calculated using the method of Rizzo and de Barros (2017).

Solute Transport Simulations

The advective particle trajectories shown in Figure 3.13 demonstrate the differences between model methods that simulate hydrofacies (object-based and MPS) and the multi-Gaussian simulations. In the object-based and MPS realisations included in Figure 3.13, there are distinct zones with a high density of particle trajectories – such contrasts are not possible in the maxentropic multi-Gaussian fields simulated here. There also appears to be greater intermingling of streamlines in the object-based and MPS realisations, as depicted by the variety of

colours in the lenses of particles throughout the cross sections (note that colours indicate the y -component of the starting position of the particle). In the multi-Gaussian realisations shown in Figure 3.13, there appears to be less intermingling of particle trajectories. The statistically anisotropic multi-Gaussian ensemble does exhibit some lens-like zones of concentrated particle trajectories, but they do not have sharply defined boundaries.

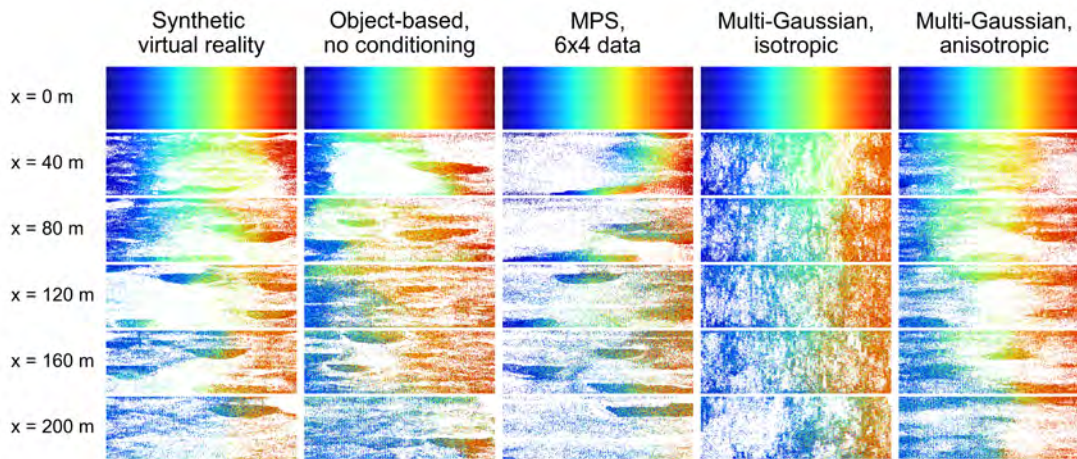


Figure 3.13: *Advective particle distributions in observation planes perpendicular to the mean flow direction for single realisations from selected model ensembles. Particle colours denote the initial y -coordinate value of the particle trajectory. Spatial dimensions of the cross sections: $70\text{ m} \times 10\text{ m}$.*

In Figure 3.14, the transverse moments of steady-state concentration distributions demonstrate the differences in solute transport between the model ensembles and the synthetic virtual reality. The object-based and multi-Gaussian models ensembles were not successful in capturing the centre of mass of the virtual reality: the ensemble means generally remain in the centre of the model domain (i.e., centre of the source zone). Of these model ensembles, the object-based methods showed more inter-percentile variation for plume centre of mass and spreading than the multi-Gaussian model ensembles. The MPS model ensembles were more successful in emulating the transverse moments of the synthetic virtual reality. Plume centres in the MPS ensemble conditioned to 6×4 data followed the centre of the synthetic virtual reality better than the ensemble conditioned to 4×2 data, demonstrating the benefit of additional conditioning data. In summary, the transverse moments of concentration distributions show that conditional model ensembles simulated using methods that incorporate both geological information and conditioning data (i.e., MPS methods) are better at predicting the location and extent of plumes in the synthetic virtual reality.

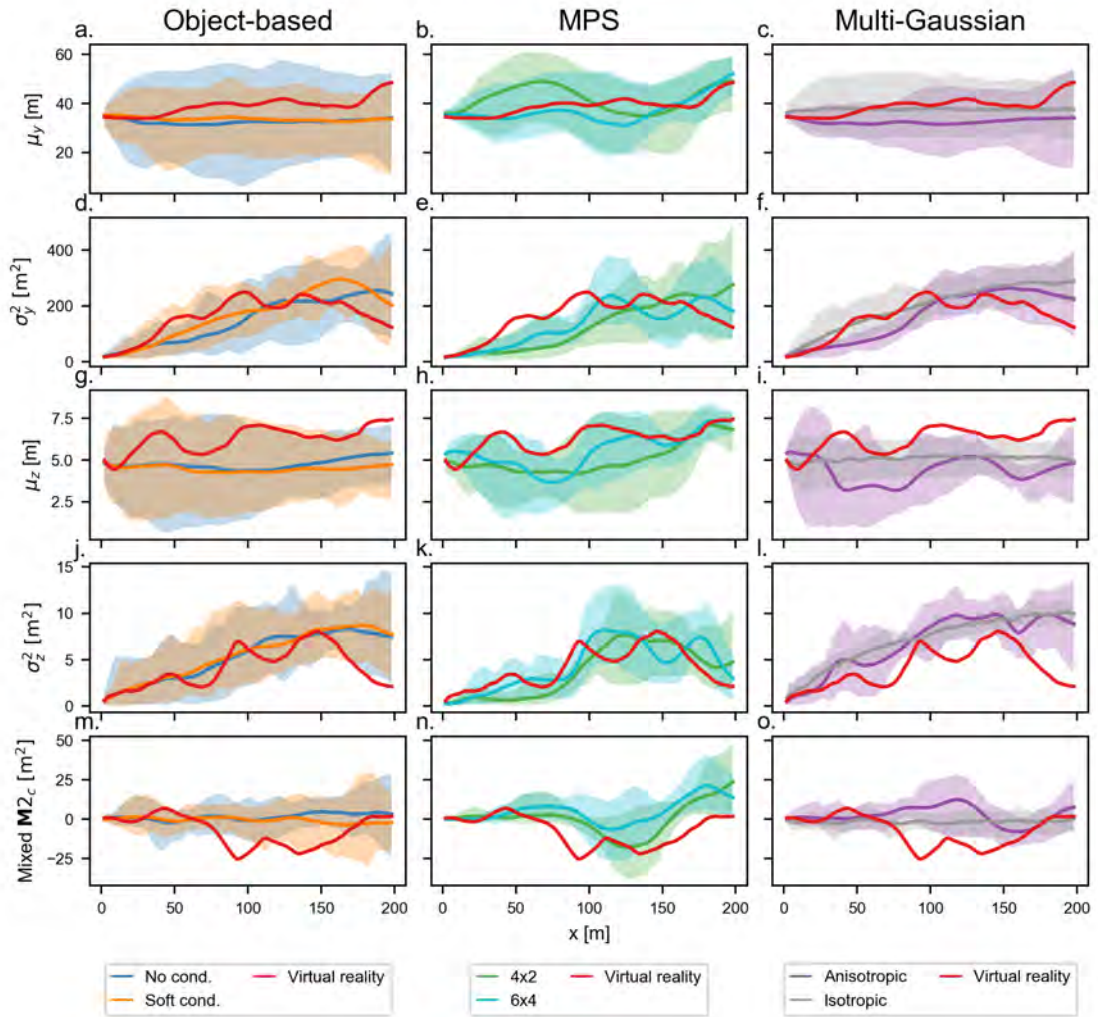


Figure 3.14: Transverse moments derived from steady-state concentration distributions. Lines represent ensemble means and shading represents 5th-95th percentiles.

3.3.3 Conclusions and Implications

In this work package, I compared the solute transport behaviour between a synthetic virtual reality and ensembles of parameter fields generated using three contrasting simulation methods: object-based, multiple-point geostatistical, and multi-Gaussian. Model ensembles simulated using the the MPS program DeeSse generally provided the most accurate predictions of solute transport in a synthetic virtual reality, particularly when conditioned to larger amounts of data. This work package has demonstrated that integrating geological conceptual information and conditioning data within a stochastic hydrogeological context can improve predictions of solute arrival-time distributions and solute plume location and extent.

A valid criticism of this work package is that the same simulation method and model parameters were used to create the synthetic virtual reality as for the object-based model ensemble.

bles and training image for MPS methods. This “inverse crime” (cf. Wirgin, 2004) requires further investigation, particularly into whether the MPS model ensemble predictions of solute transport perform as well when the training images and the virtual reality are more dissimilar. Nevertheless, this work package still provides important conclusions for the open questions of the role of parameter and model uncertainty on groundwater flow and solute transport.

4 Overall Conclusions and Outlook

Variability in sedimentary processes influences the hydrogeological parameters of subsequent deposits across multiple scales. As the spatial configuration of hydraulic parameters determines groundwater flow and solute transport, an understanding of sedimentary depositional concepts can assist in understanding subsurface heterogeneity and subsequent flow and transport behaviour. Specifically, geological conceptual knowledge can help in constraining the spatial extent of zones of similar hydraulic properties (i.e., hydrofacies), support the prediction of hydrofacies patterns based on the cyclicity of erosive and depositional events, and provide models of bedding structure that can in turn induce hydraulic anisotropy in porous media.

Realistic sedimentary anisotropy plays an important role in solute mixing (section 3.1), particularly in the transverse direction, and in some cases the heterogeneity of bedding parameters may be of greater relevance than that of isotropic hydraulic conductivity, the parameter traditionally favoured by hydrogeologists. Despite its important role, anisotropy is difficult to measure or estimate from field characterisation studies and further efforts to improve characterisation are necessary. The heterogeneity of isotropic hydraulic conductivity has a more dominant influence on longitudinal mixing than sedimentary anisotropy.

Object-based modelling approaches offer a helpful tool for translating geological knowledge into parameter fields that can be used in numerical groundwater flow and solute transport simulations. These approaches may be conceptually simple, often not very computationally demanding, and can be constrained with geometric rules, which makes the methods attractive to both sedimentologists and hydrogeological modellers. The Hydrogeological Virtual Realities (HyVR) simulation package developed during this thesis (section 3.2) is a useful addition to the resources available to groundwater modellers. However, the results of the third work package (section 3.3) demonstrate that it is still critical that parameter fields be conditioned to actual observations in order to accurately predict solute transport, even if such conditioning only extends to the large-scale boundaries present at a site (i.e., major strata or architectural elements).

Multiple-point geostatistical (MPS) methods are one way in which both geological concepts and conditioning information can be combined. The continuing improvements in the implementation of MPS (e.g., Straubhaar, 2017), as well as improved computing power, provide a powerful tool to do this, and there are plenty of opportunities to explore uncertainty in stratigraphic models using these tools. The quality of MPS depends on having appropriate training images that capture the expected heterogeneity in the porous media to be modelled. The object-based methods developed in this thesis are one way to furnish such training images. Other potential sources of training images are process-imitating models such as

FLUMY (MINES ParisTech, 2017) and HSTAR (Nicholas et al., 2013). Combining process-based model outputs with MPS may ameliorate some of the disadvantages of the former modelling approaches, such as the uncertainty in generation and forcing parameters, and difficulty in conditioning to data. However, for this to occur, the process-based model outputs need to be translated into hydrogeological parameters, e.g., by grain size–permeability relationships, model gridding, etc.

The results of this thesis are significant, as they suggest that hydrogeologists cannot simply rely on traditional methods of geostatistical characterisation and simulation if they want to accurately predict solute transport and mixing behaviour. This is especially important because mixing processes are relevant in many applications of hydrogeology, such as the attenuation of contaminants through naturally occurring means that are facilitated by abiotic processes, e.g., the mixing of ambient dissolved oxygen-rich groundwater with contaminated groundwater. It is likely that sedimentary anisotropy will play an even greater role in transient systems in the future, making this a rich area of potential research.

As practitioners and policy makers become increasingly aware of the importance and in-herece of uncertainty in environmental modelling, it is necessary to provide tools that facilitate the quantification of uncertainty within groundwater flow and solute transport models in a rigorous and defensible manner (e.g., Bode et al., 2018). This is particularly relevant for contaminated sites where individual pathways and the connectivity of sedimentary features are crucial for predicting solute transport. Developing openly available tools for improving stochastic hydrogeological modelling workflows (cf. Cirpka and Valocchi, 2016) is an essential, but time-consuming, task and hydrogeological researchers should make use of the emerging field of research software engineering to efficiently translate their concepts into tools suitable for practice.

Bibliography

- Aigner, T., J. Heinz, J. Hornung, and U. Asprien (1999). "A Hierarchical Process-Approach to Reservoir Heterogeneity: Examples from Outcrop Analogues". In: *Bulletin du Centre de Recherches Elf Exploration Production* 22.1, pp. 1–11.
- Allen-King, R. M., R. M. Halket, D. R. Gaylord, and M. J. L. Robin (1998). "Characterizing the Heterogeneity and Correlation of Perchloroethene Sorption and Hydraulic Conductivity Using a Facies-Based Approach". In: *Water Resources Research* 34.3, pp. 385–396. DOI: [10.1029/97WR03496](https://doi.org/10.1029/97WR03496).
- Allen-King, R. M., I. Kalinovich, D. F. Dominic, G. Wang, R. Polmanteer, and D. Divine (2015). "Hydrophobic Organic Contaminant Transport Property Heterogeneity in the Borden Aquifer". In: *Water Resources Research* 51.3, pp. 1723–1743. DOI: [10.1002/2014WR016161](https://doi.org/10.1002/2014WR016161).
- Allen, J. (1983). "Studies in Fluvial Sedimentation: Bars, Bar-Complexes and Sandstone Sheets (Low-Sinuosity Braided Streams) in the Brownstones (L. Devonian), Welsh Borders". In: *Sedimentary Geology* 33.4, 51, pp. 237–293. DOI: [10.1016/0037-0738\(83\)90076-3](https://doi.org/10.1016/0037-0738(83)90076-3).
- Anderson, M. P. (1989). "Hydrogeologic Facies Models to Delineate Large-Scale Spatial Trends in Glacial and Glaciofluvial Sediments". In: *Geological Society of America Bulletin* 101.4, 51, pp. 501–511. DOI: [10.1130/0016-7606\(1989\)101<0501:HFMTDL>2.3.CO;2](https://doi.org/10.1130/0016-7606(1989)101<0501:HFMTDL>2.3.CO;2).
- Anderson, M. P., W. W. Woessner, and R. J. Hunt (2015). *Applied Groundwater Modeling: Simulation of Flow and Advective Transport*. Second edition. OCLC: ocn921253555. London; San Diego, CA: Academic Press. 564 pp. ISBN: 978-0-12-058103-0.
- AR2Tech (2017). *AR2GeMS v1.0b*. Version 1.0b. Denver, CO. URL: www.ar2tech.com.
- Armstrong, M., A. Galli, H. Beucher, G. Loc'h, D. Renard, B. Doligez, R. Eschard, and F. GEFROY (2011). *Plurigaussian Simulations in Geosciences*. Berlin; Heidelberg: Springer. ISBN: 978-3-642-19607-2.
- Arnold, D. N. and F. Brezzi (1985). "Mixed and Nonconforming Finite Element Methods: Implementation, Postprocessing and Error Estimates". In: *RAIRO-Modélisation mathématique et analyse numérique* 19.1, pp. 7–32.
- Asprien, U. and T. Aigner (1999). "Towards Realistic Aquifer Models: Three-Dimensional Georadar Surveys of Quaternary Gravel Deltas (Singen Basin, SW Germany)". In: *Sedimentary Geology* 129.3–4, pp. 281–297. DOI: [10.1016/S0037-0738\(99\)00068-8](https://doi.org/10.1016/S0037-0738(99)00068-8).
- Bakker, M. and K. Hemker (2002). "A Dupuit Formulation for Flow in Layered, Anisotropic Aquifers". In: *Advances in Water Resources* 25.7, pp. 747–754. DOI: [10.1016/S0309-1708\(02\)00074-X](https://doi.org/10.1016/S0309-1708(02)00074-X).

- Bakker, M. and K. Hemker (2004). “Analytic Solutions for Groundwater Whirls in Box-Shaped, Layered Anisotropic Aquifers”. In: *Advances in Water Resources* 27.11, pp. 1075–1086. DOI: [10.1016/j.advwatres.2004.08.009](https://doi.org/10.1016/j.advwatres.2004.08.009).
- Ballarini, E., S. Bauer, C. Eberhardt, and C. Beyer (2014). “Evaluation of the Role of Heterogeneities on Transverse Mixing in Bench-Scale Tank Experiments by Numerical Modeling”. In: *Groundwater* 52.3, pp. 368–377. DOI: [10.1111/gwat.12066](https://doi.org/10.1111/gwat.12066).
- Bauer, R. D., M. Rolle, S. Bauer, C. Eberhardt, P. Grathwohl, O. Kolditz, R. U. Meckenstock, and C. Griebler (2009). “Enhanced Biodegradation by Hydraulic Heterogeneities in Petroleum Hydrocarbon Plumes”. In: *Journal of Contaminant Hydrology* 105.1-2, pp. 56–68. DOI: [10.1016/j.jconhyd.2008.11.004](https://doi.org/10.1016/j.jconhyd.2008.11.004).
- Bayer, P., P. Huggenberger, P. Renard, and A. Comunian (2011). “Three-Dimensional High Resolution Fluvio-Glacial Aquifer Analog: Part 1: Field Study”. In: *Journal of Hydrology* 405.1, pp. 1–9. DOI: [10.1016/j.jhydrol.2011.03.038](https://doi.org/10.1016/j.jhydrol.2011.03.038).
- Beaudoin, A. and J.-R. de Dreuzy (2013). “Numerical Assessment of 3-D Macrodispersion in Heterogeneous Porous Media”. In: *Water Resources Research* 49.5, pp. 2489–2496. DOI: [10.1002/wrcr.20206](https://doi.org/10.1002/wrcr.20206).
- Beerbower, J. R. (1964). “Cyclothem and Cyclic Depositional Mechanisms in Alluvial Plain Sedimentation”. In: *Kansas Geological Survey Bulletin* 169.1, pp. 31–32. URL: <http://www.kgs.ku.edu/Publications/Bulletins/169/Beerbower/>.
- Bennett, J. P., C. P. Haslauer, and O. A. Cirpka (2017). “The Impact of Sedimentary Anisotropy on Solute Mixing in Stacked Scour-Pool Structures”. In: *Water Resources Research* 53.4, pp. 2813–2832. DOI: [10.1002/2016WR019665](https://doi.org/10.1002/2016WR019665).
- Bennett, J. P., C. P. Haslauer, M. Ross, and O. A. Cirpka (2018). “An Open, Object-Based Framework for Generating Anisotropy in Sedimentary Subsurface Models”. In: *Groundwater*. DOI: [10.1111/gwat.12803](https://doi.org/10.1111/gwat.12803).
- Beres, M., P. Huggenberger, A. G. Green, and H. Horstmeyer (1999). “Using Two- and Three-Dimensional Georadar Methods to Characterize Glaciofluvial Architecture”. In: *Sedimentary Geology* 129.1-2, pp. 1–24. DOI: [10.1016/S0037-0738\(99\)00053-6](https://doi.org/10.1016/S0037-0738(99)00053-6).
- Bianchi, M. and C. Zheng (2016). “A Lithofacies Approach for Modeling Non-Fickian Solute Transport in a Heterogeneous Alluvial Aquifer”. In: *Water Resources Research* 52.1, pp. 552–565. DOI: [10.1002/2015WR018186](https://doi.org/10.1002/2015WR018186).
- Bianchi, M., C. Zheng, C. Wilson, G. R. Tick, G. Liu, and S. M. Gorelick (2011). “Spatial Connectivity in a Highly Heterogeneous Aquifer: From Cores to Preferential Flow Paths”. In: *Water Resources Research* 47.5, W05524. DOI: [10.1029/2009WR008966](https://doi.org/10.1029/2009WR008966).

- Bierkens, M. F. P. and H. J. T. Weerts (1994). "Block Hydraulic Conductivity of Cross-Bedded Fluvial Sediments". In: *Water Resources Research* 30.10, pp. 2665–2678. DOI: [10.1029/94WR01049](https://doi.org/10.1029/94WR01049).
- Bode, F., T. Ferré, N. Zigelli, M. Emmert, and W. Nowak (2018). "Reconnecting Stochastic Methods With Hydrogeological Applications: A Utilitarian Uncertainty Analysis and Risk Assessment Approach for the Design of Optimal Monitoring Networks". In: *Water Resources Research* 54.3, pp. 2270–2287. DOI: [10.1002/2017WR020919](https://doi.org/10.1002/2017WR020919).
- Boggs, J. M., S. C. Young, D. J. Benton, and Y. C. Chung (1990). *Hydrogeologic Characterization of the MADE Site*. Interim Report EN-6915. Palo Alto, California, USA: Electric Power Research Institute.
- Bohling, G. C., G. Liu, P. Dietrich, and J. J. Butler (2016). "Reassessing the MADE Direct-Push Hydraulic Conductivity Data Using a Revised Calibration Procedure". In: *Water Resources Research* 52.11, pp. 8970–8985. DOI: [10.1002/2016WR019008](https://doi.org/10.1002/2016WR019008).
- Bohling, G. C., G. Liu, S. J. Knobbe, E. C. Reboulet, D. W. Hyndman, P. Dietrich, and J. J. Butler (2012). "Geostatistical Analysis of Centimeter-Scale Hydraulic Conductivity Variations at the MADE Site". In: *Water Resources Research* 48.2. DOI: [10.1029/2011WR010791](https://doi.org/10.1029/2011WR010791).
- Bowling, J. C., D. L. Harry, A. B. Rodriguez, and C. Zheng (2007). "Integrated Geophysical and Geological Investigation of a Heterogeneous Fluvial Aquifer in Columbus Mississippi". In: *Journal of Applied Geophysics* 62.1, pp. 58–73. DOI: [10.1016/j.jappgeo.2006.08.003](https://doi.org/10.1016/j.jappgeo.2006.08.003).
- Bowling, J. C., A. B. Rodriguez, D. L. Harry, and C. Zheng (2005). "Delineating Alluvial Aquifer Heterogeneity Using Resistivity and GPR Data". In: *Ground Water* 43.6, pp. 890–903. DOI: [10.1111/j.1745-6584.2005.00103.x](https://doi.org/10.1111/j.1745-6584.2005.00103.x).
- Bridge, J. S. and J. A. Diemer (1983). "Quantitative Interpretation of an Evolving Ancient River System". In: *Sedimentology* 30.5, pp. 599–623. DOI: [10.1111/j.1365-3091.1983.tb00698.x](https://doi.org/10.1111/j.1365-3091.1983.tb00698.x).
- Brodzikowski, K. and A. Van Loon (1987). "A Systematic Classification of Glacial and Periglacial Environments, Facies and Deposits". In: *Earth-Science Reviews* 24.5, pp. 297–381. DOI: [10.1016/0012-8252\(87\)90061-4](https://doi.org/10.1016/0012-8252(87)90061-4).
- Browne, G. H. and T. R. Naish (2003). "Facies Development and Sequence Architecture of a Late Quaternary Fluvial-Marine Transition, Canterbury Plains and Shelf, New Zealand: Implications for Forced Regressive Deposits". In: *Sedimentary Geology* 158.1–2, pp. 57–86. DOI: [10.1016/S0037-0738\(02\)00258-0](https://doi.org/10.1016/S0037-0738(02)00258-0).
- Cardenas, M. B., J. L. Wilson, and V. A. Zlotnik (2004). "Impact of Heterogeneity, Bed Forms, and Stream Curvature on Subchannel Hyporheic Exchange". In: *Water Resources Research* 40.8, W08307. DOI: [10.1029/2004WR003008](https://doi.org/10.1029/2004WR003008).

- Carle, S. F. (1999). *T-PROGS: Transition Probability Geostatistical Software*. California: University of California, Davis. URL: <http://gmsdocs.aquaveo.com/t-progs.pdf>.
- Carle, S. F., E. M. Labolle, G. S. Weissmann, D. Van Brocklin, and G. E. Fogg (1998). “Conditional Simulation of Hydrofacies Architecture: A Transition Probability/Markov Approach”. In: *Hydrogeologic Models of Sedimentary Aquifers, Concepts in Hydrogeology and Environmental Geology*. Ed. by G. S. Fraser and J. M. Davis. Special Publication 1. Society for Sedimentary Geology, pp. 147–170. ISBN: 978-1-56576-052-3.
- Carling, P. and M. Glaister (1987). “Rapid Deposition of Sand and Gravel Mixtures Downstream of a Negative Step: The Role of Matrix-Infilling and Particle-Overpassing in the Process of Bar-Front Accretion”. In: *Journal of the Geological Society* 144.4, pp. 543–551. DOI: [10.1144/gsjgs.144.4.0543](https://doi.org/10.1144/gsjgs.144.4.0543).
- Chiogna, G., O. A. Cirpka, M. Rolle, and A. Bellin (2015). “Helical Flow in Three-dimensional Nonstationary Anisotropic Heterogeneous Porous Media”. In: *Water Resources Research* 51.1, pp. 261–280. DOI: [10.1002/wr.12144](https://doi.org/10.1002/wr.12144).
- Chiogna, G., M. Rolle, A. Bellin, and O. A. Cirpka (2014). “Helicity and Flow Topology in Three-Dimensional Anisotropic Porous Media”. In: *Advances in Water Resources* 73, pp. 134–143. DOI: [10.1016/j.advwatres.2014.06.017](https://doi.org/10.1016/j.advwatres.2014.06.017).
- Cirpka, O. A., G. Chiogna, M. Rolle, and A. Bellin (2015). “Transverse Mixing in Three-dimensional Nonstationary Anisotropic Heterogeneous Porous Media”. In: *Water Resources Research* 51.1, pp. 241–260. DOI: [10.1002/wr.12144](https://doi.org/10.1002/wr.12144).
- Cirpka, O. A., E. O. Frind, and R. Helmig (1999). “Numerical Simulation of Biodegradation Controlled by Transverse Mixing”. In: *Journal of Contaminant Hydrology* 40.2, pp. 159–182. DOI: [10.1016/S0169-7722\(99\)00044-3](https://doi.org/10.1016/S0169-7722(99)00044-3).
- Cirpka, O. A., Å. Olsson, Q. Ju, M. A. Rahman, and P. Grathwohl (2006). “Determination of Transverse Dispersion Coefficients from Reactive Plume Lengths”. In: *Ground Water* 44.2, pp. 212–221. DOI: [10.1111/j.1745-6584.2005.00124.x](https://doi.org/10.1111/j.1745-6584.2005.00124.x).
- Cirpka, O. A. and A. J. Valocchi (2016). “Debates—Stochastic Subsurface Hydrology from Theory to Practice: Does Stochastic Subsurface Hydrology Help Solving Practical Problems of Contaminant Hydrogeology?” In: *Water Resources Research* 52.12, pp. 9218–9227. DOI: [10.1002/wr.12144](https://doi.org/10.1002/wr.12144).
- Comunian, A., P. Renard, J. Straubhaar, and P. Bayer (2011). “Three-Dimensional High Resolution Fluvio-Glacial Aquifer Analog—Part 2: Geostatistical Modeling”. In: *Journal of Hydrology* 405.1, pp. 10–23. DOI: [10.1016/j.jhydrol.2011.03.037](https://doi.org/10.1016/j.jhydrol.2011.03.037).
- Coulthard, T. (2017). *CAESAR-Lisflood 1.9B*. Version 1.9b. URL: <https://doi.org/10.5281/zenodo.321820> (visited on 03/16/2017).
- Dagan, G. (1989). *Flow and Transport in Porous Formations*. Berlin: Springer. 465 pp.

- De Marsily, G., F. Delay, J. Gonçalves, P. Renard, V. Teles, and S. Violette (2005). “Dealing with Spatial Heterogeneity”. In: *Hydrogeology Journal* 13.1, pp. 161–183. DOI: [10.1007/s10040-004-0432-3](https://doi.org/10.1007/s10040-004-0432-3).
- Dell’Arciprete, D., C. Vassena, F. Baratelli, M. Giudici, R. Bersezio, and F. Felletti (2014). “Connectivity and Single/Dual Domain Transport Models: Tests on a Point-Bar/Channel Aquifer Analogue”. In: *Hydrogeology Journal* 22.4, pp. 761–778. DOI: [10.1007/s10040-014-1105-5](https://doi.org/10.1007/s10040-014-1105-5).
- Dentz, M., H. Kinzelbach, S. Attinger, and W. Kinzelbach (2000). “Temporal Behavior of a Solute Cloud in a Heterogeneous Porous Medium: 2. Spatially Extended Injection”. In: *Water Resources Research* 36.12, pp. 3605–3614. DOI: [10.1029/2000WR900211](https://doi.org/10.1029/2000WR900211).
- Deutsch, C. and T. Tran (2002). “FLUVSIM: A Program for Object-Based Stochastic Modeling of Fluvial Depositional Systems”. In: *Computers & Geosciences* 28.4, pp. 525–535. DOI: [10.1016/S0098-3004\(01\)00075-9](https://doi.org/10.1016/S0098-3004(01)00075-9).
- Dietrich, C. R. and G. N. Newsam (1993). “A Fast and Exact Method for Multidimensional Gaussian Stochastic Simulations”. In: *Water Resources Research* 29.8, pp. 2861–2869. DOI: [10.1029/93WR01070](https://doi.org/10.1029/93WR01070).
- Dijkstra, E. W. (1959). “A Note on Two Problems in Connexion with Graphs”. In: *Numerische mathematik* 1.1, pp. 269–271. DOI: [10.1007/BF01386390](https://doi.org/10.1007/BF01386390).
- Doherty, J. (2010). *PEST, Model-Independent Parameter Estimation*. 5th ed. Brisbane, Australia: Watermark Numerical Computing. URL: www.pesthomepage.org/getfiles.php?file=newpestmani.pdf.
- Dykaar, B. B. and P. K. Kitanidis (1992). “Determination of the Effective Hydraulic Conductivity for Heterogeneous Porous Media Using a Numerical Spectral Approach: 1. Method”. In: *Water Resources Research* 28.4, pp. 1155–1166. DOI: [10.1029/91WR03084](https://doi.org/10.1029/91WR03084).
- Engdahl, N. B. and G. S. Weissmann (2010). “Anisotropic Transport Rates in Heterogeneous Porous Media”. In: *Water Resources Research* 46.2, W02507. DOI: [10.1029/2009WR007910](https://doi.org/10.1029/2009WR007910).
- Falk, M. L. and J. S. Langer (1998). “Dynamics of Viscoplastic Deformation in Amorphous Solids”. In: *Physical Review E* 57.6, pp. 7192–7205. DOI: [10.1103/PhysRevE.57.7192](https://doi.org/10.1103/PhysRevE.57.7192).
- Fischer, A. G. (1986). “Climatic Rhythms Recorded in Strata”. In: *Annual Review of Earth and Planetary Sciences* 14.1, pp. 351–376. DOI: [10.1146/annurev.ea.14.050186.002031](https://doi.org/10.1146/annurev.ea.14.050186.002031).
- Fogg, G. E. (1986). “Groundwater Flow and Sand Body Interconnectedness in a Thick, Multiple-Aquifer System”. In: *Water Resources Research* 22.5, pp. 679–694. DOI: [10.1029/WR022i005p00679](https://doi.org/10.1029/WR022i005p00679).
- Fogg, G. E. and Y. Zhang (2016). “Debates—Stochastic Subsurface Hydrology from Theory to Practice: A Geologic Perspective”. In: *Water Resources Research* 52.12, pp. 9235–9245. DOI: [10.1002/2016WR019699](https://doi.org/10.1002/2016WR019699).

- Freeze, R. A. and J. Cherry (1979). *Groundwater*. Englewood Cliffs, New Jersey: Prentice-Hall. 604 pp. ISBN: 0-13-365312-9.
- Gelhar, L. W. (1993). *Stochastic Subsurface Hydrology*. Englewood Cliffs, N.J: Prentice-Hall. 390 pp. ISBN: 978-0-13-846767-8.
- Gómez-Hernández, J. J. and A. G. Journel (1993). “Joint Sequential Simulation of multiGaussian Fields”. In: *Geostatistics Tróia '92: Volume 1*. Ed. by A. Soares. Dordrecht: Springer Netherlands, pp. 85–94. ISBN: 978-94-011-1739-5. DOI: [10.1007/978-94-011-1739-5](https://doi.org/10.1007/978-94-011-1739-5).
- Gómez-Hernández, J. and X.-H. Wen (1998). “To Be or Not to Be Multi-Gaussian? A Reflection on Stochastic Hydrogeology”. In: *Advances in Water Resources* 21.1, pp. 47–61. DOI: [10.1016/S0309-1708\(96\)00031-0](https://doi.org/10.1016/S0309-1708(96)00031-0).
- Haldorsen, H. H. and D. M. Chang (1986). “Notes on Stochastic Shales; from Outcrop to Simulation Model”. In: *Reservoir Characterization*. Ed. by L. W. Lake and H. B. Carroll. website: <http://www.sciencedirect.com/science/article/pii/B9780124340657500204>. Academic Press, pp. 445–485. ISBN: 978-0-12-434065-7. DOI: [10.1016/B978-0-12-434065-7.50020-4](https://doi.org/10.1016/B978-0-12-434065-7.50020-4).
- Ham, P. A., R. J. Schotting, H. Prommer, and G. B. Davis (2004). “Effects of Hydrodynamic Dispersion on Plume Lengths for Instantaneous Bimolecular Reactions”. In: *Advances in Water Resources* 27.8, pp. 803–813. DOI: [10.1016/j.advwatres.2004.05.008](https://doi.org/10.1016/j.advwatres.2004.05.008).
- Haslauer, C., P. Guthke, A. Bárdossy, and E. Sudicky (2012). “Effects of Non-Gaussian Copula-based Hydraulic Conductivity Fields on Macrodispersion”. In: *Water Resources Research* 48.7. 51. DOI: [10.1029/2011WR011425](https://doi.org/10.1029/2011WR011425).
- Heinz, J. and T. Aigner (2003a). “Three-Dimensional GPR Analysis of Various Quaternary Gravel-Bed Braided River Deposits (Southwestern Germany)”. In: *Geological Society, London, Special Publications* 211.1, pp. 99–110. DOI: [10.1144/GSL.SP.2001.211.01.09](https://doi.org/10.1144/GSL.SP.2001.211.01.09).
- Heinz, J. and T. Aigner (2003b). “Hierarchical Dynamic Stratigraphy in Various Quaternary Gravel Deposits, Rhine Glacier Area (SW Germany): Implications for Hydrostratigraphy”. In: *International Journal of Earth Sciences* 92.6, pp. 923–938. DOI: [10.1007/s00531-003-0359-2](https://doi.org/10.1007/s00531-003-0359-2).
- Heinz, J., S. Kleinedam, G. Teutsch, and T. Aigner (2003). “Heterogeneity Patterns of Quaternary Glaciofluvial Gravel Bodies (SW-Germany): Application to Hydrogeology”. In: *Sedimentary Geology* 158.1-2. 51, pp. 1–23. DOI: [10.1016/S0037-0738\(02\)00239-7](https://doi.org/10.1016/S0037-0738(02)00239-7).
- Honarkhah, M. and J. Caers (2010). “Stochastic Simulation of Patterns Using Distance-Based Pattern Modeling”. In: *Mathematical Geosciences* 42.5, pp. 487–517. DOI: [10.1007/s11004-010-9276-7](https://doi.org/10.1007/s11004-010-9276-7).

- Huber, E. and P. Huguenberger (2016). “Subsurface Flow Mixing in Coarse, Braided River Deposits”. In: *Hydrology and Earth System Sciences* 20.5, pp. 2035–2046. DOI: [10.5194/hess-20-2035-2016](https://doi.org/10.5194/hess-20-2035-2016).
- Jackson, R. G. (1975). “Hierarchical Attributes and a Unifying Model of Bed Forms Composed of Cohesionless Material and Produced by Shearing Flow”. In: *Geological Society of America Bulletin* 86.11, pp. 1523–1533. DOI: [10.1130/0016-7606\(1975\)86<1523:HAAAUM>2.0.CO;2](https://doi.org/10.1130/0016-7606(1975)86<1523:HAAAUM>2.0.CO;2).
- Janković, I., D. R. Steward, R. J. Barnes, and G. Dagan (2009). “Is Transverse Macrodispersivity in Three-Dimensional Groundwater Transport Equal to Zero? A Counterexample”. In: *Water Resources Research* 45.8, W08415. DOI: [10.1029/2009WR007741](https://doi.org/10.1029/2009WR007741).
- Johnson, N. M. and S. J. Dreiss (1989). “Hydrostratigraphic Interpretation Using Indicator Geostatistics”. In: *Water Resources Research* 25.12, pp. 2501–2510. DOI: [10.1029/WR025i012p02501](https://doi.org/10.1029/WR025i012p02501).
- Journel, A. G. (1983). “Nonparametric Estimation of Spatial Distributions”. In: *Journal of the International Association for Mathematical Geology* 15.3, pp. 445–468. DOI: [10.1007/BF01031292](https://doi.org/10.1007/BF01031292).
- Jussel, P., F. Stauffer, and T. Dracos (1994). “Transport Modeling in Heterogeneous Aquifers: I. Statistical Description and Numerical Generation of Gravel Deposits”. In: *Water Resources Research* 30.6, pp. 1803–1817. DOI: [10.1029/94WR00162](https://doi.org/10.1029/94WR00162).
- Kelley, D. H. and N. T. Ouellette (2011). “Separating Stretching from Folding in Fluid Mixing”. In: *Nature Physics* 7.6, 51, pp. 477–480. DOI: [10.1038/nphys1941](https://doi.org/10.1038/nphys1941).
- Kerrou, J., P. Renard, H.-J. Hendricks Franssen, and I. Lunati (2008). “Issues in Characterizing Heterogeneity and Connectivity in Non-multiGaussian Media”. In: *Advances in Water Resources* 31.1, pp. 147–159. DOI: [10.1016/j.advwatres.2007.07.002](https://doi.org/10.1016/j.advwatres.2007.07.002).
- Kitanidis, P. K. (1992). “Analysis of Macrodispersion through Volume-Averaging: Moment Equations”. In: *Stochastic Hydrology and Hydraulics* 6.1, pp. 5–25. DOI: [10.1007/BF01581672](https://doi.org/10.1007/BF01581672).
- Kitanidis, P. K. (1988). “Prediction by the Method of Moments of Transport in a Heterogeneous Formation”. In: *Hydrologic Research: The U.S. — Japan Experience* 102.1, pp. 453–473. DOI: [10.1016/0022-1694\(88\)90111-4](https://doi.org/10.1016/0022-1694(88)90111-4).
- (1994). “The Concept of the Dilution Index”. In: *Water Resources Research* 30.7, pp. 2011–2026. DOI: [10.1029/94WR00762](https://doi.org/10.1029/94WR00762).
- Klingbeil, R., S. Kleinedam, U. Aspöck, T. Aigner, and G. Teutsch (1999). “Relating Lithofacies to Hydrofacies: Outcrop-Based Hydrogeological Characterisation of Quaternary Gravel Deposits”. In: *Sedimentary Geology* 129.3-4, pp. 299–310. DOI: [10.1016/S0037-0738\(99\)00067-6](https://doi.org/10.1016/S0037-0738(99)00067-6).

- Koltermann, C. E. and S. M. Gorelick (1992). “Paleoclimatic Signature in Terrestrial Flood Deposits”. In: *Science* 256.5065. 51, pp. 1775–1782. DOI: [10.1126/science.256.5065.1775](https://doi.org/10.1126/science.256.5065.1775).
- (1995). “Fractional Packing Model for Hydraulic Conductivity Derived from Sediment Mixtures”. In: *Water Resources Research* 31.12, pp. 3283–3297. DOI: [10.1029/95WR02020](https://doi.org/10.1029/95WR02020).
- (1996). “Heterogeneity in Sedimentary Deposits: A Review of Structure-Imitating, Process-Imitating, and Descriptive Approaches”. In: *Water Resources Research* 32.9. 51, pp. 2617–2658. DOI: [10.1029/96WR00025](https://doi.org/10.1029/96WR00025).
- Laloy, E., R. Héroult, D. Jacques, and N. Linde (2018). “Training-Image Based Geostatistical Inversion Using a Spatial Generative Adversarial Neural Network”. In: *Water Resources Research* 54.1, pp. 381–406. DOI: [10.1002/2017WR022148](https://doi.org/10.1002/2017WR022148).
- Langevin, C. D., J. D. Hughes, E. R. Banta, R. G. Niswonger, S. Panday, and A. M. Provost (2017). *Documentation for the MODFLOW 6 Groundwater Flow Model*. 6-A55. US Geological Survey, p. 197. DOI: [10.3133/tm6A55](https://doi.org/10.3133/tm6A55).
- Le Borgne, T., M. Dentz, and E. Villermanx (2015). “The Lamellar Description of Mixing in Porous Media”. In: *Journal of Fluid Mechanics* 770, pp. 458–498. DOI: [10.1017/jfm.2015.117](https://doi.org/10.1017/jfm.2015.117).
- Leeder, M. R. (1999). *Sedimentology and Sedimentary Basins: From Turbulence to Tectonics*. Oxford; Malden, MA: Blackwell Science. 592 pp. ISBN: 978-0-632-04976-9.
- Liedl, R., A. J. Valocchi, P. Dietrich, and P. Grathwohl (2005). “Finiteness of Steady State Plumes”. In: *Water Resources Research* 41.12, W12501. DOI: [10.1029/2005WR004000](https://doi.org/10.1029/2005WR004000).
- Liedl, R., P. K. Yadav, and P. Dietrich (2011). “Length of 3-D Mixing-Controlled Plumes for a Fully Penetrating Contaminant Source with Finite Width”. In: *Water Resources Research* 47.8, W08602. DOI: [10.1029/2010WR009710](https://doi.org/10.1029/2010WR009710).
- Linde, N., P. Renard, T. Mukerji, and J. Caers (2015). “Geological Realism in Hydrogeological and Geophysical Inverse Modeling: A Review”. In: *Advances in Water Resources* 86, Part A, pp. 86–101. DOI: [10.1016/j.advwatres.2015.09.019](https://doi.org/10.1016/j.advwatres.2015.09.019).
- Loschko, M., T. Wöhling, D. L. Rudolph, and O. A. Cirpka (2018). “Accounting for the Decreasing Reaction Potential of Heterogeneous Aquifers in a Stochastic Framework of Aquifer-Scale Reactive Transport”. In: *Water Resources Research* 54.1, pp. 442–463. DOI: [10.1002/2017WR021645](https://doi.org/10.1002/2017WR021645).
- Lunt, I. A., J. S. Bridge, and R. S. Tye (2004). “A Quantitative, Three-Dimensional Depositional Model of Gravelly Braided Rivers: Depositional Model of Gravel-Bed Rivers”. In: *Sedimentology* 51.3, pp. 377–414. DOI: [10.1111/j.1365-3091.2004.00627.x](https://doi.org/10.1111/j.1365-3091.2004.00627.x).
- Maizels, J. (1993). “Lithofacies Variations within Sandur Deposits: The Role of Runoff Regime, Flow Dynamics and Sediment Supply Characteristics”. In: *Sedimentary Geology* 85.1, pp. 299–325. DOI: [10.1016/0037-0738\(93\)90090-R](https://doi.org/10.1016/0037-0738(93)90090-R).

- Mariethoz, G. and J. Caers (2015). *Multiple-Point Geostatistics: Stochastic Modeling with Training Images*. Chichester, West Sussex; Hoboken, NJ: John Wiley & Sons Inc. ISBN: 978-1-118-66275-5.
- Mariethoz, G., P. Renard, F. Cornaton, and O. Jaquet (2009). “Truncated Plurigaussian Simulations to Characterize Aquifer Heterogeneity”. In: *Groundwater* 47.1, pp. 13–24. DOI: [10.1111/j.1745-6584.2008.00489.x](https://doi.org/10.1111/j.1745-6584.2008.00489.x).
- Mariethoz, G., P. Renard, and J. Straubhaar (2010). “The Direct Sampling Method to Perform Multiple-Point Geostatistical Simulations: Performing Multiple-Points Simulations”. In: *Water Resources Research* 46.11, W11536. DOI: [10.1029/2008WR007621](https://doi.org/10.1029/2008WR007621).
- Maxey, G. B. (1964). “Hydrostratigraphic Units”. In: *Journal of Hydrology* 2.2, pp. 124–129. DOI: [10.1016/0022-1694\(64\)90023-X](https://doi.org/10.1016/0022-1694(64)90023-X).
- Miall, A. D. (1977). “A Review of the Braided-River Depositional Environment”. In: *Earth-Science Reviews* 13.1, pp. 1–62. DOI: [10.1016/0012-8252\(77\)90055-1](https://doi.org/10.1016/0012-8252(77)90055-1).
- (1985). “Architectural-Element Analysis: A New Method of Facies Analysis Applied to Fluvial Deposits”. In: *Earth-Science Reviews* 22.4, 51, pp. 261–308. DOI: [10.1016/0012-8252\(85\)90001-7](https://doi.org/10.1016/0012-8252(85)90001-7).
- (1991). “Hierarchies of Architectural Units in Terrigenous Clastic Rocks and Their Relationship to Sedimentation Rate”. In: *The Three-Dimensional Facies Architecture of Terrigenous Clastic Sediments, and Its Implications for Hydrocarbon Discovery and Recovery*. Ed. by A. D. Miall and N. Tyler. CSP3. Tulsa, OK: Society for Sedimentary Geology.
- (1996). *The Geology of Fluvial Deposits: Sedimentary Facies, Basin Analysis, and Petroleum Geology*. Berlin ; New York: Springer. 582 pp. ISBN: 978-3-540-59186-3.
- (2013). *Fluvial Depositional Systems*. Springer geology. New York: Springer. ISBN: 978-3-319-00665-9.
- Miller, M. C., I. N. McCave, and P. D. Komar (1977). “Threshold of Sediment Motion under Unidirectional Currents”. In: *Sedimentology* 24.4, pp. 507–527. DOI: [10.1111/j.1365-3091.1977.tb00136.x](https://doi.org/10.1111/j.1365-3091.1977.tb00136.x).
- MINES ParisTech (2017). *FLUMY: Process-Based Channelized Reservoir Models*. Paris, France. URL: <http://cg.ensmp.fr/flumy>.
- Mitchell, J. K. (1956). “The Fabric of Natural Clays and Its Relation to Engineering Properties”. In: *Proceedings of the 35th Highway Research Board Annual Meeting*. Highway Research Board Annual Meeting. Ed. by F. Burggraf. Vol. 35. NAS-NRC publication, 426. Washington, D.C.: Highway Research Board, pp. 693–713. ISBN: 978-0-7844-7499-0.
- Mosley, M. P. (1976). “An Experimental Study of Channel Confluences”. In: *The Journal of Geology* 84.5, pp. 535–562. DOI: [10.1086/628230](https://doi.org/10.1086/628230).

- Nedelec, J. C. (1980). “Mixed Finite Elements in \mathbb{R}^3 ”. In: *Numerische Mathematik* 35.3, pp. 315–341. DOI: [10.1007/BF01396415](https://doi.org/10.1007/BF01396415).
- Nicholas, A. P., P. J. Ashworth, G. H. Sambrook Smith, and S. D. Sandbach (2013). “Numerical Simulation of Bar and Island Morphodynamics in Anabranching Megarivers: Bar and Island Morphodynamics in Megarivers”. In: *Journal of Geophysical Research: Earth Surface* 118.4, pp. 2019–2044. DOI: [10.1002/jgrf.20132](https://doi.org/10.1002/jgrf.20132).
- Nowak, W. and O. A. Cirpka (2006). “Geostatistical Inference of Hydraulic Conductivity and Dispersivities from Hydraulic Heads and Tracer Data”. In: *Water Resources Research* 42.8, W08416. DOI: [10.1029/2005WR004832](https://doi.org/10.1029/2005WR004832).
- Pollock, D. W. (1988). “Semianalytical Computation of Path Lines for Finite-Difference Models”. In: *Ground Water* 26.6, pp. 743–750. DOI: [10.1111/j.1745-6584.1988.tb00425.x](https://doi.org/10.1111/j.1745-6584.1988.tb00425.x).
- Provost, A. M., C. D. Langevin, and J. D. Hughes (2017). *Documentation for the “XT3D” Option in the Node Property Flow (NPF) Package of MODFLOW 6*. Report 6-A56. Reston, VA: United States Geological Survey, p. 50. DOI: [10.3133/tm6A56](https://doi.org/10.3133/tm6A56).
- Pryshlak, T. T., A. H. Sawyer, S. H. Stonedahl, and M. R. Soltanian (2015). “Multiscale Hyporheic Exchange through Strongly Heterogeneous Sediments”. In: *Water Resources Research* 51.11, pp. 9127–9140. DOI: [10.1002/2015WR017293](https://doi.org/10.1002/2015WR017293).
- Pyrzcz, M., J. Boisvert, and C. Deutsch (2009). “ALLUVSIM: A Program for Event-Based Stochastic Modeling of Fluvial Depositional Systems”. In: *Computers & Geosciences* 35.8, pp. 1671–1685. DOI: [10.1016/j.cageo.2008.09.012](https://doi.org/10.1016/j.cageo.2008.09.012).
- Ramanathan, R., A. Guin, R. W. Ritzi, D. F. Dominic, V. L. Freedman, T. D. Scheibe, and I. A. Lunt (2010). “Simulating the Heterogeneity in Braided Channel Belt Deposits: I. A Geometric-Based Methodology and Code”. In: *Water Resources Research* 46.4, W04515. DOI: [10.1029/2009WR008111](https://doi.org/10.1029/2009WR008111).
- Raviart, P. A. and J. M. Thomas (1977). “A Mixed Finite Element Method for 2-Nd Order Elliptic Problems”. In: *Mathematical Aspects of Finite Element Methods: Proceedings of the Conference Held in Rome, December 10–12, 1975*. Ed. by I. Galligani and E. Magenes. Berlin, Heidelberg: Springer Berlin Heidelberg, pp. 292–315. ISBN: 978-3-540-37158-8. DOI: [10.1007/BFb0064470](https://doi.org/10.1007/BFb0064470).
- Refsgaard, J. C., E. Auken, C. A. Bamberg, B. S. Christensen, T. Clausen, et al. (2014). “Nitrate Reduction in Geologically Heterogeneous Catchments — A Framework for Assessing the Scale of Predictive Capability of Hydrological Models”. In: *Science of The Total Environment* 468–469, pp. 1278–1288. DOI: [10.1016/j.scitotenv.2013.07.042](https://doi.org/10.1016/j.scitotenv.2013.07.042).
- Rehfeldt, K. R., J. M. Bogggs, and L. W. Gelhar (1992). “Field Study of Dispersion in a Heterogeneous Aquifer: 3. Geostatistical Analysis of Hydraulic Conductivity”. In: *Water Resources Research* 28.12, pp. 3309–3324. DOI: [10.1029/92WR01758](https://doi.org/10.1029/92WR01758).

- Renard, P. and D. Allard (2013). “Connectivity Metrics for Subsurface Flow and Transport”. In: *Advances in Water Resources* 51, pp. 168–196. DOI: [10.1016/j.advwatres.2011.12.001](https://doi.org/10.1016/j.advwatres.2011.12.001).
- Renard, P. and G. de Marsily (1997). “Calculating Equivalent Permeability: A Review”. In: *Advances in Water Resources* 20.5-6. Next, pp. 253–278. DOI: [10.1016/S0309-1708\(96\)00050-4](https://doi.org/10.1016/S0309-1708(96)00050-4).
- Ritzi, R. W., Z. Dai, D. F. Dominic, and Y. N. Rubin (2004). “Spatial Correlation of Permeability in Cross-Stratified Sediment with Hierarchical Architecture: Permeability Correlation in Cross-Stratified Sediment”. In: *Water Resources Research* 40.3. DOI: [10.1029/2003WR002420](https://doi.org/10.1029/2003WR002420).
- Ritzi, R. W., L. Huang, R. Ramanathan, and R. M. Allen-King (2013). “Horizontal Spatial Correlation of Hydraulic and Reactive Transport Parameters as Related to Hierarchical Sedimentary Architecture at the Borden Research Site: Cross Correlation between Sorption and Permeability”. In: *Water Resources Research* 49.4, pp. 1901–1913. DOI: [10.1002/wrcr.20165](https://doi.org/10.1002/wrcr.20165).
- Rizzo, C. B. and F. P. J. de Barros (2017). “Minimum Hydraulic Resistance and Least Resistance Path in Heterogeneous Porous Media”. In: *Water Resources Research* 53.10, pp. 8596–8613. DOI: [10.1002/2017WR020418](https://doi.org/10.1002/2017WR020418).
- Rolle, M., C. Eberhardt, G. Chiogna, O. A. Cirpka, and P. Grathwohl (2009). “Enhancement of Dilution and Transverse Reactive Mixing in Porous Media: Experiments and Model-Based Interpretation”. In: *Journal of Contaminant Hydrology* 110.3-4, pp. 130–142. DOI: [10.1016/j.jconhyd.2009.10.003](https://doi.org/10.1016/j.jconhyd.2009.10.003).
- Rubin, Y. (2003). *Applied Stochastic Hydrogeology*. Oxford; New York: Oxford University Press. 391 pp. ISBN: 978-0-19-513804-7.
- Sanchez-Vila, X. and D. Fernández-García (2016). “Debates—Stochastic Subsurface Hydrology from Theory to Practice: Why Stochastic Modeling Has Not yet Permeated into Practitioners?” In: *Water Resources Research* 52.12, pp. 9246–9258. DOI: [10.1002/2016WR019302](https://doi.org/10.1002/2016WR019302).
- Sanchez-Vila, X., A. Guadagnini, and J. Carrera (2006). “Representative Hydraulic Conductivities in Saturated Groundwater Flow”. In: *Reviews of Geophysics* 44.3, pp. 1–46. DOI: [10.1029/2005RG000169](https://doi.org/10.1029/2005RG000169).
- Scheibe, T. D. and D. L. Freyberg (1995). “Use of Sedimentological Information for Geometric Simulation of Natural Porous Media Structure”. In: *Water Resources Research* 31.12, pp. 3259–3270. DOI: [10.1029/95WR02570](https://doi.org/10.1029/95WR02570).
- Scheidegger, A. E. (1961). “General Theory of Dispersion in Porous Media”. In: *Journal of Geophysical Research* 66.10, pp. 3273–3278. DOI: [10.1029/JZ066i010p03273](https://doi.org/10.1029/JZ066i010p03273).

- Schumm, S. A. (1963). *A Tentative Classification of Alluvial River Channels an Examination of Similarities and Differences among Some Great Plains Rivers*. Report 477. 51. United States Geological Survey. URL: <http://pubs.er.usgs.gov/publication/cir477>.
- Schwartz, F. W. (1977). “Macroscopic Dispersion in Porous Media: The Controlling Factors”. In: *Water Resources Research* 13.4, pp. 743–752. DOI: [10.1029/WR013i004p00743](https://doi.org/10.1029/WR013i004p00743).
- Sequent (2018). *Leapfrog Geo [Software]*. Version 3.0. Christchurch, NZ. URL: <http://www.leapfrog3d.com/>.
- Shannon, C. E. (1948). “A Mathematical Theory of Communication”. In: *Bell System Technical Journal* 27.3, pp. 379–423. DOI: [10.1002/j.1538-7305.1948.tb01338.x](https://doi.org/10.1002/j.1538-7305.1948.tb01338.x).
- Shiklomanov, I. A. (1993). “World Fresh Water Resources”. In: *Water in Crisis: A Guide to the World's Fresh Water Resources*. Ed. by P. H. Gleick. New York: Oxford University Press. ISBN: 0-19-507627-3.
- Siegenthaler, C. and P. Huggenberger (1993). “Pleistocene Rhine Gravel: Deposits of a Braided River System with Dominant Pool Preservation”. In: *Geological Society, London, Special Publications* 75.1, pp. 147–162. DOI: [10.1144/GSL.SP.1993.075.01.09](https://doi.org/10.1144/GSL.SP.1993.075.01.09).
- Sposito, G. (2001). “Topological Groundwater Hydrodynamics”. In: *Advances in Water Resources* 24.7, pp. 793–801. DOI: [10.1016/S0309-1708\(00\)00077-4](https://doi.org/10.1016/S0309-1708(00)00077-4).
- Stauffer, F. (2007). “Impact of Highly Permeable Sediment Units with Inclined Bedding on Solute Transport in Aquifers”. In: *Advances in Water Resources* 30.11, 51, pp. 2194–2201. DOI: [10.1016/j.advwatres.2007.04.008](https://doi.org/10.1016/j.advwatres.2007.04.008).
- Straubhaar, J. (2017). *DeeSse User's Guide*. Neuchâtel, Switzerland: University of Neuchâtel. URL: <http://www.randlab.org/research/deesse/>.
- Strebelle, S. (2002). “Conditional Simulation of Complex Geological Structures Using Multiple-Point Statistics”. In: *Mathematical Geology* 34.1, pp. 1–21. DOI: [10.1023/A:1014009426274](https://doi.org/10.1023/A:1014009426274).
- Sudicky, E. A. (1986). “A Natural Gradient Experiment on Solute Transport in a Sand Aquifer: Spatial Variability of Hydraulic Conductivity and Its Role in the Dispersion Process”. In: *Water Resources Research* 22.13, pp. 2069–2082. DOI: [10.1029/WR022i013p02069](https://doi.org/10.1029/WR022i013p02069).
- Tompson, A. F. B., R. Ababou, and L. W. Gelhar (1989). “Implementation of the Three-Dimensional Turning Bands Random Field Generator”. In: *Water Resources Research* 25.10, pp. 2227–2243. DOI: [10.1029/WR025i010p02227](https://doi.org/10.1029/WR025i010p02227).
- Tuxen, N., H.-J. Albrechtsen, and P. L. Bjerg (2006). “Identification of a Reactive Degradation Zone at a Landfill Leachate Plume Fringe Using High Resolution Sampling and Incubation Techniques”. In: *Journal of Contaminant Hydrology* 85.3–4, pp. 179–194. DOI: [10.1016/j.jconhyd.2006.01.004](https://doi.org/10.1016/j.jconhyd.2006.01.004).

- Tyukhova, A. R. and M. Willmann (2016). “Connectivity Metrics Based on the Path of Smallest Resistance”. In: *Advances in Water Resources* 88, pp. 14–20. DOI: [10.1016/j.advwatres.2015.11.014](https://doi.org/10.1016/j.advwatres.2015.11.014).
- Webb, E. K. and M. P. Anderson (1996). “Simulation of Preferential Flow in Three-Dimensional, Heterogeneous Conductivity Fields with Realistic Internal Architecture”. In: *Water Resources Research* 32.3, 51, pp. 533–545. DOI: [10.1029/95WR03399](https://doi.org/10.1029/95WR03399).
- Weissmann, G. and G. Fogg (1999). “Multi-Scale Alluvial Fan Heterogeneity Modeled with Transition Probability Geostatistics in a Sequence Stratigraphic Framework”. In: *Journal of Hydrology* 226.1–2, pp. 48–65. DOI: [10.1016/S0022-1694\(99\)00160-2](https://doi.org/10.1016/S0022-1694(99)00160-2).
- Werth, C. J., O. A. Cirpka, and P. Grathwohl (2006). “Enhanced Mixing and Reaction through Flow Focusing in Heterogeneous Porous Media”. In: *Water Resources Research* 42.12, W12414. DOI: [10.1029/2005WR004511](https://doi.org/10.1029/2005WR004511).
- Whittaker, J. and G. Teutsch (1999). “Numerical Simulation of Subsurface Characterization Methods: Application to a Natural Aquifer Analogue”. In: *Advances in Water Resources* 22.8, pp. 819–829. DOI: [10.1016/S0309-1708\(98\)00056-6](https://doi.org/10.1016/S0309-1708(98)00056-6).
- Wirgin, A. (2004). “The Inverse Crime”. In: *arXiv preprint math-ph/0401050*. URL: <https://arxiv.org/abs/math-ph/0401050> (visited on 08/08/2018).
- Witt, K.-J. and J. Brauns (1983). “Permeability-anisotropy Due to Particle Shape”. In: *Journal of Geotechnical Engineering* 109.9, pp. 1181–1187. DOI: [10.1061/\(ASCE\)0733-9410\(1983\)109:9\(1181\)](https://doi.org/10.1061/(ASCE)0733-9410(1983)109:9(1181)).
- Zarlenga, A. and A. Fiori (2013). “Steady Plumes in Heterogeneous Porous Formations: A Stochastic Lagrangian Approach”. In: *Water Resources Research* 49.2, pp. 864–873. DOI: [10.1002/wrcr.20106](https://doi.org/10.1002/wrcr.20106).
- Zektser, I. S. and L. G. Everett (2004). *Groundwater Resources of the World: And Their Use*. IHP-VI Series on Groundwater 6. Paris, France: UNESCO. ISBN: 92-9220-007-0. URL: unesdoc.unesco.org/images/0013/001344/134433e.pdf (visited on 08/07/2018).
- Zhang, M. and Y. Zhang (2015). “Multiscale Solute Transport Upscaling for a Three-Dimensional Hierarchical Porous Medium”. In: *Water Resources Research* 51.3, 51, pp. 1688–1709. DOI: [10.1002/2014WR016202](https://doi.org/10.1002/2014WR016202).
- Zheng, C. and S. M. Gorelick (2003). “Analysis of Solute Transport in Flow Fields Influenced by Preferential Flowpaths at the Decimeter Scale”. In: *Ground Water* 41.2, pp. 142–155. DOI: [10.1111/j.1745-6584.2003.tb02578.x](https://doi.org/10.1111/j.1745-6584.2003.tb02578.x).
- Zimmerman, D. A., G. de Marsily, C. A. Gotway, M. G. Marietta, C. L. Axness, et al. (1998). “A Comparison of Seven Geostatistically Based Inverse Approaches to Estimate Transmissivities for Modeling Advective Transport by Groundwater Flow”. In: *Water Resources Research* 34.6, pp. 1373–1413. DOI: [10.1029/98WR00003](https://doi.org/10.1029/98WR00003).

Zinn, B. and C. F. Harvey (2003). “When Good Statistical Models of Aquifer Heterogeneity Go Bad: A Comparison of Flow, Dispersion, and Mass Transfer in Connected and Multivariate Gaussian Hydraulic Conductivity Fields”. In: *Water Resources Research* 39.3. 51, p. 1051. DOI: [10.1029/2001WR001146](https://doi.org/10.1029/2001WR001146).

A Publications

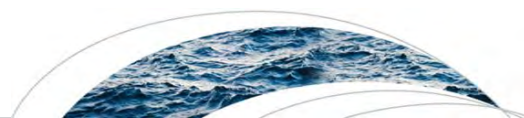
A.1 List of Publications

Accepted Publications

1. Bennett, J. P., C. P. Haslauer, and O. A. Cirpka (2017). “The impact of sedimentary anisotropy on solute mixing in stacked scour-pool structures”. In: *Water Resources Research* 53.4, 2813–2832. DOI: [10.1002/2016WR019665](https://doi.org/10.1002/2016WR019665).
2. Bennett, J. P., C. P. Haslauer, M. Ross, and O. A. Cirpka (2018). “An open, object-based framework for generating anisotropy in sedimentary subsurface models”. In *Groundwater*. DOI: [10.1111/gwat.12803](https://doi.org/10.1111/gwat.12803).

Submitted Manuscript

1. Bennett, J. P., P. Renard, C. P. Haslauer, and O. A. Cirpka (August 2018). “A multi-model analysis of solute plume behavior in a synthetic braided-river deposit”. Submitted to *Water Resources Research*.



RESEARCH ARTICLE

10.1002/2016WR019665

Key Points:

- Internal anisotropy in realistic glacial outwash deposits causes complex three-dimensional groundwater flow patterns
- Dilution of steady state plumes in anisotropic test cases is not adequately characterized by two-particle statistics
- Sedimentary anisotropy is of critical importance when considering contaminant plumes controlled by transverse mixing

Correspondence to:

O. A. Cirpka,
olaf.cirpka@uni-tuebingen.de

Citation:

Bennett, J. P., C. P. Haslauer, and O. A. Cirpka (2017), The impact of sedimentary anisotropy on solute mixing in stacked scour-pool structures, *Water Resour. Res.*, 53, 2813–2832, doi:10.1002/2016WR019665.

Received 17 AUG 2016

Accepted 12 MAR 2017

Accepted article online 17 MAR 2017

Published online 7 APR 2017

Corrected 6 JUL 2017

This article was corrected on 6 JUL 2017. See the end of the full text for details.

The impact of sedimentary anisotropy on solute mixing in stacked scour-pool structures

Jeremy P. Bennett¹ , Claus P. Haslauer¹ , and Olaf A. Cirpka¹ 

¹Center for Applied Geoscience, University of Tübingen, Tübingen, Germany

Abstract The spatial variability of hydraulic conductivity is known to have a strong impact on solute spreading and mixing. In most investigations, its local anisotropy has been neglected. Recent studies have shown that spatially varying orientation in sedimentary anisotropy can lead to twisting flow enhancing transverse mixing, but most of these studies used geologically implausible geometries. We use an object-based approach to generate stacked scour-pool structures with either isotropic or anisotropic filling which are typically reported in glacial outwash deposits. We analyze how spatially variable isotropic conductivity and variation of internal anisotropy in these features impacts transverse plume deformation and both longitudinal and transverse spreading and mixing. In five test cases, either the scalar values of conductivity or the spatial orientation of its anisotropy is varied between the scour-pool structures. Based on 100 random configurations, we compare the variability of velocity components, stretching and folding metrics, advective travel-time distributions, one and two-particle statistics in advective-dispersive transport, and the flux-related dilution indices for steady state advective-dispersive transport among the five test cases. Variation in the orientation of internal anisotropy causes strong variability in the lateral velocity components, which leads to deformation in transverse directions and enhances transverse mixing, whereas it hardly affects the variability of the longitudinal velocity component and thus longitudinal spreading and mixing. The latter is controlled by the spatial variability in the scalar values of hydraulic conductivity. Our results demonstrate that sedimentary anisotropy is important for transverse mixing, whereas it may be neglected when considering longitudinal spreading and mixing.

Plain Language Summary When sediments are deposited in stream channels they retain the “imprint” of the stream flow that deposited them. Groundwater flows more easily along the path of this streamflow imprint than against it—this is called anisotropy. Many groundwater systems are made up of deposits from many different streams and so will have many different imprints, even when the deposits are close to each other. We found that this can cause groundwater to flow along complicated and tangled paths. These tangled groundwater paths can change the way that compounds move through the system, especially at right angles to the main groundwater flow direction. This is important because groundwater scientists often do not think about the imprint, or anisotropy, of the sediments in their studies, and perhaps they should.

1. Introduction

Traditional stochastic perspectives on flow and transport in heterogeneous porous media [e.g., Dagan, 1989; Rubin, 2003] are based on the assumption that hydraulic conductivity varies in space, but is locally isotropic, that is, the local conductivity does not depend on the spatial orientation of the hydraulic gradient. Under such conditions, heterogeneity of hydraulic-conductivity values leads to velocity fluctuations which subsequently cause spreading and eventually mixing of solute plumes. However, the flow topology remains comparably simple [e.g., Sposito, 2001]: The topological relationships between streamlines remains constant and chaotic streamline trajectories [Sposito, 2001] are not possible because the helicity density, that is, the scalar product of the velocity with its curl, is zero everywhere. In porous media which show spatial variation of anisotropy in the hydraulic conductivity-tensor (\mathbf{K}), by contrast, flow topology can be more complex. Under such conditions, streamlines can be chaotic, which may lead to separation of plume elements from the main plume, deformation in transverse directions, enlargement of the plume perimeter in these directions, and consequently enhanced transverse mixing of plume-borne water with the surrounding ambient water [Chiogna et al., 2015; Cirpka et al., 2015].

The effect of anisotropic hydraulic conductivity on three-dimensional flow in water-saturated porous media was analyzed intensively by *Bakker and Hemker* [2002], who described “groundwater whirls” i.e., bundles of spiraling flow lines in three dimensions. They derived closed-form expressions for a layered, bounded system, in which the orientation of the anisotropy of the \mathbf{K} -tensor differs between the layers. This generated twisting streamlines exhibiting secondary motion (i.e., circular motion in the transverse directions superimposed on main flow in the longitudinal direction). The same authors extended their analysis to horizontal strips of material with different anisotropy in the \mathbf{K} -tensor [*Hemker and Bakker*, 2006]. *Ye et al.* [2015] performed laboratory experiments, confirming the emergence of helical flow in anisotropic media constructed by alternating layers of fine and coarse material. *Chiogna et al.* [2015] analyzed heterogeneous hydraulic-conductivity fields with an anisotropic covariance function parameterizing the spatial variability of $\ln(K)$. Hydraulic conductivity was locally isotropic so that the local helicity density was zero, but the upscaled hydraulic conductivity was anisotropic. They constructed stripes in a herringbone pattern with different orientations of anisotropy in the covariance function of $\ln(K)$ and found macroscopic flow fields similar to those reported by *Bakker and Hemker* [2002], overlain by small-scale variability. These authors concluded that the helicity density should be considered a scale-dependent metric as the locally evaluated helicity density misses the large-scale structure of the flow field. *Cirpka et al.* [2015] analyzed solute transport in the flow fields generated by *Chiogna et al.* [2015]. The secondary motion enhanced transverse mixing to an extent that could not be accounted for by any other mechanisms caused by mild heterogeneity of hydraulic conductivity. This is of relevance for fringe-controlled biodegradation of plumes (both of anthropogenic contaminants and natural reactants) because transverse mixing determines the length of steady state solute plumes which react with compounds provided by the ambient groundwater flux [e.g., *Ham et al.*, 2004; *Cirpka et al.*, 2006; *Maier and Grathwohl*, 2006; *Liedl et al.*, 2011]. It may be noted that *Di Dato et al.* [2016] observed increased values of transverse macrodispersivities for strongly heterogeneous materials made of a multitude of elongated inclusions with strong conductivity contrasts. Like *Cirpka et al.* [2015], they assumed hydraulic conductivity to be locally isotropic. The orientation angles of the individual intrusions, however, were drawn from uniform distributions between 0 and 2π , and the enhancement of transverse macrodispersion by heterogeneity was considerably smaller when spherical inclusions were assumed. The changing orientation of the elongated inclusions led to intertwining flow fields, which is similar to the observations of *Cirpka et al.* [2015], who considered a herringbone-like structure of the heterogeneity. The hydraulic-conductivity configurations used by *Bakker and Hemker*, 2002; *Chiogna et al.* [2015], *Cirpka et al.* [2015], and *Ye et al.* [2015], namely stripes with diagonally oriented principal directions, were deliberately chosen to create maximal secondary motion. However, neither these configurations nor the randomly oriented individual elongated inclusions of *Di Dato et al.* [2016] are representative of sediment architectures observed in field studies.

The lack of geological “realism” in stochastic hydrogeology has stimulated many researchers to simulate porous media that better resemble observations of sedimentary structures in order to gain further insight into groundwater flow and solute transport processes [e.g., *Schwartz*, 1977; *Scheibe and Cole*, 1994; *Ramanathan et al.*, 2010]. Such methods may integrate field observations, such as outcrop mapping and borehole data, with other structure- or process-imitating approaches [cf., *Koltermann and Gorelick*, 1996] to create spatial distributions of hydrofacies (i.e., units with similar hydrogeological characteristics) [*Anderson*, 1989]. In most applications, such simulation methods do not consider the internal anisotropy of the aquifer materials, but rather assume an isotropic hydraulic-conductivity value per hydrofacies. This may be explained by experimental difficulties in determining the full hydraulic-conductivity tensor. Also, most stochastic analyses to date either neglected local anisotropy altogether or considered it to be a secondary effect. However, these studies typically focused on longitudinal macrodispersion (and maybe longitudinal mixing) which is dominated by differences in the magnitude of K .

The present study is motivated by the numerous aquifer-analog studies that have been undertaken to gain a better understanding of heterogeneity in aquifer systems formed in glacial outwash deposits [e.g., *Heinz et al.*, 2003; *Kostic et al.*, 2005; *Bayer et al.*, 2011; *Rogiers et al.*, 2013; *Höyng et al.*, 2014; *Weissmann et al.*, 2015]. These deposits are associated with large ice masses and occur in the proglacial environment, beyond the terminal point of a glacier. These deposits are typically highly heterogeneous due to strong variation in flow conditions during deposition at multiple temporal scales. They are hydrogeologically important as they are often exploited for groundwater abstraction due to their generally large hydraulic conductivities.

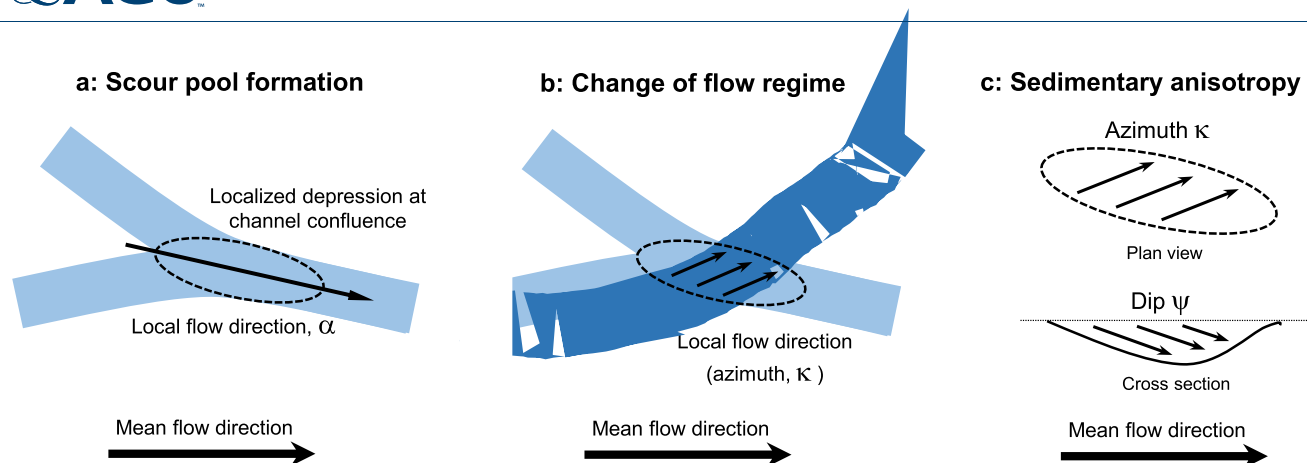


Figure 1. Conceptual model of scour-pool fill (trough) development in braided-river environments. (a) Formation of a scour at the confluence of two stable channels. (b) Filling of the scour at a later time reflecting the flow direction at the filling time in the anisotropy of the scour-fill. (c) Plan view and vertical cross section of a scour-fill feature.

These hydraulic properties also make them susceptible to contamination. Studies of glacial outwash deposits report strong heterogeneity comprising a variety of architectural elements that can often be grouped into hydrostratigraphic stories or genetic units [e.g., *Heinz et al., 2003; Bayer et al., 2011*]. These genetic units may comprise a number of different architectural elements as proposed by *Miall [1985]* and are demarcated by either erosional or depositional bounding surfaces [e.g., *Miall, 1996*]. The present study focuses on one particular architectural element: scour-pool fills.

Scour-pool fills have been observed during detailed characterization of glacial outwash deposits in numerous locations globally, in both ancient and modern settings [e.g., *Morison and Hein, 1987; Siegenthaler and Huggenberger, 1993; Khadkikar, 1999; Klingbeil et al., 1999; Heinz and Aigner, 2003a, 2003b; Beres et al., 1999; Bayer et al., 2011*]. These trough-like features are usually located within glacial outwash depositional environments. They are dominated by “cut-and-fill” elements and are considered by *Siegenthaler and Huggenberger [1993]* to be one of few structures preserved in these systems due to their low elevation relative to other depositional elements. Scour pools are formed at the confluence of large and stable channels with high discharge [*Heinz and Aigner, 2003a*] where the depression is elongated in the local flow direction with angle α to the mean flow direction (Figure 1a). After some time, the local flow direction may change and the depression is filled with sediments that are oriented according to the new flow regime (Figure 1b). The irregular orientation of sediments causes anisotropy of the hydraulic-conductivity tensor as flow occurs preferentially along the bedding planes [*Bierkens and Weerts, 1994; Borghi et al., 2015*]. Sedimentary anisotropy can then be defined by the following angles: the azimuth κ is the angle of the local flow direction in which the clasts were deposited, and the dip ψ is the angle of the bedding plane (Figure 1c). Variation in azimuth and dip is considered representative of changing paleoflow regimes [*Beres et al., 1999; Heinz and Aigner, 2003a*]. Scour-pool fills often have a well-defined (erosional) concave lower bounding surface and are planar in their upper bounding surface unless they have been eroded by another trough from above. Scour-pool lithofacies are highly heterogeneous, both internally and between features, but can be generally categorized as either gravel couplets (bimodal gravels at the base, open framework gravels at the top), or coarse, poorly sorted gravel units. Interfingering and cross stratification of sets as well as facies with significant sand content are common and these phenomena are thought to reflect the flow conditions at the time of deposition [*Siegenthaler and Huggenberger, 1993; Heinz and Aigner, 2003a; Heinz et al., 2003*].

The importance of scour-pool fills for three-dimensional groundwater flow was raised by *Heinz and Aigner [2003a]* and investigated by *Stauffer [2007]* and *Huber and Huggenberger [2016]*. *Stauffer [2007]* simulated groundwater flow and solute transport in a domain containing a single anisotropic inclusion, which was based on the observations of heterogeneous gravel deposits in Switzerland [*Jussel et al., 1994*], and found helical motion deforming the cross section of steady state advective solute plumes. *Huber and Huggenberger [2016]* modeled groundwater flow in braided-river deposits and reported strong “advective mixing” and flow deviation. They found that the variability of hydraulic conductivity was much less important

than the spatial arrangement of the different hydrofacies, particularly differences in the alignment of the scour-pool fills and the main flow direction. However, in their study the sedimentary anisotropy was restricted to one of three hydrofacies and no rotation of the hydraulic-conductivity tensor was considered.

In the present study, the depositional features simulated are analogous to the stacks of scour-pool fills observed at the Friedingen gravel pit in southwest Germany by *Heinz and Aigner* [2003a, Figure 10, body (C)]. These proglacial fluvial deposits occur in what is considered the main discharge area of the Würmian Rhine glacier that existed during the Last Glacial Maximum; the studied discharge area was distal to the maximal ice extension of this glacier [*Heinz et al.*, 2003]. The elements were primarily composed of clast-supported gravels and often included major sand constituents. Similar stacks of trough features were also reported in sections of the Canterbury Plains, New Zealand, by *Browne and Naish* [2003, Figure 7a and 7c]. We considered only one type of architectural element in order to better understand the effects of sedimentary anisotropy on flow and transport behavior.

The key question addressed in this paper is whether the findings of *Bakker and Hemker* [2002], *Chiogna et al.* [2015], and *Cirpka et al.* [2015], conducted in infinite stripes of anisotropic materials, are of any relevance in sedimentary structures with realistic internal anisotropy and geometries. The strength of anisotropy refers to ratios between the K -values in the different principal directions of the \mathbf{K} -tensor, which is formally identical to considering the ratios between the eigenvalues of the full \mathbf{K} -tensor. In the present study, we manipulate the orientation of the principal directions of the \mathbf{K} -tensor in each trough structure, that is, the eigenvectors of the full \mathbf{K} -tensor. We contrast this to cases in which local hydraulic conductivity is assumed to be isotropic, but its value changes from one trough structure to the next. In all cases, we do not resolve the variability within each trough structure but instead assign a uniform hydraulic-conductivity tensor to each structure. We expect that differences in the scalar values of hydraulic conductivity is the controlling characteristic for longitudinal spreading and mixing; whereas the spatially variable orientation of anisotropy is more important for transverse mixing.

2. Theory and Numerical Methods

2.1. Flow in Periodic Porous Media

Flow in porous media can be described by Darcy's law:

$$\mathbf{q} = -\mathbf{K}\nabla\phi(\mathbf{x}) \quad (1)$$

with the specific-discharge vector $\mathbf{q}[L T^{-1}]$, the hydraulic-head field $\phi(\mathbf{x})[L]$, the vector of spatial coordinates $\mathbf{x}[L]$ in the x , y , and z directions, respectively, and the symmetric, positive-definite, and second-order hydraulic-conductivity tensor \mathbf{K} . Under steady state conditions and without internal sources or sinks, the specific-discharge field is divergence-free:

$$\nabla \cdot \mathbf{q} = 0$$

To remove potential boundary effects we assumed an infinite periodic domain and applied a uniform-in-the-mean negative hydraulic gradient $\mathbf{J} = [J_x, J_y, J_z]$ [e.g., *Dykaar and Kitanidis*, 1992; *Cirpka et al.*, 2015]. To achieve this, we considered a model unit cell with dimensions $L \times W \times H$ and applied periodic head conditions subject to jumps meeting the mean trend [e.g., *Kitanidis*, 1992]:

$$\phi(L, y, z) = \phi(0, y, z) - L \cdot J_x \quad (2)$$

$$\phi(x, W/2, z) = \phi(x, -W/2, z) - W \cdot J_y \quad (3)$$

$$\phi(x, y, H/2) = \phi(x, y, -H/2) - H \cdot J_z \quad (4)$$

where \mathbf{J} is selected such that $\bar{\mathbf{q}}$, the volume-averaged specific discharge, is oriented along the x direction and meets a predefined value. Within a periodic conductivity field with periodic head boundary conditions, the head and velocity fields in this infinite domain are also periodic:

$$\phi(x + iL_x, y + jL_y, z + kL_z) = \phi(x, y, z) - (iL_x, jL_y, kL_z) \cdot \mathbf{J} \quad \forall i, j, k \in \mathbb{Z}, x, y, z \in \mathbb{R} \quad (5)$$

$$\mathbf{q}(x+iL_x, y+jL_y, z+kL_z) = \mathbf{q}(x, y, z) \quad \forall i, j, k \in \mathbb{Z}, x, y, z \in \mathbb{R} \quad (6)$$

2.2. Solute Transport

Steady state transport of a conservative solute in groundwater can be described by the advection-dispersion equation:

$$\mathbf{v} \cdot \nabla c - \nabla \cdot (\mathbf{D} \nabla c) = 0 \quad (7)$$

where $\mathbf{v} = \mathbf{q}/\theta [L T^{-1}]$ is the seepage-velocity vector, θ denotes porosity, $c [ML^{-3}]$ is the concentration of the conservative compound, and $\mathbf{D} [L^2 T^{-1}]$ is the local dispersion tensor. The standard linear model of Scheidegger [1961] was assumed for the local transverse dispersion coefficient:

$$D_t = D_p + \alpha_t |\mathbf{v}(\mathbf{x})| \quad (8)$$

where $D_p [L^2 T^{-1}]$ is the pore diffusion coefficient and $\alpha_t [L]$ is the transverse dispersivity, here assumed to be uniform. The local longitudinal dispersion coefficient D_ℓ was set to zero in this study. For simplicity, the orientation of the dispersion tensor \mathbf{D} was in the direction of mean velocity, rather than local velocity, resulting in:

$$\mathbf{D}(\mathbf{x}) = \begin{bmatrix} 0 & 0 & 0 \\ 0 & D_t(\mathbf{x}) & 0 \\ 0 & 0 & D_t(\mathbf{x}) \end{bmatrix} \quad (9)$$

An equivalent formulation of the time-dependent advection-dispersion equation in the limit $\Delta\tau \rightarrow 0$ is given in the Lagrangian framework of particle tracking with random walk:

$$\mathbf{x}_p(\tau + \Delta\tau) = \mathbf{x}_p(\tau) + \Delta\tau \mathbf{v}(\mathbf{x}_p) + \boldsymbol{\xi} \quad (10)$$

subject to

$$\mathbf{x}_p(0) = (0, y_{(p,0)}, z_{(p,0)}), \quad (11)$$

in which \mathbf{x}_p is the vector of particle coordinates, τ is travel time, $\Delta\tau$ is a travel-time increment, and $[y_{(p,0)}, z_{(p,0)}]$ are the y and z coordinates of the particle at the inlet plane, $x = 0$. $\boldsymbol{\xi}$ is a vector of multi-Gaussian random numbers with zero mean and covariance matrix $2\Delta\tau \mathbf{D}$.

2.3. Characterization of Groundwater Flow and Quantification of Solute Mixing

In the present study, we compared groundwater flow and solute transport characteristics in heterogeneous porous media. In order to study the mechanisms by which solute mixing is enhanced by heterogeneity and anisotropy of hydraulic conductivity, we computed and compared kinematic metrics, Lagrangian descriptors, and entropy-based metrics quantifying flow and solute transport.

2.3.1. Kinematic Descriptors of Plume Deformation

To quantify how the cross sections of circular stream tubes deform, we examined stretching and folding at cross sections throughout the model domain. These kinematic metrics of deformation were originally developed to describe time-dependent deformation [Falk and Langer, 1998; Kelley and Ouellette, 2011] and were applied to the distance-dependent development of steady state solute plumes by Chiogna *et al.* [2015]. The latter study considered deformation of stream tubes in two dimensions: in y, z planes at regular intervals in the x direction. Chiogna *et al.* [2015] quantified stream-tube deformation by observing the distance of surrounding streamlines to a central reference streamline; in the present study, we considered the distance of the streamlines to the mean cross-sectional position of N streamlines, originally forming a circle:

$$\mathbf{d}^n(x) = \mathbf{y}^n(x) - \bar{\mathbf{y}}(x) \quad (12)$$

with the index of the streamline n , the vector of y, z coordinates \mathbf{y} where the streamline crosses the plane at longitudinal position x , and $\bar{\mathbf{y}}(x)$ denoting the average position over all streamlines of the deformed circle. As mentioned earlier, at the inlet face of the model domain ($x_0 = 0$), the N streamlines form a circle with the initial radius r_0 :

$$d_y^n(x_0) = r_0 \cos(2\pi n/N) \quad (13)$$

$$d_2^n(x_0) = r_0 \sin(2\pi n/N) \tag{14}$$

The deformation of the stream tubes is quantified by comparing the distance-vector $\mathbf{d}^n(x_0 + \Delta x)$ to that at the inlet $\mathbf{d}^n(x_0)$, separating the part of the deformation that can be explained by a linear transformation of coordinates (stretching) from the nonlinear part (folding). Note that all linear transformations of circles are ellipses. That is, stretching yields a metric of the best-fit ellipse at distance Δx , whereas folding describes the deviation of the transformation from that to the best-fit ellipse. The linear least squares estimation of the transformation matrix $\mathbf{A}(\mathbf{y}, x)$ is given by:

$$\hat{\mathbf{A}} = \arg \min_{\mathbf{A}} \sum_{i=1}^N \|\mathbf{d}^n(x_0 + \Delta x) - \mathbf{A} \mathbf{d}^n(x_0)\|_2^2 \tag{15}$$

After determining the best-fit transformation matrix $\hat{\mathbf{A}}$, we computed the stretching metric A^2 as the normalized, squared L_2 -norm of the linear deformation of the circle using $\hat{\mathbf{A}}$:

$$A^2(\mathbf{y}, \Delta x) = \frac{1}{r_0^2 N} \sum_{n=1}^N \|\hat{\mathbf{A}}(\mathbf{y}, \Delta x) \mathbf{d}^n(x_0)\|_2^2 \tag{16}$$

Remembering that the linear transformation of a circle is an ellipse, A^2 can be shown to be the mean-squared stretching factor along the two main axes of the ellipse. The folding metric D^2 quantifies the nonlinear component of the deformation:

$$D^2(\mathbf{y}, \Delta x) = \frac{1}{r_0^2 N} \|\mathbf{d}^n(x_0 + \Delta x) - \mathbf{A}(\mathbf{y}, \Delta x) \mathbf{d}^n(x_0)\|_2^2 \tag{17}$$

The metrics A^2 and D^2 depend on the position of the original circle. To obtain meaningful results, it is thus necessary to compute the two metrics for multiple starting positions and average over the latter.

2.3.2. Macrodispersion

A common approach for the characterization of solute transport in heterogeneous media is by half the rate of change of the normalized second-central spatial moments, which is the operational definition of the macrodispersion tensor. Longitudinal macrodispersion can be computed by multiplying half the longitudinal gradient of the normalized second central temporal moments with the cubed effective velocity. We compared stochastic-analytical expressions of ensemble and effective macrodispersion coefficients based on linear theory [e.g., Dentz et al., 2000a; Fiori and Dagan, 2000] to numerical results of particle-tracking random walk (PT-RW) simulations. If linear stochastic theory was appropriate for the flow fields analyzed in the current study, two-point velocity statistics would be sufficient to predict second central moments; this would imply that higher-order effects, such as twisting streamlines, would not affect the evolution of second-central moments. Based on concepts introduced by Kitanidis [1988] and Dagan [1989], Dentz et al. [2000b] distinguished between the “ensemble” and “effective” dispersion tensors, \mathbf{D}^{ens} and \mathbf{D}^{eff} , respectively. For the ensemble dispersion tensor (denoted absolute dispersion by Andrićević and Cvetković [1998]), the moments are evaluated for the ensemble-averaged concentration. In effective dispersion (or relative dispersion according to Andrićević and Cvetković [1998]), the ensemble-averaging occurs after taking the spatial moments:

$$\mathbf{D}^{ens}(t) = \frac{1}{2} \frac{\partial}{\partial t} \mathbf{M}_{xx}^{2c} [E[(c(\mathbf{x}, t))]] \tag{18}$$

$$\mathbf{D}^{eff}(t) = \frac{1}{2} \frac{\partial}{\partial t} E[\mathbf{M}_{xx}^{2c}(t)] \tag{19}$$

$$\text{with } \mathbf{M}_{xx}^{2c}(t) = \frac{\int_{V_\infty} (\mathbf{x} - \mathbf{x}_c(t))^2 c(\mathbf{x}, t) d\mathbf{x}}{\int_{V_\infty} c(\mathbf{x}, t) d\mathbf{x}} \quad \text{and} \quad \mathbf{x}_c(t) = \frac{\int_{V_\infty} \mathbf{x} c(\mathbf{x}, t) d\mathbf{x}}{\int_{V_\infty} c(\mathbf{x}, t) d\mathbf{x}} \tag{20}$$

in which $E[\cdot]$ denotes the expected-value operator, and the integral $\int_{V_\infty} d\mathbf{x}$ implies integration from $-\infty$ to $+\infty$ over all spatial dimensions. \mathbf{M}_{xx}^{2c} and \mathbf{x}_c are the normalized second central moments and center of gravity of the solute cloud, respectively. That is, the effective (or relative) dispersion measures the average spread of individual plumes. Cirpka [2002] conjectured that the effective dispersion for a point-like initial

distribution, can be taken as a metric of mixing, which implicitly required that the plume is not significantly folded. *De Barros et al.* [2015, equation (22)] actually proved that at first-order, the dilution index is directly related to the three effective macrodispersivities of a point-like plume. Although not expressed in terms of dilution indices, the same result was implicit in *Fiori* [2001]. In ensemble (or absolute) dispersion, the uncertainty of tagging the plume center is added to the average spread of individual plumes. This quantity is obviously important for uncertainty analysis but does not describe mixing itself.

Dentz et al. [2000b] applied small-perturbation analysis to derive the following first-order expressions of ensemble and effective dispersion for a point source in second-order stationary velocity fields:

$$\mathbf{D}^{ens}(t) = \mathbf{D} + \int_{V_\infty} \frac{\mathbf{S}_{\mathbf{q}/\mathbf{q}^T}(\mathbf{s}) (4\pi^2 \mathbf{s}^T \mathbf{D} \mathbf{s} - 2\pi i \bar{\mathbf{v}}^T \mathbf{s}) (1 - \exp(-4\pi^2 \mathbf{s}^T \mathbf{D} \mathbf{s} + 2\pi i \bar{\mathbf{v}}^T \mathbf{s}) t)}{\theta^2 16\pi^4 (\mathbf{s}^T \mathbf{D} \mathbf{s})^2 + 4\pi^2 (\bar{\mathbf{v}}^T \mathbf{s})^2} d\mathbf{s} \quad (21)$$

$$\mathbf{D}^{eff}(t) = \mathbf{D}^{ens} - \int_{V_\infty} \frac{\mathbf{S}_{\mathbf{q}/\mathbf{q}^T}(\mathbf{s})}{\theta^2} \frac{(4\pi^2 \mathbf{s}^T \mathbf{D} \mathbf{s} + 2\pi i \bar{\mathbf{v}}^T \mathbf{s}) (\exp(-(2\pi i \bar{\mathbf{v}}^T \mathbf{s} + 4\pi^2 \mathbf{s}^T \mathbf{D} \mathbf{s}) t) - \exp(-8\pi^2 \mathbf{s}^T \mathbf{D} \mathbf{s} t))}{16\pi^4 (\mathbf{s}^T \mathbf{D} \mathbf{s})^2 + 4\pi^2 (\bar{\mathbf{v}}^T \mathbf{s})^2} d\mathbf{s} \quad (22)$$

with the local dispersion tensor \mathbf{D} , the power-spectral density function $\mathbf{S}_{\mathbf{q}/\mathbf{q}^T}(\mathbf{s})$ of specific-discharge fluctuations being the Fourier transform of the corresponding spatial covariance function, the spectral coordinates (or frequency) vector \mathbf{s} , the porosity θ , the imaginary unit i , the uniform mean seepage velocity field $\bar{\mathbf{v}}$, and time t since injection of the point source (in steady state analysis, t is replaced by x/\bar{v}_x). Ensemble and effective dispersivities can then be calculated by multiplying the dispersion coefficients by the mean seepage velocity in the x direction \bar{v}_x , calculated by dividing the length of the model domain by the mean arrival time at the model outlet.

The values derived from linear stochastic theory above can be compared to corresponding bulk ensemble and effective dispersivities calculated using numerical two-particle statistics:

$$\alpha_l^{ens} = \frac{1}{2} \frac{d\sigma_\tau^2}{dx} \bar{v}^2, \alpha_l^{eff} = \frac{1}{2} \frac{d\gamma_\tau}{dx} \bar{v}^2 \quad (23)$$

$$\alpha_y^{ens} = \frac{1}{2} \frac{d\sigma_y^2}{dx}, \alpha_y^{eff} = \frac{1}{2} \frac{d\gamma_y}{dx} \quad (24)$$

$$\alpha_z^{ens} = \frac{1}{2} \frac{d\sigma_z^2}{dx}, \alpha_z^{eff} = \frac{1}{2} \frac{d\gamma_z}{dx} \quad (25)$$

with the variances σ^2 and semivariograms γ of travel times and displacements in the y and z directions (τ , y , and z , respectively). To determine values of σ^2 and γ , we performed particle-tracking random walk (PT-RW), restricting the random displacement ξ in equation (10) to the (y , z) directions. Pairs of particles were introduced at the same location at the inlet face and variances σ^2 and semivariograms γ of travel times and displacements in the y and z directions (τ , y , and z , respectively) were calculated as a function of longitudinal distance x according to:

$$\sigma_\tau^2(x) = \frac{1}{2} \left(E[(\tau_1(x) - E[\tau_1(x)])^2] + E[(\tau_2(x) - E[\tau_2(x)])^2] \right), \gamma_\tau(x) = \frac{1}{2} E[(\tau_1(x) - \tau_2(x))^2] \quad (26)$$

$$\sigma_y^2(x) = \frac{1}{2} \left(E[(y_1(x) - E[y_1(x)])^2] + E[(y_2(x) - E[y_2(x)])^2] \right), \gamma_y(x) = \frac{1}{2} E[(y_1(x) - y_2(x))^2] \quad (27)$$

$$\sigma_z^2(x) = \frac{1}{2} \left(E[(z_1(x) - E[z_1(x)])^2] + E[(z_2(x) - E[z_2(x)])^2] \right), \gamma_z(x) = \frac{1}{2} E[(z_1(x) - z_2(x))^2] \quad (28)$$

in which $\tau_i(x)$, $y_i(x)$, and $z_i(x)$ are the travel time, and displacements in the y and z directions of particle i at distance x , respectively.

2.3.3. Plume Dilution

Non-Gaussian plume dilution cannot be adequately described using second spatial moments; therefore *Kitanidis* [1994] introduced the concept of the (volumetric) dilution index. *Rolle et al.* [2009] transferred the concept to steady state plumes by introduction of the flux-related dilution index $E_Q(x) [L^3 T^{-1}]$ providing an Eulerian metric of transverse solute mixing:

$$E_Q(x) = \exp \left[- \int_{-\infty}^{+\infty} \int_{-\infty}^{+\infty} p_Q(x, y, z) \cdot \ln(p_Q(x, y, z)) \cdot q_x(x, y, z) dy dz \right] \quad (29)$$

in which $p_Q(x, y, z) [T L^{-3}]$ denotes the flux-related density of the solute mass within the control plane at distance x :

$$p_Q(x, y, z) = c(x, y, z) \left(\int_{-\infty}^{+\infty} \int_{-\infty}^{+\infty} c(x, y', z') q_x(x, y', z') dy' dz' \right)^{-1} \quad (30)$$

and q_x denotes the specific-discharge component in the x direction. The flux-related dilution index is based on the Shannon entropy of the distribution of the advective solute flux over the volumetric flux. It has units of a discharge, and can be interpreted as an effective volume flux occupied by the mass flux. Although equation (29) contains dimensional quantities in the logarithm and exponential, it is dimensionally correct, as it can be seen as the limit of a discrete expression with dimensionless terms in the exponent and logarithm. Unlike transverse moments, the flux-related dilution index corrects for the compression and expansion of the plume cross section in high and low-velocity zones, respectively. Also, strictly kinematic plume deformation has no direct effect on the flux-related dilution index, whereas indirect effects caused by enhanced transverse-dispersive mass transfer across the extended plume surface influence E_Q .

If the two-particle semivariograms of transverse displacement for zero initial separation ($\gamma_y(x)$ and $\gamma_z(x)$) were correct descriptors of transverse mixing, the analytical transverse concentration distribution c_{an} in a uniform flow field, subject to the cumulative mixing coefficients $\gamma_y(x)$ and $\gamma_z(x)$, should have the same flux-related dilution index as the steady state plume in the heterogeneous domain. Accounting for the source geometry (inflow concentration of unity for $y_{lef} \leq y \leq y_{rig}$, $z_{bot} \leq z \leq z_{top}$, and zero otherwise) and periodicity in the y and z directions with the width W and height H of the unit cell, the corresponding analytical solution for uniform flow (adapted from Domenico and Palciauskas [1982, equation (18)]) reads as:

$$c_{an}(x, y, z) = \sum_{i=-\infty}^{\infty} \sum_{j=-\infty}^{\infty} \frac{1}{4} \left(\operatorname{erf} \left(\frac{y - y_{lef} + jW}{\sqrt{2\gamma_y(x)}} \right) - \operatorname{erf} \left(\frac{y - y_{rig} + jW}{\sqrt{2\gamma_y(x)}} \right) \right) \cdot \left(\operatorname{erf} \left(\frac{z - z_{bot} + iH}{\sqrt{2\gamma_z(x)}} \right) - \operatorname{erf} \left(\frac{z - z_{top} + iH}{\sqrt{2\gamma_z(x)}} \right) \right) \quad (31)$$

In the practical evaluation, it is sufficient to run the summation over indices i and j from -2 to 2 . We computed the flux-related dilution index $E_Q(c_{an}(x, y, z))$ for all distances x using the uniform mean specific discharge \bar{q}_x and compared that to the ensemble-averaged flux-related dilution index of the numerical steady state plumes for all four cases.

3. Model Setup and Methods

3.1. Model Setup

In this study, we considered a three-dimensional, infinite, periodic porous medium. The model domain was populated with scour-pool fills, also called "troughs". The hydraulic-conductivity tensor $\mathbf{K} [L T^{-1}]$ was block-wise homogeneous in these troughs. The dimensions of the unit cells, making up the periodic domain, were $L \times W \times H = 200 \text{ m} \times 70 \text{ m} \times 10 \text{ m}$. The grid spacing was $\Delta x \times \Delta y \times \Delta z = 1 \text{ m} \times 1 \text{ m} \times 0.1 \text{ m}$.

Trough features were simulated using an object-based modeling approach [e.g., Jussel et al., 1994]. Model grid cells were assigned a trough index based on half-ellipsoid trough structures, in which point (x, y, z) belongs to trough i if the following conditions are met:

$$\frac{((x - X_i) \cos(\alpha_i) + (y - Y_i) \sin(\alpha_i))^2}{\ell^2} + \frac{((x - X_i) \sin(\alpha_i) + (y - Y_i) \cos(\alpha_i))^2}{w^2} + \frac{(z - Z_i)^2}{d^2} \leq 1 \wedge z \leq Z_i \quad (32)$$

in which X_i , Y_i , and Z_i are the central coordinates of trough i , α_i is the angle between the major axis of the trough and the mean flow direction, and ℓ , w , and d are the half-length, half-width, and depth of the

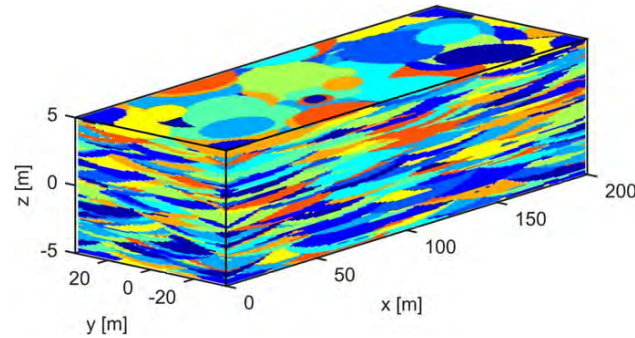


Figure 2. Representative realization of the generated trough geometry.

troughs, respectively, chosen to be identical for all troughs. The parameters X_i and Y_i were drawn from a uniform random distribution such that $x \in [0, L]$, and $y \in [-\frac{W}{2}, \frac{W}{2}]$. The troughs were generated iteratively starting from the bottom of the model domain ($\min(z)$). With each iteration, the Z_r -value of the trough increased by an aggradation thickness, set to 0.02 m in this study. Where troughs overlapped, the trough with a larger index i (i.e., the upper trough) superseded (or “eroded”) the trough below.

It was also possible for troughs to be entirely removed in this way. The troughs were rotated by the trough-specific angle α_{i_j} considered to be representative of the local (or paleo-) flow regime present during the formation of the trough (see Figure 1a). To ensure periodicity of the model, troughs that extended laterally outside of the model domain were reintroduced on the opposite boundary of the domain by subtracting the total width of the domain from the trough coordinates. In total, one hundred realizations of the trough geometries were generated; Figure 2 shows an example of a single realization.

In order to analyze the effects of heterogeneity and anisotropy on solute transport, five test cases were devised (summarized in Table 1). The hydraulic-conductivity tensor \mathbf{K}_i of each trough i is generated independently as the product of a scalar value of isotropic hydraulic conductivity K_i^{iso} , a rotation matrix \mathbf{R}_i , and a diagonal anisotropy matrix \mathbf{M}_i :

$$\mathbf{K}_i = K_i^{iso} \mathbf{R}_i \mathbf{M}_i \mathbf{R}_i^T \tag{33}$$

$$\mathbf{R}_i = \begin{bmatrix} \cos(\kappa) \cos(\psi) & \sin(\kappa) & \cos(\kappa) \sin(\psi) \\ -\sin(\kappa) \cos(\psi) & \cos(\kappa) & -\sin(\kappa) \sin(\psi) \\ -\sin(\psi) & 0 & \cos(\psi) \end{bmatrix} \tag{34}$$

The rotation of the system of coordinates by \mathbf{R}_i was performed according to the dip and azimuth angles, ψ and κ , respectively, that account for sedimentary anisotropy (see Figure 1). In cases 1 and 3, κ and ψ equal zero and the anisotropy matrix \mathbf{M}_i is the identity matrix, resulting in isotropic hydraulic conductivity. In cases 2 and 4, that account for sedimentary anisotropy, azimuth and dip angles were drawn from a uniform random distribution within a set range. In cases 1 and 2, K_i^{iso} was set to a uniform value for all troughs, whereas in case 3 and 4, K_i^{iso} was drawn from a log-normal distribution with the same geometric mean and variance of $\ln(K_i^{iso})$ for these test cases. Grid cells outside of troughs were given a background K_i^{iso} value. In order to assess what effect greater heterogeneity in the K^{iso} term would have on flow and transport an additional subcase of case 3 was included with a larger variance, referred to as “case 3-high.” All other parameters for this case were the same as case 3. The anisotropy matrix \mathbf{M}_i for cases 2 and 4 was a diagonal matrix with elements (1, 1, 0.1) and accounted for anisotropy in the rotated \mathbf{K} -tensor, between the bedding plane and perpendicular to it.

In case 1, the hydraulic-conductivity values of all troughs were identical and isotropic (uniform, isotropic K -field). In case 2, the isotropic hydraulic-conductivity values were identical in all troughs, but the spatial orientation of the anisotropy differed among the troughs.

This is expressed by independently generated values of dip and azimuth of each individual trough. Case 3 comprised a mildly heterogeneous field of locally isotropic hydraulic conductivity; case 3-high was similar but with a higher variance of log-hydraulic conductivity than the other test cases. Case 4 was both heterogeneous and anisotropic. One hydraulic-

Table 1. Summary of Test Cases

Isotropic Hydraulic Conductivity K^{iso}	Local K-Tensor	
	Isotropic	Anisotropic, Rotated
Homogeneous	Case 1	Case 2
Heterogeneous ($\sigma_{ln,K}^2 = 1$)	Case 3	Case 4
Heterogeneous ($\sigma_{ln,K}^2 = 2.3$)	Case 3-high	

Table 2. Geometric and Hydraulic Parameters of the Troughs

Parameter	Value
Length, ℓ	40 m ^a
Width, w	25 m ^a
Depth, h	1.7 m ^a
Paleoflow direction range, α	$[-25^\circ, +25^\circ]^b$
Dip range, ψ	$[0^\circ, +25^\circ]^c$
Azimuth range, κ	$[-45^\circ, +45^\circ]$
Aggradation thickness	0.02 m
Geometric mean of K^{iso}	$1 \times 10^{-3} \text{ m s}^{-1d}$
$\sigma_{\ln(K^{iso})}^2$ — cases 3 and 4	1
$\sigma_{\ln(K^{iso})}^2$ — case 3-high	2.3
Infill K^{iso} — cases 2, 3, 3-high and 4	$1 \times 10^{-4} \text{ m s}^{-1}$
Infill K^{iso} — case 1	$1 \times 10^{-3} \text{ m s}^{-1d}$
Anisotropy ratio, $K_{beddingplane}/K_{\perp}$ — cases 2 and 4	10 ^d
Porosity, n	0.3 ^d

^aHeinz and Aigner [2003a].
^bcf., Beres et al. [1999].
^cSiegenthaler and Huggenberger [1993, p.154].
^dKlingbeil et al. [1999, Table 3].

zones of the Rhine glacier [see Heinz et al., 2003, Figure 5]; these features were on average 40 m in length, 25 m wide, and 1.7 m deep. The paleoflow direction α_i was drawn from a uniform distribution ranging between $[-25^\circ, +25^\circ]$ with respect to the x direction; this range is similar to long-axis azimuth angles of $\pm 23^\circ$ incident to mean flow direction reported in a site the Upper Rhine by Beres et al. [1999]. The dip ψ ranged between 0° and 25° , corresponding to values reported by Siegenthaler and Huggenberger [1993, p.154]. The range of azimuth κ was randomly drawn from a uniform distribution with a range between -45° and 45° (0° equal to the mean flow direction) to reflect the larger variance in flow conditions in which sediments may be deposited in the trough.

Hydraulic parameters were selected from relevant characterization studies and similar numerical setups. The “P/T/H” hydrofacies described in Klingbeil et al. [1999, Table 3] may be considered analogous to the troughs in the present study. We have adopted their value of K_h as our geometric mean of K^{iso} , their ratio of K_h/K_v as our anisotropy ratio in cases 2 and 4, and their porosity n . (Rounding the adopted values to one significant figure was considered sufficient for the purposes of the present study.) In cases 1 and 2, K_i^{iso} was set to $1 \times 10^{-3} \text{ m s}^{-1}$ for all troughs, whereas in cases 3 and 4 K_i^{iso} was drawn from a log-normal distribution with geometric mean of $1 \times 10^{-3} \text{ m s}^{-1}$ and a variance of $\ln(K^{iso})$ of unity. Case 3-high had the same geometric mean as cases 3 and 4, but the variance was higher at $\sigma_{\ln(K^{iso})}^2 = 2.3$. The background K_i^{iso} value was $1 \times 10^{-3} \text{ m s}^{-1}$ in case 1 and $1 \times 10^{-4} \text{ m s}^{-1}$ in cases 2, 3, 3-high, and 4 [after Janković et al., 2009]. Porosity was set to a uniform value of 0.3 in all test cases. The geometrical and hydraulic model parameters are summarized in Table 2.

Table 3. Model Parameters for Flow, Advective Particle Tracking, Evaluation of Stretching and Folding Metrics, and Advective-Dispersive Transport

Parameter	Value
Model unit cell dimensions $X \times Y \times Z$	$200 \times 70 \times 10 \text{ m}$
Grid cell dimensions $\Delta x \times \Delta y \times \Delta z$	$1 \times 1 \times 0.1 \text{ m}$
Mean specific discharge \bar{q}	$[1 \times 10^{-5}, 0, 0] \text{ m s}^{-1}$
Advective particle tracking	
Particle inlet spacing $\Delta y \times \Delta z$	$0.2 \times 0.1 \text{ m}$
Number of particles tracked	35,000
Tracking distance over x	200 m
Stretching and folding	
Number of particles N per circle	12
Radius r_0 of initial circle	0.1 m
Tracking distance over x	200 m
Local dispersion (PT-RW, linear theory, ADE)	
Pore diffusion coefficient D_p	$10^{-9} \text{ m}^2 \text{ s}^{-1}$
Local transverse dispersivity α_t	10^{-3} m

conductivity tensor was assigned to each trough index according to the conditions of the test case. There was no correlation of hydraulic conductivity between the different troughs. For each of the 100 realizations of the trough geometry, one hydraulic-conductivity field was generated according to the test cases 2, 3, 3-high, and 4. For test case 1, there was no need to generate an ensemble, because all fields were identical.

3.2. Model Parameters

Where possible, geometric model parameters resembled observations of scour-pool fills in the Upper Rhine valley. The length ℓ , width w , and depth d of the trough features were chosen according to measurements of scour-pool fills in western paleodischarge

3.3. Numerical Methods

Steady state groundwater flow was solved using the mixed-hybrid finite element method [e.g., Arnold and Brezzi, 1985] using three-dimensional Raviart-Thomas elements of zero-order (RT_0) on cuboid elements [Raviart and Thomas, 1977]. The mean hydraulic gradient was adjusted such that the volume-averaged specific discharge \bar{q}_x was aligned to the main direction of flow and equaled $1 \times 10^{-5} \text{ m s}^{-1}$.

The advective component of conservative solute transport was solved by particle tracking. In each realization, 35,000 particles were placed across the inlet face ($x = 0 \text{ m}$) with a grid spacing of $\Delta y \times \Delta z = 0.2 \text{ m} \times 0.1 \text{ m}$. The particles were tracked over one unit length (200 m) in the x

direction. The periodic boundary conditions and hydraulic-conductivity field yielded a velocity field that repeated itself infinitely; this allowed the particles to be tracked through neighboring unit cells. Particle tracking was performed using the semianalytical method of Pollock [1988] implemented in Matlab, thereby utilizing the parallel computing capabilities of the graphical processing unit. The random-walk component ξ of equation (10) was not included in this calculation.

Stretching and folding was calculated by advective particle-tracking, placing circles of $N = 12$ particles according to equation (14) with an initial radius r_0 of 0.1 m in the plane perpendicular to the x axis. The value of r_0 was chosen such that the particles of a circle would begin in the same trough structure. The particle circles were placed across the inlet face (excluding the unit cell boundaries), centered at 1 m intervals in the y and z directions, and then tracked until $x = 200$ m. For each realization, 621 particle circles, comprising 7452 individual particles in total, were tracked for the quantification of stretching and folding. The random-walk component ξ of equation (10) was not included in this calculation.

To obtain numerical ensemble and effective macrodispersivities for a point-like injection, we performed particle-tracking random walk using equation (10), placing particle pairs at identical starting points. The particle pairs were injected at the inlet face ($x = 0$ m) with a grid spacing of $\Delta y \times \Delta z = 1 \text{ m} \times 0.1 \text{ m}$; in each realization 7000 particle pairs were tracked. The pore diffusion coefficient and local transverse dispersivity were set to $10^{-9} \text{ m}^2 \text{ s}^{-1}$ and 10^{-3} m , respectively. First-order ensemble and effective macrodispersion coefficients for point-like injection according to linear stochastic theory were computed by equations (21) and (22) using the velocity power-spectral density functions $\mathbf{S}_{\mathbf{q}\mathbf{q}}$ of the numerical velocity fields. Periodicity of the velocity fields facilitated spectral analysis by discrete Fourier transformation.

Steady state conservative advective-dispersive transport was solved using the scheme described by Cirpka et al. [2015]. In this scheme, advection is solved along streamlines and transverse dispersion by cell-centered Finite Volumes based on Voronoi polygons in the (y, z) -plane. (For details, please refer to Cirpka et al. [2015, section 3]). The coefficients of local transverse dispersion were identical to those used in particle-tracking random walk, and in the approximation by linear stochastic theory. We defined a rectangular source zone in the inlet plane with dimensions of $W \times H = 35 \text{ m} \times 5 \text{ m}$ located at the center of the inlet plane ($x = 0 \text{ m}$, $y \in [-17.5, 17.5 \text{ m}]$, $z \in [-0.25, 0.25 \text{ m}]$). The inflow concentration for streamlines belonging to the source zone was set to one, and for the other streamlines to zero. A summary of all model parameters is given in Table 3.

4. Results and Discussion

4.1. Groundwater Flow and Kinematic Descriptors

4.1.1. Groundwater Flow Fields

Hydraulic-head distributions for all test cases show little variation between one another which suggests that isotropic hydraulic-conductivity values K^{iso} and the orientation of anisotropy have only a minor effect on these distributions. The variability in hydraulic conductivity had a greater impact on the variability of groundwater velocity than that of hydraulic heads, which has been noted before [e.g., Poeter and Gaylord, 1990].

The variability of specific discharge demonstrates the differences between the four test cases more clearly. As a simple statistical metric, we calculated ensemble averages of the standard deviation of specific discharge in the three principal directions (q_x, q_y, q_z) normalized by the mean specific discharge in the x direction \bar{q}_x (Table 4). In case 1, the velocity field was uniform. In cases 3, 3-high, and 4, where isotropic

hydraulic-conductivity values K^{iso} fluctuated, the coefficients of variation of the longitudinal velocity component q_x equaled 1.18, 2.00, and 1.20, respectively. These values are one-order of magnitude larger than in case 2 (0.225), where only the orientation of the anisotropic \mathbf{K} -tensor varied, but K^{iso} remained uniform. Rotation of the \mathbf{K} -tensor had a great influence on the variability of q_y for cases with mild heterogeneity: among these cases, case 4 showed the highest normalized standard deviation in this direction

Table 4. Normalized Standard Deviations of Specific-Discharge Components in the Four Test Cases (Volume and Ensemble-Averaged)

Case	σ_{q_x} / \bar{q}_x	σ_{q_y} / \bar{q}_x	σ_{q_z} / \bar{q}_x
1	0	0	0
2	0.225	0.165	0.0217
3	1.18	0.124	0.0617
3-high	2.00	0.331	0.102
4	1.20	0.279	0.0517

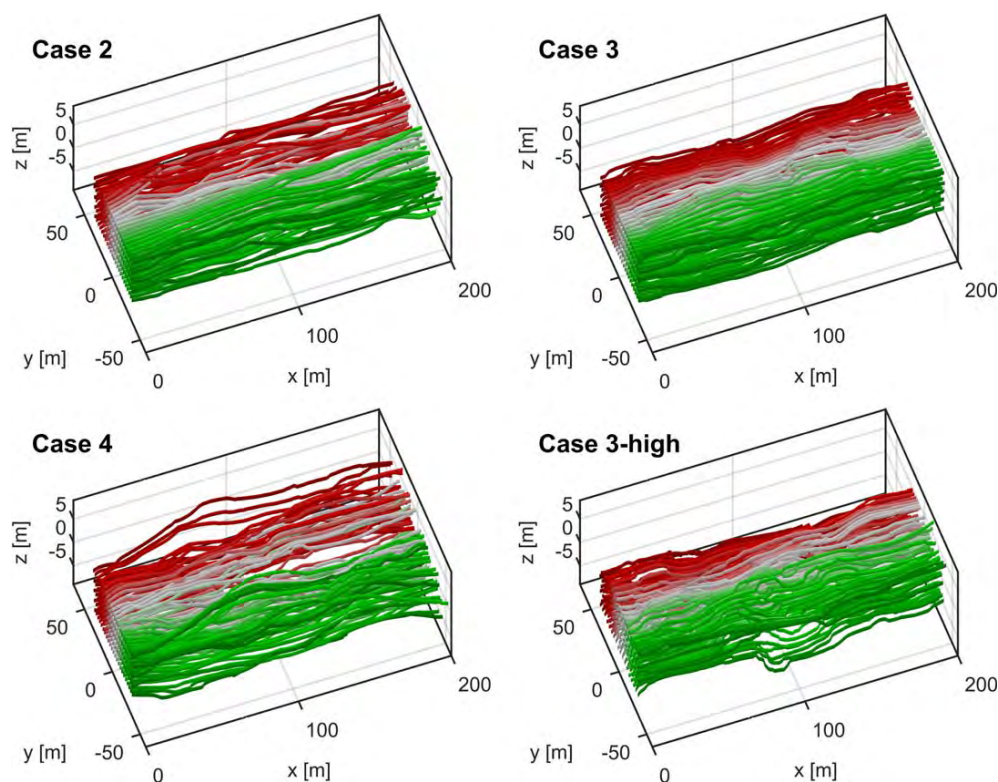


Figure 3. Streamlines in the four test cases. Color of the streamlines denotes the initial y coordinate value of the streamline. Cases according to Table 1.

(0.279), followed by case 2 (0.165), and then case 3 (0.124). The difference between cases 2 and 4 suggests that spatial variability of K^{iso} influences the variability of horizontal transverse velocity, in addition to the influence by spatially variable anisotropy. This is confirmed by case 3-high, where the significantly larger heterogeneity in isotropic conductivity led to an increase in the variability of q_y , exceeding that of case 4. The normalized standard deviations of q_z are significantly smaller than that of q_y . Variations of the vertical velocity reflect that water parcels tend to move vertically when diverging around low-conductivity troughs.

4.1.2. Streamline Patterns

Figure 3 shows streamlines for the four non-trivial test cases belonging to a single realization of the trough geometry. Case 1 (not shown) was trivial, as the velocity field is uniform. In case 2, some interweaving of streamlines occurred. Conversely, case 3 showed little interweaving of streamlines, even though some transverse oscillations were visible. Case 3-high, with larger heterogeneity in K^{iso} , exhibited abrupt fluctuations of streamline trajectories, however the streamline configurations (i.e., the location with respect to neighboring streamlines) appeared to stay predominantly constant. Case 4 showed the most chaotic streamline trajectories, with much interweaving of streamlines occurring. Comparison of advective streamline patterns, particularly between case 3-high and case 4, demonstrated the large effect of anisotropy on solute transport. Despite having the highest variability of isotropic hydraulic conductivity and of horizontal transverse velocity components, the streamline patterns in case 3-high were not as chaotic as those in case 4.

Stretching and folding metrics were greatly affected by sedimentary anisotropy, as demonstrated by the ensemble means of these metrics for each test case, depicted in Figure 4. (Case 1 is omitted from this analysis and Figure 4 because stretching and folding do not occur in uniform flow fields). Stretching, or linear deformation of the particle circles in the plane perpendicular to the direction of mean flow, was greater in the locally anisotropic cases 2 and 4 than in the locally isotropic cases 3 and 3-high. Close to the model inlet, the difference between the isotropic and anisotropic cases in A^2 was about one-order of magnitude, which increased to more than two-orders of magnitude at the model outlet. Stretching increased almost linearly

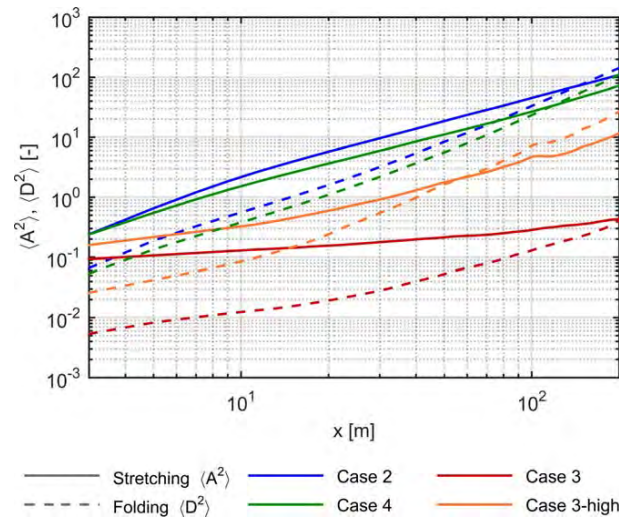


Figure 4. Stretching and folding metrics, A^2 and D^2 according to equations (16) and (17) for cases 2–4 (ensemble mean for each test case, initial tracker radius $r_0=0.1$ m). Case 1 is excluded because the deformation in uniform flow is zero.

namely at $x \approx 146$ m in the nonstationary anisotropic but otherwise homogeneous case 2, at $x \approx 60$ m for the isotropic but high- $\sigma_{\ln K}^2$ case 3-high, and at $x \approx 120$ m in the heterogeneous, anisotropic case 4. Folding did not exceed stretching within the model domain for the locally isotropic, heterogeneous case 3, although at the model outlet the crossover appeared imminent. The early transition to a folding-dominated system in case 3-high suggests that nonlinear plume deformation is more rapid with higher heterogeneity of K^{iso} -values, however, values of A^2 and D^2 in this test case were not as large as in cases with sedimentary anisotropy. Stretching and folding were slightly greater in case 2 than in case 4 which suggests that heterogeneity in isotropic hydraulic-conductivity values reduces deformation of the particle circles. The large difference between A^2 and D^2 in cases 3 and 4 implies that anisotropy (i.e., the rotation of the \mathbf{K} -tensor) had the greatest influence on these kinematic metrics. Analysis of A^2 and D^2 for different initial radii did not affect the rates of increase of these values; this is consistent with results reported by Kelley and Ouellette [2011] and Chiogna et al. [2015]. Increased deformation of plumes in the anisotropic test cases creates larger surface areas which can facilitate mixing between ambient and plume groundwater.

4.2. Solute Transport

4.2.1. Advective Arrival Time Distributions

Figure 5 shows breakthrough curves for advective transport, averaged over the outflow face of the domain, for each test case. These breakthrough curves reflect the variability and correlation structure of the longitudinal velocity component.

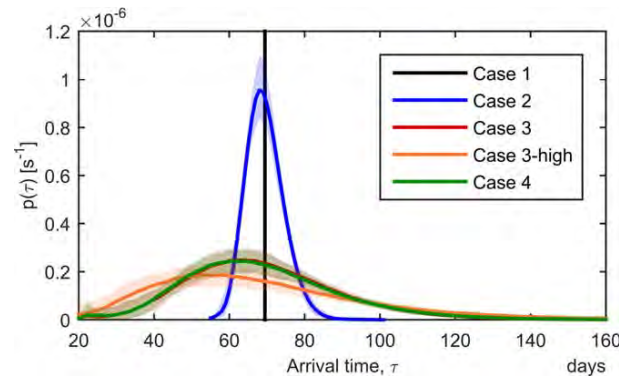


Figure 5. Advective arrival time distributions (ensemble average) for all test cases at the model outlet ($x = 200$ m). Shading denotes 5th–95th percentiles. Cases according to Table 1.

in the anisotropic test cases 2 and 4 (linear trend in the log-log plot with slope ≈ 1), whereas in the heterogeneous, locally isotropic cases 3 and 3-high a power-law with exponent < 1 could be observed. Folding, or nonlinear deformation of circular streamtubes with distance, showed a power law behavior with an exponent > 1 for all test cases. Similar to stretching, folding in the test cases accounting for local anisotropy was much greater than in those with locally isotropic conductivity, namely over two-orders of magnitude at the model outlet for case 3 and one-order of magnitude for case 3-high. Folding exceeds stretching within the model domain for cases 2, 3-high, and 4. The “crossover” point occurred at a different longitudinal distance x for each of these test cases;

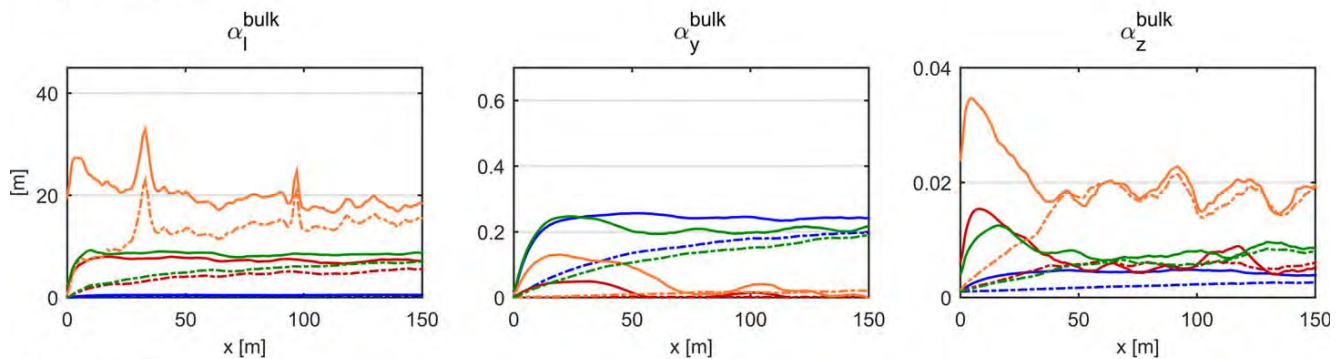
Case 1 (uniform flow) showed therefore a Dirac delta function as a breakthrough curve. Case 2 with uniform K^{iso} showed some spreading, but the effect was comparably small, which corresponds to the small variation of the longitudinal velocity component. Cases 3 and 4, with spatially variable K^{iso} , hardly differed in peak height and spread. Case 3-high, with $\sigma_{\ln K}^2=2.3$, had an earlier peak arrival time and a larger spread than the test cases with $\sigma_{\ln K}^2=1$. These results confirm that spatial variability of the isotropic hydraulic-conductivity values controls longitudinal spreading

because it governs the spatial variation of the longitudinal velocity component. Internal anisotropy appears to be irrelevant for longitudinal spreading, implying that the traditional approach of considering only spatial variability of isotropic hydraulic conductivity is appropriate in studies of longitudinal macrodispersion.

4.2.2. Bulk Dispersivities by Two-Point Particle Tracking and Linear Theory

We compared ensemble and effective dispersivities derived from linear stochastic theory (equations (21) and (22)) with those derived from particle tracking with a transverse random walk component (equations (23–25)). Figure 6 shows ensemble averages of bulk longitudinal and transverse dispersivities, that is, dispersion coefficients normalized by the mean absolute velocity, for each case (excluding case 1) computed from either particle-tracking random walk (PT-RW) or by linear stochastic theory (LT). Bulk ensemble and effective dispersivities in the longitudinal direction α_l^{bulk} for the cases with spatially variable K^{iso} -values, cases 3 and 4, were similar to each other, implying that the structure of the longitudinal velocity fluctuations is hardly affected by the internal anisotropy of the trough features. This is confirmed by the larger α_l^{bulk} -values for case 3-high. However, longitudinal dispersivities evaluated from particle-tracking random walk were about half as large as expected by linear theory for the given velocity covariance for cases with spatially variable K^{iso} -values. In principle, it is a known shortcoming of linear stochastic theory that it does not estimate macrodispersion coefficients well in cases of higher variances of the corresponding velocity component [e.g., Dagan, 1994; Beaudoin and de Dreuzy, 2013]. The values of α_l^{bulk} for case 2 (uniform K^{iso} , spatially variable orientation of anisotropy) were much smaller than those of cases 3, 3-high, and 4, which is congruent with a much smaller coefficient of variation of the longitudinal velocity component (see Table 4). In case 2, there was a good agreement between the numerical (PT-RW) and analytical solutions (LT) of α_l^{bulk} , which corresponds to linear theory being well applicable for cases of small velocity fluctuations. Longitudinal macrodispersion strongly depends on the velocity fluctuations in the longitudinal direction which are greatly influenced by heterogeneity of the isotropic hydraulic-conductivity values, and much less so by spatial variation of internal anisotropy.

A. Particle tracking



B. Linear Theory

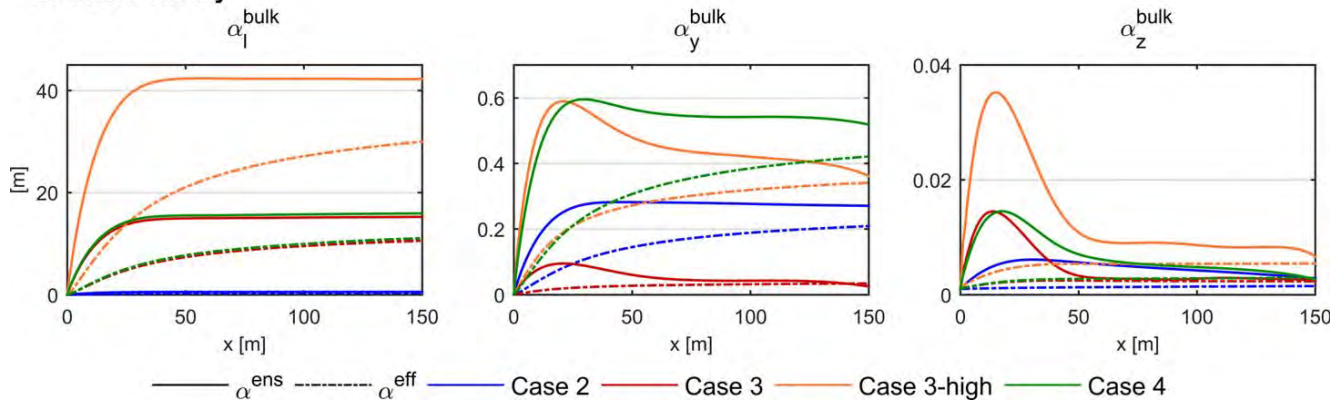


Figure 6. Bulk longitudinal and transverse dispersivities as function of longitudinal distance x , calculated from particle tracking, (equations (23)–(25)), and linear theory (equations (21) and (22)). Note that the entire length of the unit cell is not depicted due to artifacts caused by periodicity.

Bulk dispersivities in the transverse horizontal direction α_y^{bulk} were more than one-order of magnitude smaller than in the longitudinal direction. Both ensemble and effective values of α_y^{bulk} derived from PT-RW were similar between the locally anisotropic cases 2 and 4, suggesting that the spatial variation of anisotropy in the \mathbf{K} -tensor is important for macrodispersion in this direction. There is again good agreement between PT-RW and linear theory for values of α_y^{bulk} in case 2. However, the values of α_y^{bulk} derived from PT-RW for cases 3, 3-high, and 4 were much lower than those estimated from linear theory with hardly any scale effects at all.

Bulk ensemble and effective dispersivities in the transverse vertical direction α_z^{bulk} were another order of magnitude smaller than in the transverse horizontal direction. For case 2, the dispersivities were similar between both PT-RW and linear theory. Ensemble bulk dispersivities α_z^{bulk} for cases 3, 3-high, and 4 rose sharply to a peak and then tailed off in both the PT-RW and linear theory analysis. In the locally isotropic but heterogeneous cases 3 and 3-high, the peak appeared earlier and was also larger in the PT-RW calculations. In the locally anisotropic and heterogeneous case 4 with PT-RW, the peak was slightly lower but then it remained mostly higher than in case 3 but about half as large as case 3-high. In case 3-high from approximately $x=40$ m, the ensemble and effective dispersivities from PT-RW were very similar. As expected, ensemble dispersivities for all cases and directions were larger than effective dispersivities.

In summary, bulk dispersivity values in the longitudinal direction were strongly influenced by isotropic hydraulic-conductivity values, as demonstrated in Figure 6 by the similarity between cases 3 and 4 and the larger values of case 3-high. However, the anisotropy introduced in cases 2 and 4 lead to larger dispersivities in the transverse horizontal directions than for isotropic test cases. In order to traverse areas of lower hydraulic conductivity in anisotropic test cases, a substantial fraction of particles move horizontally around those zones. Dispersivities in the vertical direction were much smaller, which reflects the geometry of the trough fills (and in the anisotropic cases also the lower conductivity in the z direction). Bulk dispersivities calculated using linear stochastic theory were consistent with particle tracks for case 2, whereas in cases 3 and 4 they differed significantly.

Discrepancies between dispersivities derived from PT-RW and linear stochastic theory may indicate that the spreading of plumes originating from point sources does not solely depend on the velocity covariance function within the domain; the flow topology may also play a role in determining transport behavior. Similar conclusions were made by *Janković et al.* [2009] and *Di Dato et al.* [2016], albeit in locally isotropic porous media. The results of the present study demonstrate the impact of flow topology even in porous media with weak heterogeneity of hydraulic conductivity. Another likely cause for these discrepancies is that in linear stochastic theory the velocity covariance is sampled along the mean trajectory, whereas the true particle trajectories obtained by PT-RW are tortuous, so that the velocity fluctuations are also sampled along non-straight lines. The results above suggest that linear theory is at the limit of its applicability in this geologically plausible model context.

4.2.3. Concentration Distributions in Steady State Advective-Dispersive Transport

Steady state concentrations in advective-dispersive transport varied greatly between the test cases. Figure 7 shows the concentration distribution at various distances in cross sections perpendicular to the mean direction of flow for one trough simulation. In the homogeneous, isotropic case 1, the cross section of the plume did not change throughout the modeled distance from the shape imposed by the source, apart from some slight mixing at the plume fringe due to dispersion. The nonstationary, anisotropic case 2 exhibited considerable deformation of the plume cross section from $x=50$ m onward, particularly in the transverse horizontal direction where parts of the plume separated from the main plume body (which would be impossible with a simple flow topology) and other parts formed fin-like structures that resemble fingers in the two-dimensional cross sections. The original shape of the source zone could no longer be easily identified at these travel distances. The enlarged surface area of the plume enhances mixing between plume-borne and ambient water, which can be seen by the occurrence of intermediate concentrations. In cases 3 and 3-high, which account for spatially variable isotropic hydraulic conductivity, the steady state plume remained fairly compact in its cross section perpendicular to the mean flow direction; this is due to the less chaotic variation in the transverse velocity components in comparison to the cases with local anisotropy. Some deformation occurs but lateral spreading was minimal, which also agrees with the small values of stretching and folding as well as dilution observed for this case. Transverse mixing with the surrounding ambient water was smaller than in the cases accounting for nonstationary anisotropy (cases 2 and 4), which

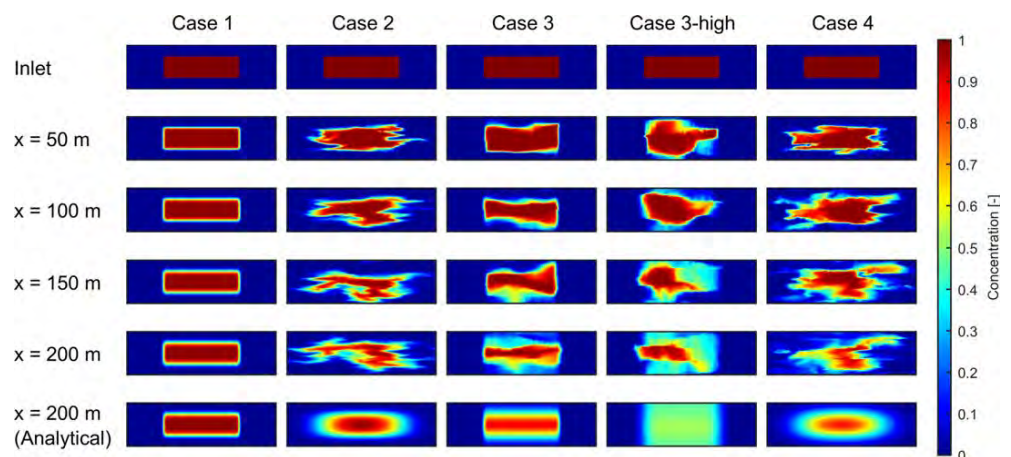


Figure 7. Steady state concentration distributions in observation planes perpendicular to the mean flow direction for all test cases in one trough simulation. The bottom row shows the analytical concentration distribution at $x = 200$ m calculated using equation (31) and the two-particle semivariograms of transverse displacement, γ_y and γ_z , from particle-tracking random walk. Spatial dimensions of the cross sections: $70 \text{ m} \times 10 \text{ m}$ ($20\times$ vertical exaggeration).

is expressed by the rare occurrence of intermediate concentrations. The nonstationary, anisotropic, and heterogeneous case 4 exhibited a similar behavior to that of case 2, yet even more intensive, with extensive lateral spreading, detachment of plume sections, and intensive mixing facilitated by the enlarged surface area.

The bottom row of Figure 7 depicts the concentration distributions at $x = 200$ m using the analytical solution based on semivariograms of two-particle displacements from PT-RW (equation (31)). There were strong differences between the analytical and numerical spatial concentration distributions (c_{an} and c_{num} , respectively) for all test cases, except case 1. While the differences in the spatial patterns were expected because the analytical solution assumes uniform flow, differences in the empirical cumulative density function of the flux-weighted concentration values over the entire cross section gave information on the validity of using γ_y and γ_z as metrics of transverse mixing. We found that the cumulative densities of intermediate values were much higher and the maximum concentrations were lower in the analytical concentration fields c_{an} than in the numerical concentration distributions c_{num} . The analytical solution assumes that the concentration distribution of a point source is Gaussian and therefore maximizes the entropy for given second central moments. In reality, plumes originating from point sources in the locally anisotropic cases 2 and 4 (not shown) are not Gaussian, indicating less dilution than anticipated by equation (31). In case 1, the analytical solution of equation (31) is exact, because all coefficients are indeed uniform. In the locally isotropic but mildly heterogeneous case 3, c_{an} at $x = 200$ m resembles the rectangular shape of the inlet distribution, but heterogeneity enhances dilution; this effect is much more pronounced in the higher $\sigma_{in,K}^2$ case 3-high, particularly in the vertical direction. In the locally anisotropic cases 2 and 4, the analytical solution cannot capture the complex configuration of the numerical concentration distributions. Maximum concentration values are higher in case 2 than in case 4, implying that heterogeneity in K^{iso} also increases dilution of the plume, additional to sedimentary anisotropy.

4.2.4. Flux-Related Dilution Indices

We normalized the computed flux-related dilution indices E_Q by their values at the inlet face ($E_Q(x)/E_Q(0)$) and took ensemble averages for each test case. Figure 8 shows the resulting evolution of the normalized flux-related dilution index with distance x . In general, $E_Q(x)/E_Q(0)$ increased monotonically with distance from the inlet face, which is in agreement with a strictly increasing entropy of the concentration distribution. The homogeneous, isotropic case 1 showed a very small increase in $E_Q(x)/E_Q(0)$ which is due to local transverse dispersion. Dilution in the nonstationary, anisotropic case 2 with uniform K^{iso} increased almost linearly. The value of 1.94 at the model outlet indicates that the solute flux at the outlet is distributed over twice the volume flux in comparison to the inlet. Conversely, dilution in the locally isotropic, but mildly heterogeneous case 3 did not increase at the same rate and falls between cases 1 and 2 with a value of 1.60. The introduction of greater heterogeneity in case 3-high increased dilution in the first 100 m of the model, however at the model outlet dilution was 2.05 — lower than for case 4. The most complex case 4 had the

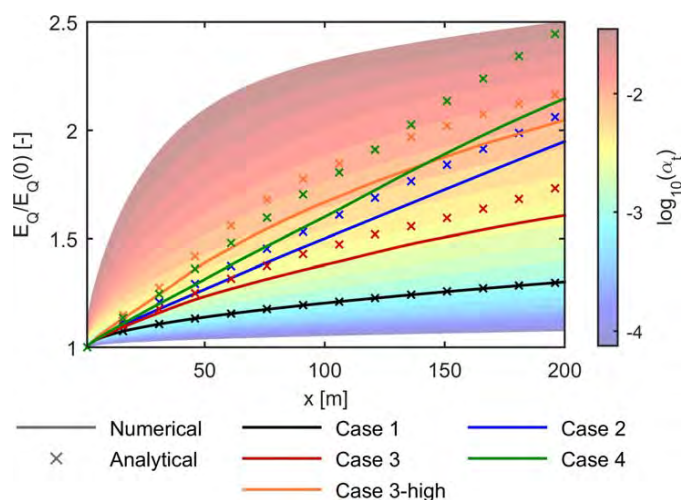


Figure 8. Ensemble averages of normalized flux-related dilution indices for all test cases. Numerical values are derived from steady state conservative advective-dispersive distributions as shown in Figure 7. Analytical values are derived from concentration distributions calculated using equation (31), based on two-particle displacement semivariograms obtained by particle-tracking random walk. Background contours are equivalent values of transverse dispersivity in an isotropic domain.

trivial case 1, the analytical and numerical concentrations were identical. In the other test cases, the analytically derived concentration distributions showed larger dilution than the respective numerical solutions. The analytical solution overpredicted $E_Q(x)/E_Q(0)$ consistently compared to the numerical solutions at the model outlet for cases 2, 3, and 3-high (7%, 8%, and 7%, respectively). For case 4, the difference was 15%, which suggests that both sedimentary anisotropy and heterogeneity in K^{iso} -values contribute to the discrepancy between the numerical and analytical solutions of flux-related dilution indices. The underlying assumption of Gaussianity in the analytical solution maximizes the entropy for the given second central moments. Thus, the analytical solution represents the upper limit of entropy, and therefore dilution.

Figure 8 also depicts the values of an equivalent isotropic transverse dispersivity α_t^{equ} needed to obtain the same flux-related dilution index in a three-dimensional domain of identical dimensions with uniform velocity. In comparison to the effective dispersivities obtained by particle-tracking random walk or linear stochastic theory, the values resulting from matching the dilution index were higher than the effective α_z -values, and significantly smaller than the effective α_y -values. It may be noted that *Cirpka et al.* [2015] observed an increase of α_t^{equ} by almost two-orders of magnitude, whereas the current study indicates smaller mixing enhancement. This may be explained by secondary motion being less consistent in the spatially limited trough-fill structures in comparison to the extended stripes of particular orientation of anisotropy.

5. Conclusions

The model results of the present study suggest that sedimentary anisotropy is highly relevant when examining transverse deformation and mixing of solute plumes in groundwater; this is consistent with the conclusions of *Bakker and Hemker* [2002], *Chiogna et al.* [2015], and *Cirpka et al.* [2015], however in more realistic porous media. Variation in sedimentary anisotropy in porous media causes shearing and subsequent deformation of material surfaces, as demonstrated by greater stretching and folding metrics in the cases with spatially variable local hydraulic anisotropy. This deformation enlarges the surface area over which mass transfer between plume-borne water and ambient groundwater is facilitated. This is supported by larger values of flux-related dilution indices for test cases with sedimentary anisotropy present than in cases without sedimentary anisotropy. Larger transverse mixing is accompanied by higher local velocities in the y direction in test cases accounting for anisotropy (see Table 4). Unless one studies layers with different orientations of hydraulic anisotropy in an infinite domain, extended shearing in directions transverse to the mean direction of flow is not possible without twisting of streamlines and folding of plumes. In isotropic

highest increase in the normalized flux-related dilution index with a value of 2.15 at 200 m. The two cases with anisotropic **K**-tensors both showed a marked increase in dilution over distance which suggests that sedimentary anisotropy accentuates transverse mixing of the plume. Higher heterogeneity in isotropic hydraulic-conductivity values, as in case 3-high, also increases dilution although not to the same extent as sedimentary anisotropy.

The ensemble mean of analytical values of $E_Q(x)/E_Q(0)$, based on the analytical concentration distributions derived from the two-particle semivariograms in equation (31) are displayed in Figure 8 as cross symbols. In the

porous media, where \mathbf{K} -tensors and the mean groundwater flow direction are congruent, transverse shearing may be caused by spatial variability of the scalar hydraulic conductivity. However, the results of the present study demonstrate that transverse shearing is enhanced by spatial variation of sedimentary anisotropy.

Variability in the scalar values of hydraulic conductivity is important for the variability of the longitudinal component of groundwater velocity and thus longitudinal spreading and mixing. This was shown by the similarity in advective travel-time distributions of the test cases 3 and 4 (with spatially variable K^{iso} -values) in Figure 5 which are in agreement with large coefficients of variation of longitudinal velocity σ_{q_x}/\bar{q}_x in these test cases (Table 4). However, the degree of variability in K^{iso} ($\sigma_{\ln(K^{iso})}^2 = 1$) does not support a strong impact of this type of variability on transverse mixing. As demonstrated by *Beaudoin and de Dreuzy* [2013], greater heterogeneity in isotropic hydraulic conductivity ($\sigma_{\ln(K^{iso})}^2 \geq 1$) can induce intertwining of streamlines, which has a subsequent impact on transverse dispersion coefficients. The results of the present study suggest that realistic sedimentary anisotropy can also induce such behavior at relatively low levels of heterogeneity ($\sigma_{\ln(K^{iso})}^2 = 1$). Therefore, when considering transverse mixing in porous media, we advise that not only scalar hydraulic conductivities are analyzed, but also the anisotropic structure of the sedimentary units. Ultimately, we should aim at relating sedimentary processes to the anisotropy of hydraulic conductivity and its spatial variation.

We also tested the conjecture of *Cirpka* [2002] that effective dispersion for point-like injection would be a suitable measure of actual mixing. We could not confirm this conjecture for transverse mixing in three-dimensional flow. While steady state plumes subject to advective-dispersive transport in complex flow fields showed strong deformation, their flux-related dilution indices were comparably small. Computing the flux-related dilution indices for uniform flow, using the two-point semivariograms of lateral displacement as dispersive mixing metrics, led to more strongly diluted plumes. In flow fields leading to plume deformation, a plume originating from a point source is subjected to the deformation as soon as transverse dispersion has led to cross-sectional expansion of the plume. However, this implies that second-central spatial moments of such plumes not only express mixing, but also the irregularity of the deformed plume cross section. This puts the first-order analytical results on the relationship between the dilution index and the effective dispersion tensor by *de Barros et al.* [2015] into question when flow fields are topologically more complex.

The present study has focused solely on scour-pool fills, a sedimentary feature commonly reported in braided-river depositional environments. However, such environments are typically composed of many different architectural elements. Modeling studies in more complex configurations of architectural elements may offer insight into solute transport processes at multiple scales. At the present time, it is not possible to measure complex groundwater velocity fields induced by sedimentary anisotropy, or indeed anisotropic hydraulic conductivity, at the field-scale. Novel characterization of complex groundwater velocity fields will help to further quantify transverse mixing in aquifers, which has a large impact on the length of steady state, mixing-controlled plumes.

Acknowledgments

This work was funded by the German Research Foundation (DFG) within the Research Training Group "Integrated Hydrosystem Modelling" (RTG 1829) at the University of Tübingen. The authors would like to thank Gabriele Chiogna for his assistance with the stretching and folding algorithm. We also thank the associate editor and three anonymous reviewers for their invaluable input. The source code for the models used in this study is available from the authors upon request (olaf.cirpka@uni-tuebingen.de).

References

- Anderson, M. P. (1989), Hydrogeologic facies models to delineate large-scale spatial trends in glacial and glaciofluvial sediments, *Geol. Soc. Am. Bull.*, *101*(4), 501–511, doi:10.1130/0016-7606(1989)101<0501:HFMTDL>2.3.CO;2.
- Andrićević, R., and V. Cvetković (1998), Relative dispersion for solute flux in aquifers, *J. Fluid Mech.*, *361*, 145–174, doi:10.1017/S0022112098008751.
- Arnold, D. N., and F. Brezzi (1985), Mixed and nonconforming finite element methods: Implementation, postprocessing and error estimates, *RAIRO Modél. Math. Anal. Numér.*, *19*(1), 7–32.
- Bakker, M., and K. Hemker (2002), A Dupuit formulation for flow in layered, anisotropic aquifers, *Adv. Water Resour.*, *25*(7), 747–754, doi:10.1016/S0309-1708(02)00074-X.
- Bayer, P., P. Huggenberger, P. Renard, and A. Comunian (2011), Three-dimensional high resolution fluvio-glacial aquifer analog: Part 1: Field study, *J. Hydrol.*, *405*(1), 1–9.
- Beaudoin, A., and J.-R. de Dreuzy (2013), Numerical assessment of 3-D macrodispersion in heterogeneous porous media, *Water Resour. Res.*, *49*, 2489–2496, doi:10.1002/wrcr.20206.
- Beres, M., P. Huggenberger, A. G. Green, and H. Horstmeyer (1999), Using two- and three-dimensional georadar methods to characterize glaciofluvial architecture, *Sediment. Geol.*, *129*(1–2), 1–24, doi:10.1016/S0037-0738(99)00053-6.
- Bierkens, M. F. P., and H. J. T. Weerts (1994), Block hydraulic conductivity of cross-bedded fluvial sediments, *Water Resour. Res.*, *30*(10), 2665–2678, doi:10.1029/94WR01049.
- Borghi, A., P. Renard, and G. Courrioux (2015), Generation of 3D spatially variable anisotropy for groundwater flow simulations, *Groundwater*, *53*, 955–958, doi:10.1111/gwat.12295.
- Browne, G. H., and T. R. Naish (2003), Facies development and sequence architecture of a late Quaternary fluvial-marine transition, Canterbury Plains and shelf, New Zealand: Implications for forced regressive deposits, *Sediment. Geol.*, *158*(1–2), 57–86, doi:10.1016/S0037-0738(02)00258-0.
- Chiogna, G., O. A. Cirpka, M. Rolle, and A. Bellin (2015), Helical flow in three-dimensional nonstationary anisotropic heterogeneous porous media, *Water Resour. Res.*, *51*, 261–280, doi:10.1002/2014WR015330.

- Cirpka, O. A. (2002), Choice of dispersion coefficients in reactive transport calculations on smoothed fields, *J. Contam. Hydrol.*, *58*(3–4), 261–282, doi:10.1016/S0169-7722(02)00039-6.
- Cirpka, O. A., Å. Olsson, Q. Ju, M. A. Rahman, and P. Grathwohl (2006), Determination of transverse dispersion coefficients from reactive plume lengths, *Ground Water*, *44*(2), 212–221, doi:10.1111/j.1745-6584.2005.00124.x.
- Cirpka, O. A., G. Chiogna, M. Rolle, and A. Bellin (2015), Transverse mixing in three-dimensional nonstationary anisotropic heterogeneous porous media, *Water Resour. Res.*, *51*, 241–260, doi:10.1002/2014WR015331.
- Dagan, G. (1989), *Flow and Transport in Porous Formations*, Springer, Berlin.
- Dagan, G. (1994), The significance of heterogeneity of evolving scales to transport in porous formations, *Water Resour. Res.*, *30*(12), 3327–3336, doi:10.1029/94WR01798.
- de Barros, F. P. J., A. Fiori, F. Boso, and A. Bellin (2015), A theoretical framework for modeling dilution enhancement of non-reactive solutes in heterogeneous porous media, *J. Contam. Hydrol.*, *175–176*, 72–83, doi:10.1016/j.jconhyd.2015.01.004.
- Dentz, M., H. Kinzelbach, S. Attinger, and W. Kinzelbach (2000a), Temporal behavior of a solute cloud in a heterogeneous porous medium: 2. Spatially extended injection, *Water Resour. Res.*, *36*(12), 3605–3614, doi:10.1029/2000WR900211.
- Dentz, M., H. Kinzelbach, S. Attinger, and W. Kinzelbach (2000b), Temporal behavior of a solute cloud in a heterogeneous porous medium: 1. Point-like injection, *Water Resour. Res.*, *36*(12), 3591–3604, doi:10.1029/2000WR900162.
- Di Dato, M., F. P. J. de Barros, A. Fiori, and A. Bellin (2016), Effects of the hydraulic conductivity microstructure on macrodispersivity, *Water Resour. Res.*, *52*, 6818–6832, doi:10.1002/2016WR019086.
- Domenico, P. A., and V. V. Palciauskas (1982), Alternative boundaries in solid waste management, *Ground Water*, *20*(3), 303–311, doi:10.1111/j.1745-6584.1982.tb01351.x.
- Dykaar, B. B., and P. K. Kitanidis (1992), Determination of the effective hydraulic conductivity for heterogeneous porous media using a numerical spectral approach: 1. Method, *Water Resour. Res.*, *28*(4), 1155–1166, doi:10.1029/91WR03084.
- Falk, M. L., and J. S. Langer (1998), Dynamics of viscoplastic deformation in amorphous solids, *Phys. Rev. E*, *57*(6), 7192–7205, doi:10.1103/PhysRevE.57.7192.
- Fiori, A. (2001), The Lagrangian concentration approach for determining dilution in aquifer transport: Theoretical analysis and comparison with field experiments, *Water Resour. Res.*, *37*(12), 3105–3114, doi:10.1029/2001WR000228.
- Fiori, A., and G. Dagan (2000), Concentration fluctuations in aquifer transport: A rigorous first-order solution and applications, *J. Contam. Hydrol.*, *45*(1–2), 139–163, doi:10.1016/S0169-7722(00)00123-6.
- Ham, P. A., R. J. Schotting, H. Prommer, and G. B. Davis (2004), Effects of hydrodynamic dispersion on plume lengths for instantaneous bimolecular reactions, *Adv. Water Resour.*, *27*(8), 803–813, doi:10.1016/j.advwatres.2004.05.008.
- Heinz, J., and T. Aigner (2003a), Hierarchical dynamic stratigraphy in various Quaternary gravel deposits, Rhine glacier area (SW Germany): Implications for hydrostratigraphy, *Int. J. Earth Sci.*, *92*(6), 923–938, doi:10.1007/s00531-003-0359-2.
- Heinz, J., and T. Aigner (2003b), Three-dimensional GPR analysis of various Quaternary gravel-bed braided river deposits (southwestern Germany), *Geol. Soc. Spec. Publ.*, *211*(1), 99–110, doi:10.1144/GSL.SP.2001.211.01.09.
- Heinz, J., S. Kleineidam, G. Teutsch, and T. Aigner (2003), Heterogeneity patterns of Quaternary glaciofluvial gravel bodies (SW-Germany): Application to hydrogeology, *Sediment. Geol.*, *158*(1–2), 1–23, doi:10.1016/S0037-0738(02)00239-7.
- Hemker, K., and M. Bakker (2006), Analytical solutions for whirling groundwater flow in two-dimensional heterogeneous anisotropic aquifers, *Water Resour. Res.*, *42*, W12419, doi:10.1029/2006WR004901.
- Höyng, D., F. M. D’Affonseca, P. Bayer, E. G. de Oliveira, J. A. J. Perinotto, F. Reis, H. Weiß, and P. Grathwohl (2014), High-resolution aquifer analog of fluvial–aeolian sediments of the Guarani aquifer system, *Environ. Earth Sci.*, *71*(7), 3081–3094, doi:10.1007/s12665-013-2684-5.
- Huber, E., and P. Huggenberger (2016), Subsurface flow mixing in coarse, braided river deposits, *Hydrol. Earth Syst. Sci.*, *20*(5), 2035–2046, doi:10.5194/hess-20-2035-2016.
- Janković, I., D. R. Steward, R. J. Barnes, and G. Dagan (2009), Is transverse macrodispersivity in three-dimensional groundwater transport equal to zero? A counterexample, *Water Resour. Res.*, *45*, W08415, doi:10.1029/2009WR007741.
- Jussel, P., F. Stauffer, and T. Dracos (1994), Transport modeling in heterogeneous aquifers: 1. Statistical description and numerical generation of gravel deposits, *Water Resour. Res.*, *30*(6), 1803–1817, doi:10.1029/94WR00162.
- Kelley, D. H., and N. T. Ouellette (2011), Separating stretching from folding in fluid mixing, *Nat. Phys.*, *7*(6), 477–480, doi:10.1038/nphys1941.
- Khadkikar, A. S. (1999), Trough cross-bedded conglomerate facies, *Sediment. Geol.*, *128*(1–2), 39–49, doi:10.1016/S0037-0738(99)00060-3.
- Kitanidis, P. K. (1988), Prediction by the method of moments of transport in a heterogeneous formation, *Hydrol. Res.*, *102*(1), 453–473, doi:10.1016/0022-1694(88)90111-4.
- Kitanidis, P. K. (1992), Analysis of macrodispersion through volume-averaging: Moment equations, *Stochastic Hydrol. Hydraul.*, *6*(1), 5–25, doi:10.1007/BF01581672.
- Kitanidis, P. K. (1994), The concept of the dilution index, *Water Resour. Res.*, *30*(7), 2011–2026, doi:10.1029/94WR00762.
- Klingbeil, R., S. Kleineidam, U. Aspöhn, T. Aigner, and G. Teutsch (1999), Relating lithofacies to hydrofacies: Outcrop-based hydrogeological characterisation of Quaternary gravel deposits, *Sediment. Geol.*, *129*(3–4), 299–310, doi:10.1016/S0037-0738(99)00067-6.
- Koltermann, C. E., and S. M. Gorelick (1996), Heterogeneity in sedimentary deposits: A review of structure-imitating, process-imitating, and descriptive approaches, *Water Resour. Res.*, *32*(9), 2617–2658, doi:10.1029/96WR00025.
- Kostic, B., A. Becht, and T. Aigner (2005), 3-D sedimentary architecture of a Quaternary gravel delta (SW-Germany): Implications for hydrostratigraphy, *Sediment. Geol.*, *181*(3–4), 147–171, doi:10.1016/j.sedgeo.2005.07.004.
- Liedl, R., P. K. Yadav, and P. Dietrich (2011), Length of 3-D mixing-controlled plumes for a fully penetrating contaminant source with finite width, *Water Resour. Res.*, *47*, W08602, doi:10.1029/2010WR009710.
- Maier, U., and P. Grathwohl (2006), Numerical experiments and field results on the size of steady state plumes, *J. Contam. Hydrol.*, *85*(1–2), 33–52, doi:10.1016/j.jconhyd.2005.12.012.
- Miall, A. D. (1985), Architectural-element analysis: A new method of facies analysis applied to fluvial deposits, *Earth Sci. Rev.*, *22*(4), 261–308, doi:10.1016/0012-8252(85)90001-7.
- Miall, A. D. (1996), *The Geology of Fluvial Deposits: Sedimentary Facies, Basin Analysis, and Petroleum Geology*, Springer, Berlin.
- Morison, S. R., and F. J. Hein (1987), Sedimentology of the white channel gravels, Klondike area, Yukon Territory: Fluvial deposits of a confined valley, in *Recent Developments in Fluvial Sedimentology, Special Publication*, vol. 39, edited by F. Ethridge, R. Flores, and M. Harvey, pp. 205–216, The Soc. of Econ. Paleontol. and Mineral., Tulsa.
- Poeter, E., and D. R. Gaylord (1990), Influence of aquifer heterogeneity on contaminant transport at the Hanford site, *Ground Water*, *28*(6), 900–909, doi:10.1111/j.1745-6584.1990.tb01726.x.

- Pollock, D. W. (1988), Semianalytical computation of path lines for finite-difference models, *Ground Water*, 26(6), 743–750, doi:10.1111/j.1745-6584.1988.tb00425.x.
- Ramanathan, R., A. Guin, R. W. Ritz, D. F. Dominic, V. L. Freedman, T. D. Scheibe, and I. A. Lunt (2010), Simulating the heterogeneity in braided channel belt deposits: 1. A geometric-based methodology and code, *Water Resour. Res.*, 46, W04515, doi:10.1029/2009WR008111.
- Raviart, P.-A., and J.-M. Thomas (1977), A mixed finite element method for 2-nd order elliptic problems, in *Mathematical Aspects of Finite Element Methods, Lecture Notes in Mathematics*, edited by I. Galligani, and E. Magenes, vol. 606, pp. 292–315, Springer, Berlin, Heidelberg.
- Rogiers, B., K. Beerten, T. Smeeckens, D. Mallants, M. Gedeon, M. Huysmans, O. Batelaan, and A. Dassargues (2013), The usefulness of outcrop-analogue air-permeameter measurements for analysing aquifer heterogeneity: Testing outcrop hydrogeological parameters with independent borehole data, *Hydrol. Earth Syst. Sci.*, 17(12), 5155–5166, doi:10.5194/hess-17-5155-2013.
- Rolle, M., C. Eberhardt, G. Chiogna, O. A. Cirpka, and P. Grathwohl (2009), Enhancement of dilution and transverse reactive mixing in porous media: Experiments and model-based interpretation, *J. Contam. Hydrol.*, 110(3-4), 130–142, doi:10.1016/j.jconhyd.2009.10.003.
- Rubin, Y. (2003), *Applied Stochastic Hydrogeology*, Oxford Univ. Press, Oxford, New York.
- Scheibe, T. D., and C. R. Cole (1994), Non-Gaussian particle tracking: Application to scaling of transport processes in heterogeneous porous media, *Water Resour. Res.*, 30(7), 2027–2039, doi:10.1029/94WR00587.
- Scheidegger, A. E. (1961), General theory of dispersion in porous media, *J. Geophys. Res.*, 66(10), 3273–3278, doi:10.1029/JZ066i010p03273.
- Schwartz, F. W. (1977), Macroscopic dispersion in porous media: The controlling factors, *Water Resour. Res.*, 13(4), 743–752, doi:10.1029/WR013i004p00743.
- Siegenthaler, C., and P. Huggenberger (1993), Pleistocene Rhine gravel: Deposits of a braided river system with dominant pool preservation, *Geol. Soc. Spec. Publ.*, 75(1), 147–162, doi:10.1144/GSL.SP.1993.075.01.09.
- Sposito, G. (2001), Topological groundwater hydrodynamics, *Adv. Water Resour.*, 24(7), 793–801, doi:10.1016/S0309-1708(00)00077-4.
- Stauffer, F. (2007), Impact of highly permeable sediment units with inclined bedding on solute transport in aquifers, *Adv. Water Resour.*, 30(11), 2194–2201, doi:10.1016/j.advwatres.2007.04.008.
- Weissmann, G., A. Pickel, K. McNamara, J. Frechette, I. Kalinovich, R. Allen-King, and I. Jankovic (2015), Characterization and quantification of aquifer heterogeneity using outcrop analogs at the Canadian Forces Base Borden, Ontario, Canada, *Geol. Soc. Am. Bull.*, 127(7-8), 1021–1035, doi:10.1130/B31193.1.
- Ye, Y., G. Chiogna, O. A. Cirpka, P. Grathwohl, and M. Rolle (2015), Experimental evidence of helical flow in porous media, *Phys. Rev. Lett.*, 115(19), 194502, doi:10.1103/PhysRevLett.115.194502.

Erratum

In the originally published version of this article, equations 33 and 34 were incorrectly typeset. The equations have now been corrected, and this may be considered the official version of record.

An Open, Object-Based Framework for Generating Anisotropy in Sedimentary Subsurface Models

by Jeremy P. Bennett¹, Claus P. Haslauer², Martin Ross³, and Olaf A. Cirpka²

Abstract

The spatial distribution of hydraulic properties in the subsurface controls groundwater flow and solute transport. However, many approaches to modeling these distributions do not produce geologically realistic results and/or do not model the anisotropy of hydraulic conductivity caused by bedding structures in sedimentary deposits. We have developed a flexible object-based package for simulating hydraulic properties in the subsurface—the Hydrogeological Virtual Realities (HyVR) simulation package. This implements a hierarchical modeling framework that takes into account geological rules about stratigraphic bounding surfaces and the geometry of specific sedimentary structures to generate realistic aquifer models, including full hydraulic-conductivity tensors. The HyVR simulation package can create outputs suitable for standard groundwater modeling tools (e.g., MODFLOW), is written in Python, an open-source programming language, and is openly available at an online repository. This paper presents an overview of the underlying modeling principles and computational methods, as well as an example simulation based on the Macrodispersion Experiment site in Columbus, Mississippi. Our simulation package can currently simulate porous media that mimic geological conceptual models in fluvial depositional environments, and that include fine-scale heterogeneity in distributed hydraulic parameter fields. The simulation results allow qualitative geological conceptual models to be converted into digital subsurface models that can be used in quantitative numerical flow-and-transport simulations, with the aim of improving our understanding of the influence of geological realism on groundwater flow and solute transport.

Introduction

Hydrogeologists typically need to characterize and represent the spatial distribution of hydraulic conductivity and porosity of recent (~last 2 million years) geological material deposited in continental settings. Geological conceptual models can provide a framework for understanding subsurface heterogeneity (Anderson 1989). Sedimentologists have also long recognized a hierarchy of bedding and structures within sedimentary deposits and have developed approaches to assist in the characterization of heterogeneous deposits that vary over large spatial and temporal scales (e.g., Miall 1991; Aigner et al. 1999).

¹Corresponding author: Center for Applied Geosciences, University of Tübingen, Tübingen, Germany; jeremypaul-bennett@gmail.com

²Center for Applied Geosciences, University of Tübingen, Tübingen, Germany.

³Department of Earth and Environmental Sciences, University of Waterloo, Waterloo, ON, Canada.

Article impact statement: Generate hydrogeological virtual realities and analyze three-dimensional conceptual models using a flexible open-source Python package.

Received February 2018, accepted May 2018.

© 2018, National Ground Water Association.

doi: 10.1111/gwat.12803

Continental sedimentary deposits (e.g., glacial and fluvial sequences), and their associated hydraulic parameter distributions, can thus be represented at various scales, starting with stratigraphic contacts—these represent erosional events of depositional hiatuses that may form important hydraulic boundaries separating contrasting hydrostratigraphic units. Larger hydrostratigraphic units can be further subdivided at various internal scales to better represent the spatial distribution of hydraulic properties that is controlled by smaller sedimentary depositional features. Variable sediment transport regimes can lead to the development of bedforms and sediment textures with varying orientation, which can cause these typically unconsolidated features to be hydraulically anisotropic. Previous studies have shown that variable anisotropy based on observed sediment bedding structures can affect groundwater flow (e.g., Borghi et al. 2015; Bennett et al. 2017) and solute transport and mixing (Bennett et al. 2017). It is therefore important to generate more realistic hydraulically anisotropic fields to further test hypotheses on the effects of heterogeneity and anisotropy in hierarchical sediments.

Numerous studies have applied hierarchical modeling frameworks to model aquifer materials (e.g., Scheibe

and Freyberg 1995; Weissmann and Fogg 1999; Barrash and Clemo 2002; Dai et al. 2004; Ritzi et al. 2004) using a variety of modeling approaches (Koltermann and Gorelick 1996). Object-based (or morphological) modeling approaches, which focus on the characteristic geometries of a sedimentary deposit, have been used in many hydrogeological studies (e.g., Jussel et al. 1994; Scheibe and Freyberg 1995; Miller et al. 2000). In such approaches, the various sedimentary deposits observed are approximated by geometric forms and placed into the model domain. Within a hierarchical modeling framework, larger units are composed of smaller units (e.g., hydrofacies assemblages make up architectural elements). Object-based methods have not been well-utilized in groundwater research in the last 20 years, possibly due to the lack of available simulation packages. This paper presents an object-based simulation methodology where the full hydraulic conductivity tensor can be constructed at every grid cell using isotropic hydraulic conductivity, bedding parameters (dip and azimuth), and anisotropy ratios that are defined at every location within the domain. The simulation package we present fills the gap of an open-source object-based code for simulating geologically plausible realizations of anisotropic hydraulic conductivity fields.

The present study introduces a new framework for generating ensembles of hydrogeological conceptual models (or “virtual realities”). The key goals in the framework development are:

- The simulation of virtual spatial distributions of hydraulic parameters (particularly spatial distributions of full hydraulic-conductivity tensors) that are informed by sedimentary erosional and depositional concepts
- The development of an aquifer simulation platform that can be customized and extended by users to suit their particular research needs.

We have developed a new tool for modeling subsurface heterogeneity at a scale that cannot be practically captured by aquifer-analog investigations and is relevant for groundwater studies at contaminated sites ($\sim 10^1$ to 10^3 m). The Hydrogeological Virtual Realities (HyVR) simulation package can currently model sedimentary structures derived from fluvial hierarchical framework models. The ensembles of virtual realities generated can be used to investigate the effect of specific sedimentary structures on groundwater flow and solute transport dynamics.

The main purpose of the simulation package is to give hydrogeologists the opportunity to test how different conceptual models of sedimentary deposits and their uncertainty affect groundwater flow and transport. The package does not include methods to calibrate the models on observations. For the latter, multiple fields generated by HyVR could be used as training images in multiple-point-geostatistics packages that do not apply geometrical rules but are better suited for conditioning.

In the following sections we introduce the modeling concepts and the computational methods implemented in HyVR; subsequently, the methods are applied in an example conceptual model based on the Macrodispersion Experiment (MADE) site in Columbus, Mississippi. Further details about computational methods and implementation of the HyVR simulation package can be found in the electronic repositories listed in the Supporting Information.

Modeling Concepts

The modeling approach used in the current study is underpinned by a hierarchical modeling framework that incorporates architectural element analysis, and by object-based modeling approaches. This section outlines these concepts as they apply to fluvial deposits, which constitute common and extensive aquifers.

Hierarchical Modeling Framework

We use a hierarchical modeling framework (e.g., Miall 1991; Aigner et al. 1999) to characterize sedimentary features in the current study. We consider five hierarchical scales that we define as stratigraphic contacts, architectural elements, hydrofacies assemblages, hydrofacies, and microstructure.

Stratigraphic contacts are the largest scale of features ($\sim 10^2$ to 10^4 m in lateral extent) that we consider here. In recent (\sim last 2 million years) fluvial deposits, stratigraphic contacts represent allocyclic changes to depositional settings that are controlled by tectonic or climatic changes (e.g., Milankovitch cycles, Fischer 1986). Examples of major strata bounded by stratigraphic contacts include deposits from glacial and fluvial systems.

Architectural elements (Miall 1985) are three-dimensional sedimentary features (e.g., channels) that are formed by autocyclic processes that occur within depositional systems (Beerbower 1964). They are often superimposed on allocyclic sequences by higher-frequency events that occur over periods of tens to thousands of years (Miall 2013). Different fluvial systems will have their own characteristic architectural elements, and these may range from 10^1 to 10^2 m in lateral extent (Miall 1985). Architectural elements are recognized by their outer bounding surfaces, which are often erosional, as well as by their internal facies assemblages (Allen 1983).

Facies assemblages are internal structures within architectural elements that have a predictable or coherent spatial arrangement and relationship; these have been extensively studied in both modern environments (e.g., Heinz et al. 2003) and ancient deposits (e.g., Allen 1983). For example, a tabular body formed of amalgamated gravel bars (a type of architectural element; see below) can consist of cyclical (i.e., interstratified) layers or assemblages of massive gravel, openwork gravel, and various crossbeds (e.g., Heinz et al. 2003). Each cycle would represent one assemblage. These assemblages often form hydrogeologically distinct zones, referred to as hydrofacies assemblages (e.g., Atkinson et al. 2014), that may have a lateral extent of $\sim 10^0$ to 10^2 m.

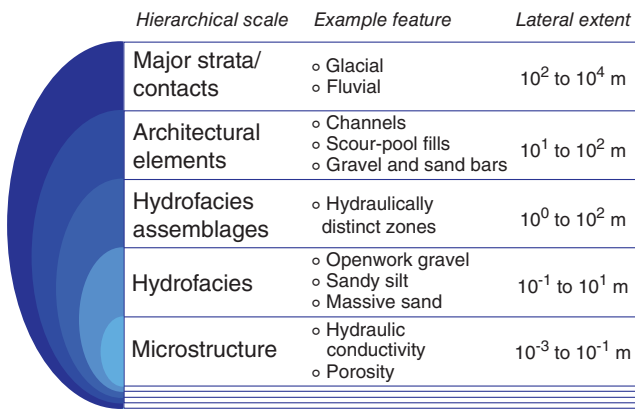


Figure 1. Hierarchical modeling framework diagram.

**Table 1
Selected Architectural Elements Generated Using
the HyVR Simulation Package**

Architectural Element	Object Geometry
Channels	Extruded parabolas
Scour-pool fills	Truncated ellipsoids
Gravel and sand bars	Sheets
Laminated sand	Sheets
Clay lenses	Truncated ellipsoids

Finally, these assemblages are made up of individual sediment facies such as openwork gravel and massive sand, which may correspond to hydrofacies—units of similar hydraulic properties (Anderson 1989). These may vary laterally on the order of 10^{-1} to 10^1 m. Within hydrofacies, the hydraulic conductivity and porosity may vary—which we denote microstructure, representing variations at scales ranging between $\sim 10^{-3}$ and $\sim 10^{-1}$ m. The hierarchical modeling framework is summarized in Figure 1.

The HyVR simulation package described in this study focuses on selected fluvial architectural elements and their associated hydrofacies assemblages. In its current state of development, the package can simulate geometries that can be used to represent several fluvial architectural elements, including (but not limited to): channels (CH), scour-pool fills (HO), gravel and sand bars (GB, SB), and laminated sand (LS) or laminated fines. Table 1 lists the architectural elements along with their typical geometries.

Object-Based Modeling Approaches

Object-based methods have been implemented widely in subsurface simulation (e.g., Jussel et al. 1994; Scheibe and Freyberg 1995; Deutsch and Tran 2002) as they can preserve the three-dimensional forms of geobodies, are generally computationally efficient, and can be parameterized using geometric constraints and probabilistic rules derived from geological observations (Koltermann and Gorelick 1996). Therefore, we use an object-based approach for simulating hydrofacies assemblages within

architectural elements. The HyVR simulation package can simulate three simplified geometries: extruded parabolas, truncated ellipsoids, and sheets (Figure 2); these can then be used to build a variety of architectural elements and hydrofacies assemblages (Table 1). The implementation of this approach in the HyVR algorithm is outlined in the following section.

Extruded Parabolas

Parabolas extruded along arbitrary curves with variable sinuosity are useful to represent channels, which are ubiquitous in fluvial systems. Channels are preserved in the sedimentological record following some disturbance to the flow regime (e.g., channel avulsion). While they often contain channel deposits, they can also be filled by various types of material including fines and organics due to channel abandonment (e.g., oxbow lakes). In some depositional systems (e.g., glaciofluvial systems) the flow and sediment transport may be too dynamic for continuous channels to be preserved in the stratigraphic record. However, in lower energy environments (e.g., meander systems), channels are often preserved and may represent important controls (both barriers and conduits) to groundwater flow.

Truncated Ellipsoids

Truncated ellipsoids are discrete features that have concave-up lower contact surfaces and generally flat top contact surfaces. They have been used in a number of studies (e.g., Jussel et al. 1994; Huber and Huggenberger 2015; Bennett et al. 2017) to represent trough features (i.e., scour-pool fills) present in braided river deposits. Siegenthaler and Huggenberger (1993) presented a conceptual model in which these features are formed at stable channel confluences where scour occurs. Changes in the discharge regime of surface-water flow may cause migration of the pool, and/or infilling of the scour pools. The former process can produce sets of cross-bedded troughs. Their persistence in sedimentary deposits is likely due to their low position within the stratigraphic record (Siegenthaler and Huggenberger 1993). Truncated ellipsoids can also be used to represent discrete lenses embedded in a matrix of different material.

Sheets

Tabular, laterally extensive depositional units can be approximated as sheets. Sheet-type features are found with many different grain sizes, including fine-grained overbank deposits, laminated lacustrine bed deposits, and poorly sorted gravel traction sheets. The three-dimensional forms of these features depend on the flow regimes in which they were deposited and are therefore highly heterogeneous. They are often difficult to characterize, and it may therefore be appropriate to approximate these forms as sheets with more complex internal structures, such as approximating certain architectural elements (e.g., gravel bars and bedforms) as sheet geometries with dipping internal structure. This approach is used in the present study.



Figure 2. Object geometries currently implemented in HyVR.

Generating Hydrogeological Virtual Realities

To achieve our modeling aims we have developed a new algorithm for the simulation of hydrogeological parameter fields, denoted the Hydrogeological Virtual Reality simulation package (HyVR). The most important aspects of the HyVR package are summarized in this section. HyVR has been written in Python 3 and is openly available online, facilitating user customization of the program.

During HyVR simulations, properties are assigned to regular model grids of three-dimensional, cuboid cells Ω . The workflow of simulations follows the sequence of hierarchical units, from largest to smallest (Figure 1). Simulations begin with the generation of major stratigraphic contact surfaces Z_{MS} , followed by simulating the initial contact surfaces of architectural elements Z_{AE} . Hydrofacies assemblages and associated hydrofacies are then simulated within each architectural element. Finally, the microstructure of the generated features is generated. Thus, each model grid cell is assigned a value for each hierarchical level. The computational methods used in the HyVR algorithm are briefly described in the rest of this section and summarized in Figure 3. For more detailed information about the computational methods implemented in HyVR, please refer to the online technical documentation (<https://driftingtides.github.io/hyvr/>).

Simulating Contact Surfaces of Major Strata and Architectural Elements

Major strata are defined by their upper mean elevations and the architectural elements that are to be included within them. In this way, they act as scaffolds for subsequent smaller-scale simulation of heterogeneity. The contact surfaces Z_{MS} generated using the mean elevations can either be “flat” or “random,” where the deviation from the mean plane is modeled using a multivariate standard normal dependence model. We used Gaussian covariance models in the present study to represent smoothly varying contact surfaces.

Architectural elements are initially defined using a lookup table that lists: the average bottom and top elevations of the unit, its name, and a stratum identifier. The lookup table can be specified by the user or randomly generated using input parameters defined for each stratum. The random generation of lookup tables begins with the random choice of an architectural element from those defined for an individual stratum; the probability of each architectural element being chosen is defined in the model parameter file. The thickness

of the architectural element is then drawn from an independent random normal distribution defined for each stratum. To account for the erosive nature of many contact surfaces, the algorithm may erode the underlying elements—here the “avulsion” thickness is subtracted from the bottom and top of the architectural element. Once the architectural element lookup table has been populated, architectural element contact surfaces Z_{AE} are generated using the same procedure as used for major strata contact surfaces. External hydrofacies assemblage geometries and hydrofacies are then simulated within the generated architectural element boundaries.

Simulating the Geometry of Hydrofacies Assemblages and Hydrofacies

The generation of hydrofacies assemblages and internal hydrofacies occurs stratum- and architectural-element-wise, beginning with the lowest architectural element in the lowest stratum. The simulation of hydrofacies assemblages is object-based, with random placement of geometric shapes within the architectural element. Currently, three shapes are supported: truncated ellipsoids, extruded parabolas, and sheets (Figure 2). Truncated ellipsoids and extruded parabolas are “erosive” features—they are able to erode underlying units, and therefore the architectural element (and strata) boundaries may be altered during the course of the simulation.

Hydrofacies assemblages are assigned to each architectural element starting from the lowest depth of the element. Simulation proceeds layer-wise, with the thickness of each layer determined by an aggradation input parameter $Z_{aggradation}$; the number of assemblages assigned in each layer is an input parameter. Assemblage outer boundaries are generated, and model grid nodes that fall within these boundaries are assigned corresponding values, including: the unique identifier of the individual hydrofacies assemblage generated and its geometry type; the hydrofacies code; and azimuth κ and dip ψ , properties denoting the angle of the bedding plane from the mean direction of flow and from the horizontal plane, respectively.

Truncated ellipsoids represent trough-like features. The method for generating the boundaries of these features uses geometries and “paleoflow” angles from the input parameters; this has been described previously by Bennett et al. (2017). The internal structure of truncated ellipsoids can be defined in the following ways: (1) trough-wise homogeneous, with constant azimuth and dip; (2) bulb-dip-type, with azimuth and dip values based on the three-dimensional gradient at the ellipsoid boundary;

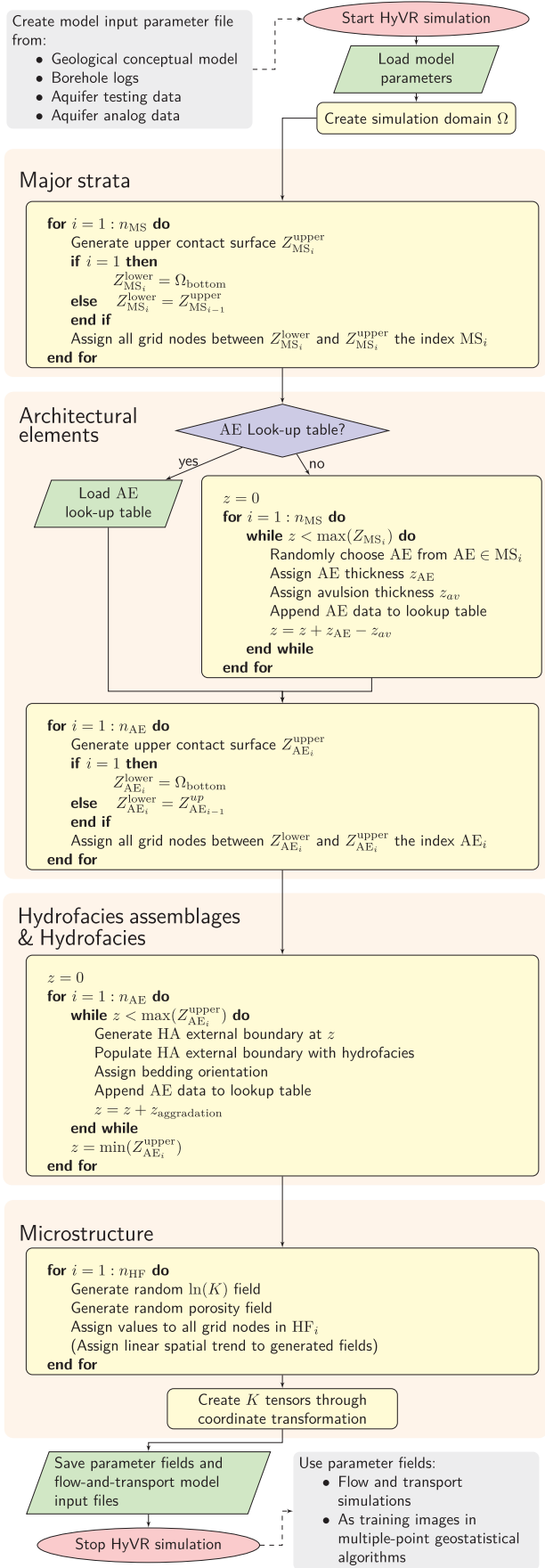


Figure 3. HyVR simulation algorithm.

(3) bulb sets, comprising nested alternating hydrofacies with azimuth and dip values generated as for bulb-dip-type; and (4) dip-set internal structure, where the features have a constant azimuth and dip but the assigned hydrofacies alternate throughout the truncated ellipsoid. Figure 4 shows the internal structures of truncated ellipsoid assemblages that can be generated. Alternating hydrofacies that comprise the internal structure have a set thickness.

Extruded parabolas are assigned along arbitrary curves (or centerlines). Extruded parabola centerlines in HyVR are parameterized using the disturbed periodic model implemented by Ferguson (1976); we use the second-order autoregressive model approximation described in equation (15) of that work (see also Pyrcz et al. 2009). Two-dimensional “channel” velocities \vec{v} are evaluated at the centerline and then interpolated to grid cells using an inverse-distance-weighted interpolation; azimuth values are derived from these velocities. Dip values of grid cells within the extruded parabola are assigned based on input parameters. To account for the multiple channels that are often concurrently present in many river systems, multiple extruded parabolas can be generated at each simulation depth. Note that in HyVR there is no interaction of extruded parabolas, and subsequent extruded parabolas will supersede—or “erode”—those previously generated. Once the predefined number of extruded parabola has been simulated, a three-dimensional migration vector may be added to the extruded parabola centerlines and the extruded parabola assignment to model grid cells begins again.

Sheets are comparatively simple to generate as they are laterally extensive within major strata boundaries. The internal structure of sheet features may be homogeneous (i.e., without internal structure), or laminations can be generated. Dipping set structures can also be incorporated into these features; these structures may vary in orientation.

Hydrofacies assemblages may be populated with dipping hydrofacies structures. To account for cyclicity of hydrofacies, it is possible to control the sequence of hydrofacies assignment within internal structures (e.g., by juxtaposing openwork gravels with sandy gravels). Lag surfaces can also be simulated at the bottom of erosive features and assigned a different hydrofacies value. The HyVR package also allows for linear trends in hydrofacies assemblage geometry sizes with increasing elevation or horizontal direction (x -direction only). Such trends may be set for each architectural element included in the model parameter input file.

Simulating the Microstructure of Hydraulic Parameters

Spatially distributed hydraulic parameters are simulated once all hydrofacies assemblages (and hydrofacies) have been generated. The hydraulic parameter outputs of HyVR are: the porosity $\theta(x, y, z)$ and an isotropic hydraulic conductivity $K_{iso}(x, y, z)$ value (later used as the within-bedding conductivity), the ratio of within-bedding to across-bedding hydraulic conductivity $K_{||}/K_{\perp}$, and the associated full hydraulic-conductivity tensor $\mathbf{K}(x, y, z)$ in each model grid cell.



Figure 4. Internal structure of truncated ellipsoid geometries.

The microstructure of hydraulic parameters is first generated for each individual hydrofacies assemblage simulated in the previous steps. Spatially varying $\ln(K_{iso})$ and θ fields are generated for each hydrofacies present in an assemblage using spectral methods to simulate random multi-Gaussian fields with exponential covariance functions (Dietrich and Newsam 1993). These methods are identical to those used simulating contact surfaces, but in three dimensions. An anisotropy ratio is also assigned to each model grid cell according to the hydrofacies present; these ratios are globally constant for each hydrofacies. Background heterogeneity is simulated for model grid cells that are not within assemblages using values defined for each architectural-element type. The associated simulation methods for these are the same as for the within-element microstructure. Once isotropic hydraulic-conductivity values have been assigned to all model grid cells, spatial trends may also be applied. As for trends in hydrofacies assemblage geometry, K_{iso} trends are assigned using a linearly interpolated factor in the x - and/or z -direction. The K_{iso} value of each model grid cell is then multiplied by these trend factors.

The full hydraulic-conductivity tensors \mathbf{K} for each model grid cell are then approximated by rotating the diagonal tensor of principal hydraulic-conductivity values to the orientation of the local bedding structure, represented by dip ψ and azimuth κ (see Bennett et al. 2017, or the technical documentation, for further details). Lateral hydraulic conductivity in the bedding plane is assumed to be isotropic (i.e., $K_{xx} = K_{yy}$) and vertical conductivity is calculated by dividing the lateral conductivity by the anisotropy ratio $K_{||}/K_{\perp}$. Once \mathbf{K} has been calculated, the simulated parameter files are saved and can be used for groundwater flow and solute transport simulations.

Model Inputs and Outputs

Model input parameters are contained in *.ini files which can be easily customized using a text editor. This format was chosen for its readability and the ability to be used with numerous programming languages.

It is an important goal of the development of the HyVR simulation package that outputs should be suitable for hydrogeological applications. Therefore, HyVR simulation outputs can currently be saved in a variety of formats including: native Python (pickle/Numpy), HDF5 and MATLAB data formats; VTK rectilinear grid files, to facilitate visualization in ParaView (Ayachit 2015); HydroGeoSphere input files (Aquanty 2012);

Table 2
Selected Strata Simulation Input Parameters

Major Strata	Mean Elevation of Contact Surfaces (mbgs)	Architectural Elements
Meander	0.0–3.0	Meander channel Silt sheet
Glaciofluvial	3.0–8.0	Cross-bedded scour Sandy gravel
Transition	8.0–9.5	Sand sheet Clay lens
Clay	9.5–11.0	Clay sheet

MODFLOW-2005 layer property flow input files (Harbaugh 2005); and, using the FloPy package (Bakker et al. 2016), MODFLOW 6 node property input files (Hughes et al., 2017), allowing for the use of the XT3D option (Provost et al., 2017). Due to the constraints of the MODFLOW-2005 model, simulation outputs in this format are restricted to the isotropic hydraulic-conductivity values and the anisotropy ratios $K_{||}/K_{\perp}$ at each model grid cell.

An Example Simulation

To demonstrate the HyVR simulation package, we provide an example parameter field simulation mimicking the MADE site at the Columbus Air Force Base, Mississippi. The MADE site has been the focus of numerous hydrogeological investigations (e.g., Boggs et al. 1990; Bowling et al. 2005; Bohling et al. 2016).

HyVR Input Parameters

Based on the geological conceptual model of Bowling et al. (2005, figure 13), we divided the stratigraphy of the MADE site into four major strata with approximate mean elevations below ground surface (Table 2): Meandering fluvial stratum (0 to 3 m below ground surface); braided fluvial stratum (3 to 8 mbgs); transitional sand stratum (8 to 9.5 mbgs); and marine sand stratum (9.5 to 11 mbgs). The meandering fluvial stratum consists of horizontally stratified floodplain clayey silts that are interspersed with channels filled with finer-grained silty clay and a coarse sandy gravel lag (Bowling et al. 2007). The braided fluvial stratum below comprises a sandy gravel matrix

(Boggs et al. 1990) that includes cross-bedded dipping units (Bowling et al. 2007) which we interpret as discrete scour-pool fill architectural elements (cf. Siegenthaler and Huggenberger 1993). The transition stratum is expressed as fine-grained sands with occasional silt and clay laminations (Boggs et al. 1990). The lowermost stratum included in this subsurface model is the Cretaceous Eutaw Formation that consists of marine clays that we assume to be poorly lithified.

Seven architectural elements were identified for the example simulation. Laterally continuous features were modeled as sheet-type architectural elements. These elements were assigned one lens thickness and hydrofacies. Discrete hydrofacies assemblages within clay lenses and scour architectural elements were modeled as truncated ellipsoids. For the clay lenses, the dimensions of the assemblages were estimated; for the cross-bedded scour-pool fills, dimensions were derived from similar features observed in gravel pits in northeastern Switzerland by Jussel et al. (1994). The meander channel was simulated using extruded parabolas, with parameters were derived from outcrop analogs described by Bowling et al. (2007, figure 8a). Selected architectural element input parameters are summarized in Table S1, Supporting Information.

Hydrofacies for the MADE site example simulation are sandy gravel, sandy clayey gravel, openwork gravel, sand, fine sand, clay, and silty clay. The first four hydrofacies in this list were categorized by Rehfeldt et al. (1992) in the braided fluvial system and we have used the hydraulic-conductivity values that are reported therein. Additional hydrofacies were necessary for the other strata present at the site, based on the characterization of Bowling et al. (2005). Hydraulic conductivity and other hydraulic parameter values for these hydrofacies were derived from a variety of sources (Mitchell 1956; Witt and Brauns 1983; Jussel et al. 1994). Selected simulation input parameters for hydrofacies have been included here (Table 3). More information about the hydrofacies parameters and their derivation (Table S2), as well as the parameter file with all simulation input parameters (Appendix S3) are included in Supporting Information.

Model Results

The results of a single HyVR realization of the MADE site example look similar to the geological conceptual model from which the input parameters were derived (Figure 5). The cross-bedded structures observed by Bowling et al. (2005) are visible and the isotropic hydraulic-conductivity, porosity, dip, and azimuth parameter fields vary based on their location within (and outside of) the simulated architectural elements. Comparison of univariate distributions of log-isotropic hydraulic conductivity derived from flowmeter and direct-push injection logger (DPIL) experimental data at the MADE site and a single HyVR realization (Figure 6) are similar. An obvious difference is a peak of high conductivity in the HyVR realization; this discrepancy may be due to the inability of the experimental methods to capture areas of high K (e.g., Bohling et al. 2016). The HyVR

Table 3
Selected Simulation Input Parameters for Hydrofacies

Hydrofacies	ID	K_h (m/s)	$\frac{K_h}{K_v}$	ϕ
Sandy gravel	0	1×10^{-5} ¹	1	0.20 ⁴
Sandy clayey gravel	1	1×10^{-7} ¹	0.25	0.17 ⁴
Openwork gravel	2	1×10^{-1} ¹	0.025	0.35 ⁴
Sand	3	1×10^{-4} ¹	1	0.43 ⁴
Fine sand	4	1×10^{-5} ²	2.3	0.43 ⁴
Clay	5	2×10^{-9} ³	2.3	0.52 ³
Silty clay	6	3×10^{-9} ³	1.7	0.45 ³

¹Jussel et al. (1994).

²Chapuis and Gill (1989) and Witt and Brauns (1983).

³Rehfeldt et al. (1992).

⁴Freeze and Cherry (1979, table 2.2).

⁵Derived from Mitchell (1956); see Supporting Information.

simulation package takes approximately 20 min to generate a parameter model with a model domain size of $\ell \times w \times d = 200 \text{ m} \times 70 \text{ m} \times 11 \text{ m}$ and a model grid resolution of $\Delta x \times \Delta y \times \Delta z = 0.5 \text{ m} \times 0.5 \text{ m} \times 0.1 \text{ m}$.

Discussion

The HyVR package has been developed with the goal of simulating clastic sedimentary deposits, with a focus on fluvial systems. Apart from the current suite of geometries possible in HyVR (extruded parabolas, truncated ellipsoids, and sheets) there are numerous other geometries that could be implemented (e.g., lobes, wedges, ribbons) to represent additional fluvial architectural elements (e.g., lateral accretion units, levees, crevasse splays). The key requirement for simulating these features is that their form can be parameterized and applied to the simulation model grids. There is also scope for deriving input parameters from geostatistical analysis of site observations. For example, Markov chains or transitional probabilities (Carle and Fogg 1996) based on borehole information could be used to constrain the probability of an architectural element being generated, or the mean geometry of simulated hydrofacies assemblages. The HyVR simulation package has been developed to be flexible, has extensive code commenting and documentation, and is openly available so that it can be extended according to the specific research needs of users.

The intent of HyVR is to generate sedimentary deposits that mimic a specific site with respect to the sedimentary features found there. Geological conceptual models can thus be converted from qualitative drawings to digital subsurface models that can be assessed quantitatively in numerical simulations of groundwater flow and solute transport, allowing the influence of sedimentary structures on these processes to be explored. Although the fields simulated with HyVR cannot honor direct measurements at given sites (e.g., borehole information), other site data (e.g., mean strata boundaries, mean assemblage geometries, hydrofacies present) and associated

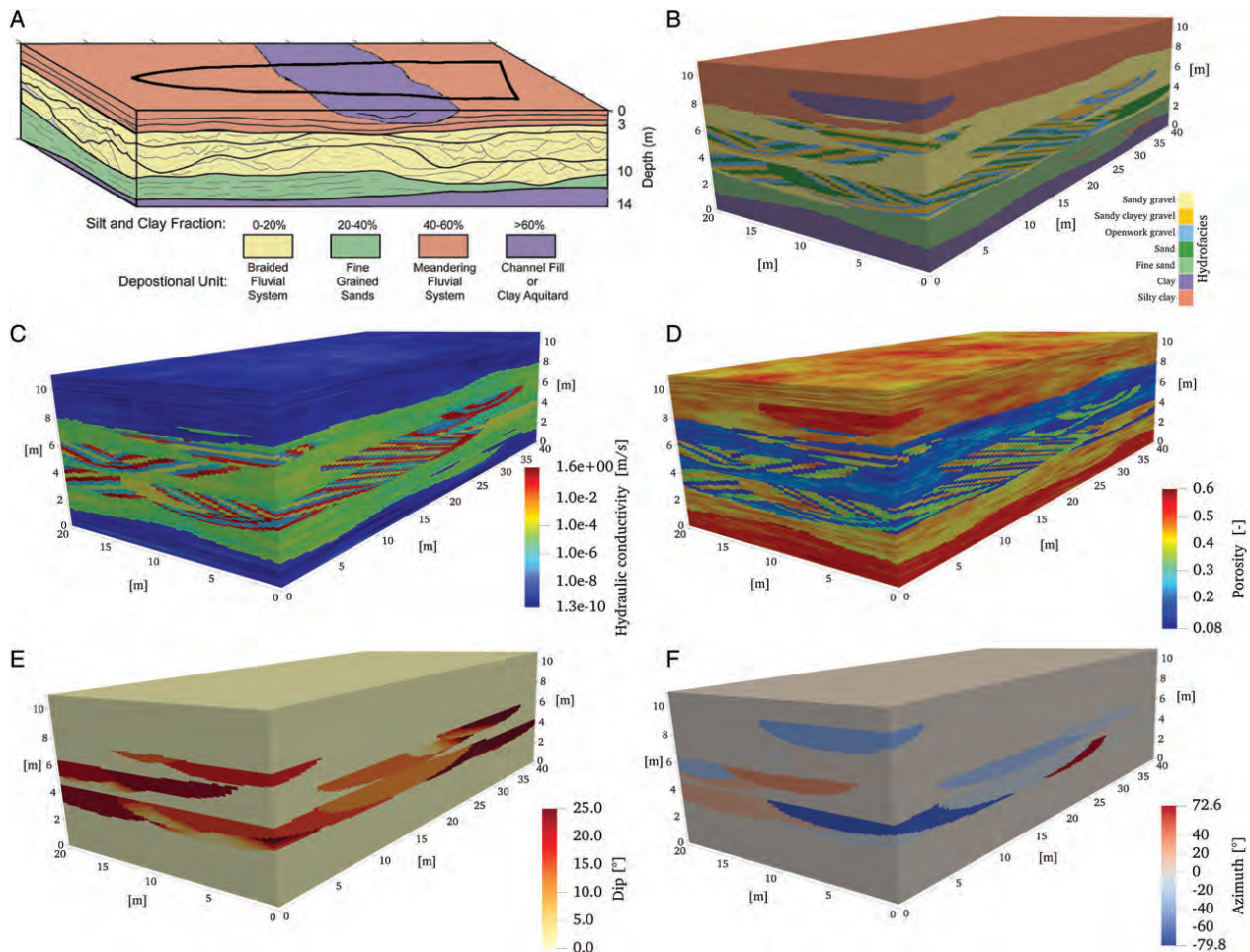


Figure 5. (A) Geological conceptual model of the MADE site amended from Bowling et al. (2005, figure 13, 901). (B) to (F) Distributed parameter fields from a single realization of the HyVR simulation using input parameters derived from characterization of the MADE site.

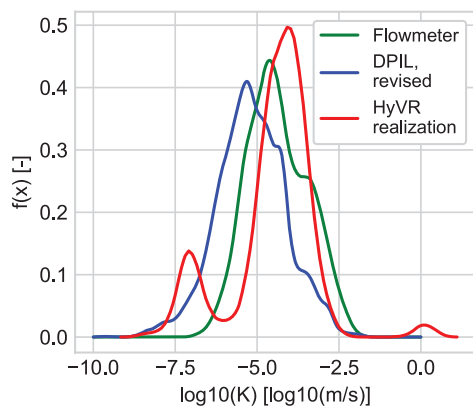


Figure 6. Univariate distributions of log-isotropic hydraulic conductivity from Bohling et al. (2016) and a single HyVR realization using the MADE site model parameters. Note that values above 2 m below ground surface and within the lowest clay stratum were omitted from the HyVR distribution as locations were not included in the field measurements.

statistics (e.g., mean and variance of hydraulic conductivity) can be incorporated to develop site-specific conceptual models in data formats that are suitable for groundwater flow and solute transport simulations. We do not expect

that such flow-and-transport simulations will match site measurements of hydraulic head and concentrations—the latter would require calibration and conditional simulations (see below). However, HyVR allows users to build ensembles of plausible conceptual models that can be used for hydrogeological scenario testing.

Process-based sedimentological models (e.g., Nicholas et al. 2013; MINES ParisTech/ARMINES 2017) provide increasingly detailed models of fluvial stratigraphy. The adaptation of these existing process-based models for hydrogeological studies provides an alternative way forward in the goal of simulating parameter fields that resemble observed deposits, albeit more computationally demanding. Currently, the lack of bedding structure outputs (i.e., dip and azimuth) from many process-based sediment deposition models is a barrier to their ability to simulate full hydraulic-conductivity tensors. One option would be to derive the necessary bedding structures from the simulated contact surfaces. Such a method could be used with a variety of existing models in order to simulate the full hydraulic-conductivity tensor.

The HyVR algorithm may also be a useful tool for the generation of three-dimensional training images for multiple-point geostatistics algorithms that allow for

conditioning to hydraulic-conductivity observations (e.g., Mariethoz et al. 2010). The creation of suitable three-dimensional training images is an ongoing challenge for implementing multiple-point geostatistics, and conditioning training images to measurements of dependent quantities, such as hydraulic heads or concentrations, is a much more complex task than conditioning on conductivity measurements (Linde et al. 2015).

Conclusion

In the present study we have introduced a new framework for simulating subsurface models that are informed by geological depositional concepts. The HyVR simulation package produces spatially distributed parameter models, including full hydraulic-conductivity tensors and porosity. The parameter fields generated are suitable for standard flow-and-transport simulation packages, such as the MODFLOW family of programs. HyVR is openly available so that it forms a codebase that can be used by hydrogeological researchers and practitioners to explore subsurface heterogeneity in clastic sedimentary systems and its influence on groundwater flow and solute transport.

Authors' Note

The authors do not have any conflicts of interest or financial disclosures to report.

Acknowledgments

This work was funded by the German Research Foundation (DFG) within the Research Training Group “Integrated Hydrosystem Modelling” (RTG 1829) at the University of Tübingen. We thank Michael Fienen, Jui-Pin Tsai, and one anonymous reviewer for suggestions to the manuscript and associated Python package.

Supporting Information

The most current versions of the simulation package and technical documentation are available at <https://github.com/driftingtides/HyVR> and <https://driftingtides.github.io/hyvr/> respectively. Additional supporting information may be found online in the Supporting Information section at the end of the article. Supporting Information is generally *not* peer reviewed.

Table S1. Selected architectural element parameters.

Table S2. Hydraulic properties of natural clays. Adapted from Mitchell (1956).

Appendix S1. Example model input parameter file for MADE site simulation.

References

- Aigner, T., J. Heinz, J. Hornung, and U. Asprion. 1999. A hierarchical process-approach to reservoir heterogeneity: Examples from outcrop analogues. *Bulletin Du Centre de Recherches Elf Exploration Production* 22, no. 1: 1–11.
- Allen, J.R.L. 1983. Studies in fluvial sedimentation: Bars, bar-complexes and sandstone sheets (low-sinuosity braided streams) in the brownstones (L. Devonian), Welsh borders. *Sedimentary Geology* 33, no. 4: 237–293. [https://doi.org/10.1016/0037-0738\(83\)90076-3](https://doi.org/10.1016/0037-0738(83)90076-3)
- Anderson, M.P. 1989. Hydrogeologic facies models to delineate large-scale spatial trends in glacial and glaciofluvial sediments. *Geological Society of America Bulletin* 101, no. 4: 501–511. [https://doi.org/10.1130/0016-7606\(1989\)101<0501:HFMTDL>2.3.CO;2](https://doi.org/10.1130/0016-7606(1989)101<0501:HFMTDL>2.3.CO;2)
- Aquanty. 2012. HydroGeoSphere [Software]. Waterloo, Ontario, Canada: Aquanty. Retrieved from <http://www.aquanty.com/hydrogeosphere/>
- Atkinson, L.A., M. Ross, and A.J. Stumpf. 2014. Three-dimensional hydrofacies assemblages in ice-contact/proximal sediments forming a heterogeneous “hybrid” hydrostratigraphic unit in central Illinois, USA. *Hydrogeology Journal* 22, no. 7: 1605–1624. <https://doi.org/10.1007/s10040-014-1156-7>
- Ayachit, U. 2015. *The ParaView Guide: Updated for ParaView Version 4.3 (full color version)*, ed. L. Avila. Los Alamos: Kitware.
- Bakker, M., V. Post, C.D. Langevin, J.D. Hughes, J.T. White, J.J. Starn, and M.N. Fienen. 2016. Scripting MODFLOW model development using Python and FloPy. *Groundwater* 54, no. 5: 733–739. <https://doi.org/10.1111/gwat.12413>
- Barrash, W., and T. Clemo. 2002. Hierarchical geostatistics and multifacies systems: Boise Hydrogeophysical Research Site, Boise, Idaho. *Water Resources Research* 38, no. 10: 1196. <https://doi.org/10.1029/2002WR001436>
- Beerbower, J.R. 1964. Cyclothem and cyclic depositional mechanisms in alluvial plain sedimentation. *Kansas Geological Survey Bulletin* 169, no. 1: 31–32.
- Bennett, J., C.P. Haslauer, and O.A. Cirpka. 2017. The impact of sedimentary anisotropy on solute mixing in stacked scour-pool structures. *Water Resources Research* 53, no. 4: 2813–2832. <https://doi.org/10.1002/2016WR019665>
- Boggs, J.M., S.C. Young, D.J. Benton, and Y.C. Chung. 1990. Hydrogeologic characterization of the MADE site. Interim Report No. EN-6915. Palo Alto, California: Electric Power Research Institute.
- Bohling, G.C., G. Liu, P. Dietrich, and J.J. Butler. 2016. Reassessing the MADE direct-push hydraulic conductivity data using a revised calibration procedure. *Water Resources Research* 52, no. 11: 8970–8985. <https://doi.org/10.1002/2016WR019008>
- Borghesi, A., P. Renard, and G. Courrioux. 2015. Generation of 3D spatially variable anisotropy for groundwater flow simulations. *Groundwater* 53, no. 6: 955–958. <https://doi.org/10.1111/gwat.12295>
- Bowling, J.C., D.L. Harry, A.B. Rodriguez, and C. Zheng. 2007. Integrated geophysical and geological investigation of a heterogeneous fluvial aquifer in Columbus, Mississippi. *Journal of Applied Geophysics* 62, no. 1: 58–73. <https://doi.org/10.1016/j.jappgeo.2006.08.003>
- Bowling, J.C., A.B. Rodriguez, D.L. Harry, and C. Zheng. 2005. Delineating alluvial aquifer heterogeneity using resistivity and GPR data. *Groundwater* 43, no. 6: 890–903. <https://doi.org/10.1111/j.1745-6584.2005.00103.x>
- Carle, S.F., and G.E. Fogg. 1996. Transition probability-based indicator geostatistics. *Mathematical Geology* 28, no. 4: 453–476. <https://doi.org/10.1007/BF02083656>
- Chapuis, R.P., and D.E. Gill. 1989. Hydraulic anisotropy of homogeneous soils and rocks: Influence of the densification process. *Bulletin of the International Association of Engineering Geology* 39, no. 1: 75–86. <https://doi.org/10.1007/BF02592538>
- Dai, Z., R.W. Ritzi, C. Huang, Y.N. Rubin, and D.F. Dominic. 2004. Transport in heterogeneous sediments with multimodal conductivity and hierarchical organization across scales. *Journal of Hydrology* 294, no. 1–3: 68–86. <https://doi.org/10.1016/j.jhydrol.2003.10.024>

- Deutsch, C.V., and T.T. Tran. 2002. FLUVSIM: A program for object-based stochastic modeling of fluvial depositional systems. *Computers & Geosciences* 28, no. 4: 525–535. [https://doi.org/10.1016/S0098-3004\(01\)00075-9](https://doi.org/10.1016/S0098-3004(01)00075-9)
- Dietrich, C.R., and G.N. Newsam. 1993. A fast and exact method for multidimensional Gaussian stochastic simulations. *Water Resources Research* 29, no. 8: 2861–2869. <https://doi.org/10.1029/93WR01070>
- Ferguson, R.I. 1976. Disturbed periodic model for river meanders. *Earth Surface Processes* 1, no. 4: 337–347. <https://doi.org/10.1002/esp.3290010403>
- Fischer, A.G. 1986. Climatic rhythms recorded in strata. *Annual Review of Earth and Planetary Sciences* 14, no. 1: 351–376. <https://doi.org/10.1146/annurev.ea.14.050186.002031>
- Freeze, R.A., and J. Cherry. 1979. *Groundwater*. Englewood Cliffs, New Jersey: Prentice-Hall.
- Harbaugh, A.W. 2005. MODFLOW-2005, the US Geological Survey modular ground-water model: The ground-water flow process. Reston, Virginia: U.S. Department of the Interior, U.S. Geological Survey.
- Heinz, J., S. Kleinedam, G. Teutsch, and T. Aigner. 2003. Heterogeneity patterns of quaternary glaciofluvial gravel bodies (SW-Germany): Application to hydrogeology. *Sedimentary Geology* 158, no. 1–2: 1–23. [https://doi.org/10.1016/S0037-0738\(02\)00239-7](https://doi.org/10.1016/S0037-0738(02)00239-7)
- Huber, E., and P. Huggenberger. 2015. Morphological perspective on the sedimentary characteristics of a coarse, braided reach: Tagliamento River (NE Italy). *Geomorphology* 248: 111–124. <https://doi.org/10.1016/j.geomorph.2015.07.015>
- Hughes, J.D., C.D. Langevin, and E.R. Banta. 2017. Documentation for the MODFLOW 6 framework (No. 2328–7055). Reston, Virginia: US Geological Survey.
- Jussel, P., F. Stauffer, and T. Dracos. 1994. Transport modeling in heterogeneous aquifers: 1. Statistical description and numerical generation of gravel deposits. *Water Resources Research* 30, no. 6: 1803–1817. <https://doi.org/10.1029/94WR00162>
- Koltermann, C.E., and S.M. Gorelick. 1996. Heterogeneity in sedimentary deposits: A review of structure-imitating, process-imitating, and descriptive approaches. *Water Resources Research* 32, no. 9: 2617–2658. <https://doi.org/10.1029/96WR00025>
- Linde, N., P. Renard, T. Mukerji, and J. Caers. 2015. Geological realism in hydrogeological and geophysical inverse modeling: A review. *Advances in Water Resources* 86, no. Part A: 86–101. <https://doi.org/10.1016/j.advwatres.2015.09.019>
- Mariethoz, G., P. Renard, and J. Straubhaar. 2010. The direct sampling method to perform multiple-point geostatistical simulations: Performing multiple-points simulations. *Water Resources Research* 46, no. 11: W11536. <https://doi.org/10.1029/2008WR007621>
- Miall, A. 2013. *Fluvial Depositional Systems*. New York: Springer.
- Miall, A.D. 1991. Hierarchies of architectural units in terrigenous clastic rocks and their relationship to sedimentation rate. In *The Three-Dimensional Facies Architecture of Terrigenous Clastic Sediments, and its Implications for Hydrocarbon Discovery and Recovery*, ed. A.D. Miall and N. Tyler. Tulsa, Oklahoma: Society for Sedimentary Geology.
- Miall, A.D. 1985. Architectural-element analysis: A new method of facies analysis applied to fluvial deposits. *Earth-Science Reviews* 22, no. 4: 261–308. [https://doi.org/10.1016/0012-8252\(85\)90001-7](https://doi.org/10.1016/0012-8252(85)90001-7)
- Miller, R.B., J.W. Castle, and T.J. Temples. 2000. Deterministic and stochastic modeling of aquifer stratigraphy, South Carolina. *Groundwater* 38, no. 2: 284–295. <https://doi.org/10.1111/j.1745-6584.2000.tb00339.x>
- MINES ParisTech/ARMINES. 2017. FLUMY: Process-based channelized reservoir models. Paris, France: MINES Paris-Tech/ARMINES. <http://cg.ensmp.fr/flumy>
- Mitchell, J.K. 1956. The fabric of natural clays and its relation to engineering properties. In *Proceedings of the 35th Highway Research Board Annual Meeting*, ed. F. Burggraf, 693–713. Washington, D.C.: Highway Research Board.
- Nicholas, A.P., P.J. Ashworth, G.H. Sambrook Smith, and S.D. Sandbach. 2013. Numerical simulation of bar and island morphodynamics in anabranching megarivers: Bar and island morphodynamics in megarivers. *Journal of Geophysical Research: Earth Surface* 118, no. 4: 2019–2044. <https://doi.org/10.1002/jgrf.20132>
- Provost, A.M., C.D. Langevin, and J.D. Hughes 2017. Documentation for the “XT3D” option in the node property flow (NPF) Package of MODFLOW 6. Techniques and Methods 6-A56, 50. Reston, Virginia: USGS. <https://doi.org/10.3133/tm6A56>
- Pyrzcz, M.J., J.B. Boisvert, and C.V. Deutsch. 2009. ALLU-VSIM: A program for event-based stochastic modeling of fluvial depositional systems. *Computers & Geosciences* 35, no. 8: 1671–1685. <https://doi.org/10.1016/j.cageo.2008.09.012>
- Rehfeldt, K.R., J.M. Boggs, and L.W. Gelhar. 1992. Field study of dispersion in a heterogeneous aquifer: 3. Geostatistical analysis of hydraulic conductivity. *Water Resources Research* 28, no. 12: 3309–3324. <https://doi.org/10.1029/92WR01758>
- Ritzi, R.W., Z. Dai, D.F. Dominic, and Y.N. Rubin. 2004. Spatial correlation of permeability in cross-stratified sediment with hierarchical architecture: Permeability correlation in cross-stratified sediment. *Water Resources Research* 40, no. 3: W03513. <https://doi.org/10.1029/2003WR002420>
- Scheibe, T.D., and D.L. Freyberg. 1995. Use of sedimentological information for geometric simulation of natural porous media structure. *Water Resources Research* 31, no. 12: 3259–3270.
- Siegenthaler, C., and P. Huggenberger. 1993. Pleistocene Rhine gravel: Deposits of a braided river system with dominant pool preservation. *Geological Society London Special Publications* 75, no. 1: 147–162. <https://doi.org/10.1144/GSL.SP.1993.075.01.09>
- Weissmann, G.S., and G.E. Fogg. 1999. Multi-scale alluvial fan heterogeneity modeled with transition probability geostatistics in a sequence stratigraphic framework. *Journal of Hydrology* 226, no. 1–2: 48–65. [https://doi.org/10.1016/S0022-1694\(99\)00160-2](https://doi.org/10.1016/S0022-1694(99)00160-2)
- Witt, K.-J., and J. Brauns. 1983. Permeability-anisotropy due to particle shape. *Journal of Geotechnical Engineering* 109, no. 9: 1181–1187. [https://doi.org/10.1061/\(ASCE\)0733-9410\(1983\)109:9\(1181\)](https://doi.org/10.1061/(ASCE)0733-9410(1983)109:9(1181))

Supporting Information for the following manuscript submitted to *Groundwater*:

An open, object-based framework for generating anisotropy in sedimentary subsurface models

Jeremy P. Bennett

Center for Applied Geosciences, University of Tübingen, Germany

Corresponding author (jeremy.bennett@uni-tuebingen.de, +49 176 8464 7072)

Claus P. Haslauer

Center for Applied Geosciences, University of Tübingen, Germany

Martin Ross

Department of Earth and Environmental Sciences, University of Waterloo, Ontario, Canada

Olaf A. Cirpka

Center for Applied Geosciences, University of Tübingen, Germany

Table S1. Selected architectural element parameters

Parameter	Clay sheet	Sand sheet	Clay lens	Cross-bedded scour	Sandy gravel	Silt sheet	Meander channel
Geometry	Sheet	Sheet	Truncated ellipsoid	Truncated ellipsoid	Sheet	Sheet	Extruded parabola
Aggradation height or lens thickness [m]	0.2	0.3	0.2	0.2	-	0.1	0.5
Hydrofacies	5	4	6	1, 2, 3	0	6	5, 0 (lag)
Internal structure	None	None	None	Random (dip-set, bulb set)	None	None	Lag surface
$w \times d$ [$\times \ell$] [m]	-	-	$8 \times 0.3 \times 10$	$10.4 \times 1.2 \times 22^a$	-	-	10×1.5
Frequency per layer [$1/m^2$]	-	-	1×10^{-3}	3×10^{-3}	-	-	-
Paleoflow [°]	-	-	[-90, 90]	[-45, 45] ^a	-	-	-
Dip [°]	-	-	-	[10, 25]	-	-	-
Azimuth [°]	-	-	-	[-45, 45]	-	-	-
Set thickness [m]	-	-	-	0.1 (bulb set) 0.7 (dip set)	-	-	-
Background hydrofacies	-	-	4	0	-	-	6

^a(Jussel, Stauffer, & Dracos, 1994)

For generating internal heterogeneity of hydrofacies, horizontal and vertical correlation lengths of $\lambda_h = 13$ m and $\lambda_v = 1.6$ m reported by Rehfeldt et al. (1992) were used for both hydraulic conductivity and porosity. Variance of log-normal distributions of hydraulic conductivity and normal distributions of porosity were set to 1 and 5×10^{-4} respectively for all hydrofacies.

Table S2: Hydraulic properties of natural clays. Adapted from Mitchell (1956).

Location	Depositional environment	Notes	K_h [m/s]	K_v [m/s]	$\frac{K_h}{K_v}$	ϕ
Boston blue	Marine		2.70×10^{-9}	1.57×10^{-9}	1.7	0.47
Boston blue	Marine		3.80×10^{-9}	1.05×10^{-9}	3.6	0.48
Fore river	Marine	Silty	1.65×10^{-9}	7.51×10^{-10}	2.2	0.51
Goose Bay	Marine	Silty	9.10×10^{-10}	2.68×10^{-10}	3.4	-
Chicago	Lacustrine		6.71×10^{-10}	4.80×10^{-10}	1.4	0.51
Beauharnois	Marine		2.71×10^{-9}	1.17×10^{-9}	2.3	0.63
St Lawrence	Marine		1.60×10^{-9}	1.07×10^{-9}	1.5	0.62
Dow Field	Marine (?)	Silty	5.79×10^{-9}	4.75×10^{-9}	1.2	-
Mexico City	Lacustrine		1.51×10^{-9}	2.51×10^{-9}	0.6	-
Cincinnati	Freshwater	Silty	2.28×10^{-9}	1.03×10^{-9}	2.2	0.39
Texas	Freshwater		1.21×10^{-9}	3.10×10^{-10}	3.9	-
Louisiana	Freshwater		4.35×10^{-10}	4.81×10^{-10}	0.9	0.51
Pump site	Freshwater		2.08×10^{-9}	6.91×10^{-9}	0.3	0.44
	Mean values	Silty	2.66×10^{-9}	1.70×10^{-9}	2.26	0.45
		Non-silty	2.00×10^{-9}	1.82×10^{-9}	1.68	0.52

A number of hydraulic parameters for fine-grained/cohesive hydrofacies was derived from Mitchell (1956) who performed laboratory tests on natural clays. Mean hydraulic parameter values were derived from this data by calculating the anisotropic ratio K_h/K_v for each sample and then averaging all samples that were silty or non-silty. Note that we only considered undisturbed sample results.

Appendix S3: Example model input parameter file for MADE site simulation. The most up-to-date working version of this parameter file can be accessed at

<https://github.com/driftingtides/hyvr/blob/master/testcases/made.ini> .

```
## Example HyVR model parameter input file
# HyVR 0.2 simulation package
# https://github.com/driftingtides/hyvr/
# Jeremy P. Bennett, University of Tuebingen, 2017-2018

[run]
# -----
# Run parameters
# -----

# Name of model simulation run
runname = made

# Number of realisations
numsim = 1

## Outputs
# Required outputs
# vtk: *.vtk
# py: python pickle
# mat *.mat
dataoutputs = [vtk,mat,py]
modeloutputs = [mf6]

# Full Filepath/directory for outputs
# Default is the directory of the parameter initialization file
# if modeldir == 'select'
#modeldir = select

# Overwrite parameter files
flag_ow = true

# Will anisotropy be assigned?
anisotropy = true
het = true

[model]
# -----
# Model parameters
# -----
# Grid cell dimensions [m]
dx = 0.5
dy = 0.5
dz = 0.1

# Model dimensions [m]
lx = 200
ly = 70
lz = 11

# Is domain periodic?
periodic = false

# Lowest hierarchical level of heterogeneity to assign
# -ae
# -facies
# -internal
hetlev = internal
```



```

[strata]
# -----
# Strata parameters
# -----
## List of sequences
ssm = [clay, transition, glaflu, meander]

## List of sequence top contact depths
ssm_top = [1.5, 3, 8, 11]

# [variance, correlation length x, corr. length. y]
ssm_contact_model = [[0.05,6,6],[0.05,6,6],[0.05,6,6],[0.05,6,6]]

## Architectural element lookup table
#ae_table = ae_lu_19-09-2017_10.39.18.txt

## Contact surfaces
# flat:          horizontal contacts <default>
# random:        random surfaces
#                - requires geostatistical model "l_contact_model"
# user:          Use-defined contact surfaces
#                - requires input path "contact_file"
ssm_contact = random

# List of architectural elements in model
ae = [clay_sheet, sand_sheet, clay_lens, crossbedded_scour, sandy_gravel, mc_sheet, meander_channel]

# Which architectural elements are included in each sequence
# - Must have same length as l_seq,
# - Architectural elements must be identical to section names (except [model],[hydraulics])
ssm_ae = [[clay_sheet],[sand_sheet,clay_lens],[crossbedded_scour, sandy_gravel],[mc_sheet,
meander_channel]]

# The probability of an architectural element occurring
ae_prob = [[1.0],[0.4,0.6],[0.7,0.3],[0.3, 0.7]]

# Mean thickness of architectural element
ae_z_mean = [[3.0],[0.3,0.3],[1.7, 0.5],[1.0, 2.0]]

## Erosion / deposition rules
# Avulsion probability
avul_prob = [[0],[0],[0.7],[0]]

# Avulsion depth range [m]
avul = [[0.0,0.0],[0.0,0.0],[0.2, 0.4],[0.0,0.0]]

# Background parameters for unassigned cells
# [fac, azim, dip]
bg = [0, 0, 0]

[crossbedded_scour]
# -----
# Scour pool element
# -----
geometry = trunc_ellip

# Internal structure
structure = random
agg = 0.2

# Contact type
contact = random
# [variance, correlation length x, corr. length. y]
contact_model = [0.01,6,6]

# Number of elements per simulation elevation
el_z = 1e-3

# Migration of troughs [mean & var migration in x, y]
migrate = [10, 0.5, 10, 0.5]

# Do not generate troughs close to bottom contact
# Value is proportion of trough depth

```

```

buffer = 0.8

# Mean trough geometry [m]
length = 22
width = 10.4
depth = 1.2

# Mean angles [deg]
paleoflow = [-45, 45]
dip = [10, 25]
azimuth = [-45, 45]

# Hydrofacies (refer to [hydraulics]l_hydro; 0-indexed)
facies = [1,2,3]

# Alternating facies
# List of what hydrofacies can follow those listed in l_facies
# To generate cyclical facies each list entry should have only one facies value
altfacies = [[1,2],[1,2],[3]]

# Thickness of lenses (or) spatial period (lambda) of inclined set [m]
bulbset_d = 0.1
dipset_d = 0.7

# Background parameters for unassigned cells
# [fac, azim, dip]
bg = [0, 0, 0]

# Geometry trend with elevation
# Trends are linear, moving from bottom to top of domain
# Percentage change of mean value with dx = 1m
geo_ztrend = [2, 0.5]

[meander_channel]
# -----
# Meander channel element
# -----
geometry = ext_par
agg = 1
width = 10
depth = 1.5

# Internal structure
structure = massive

# Contact type
contact = random
# [variance, correlation length x, corr. length. y]
contact_model = [0.001,12,6]

# Migration of channels [mean & var migration in x, y]
#migrate = [10, 0.5, 10, 0.5]

# Channel shape parameters
h = 0.4
# Wavenumber
k = 0.5
# Channel distance for calculations
ds = 1
eps_factor = 0.1

# Channels per iteration
channel_no = 1

# Dip range ([0,0] = massive bedding without any dip)
dip = [0, 0]

# Do not generate troughs close to bottom contact
# Value is proportion of trough depth
buffer = 0.4

# Hydrofacies (refer to [hydraulics]l_hydro; 0-indexed)
facies = [5]

```

```

# Lag surface at bottom of feature
# [lag depth, hydrofacies]
lag = [0.3, 0]

# Background parameters for unassigned cells
# [fac, azim, dip]
bg = [6, 0, 0]

[sandy_gravel]
# -----
# Sandy gravel sheet element
# -----
# Geometry
geometry = sheet
lens_thickness = -1
structure = massive

# Contact type
contact = random
# [variance, correlation length x, corr. length. y]
contact_model = [0.05,6,6]

# Hydrofacies (refer to [hydraulics]1_hydro)
facies = [0]

[sand_sheet]
# -----
# Sand sheet element
# -----
# Geometry
geometry = sheet
lens_thickness = 0.3
structure = massive

# Contact type
contact = flat

# [variance, correlation length x, corr. length. y]
contact_model = [0.01,6,6]

# Dip range ([0,0] = massive bedding without any dip)
dip = [0, 0]

# Spatial period (lambda) of inclined set [m]
setlamb = 0.3

# Hydrofacies (refer to [hydraulics]1_hydro)
facies = [4]

# Global hydraulics trend with elevation
# Trends are linear, moving from bottom to top of domain
k_ztrend = [0.5, 5]

[clay_sheet]
# -----
# Clay sheet element
# -----
# Geometry
geometry = sheet
lens_thickness = 0.2
structure = massive

# Contact type
contact = flat
# [variance, correlation length x, corr. length. y]
contact_model = [0.01,6,6]

# Dip range ([0,0] = massive bedding without any dip)
dip = [0, 0]

```

```

# Spatial period (lambda) of inclined set [m]
setlamb = 3

# Hydrofacies (refer to [hydraulics]l_hydro)
facies = [5]

# Global hydraulics trend with elevation
# Trends are linear, moving from bottom to top of domain
k_ztrend = [0.5, 2]

[mc_sheet]
# -----
# silt/clay sheet element
# -----
# Geometry
geometry = sheet
lens_thickness = 0.1
structure = massive

# Contact type
contact = flat
contact_model = [0.01,6,6]

# Spatial period (lambda) of inclined set [m]
setlamb = 3

# Dip range ([0,0] = massive bedding without any dip)
dip = [0, 0]

# Hydrofacies (refer to [hydraulics]l_hydro)
facies = [6]

[clay_lens]
# -----
# Clay/silt lens
# -----
geometry = trunc_ellip

# Internal structure
structure = flat
agg = 0.2

# Contact type
contact = flat
# [variance, correlation length x, corr. length. y]
contact_model = [0.01,6,6]

# Number of elements per simulation elevation
el_z = 1e-3

# Migration of troughs [mean & var migration in x, y]
#migrate = [20, 1, 10, 1]

# Do not generate troughs close to bottom contact
# Value is proportion of trough depth
# buffer = 0.2

# Mean trough geometry [m]
length = 10
width = 8
depth = 0.3

# Mean angles [degrees]
paleoflow = [-90, 90]
dip = [0, 0]
azimuth = [0, 0]

# Hydrofacies (refer to [hydraulics]l_hydro; 0-indexed)
facies = [6]

# Alternating facies

```

```

# List of what hydrofacies can follow those listed in l_facies
# To generate cyclical facies each list entry should have only one facies value
altfacies = [[6]]

# Thickness of lenses (or) spatial period (lambda) of inclined set [m]
setlamb = 0.2

# Background parameters for unassigned cells
# [mat, fac, azim, dip]
bg = [4, 0, 0]

# Geometry trend with elevation
# Trends are linear, moving from bottom to top of domain
# Percentage change of mean value with dx = 1m
geo_ztrend = [1, 1]

[hydraulics]
# -----
# Hydraulic parameters
# -----
# Simulation of hydraulic parameters?
gen = true

# List of hydrofacies codes
hydro = [sG, scG, oG, S, fS, C, mS]

# mean horizontal hydraulic conductivity [m/s]
k_h = [1e-5, 1e-7, 1e-1, 1e-4, 1e-5, 2e-9, 3e-9]

# variance of log hydraulic conductivity [-]
sig_y = [1, 1, 1, 1, 1, 1, 1]

# default correlation lengths for log(K) in each hydrofacies in x,y,z-directions
ycorlengths = [[13,13,1.6],[13,13,1.6],[13,13,1.6],[13,13,1.6],[13,13,1.6],[13,13,1.6],[13,13,1.6]]

# List of perpendicular anisotropy ratios (i.e K_h/K_v) [-]
k_ratio = [1, 0.25, 0.025, 1, 2.3, 2.3, 1.7]

# list of mean porosity values [-]
n = [0.2, 0.17, 0.35, 0.43, 0.43, 0.52, 0.45]

# variance of porosity values [-]
sig_n = [0.0005, 0.0005, 0.0005, 0.0005, 0.0005, 0.0005, 0.0005]

# default correlation lengths for n in each hydrofacies in x,y,z-directions
ncorlengths = [[3,3,0.3],[3,3,0.3],[3,3,0.3],[3,3,0.3],[3,3,0.3],[3,3,0.3],[3,3,0.3]]

# Global hydraulics trend with elevation
# Trends are linear, moving from bottom to top of domain
#k_ztrend = [1.5, 0.9]
#k_xtrend = [1.5, 0.9]

[flowtrans]
# -----
# Flow and transport modelling parameters
# -----
# Boundary conditions (head in/out [m])
hin = [1, 0, 0]
hout = [0, 0, 0]

```

References

- Jussel, P., Stauffer, F., & Dracos, T. (1994). Transport modeling in heterogeneous aquifers: 1. Statistical description and numerical generation of gravel deposits. *Water Resources Research*, 30(6), 1803–1817. <https://doi.org/10.1029/94WR00162>
- Mitchell, J. K. (1956). The fabric of natural clays and its relation to engineering properties. In F. Burggraf (Ed.), *Proceedings of the 35th Highway Research Board Annual Meeting*. Washington, D.C.: Highway Research Board.
- Rehfeldt, K. R., Boggs, J. M., & Gelhar, L. W. (1992). Field study of dispersion in a heterogeneous aquifer: 3. Geostatistical analysis of hydraulic conductivity. *Water Resources Research*, 28(12), 3309–3324. <https://doi.org/10.1029/92WR01758>

A Multi-Model Analysis of Solute Plume Behavior in a Synthetic Braided-River Deposit

Jeremy P. Bennett ¹, Philippe Renard ², Claus P. Haslauer ¹, and Olaf A. Cirpka ¹

¹Center for Applied Geosciences, University of Tübingen, Hölderlinstr. 12, 72074 Tübingen, Germany.

²Center for Hydrogeology and Geothermics, University of Neuchâtel, Rue Emile-Argand 11, 2000

Neuchâtel, Switzerland.

Key Points:

- A realistic synthetic braided-river deposited was simulated and acts as a base case.
- Object-based, multiple-point geostatistical, and multi-Gaussian ensembles simulated.
- Both data conditioning and inclusion of geological concepts are important for transport estimation.

Corresponding author: Olaf A. Cirpka, olaf.cirpka@uni-tuebingen.de

Abstract

14 **Abstract**
15 The spatial configuration of units with distinct hydraulic properties in the subsurface
16 is intrinsically linked to the sedimentary processes in which they were deposited. Although
17 these spatial configurations strongly influence groundwater flow and solute transport,
18 geological knowledge about their deposition is often neglected in groundwater modeling.
19 In order to test how the omission of geological knowledge affects predictions of solute trans-
20 port, we created a synthetic virtual reality that mimics braided-river deposits using an
21 object-based simulation method. We generated ensembles of parameter fields that im-
22 itate the synthetic virtual reality using object-based, multiple-point geostatistical, and
23 sequential Gaussian simulation methods. The model ensembles were conditioned to small-
24 and large-scale information from the synthetic virtual reality. We then performed for-
25 ward steady-state flow-and-transport simulations. In general, the multiple-point geosta-
26 tistical model ensembles were better able to reproduce the spatial characteristics of the
27 synthetic virtual reality, including juxtapositions of contrasting hydraulic conductivity,
28 bedding structures (which affect hydraulic anisotropy), and static connectivity metrics.
29 All model ensembles that included additional conditioning information could predict advective-
30 dispersive arrival times relatively well, despite large differences in connectivity. However,
31 the multiple-point geostatistical model ensemble provided the best estimates of the lo-
32 cation and spreading of a steady-state conservative solute plume. The results of this study
33 suggest that modeling approaches which integrate both geological conceptual informa-
34 tion and conditioning data provide more accurate characterization of the flow and trans-
35 port behavior in the synthetic virtual reality than approaches neglecting either geolog-
36 ical insight or conditioning data. This is relevant to hydrogeological researchers seeking
37 to apply stochastic concepts in practical applications.

1 Introduction

Predicting groundwater flow and transport is the most important task of applied hydrogeology. However, it is hampered by the inherent heterogeneity of subsurface hydraulic properties, which can often not be assessed in a practical manner. In order to deal with this uncertainty, stochastic subsurface hydrologists have implemented a range of methods for characterizing subsurface heterogeneity and propagating it to flow and transport. These methods are typically based on simplifying assumptions about the distribution of subsurface properties (e.g., multi-Gaussianity, ergodicity). Such assumptions can significantly affect flow and transport modelling efforts [e.g., *Gómez-Hernández and Wen, 1998; Kerrou et al., 2008; Haslauer et al., 2012*]. Alternative methods for simulating subsurface properties make use of geological concepts, but these methods are typically difficult to condition to observed data [*Linde et al., 2015*]. While it is clear that there is a trade-off between the match (or fidelity) of the simulations to observed data and the realism of geological concepts, it remains an open question in hydrogeological research as to how this affects solute transport behavior.

Comparisons of different modeling methods in water resources can be traced back to Chamberlain's method of multiple working hypotheses [*Chamberlain, 1890*]. *Wen and Kung [1993]* compared Gaussian and non-Gaussian simulation methods and found that the incorporation of soft data (hydraulic conductivity intervals) improved the characterization of solute transport behavior in two synthetic two-dimensional reference fields. *Teles et al. [2006]* found that genetic simulation methods could better represent solute transport processes in a range of alluvial aquifer settings than sequential Gaussian simulation methods. *Kerrou et al. [2008]* considered a two-dimensional transmissivity field conditioned to varying synthetic transmissivity and head measurements, and found that the inability of multi-Gaussian techniques to capture the connectivity of the field led to erroneous flow and transport predictions. *Zhang and Zhang [2015]* also found that explicitly accounting for the connectivity of features in hydrostratigraphic models could improve predictions of plume evolution. *Pirot et al. [2015]* compared flow and transport behavior in porous media mimicking the MADE site [e.g., *Zheng et al., 2011*] using three differing methods (multi-Gaussian, object-based, and pseudo-genetic) to generate these fields. They concluded that correctly identifying the initial plume conditions was most critical, and that multi-model approaches to flow-and-transport problems should be utilized – no single modeling method gave consistently good results. To the best of our knowl-

71 edge, none of the multi-model solute transport studies to date have made use of multiple-
72 point geostatistical methods which can account for connectivity and geological concepts,
73 whilst honoring conditioning data, such as borehole information.

74 In order to compare different modeling methods, we simulated a braided-river de-
75 posit that is analogous to features that have been extensively characterized in the Up-
76 per Rhine Valley of southern Germany and northern Switzerland [e.g., *Siegenthaler and*
77 *Huggenberger, 1993; Heinz and Aigner, 2003*]. Braided-river deposits are often highly
78 permeable and thus suitable for high levels of groundwater abstraction. Many braided-
79 river aquifers were formed during the last ice age and are therefore close the surface and
80 easy to exploit; however, they are also more susceptible to contamination from surficial
81 contaminant sources. The sediments in braided-river deposits typically include well-sorted,
82 competent clasts, which are often mined as gravel for construction activities. The lat-
83 ter increases the vulnerability of gravel aquifers. Active gravel mining has also been ex-
84 ploited by sedimentologists who have progressively mapped sedimentary features as ma-
85 terial has been removed [e.g., *Bayer et al., 2011*]. For hydrogeological purposes, sedimen-
86 tary features have also been addressed as hydrofacies in order to better understand the
87 nature of subsurface heterogeneity affecting flow and transport [e.g., *Anderson et al., 1999;*
88 *Klingbeil et al., 1999; Felletti et al., 2006*]. Braided-river deposits are highly variable with
89 respect to their hydraulic properties, and include sharp erosive contacts that cannot be
90 characterized using traditional two-point geostatistical techniques.

91 Methods for simulating subsurface heterogeneity that honor geological principles
92 may induce different flow and transport behavior than geostatistical methods based on
93 minimum information, such as simulators that use standard, second-order stationary two-
94 point geostatistics. While being more “realistic”, simulations based on geological con-
95 cepts and genetic or process-based simulation methods are typically difficult to condi-
96 tion to actual observations, and can also require more computational effort than stan-
97 dard geostatistical simulators. With this in mind, we want to investigate whether it pays
98 off to simulate geologically realistic ensembles, particularly in contaminant hydrogeol-
99 ogy, where groundwater and solute pathways are of paramount importance.

100 The present study is also in part motivated by the Water Resources Research 2016
101 Debates on “Stochastic subsurface hydrology from theory to practice”, where there was
102 general lament at the lack of stochastic methods being implemented in hydrogeological

103 practice. We aim to show how stochastic methods may be applied in a typical hydro-
 104 geological scenario - determining breakthrough curves in an extended observation plane
 105 and predicting the position, extent and dilution of a steady-state solute plume in a het-
 106 erogeneous porous medium. In keeping with the statements of *Cirpka and Valocchi* [2016],
 107 we have used a number of openly available tools for characterizing geological heterogene-
 108 ity as well as performing flow-and-transport simulations [e.g., MODFLOW 6, *Langevin et al.*,
 109 2017]. The importance of geological structures in stochastic methods [e.g., *Fogg and Zhang*,
 110 2016; *Sanchez-Vila and Fernàndez-Garcia*, 2016] has been accounted for by using object-
 111 based simulation methods [*Bennett et al.*, 2018], combined with multiple-point geosta-
 112 tistical methods [*Mariethoz et al.*, 2010] for conditioning of ensemble realizations to “bore-
 113 hole data” derived from a synthetic virtual reality.

114 In order to achieve our aims of the study, we establish a single synthetic virtual re-
 115 ality using an object-based simulation package [*Bennett et al.*, 2018]. We then attempt
 116 to mimic the hydraulic parameter fields using three methods: the same object-based sim-
 117 ulation package used for the generation of the virtual reality; the multiple-point geosta-
 118 tistical algorithm DeeSse [*Straubhaar*, 2017]; and the sequential Gaussian co-simulation
 119 algorithm GCOSIM3D [*Gómez-Hernández and Journel*, 1993]. Theory of groundwater flow
 120 and solute transport is explained in section 2. The simulation of the synthetic virtual
 121 reality and model ensembles is described in section 3. We discuss the results of param-
 122 eter field simulation and forward flow-and-transport modeling in section 5 and provide
 123 conclusions in section 6.

124 2 Theory of Groundwater Flow and Solute Transport

125 2.1 Flow in Porous Media

126 Darcy’s Law describes flow in porous media:

$$\mathbf{q} = -\mathbf{K}\nabla\phi \quad (1)$$

127 with the specific-discharge vector field $\mathbf{q}(\mathbf{x})$, the hydraulic-head field $\phi(\mathbf{x})$, the symmet-
 128 ric, positive-definite, second-order hydraulic-conductivity tensor field $\mathbf{K}(\mathbf{x})$, and the vec-
 129 tor of spatial coordinates \mathbf{x} in the x -, y -, and z - directions, respectively. The specific-

130 discharge field is divergence-free under steady state conditions without internal sources
 131 or sinks:

$$\nabla \cdot \mathbf{q} = 0 \quad (2)$$

132 which needs to be amended by suitable boundary conditions to define a well-posed prob-
 133 lem.

134 2.2 Solute Transport

135 The advection-dispersion equation (ADE) is the most common parameterization
 136 of solute transport in groundwater:

$$\frac{\partial c}{\partial t} + \mathbf{v} \cdot \nabla c - \nabla \cdot (\mathbf{D} \nabla c) = 0 \quad (3)$$

137 with the seepage velocity $\mathbf{v} = \mathbf{q}/\theta$ [$\text{L}^2 \text{T}^{-1}$], porosity θ [-], concentration of the solute
 138 c [M L^{-3}], and the local dispersion tensor \mathbf{D} [$\text{M}^2 \text{T}^{-1}$]. For a conservative solute with a
 139 constant inlet concentration, the first term of equation (3) may be omitted at sufficiently
 140 late time when there is no temporal change in the groundwater flow field. In the present
 141 study, we assumed the standard linear model of *Scheidegger* [1961] for the local trans-
 142 verse dispersion coefficient:

$$D_t = D_p + \alpha_t |\mathbf{v}(\mathbf{x})| \quad (4)$$

143 with the pore diffusion coefficient D_p [$\text{L}^2 \text{T}^{-1}$], and the transverse dispersivity α_t [L], which
 144 we assumed to be uniform. Because local longitudinal dispersion has only a minor ef-
 145 fect on solute transport in heterogeneous porous media [e.g., *Zarlenga and Fiori*, 2013],
 146 we set it to zero in this study. Furthermore, we orient the dispersion tensor \mathbf{D} in the x -
 147 direction, which is the direction of mean velocity, rather than the local velocity, result-
 148 ing in the dispersion tensor \mathbf{D} :

$$\mathbf{D}(\mathbf{x}) = \begin{bmatrix} 0 & 0 & 0 \\ 0 & D_t(\mathbf{v}(\mathbf{x})) & 0 \\ 0 & 0 & D_t(\mathbf{v}(\mathbf{x})) \end{bmatrix} \quad (5)$$

149 The time-dependent advection-dispersion equation can be formulated in the La-
 150 grangian framework of particle tracking with random walk:

$$\mathbf{x}_p(\tau + \Delta\tau) = \mathbf{x}_p(\tau) + \Delta\tau\mathbf{v}(\mathbf{x}_p) + \boldsymbol{\xi} \quad (6)$$

151 subject to

$$\mathbf{x}_p(0) = (0, y_{(p,0)}, z_{(p,0)}), \quad (7)$$

152 where \mathbf{x}_p is the vector of particle coordinates, τ is travel time, $\Delta\tau$ is a travel-time in-
 153 crement, and $[y_{(p,0)}, z_{(p,0)}]$ are the y, z coordinates of the particle at the inlet plane, here
 154 $x = 0$ m. $\boldsymbol{\xi}$ is a vector of random numbers with a multi-Gaussian distribution and zero
 155 mean, and covariance matrix $2\Delta\tau\mathbf{D}$. In our calculations, we perform the tracking from
 156 one observation plane to the next with spacing Δx , so that $2\Delta\tau D_t$ becomes $2\Delta\tau D_p +$
 157 $2\Delta x\alpha_t$, which makes the effect of transverse dispersion on the particle distribution more
 158 uniform, justifying that we neglect the drift term related to spatial variation in \mathbf{D} [*Kinzel-*
 159 *bach, 1988*].

160 **2.3 Characterizing Heterogeneous Porous Media and their Solute Trans-** 161 **port Behavior**

162 ***2.3.1 Connectivity Based on Minimum Hydraulic Resistance***

163 The concept of connectivity has been used to imply the existence (or lack thereof)
 164 of highly conductive pathways in a porous medium through which water and solutes may
 165 preferentially move [*Renard and Allard, 2013*]. Such preferential pathways are impor-
 166 tant for understanding groundwater flow and solute transport in heterogeneous aquifer
 167 systems [e.g., *Fogg, 1986; Zheng and Gorelick, 2003*]. It has been discussed that differ-
 168 ences in methods to simulate hydraulic-conductivity fields will lead to differences in con-
 169 nectivity [e.g., *Kerrou et al., 2008; Bianchi et al., 2011*]. Therefore, comparing the con-
 170 nectivity of the hydraulic-conductivity field ensembles originating from different simu-
 171 lation methods can offer insight into the different characteristics of these methods.

172 In the present study, we only consider static connectivity: that is, the spatial dis-
 173 tributions are considered without regard to a specific physical process (i.e., solute trans-

174 port) [Renard and Allard, 2013]. We analyzed the static connectivity of hydraulic con-
 175 ductivity fields between control planes located at the model inlet and outlet, respectively.
 176 To do this, we use the minimum hydraulic resistance, as defined by Rizzo and de Bar-
 177 ros [2017]. Here, the hydraulic resistance $[\mathcal{T}]$ is a line integral:

$$\mathcal{R}_\Gamma = \int_\Gamma \frac{1}{K} d\gamma. \quad (8)$$

178 where Γ belongs to the set of all possible curves that connect the planes at the model
 179 inlet and outlet. The minimum hydraulic resistance for each hydraulic conductivity field
 180 is therefore the lowest of these values. We used the method of Rizzo and de Barros [2017]
 181 that is based on the graph-theory approach of Dijkstra's algorithm [Dijkstra, 1959] to
 182 efficiently compute the minimum hydraulic resistance.

183 **2.3.2 Temporal Moments of Advective-Dispersive Travel Time Distri-** 184 **butions**

185 Temporal moments of advective-dispersive travel time distributions can be help-
 186 ful for characterizing transport in heterogeneous porous media. The zeroth raw moment
 187 $\mu_0(\mathbf{x})$, the mean breakthrough time $\bar{t}(\mathbf{x})$, and the central moment $\sigma_\tau^2(\mathbf{x})$ can be calcu-
 188 lated with the following equations:

$$\mu_0(\mathbf{x}) = \int_{t=0}^{\infty} c(\mathbf{x}, t) dt \quad (9)$$

$$\bar{t}(\mathbf{x}) = \int_{t=0}^{\infty} t c(\mathbf{x}, t) dt / \mu_0(\mathbf{x}) \quad (10)$$

$$\sigma_\tau^2(\mathbf{x}) = \int_{t=0}^{\infty} (t - \bar{t})^2 c(\mathbf{x}, t) dt / \mu_0(\mathbf{x}) \quad (11)$$

189 **2.3.3 Transverse Moments of Steady-State Concentration Distributions**

190 The exact distribution of solute plumes in groundwater can be difficult to quan-
 191 tify, and therefore the statistical moments of concentration distributions can be helpful
 192 to characterize solute transport in steady-state plumes with extended but finite initial
 193 size. In the present study, we consider the flux-weighted transverse moments of concen-
 194 tration distributions at cross sections throughout the model domain. We consider the

195 zeroth moment $m_0(x)$ as well as the normalized first $\mathbf{m}_1(x)$ and second central moments
 196 $\mathbf{M}_{2c}(x)$ in the transverse direction, as defined by:

$$m_0(x) = \int_0^{\ell_y} \int_0^{\ell_z} c(\mathbf{y}, x) q_x^{in}(\mathbf{y}) dydz \quad (12)$$

$$\mathbf{m}_1(x) = \int_0^{\ell_y} \int_0^{\ell_z} \mathbf{y} c(\mathbf{y}, x) q_x^{in}(\mathbf{y}) dydz / m_0(x) \quad (13)$$

$$\mathbf{M}_{2c}(x) = \int_0^{\ell_y} \int_0^{\ell_z} (\mathbf{y} - \bar{\mathbf{y}}) \otimes (\mathbf{y} - \bar{\mathbf{y}}) c(\mathbf{y}, x) q_x^{in}(\mathbf{y}) dydz / m_0(x) \quad (14)$$

197 in which $c(\mathbf{y}, x)$ the concentration of particles at cross section x with the transverse co-
 198 ordinates $\mathbf{y} = (y, z)$ and $q_x^{in}(\mathbf{y})$ is the corresponding initial specific discharge at the model
 199 inlet face. The zeroth moment is the total mass flux across the plane, the first normal-
 200 ized moment represents the center of mass of the plume, and the normalized second cen-
 201 tral moment describe the spreading of the solute plume about the center of mass.

202 **2.3.4 Plume Dilution**

203 While second-central moments are an adequate metric for the spread of the plume,
 204 they do not adequately describe the mixing of a plume with the surrounding solution.
 205 In steady-state transport, the latter may be quantified by the flux-related dilution in-
 206 dex E_Q [$L^3 T^{-1}$] of *Rolle et al.* [2009], which may be interpreted as the effective volume
 207 flux that is occupied by the mass flux of the solute:

$$E_Q(x) = \exp \left[- \int_{-\infty}^{+\infty} \int_{-\infty}^{+\infty} p_Q(x, y, z) \cdot \ln(p_Q(x, y, z)) \cdot q_x(x, y, z) dydz \right] \quad (15)$$

208 with the flux-weighted density of the solute mass $p_Q(x, y, z)$ [$T L^{-3}$] within the control
 209 plane at distance x :

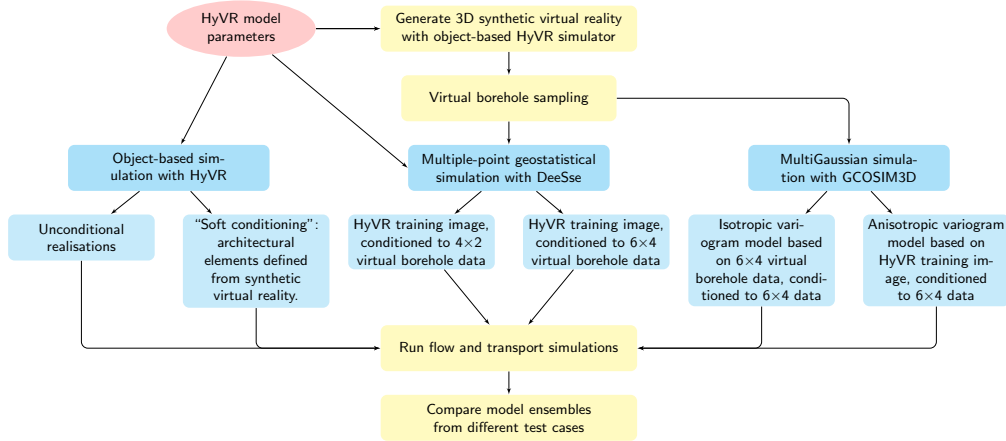
$$p_Q(x, y, z) = c(x, y, z) \left(\int_{-\infty}^{+\infty} \int_{-\infty}^{+\infty} c(x, y', z') q_x(x, y', z') dy' dz' \right)^{-1} \quad (16)$$

210 and the specific-discharge component q_x in the x -direction. A flux-weighted reactor ra-
 211 tio $M_Q(x)$ can be calculated by normalizing $E_Q(x)$ with the total discharge across the
 212 model inlet/outlet planes Q (i.e., the upper limit of the flux-weighted dilution index, [*Rolle*
 213 *et al.*, 2009]):

$$M_Q(x) = \frac{E_Q(x)}{Q}. \quad (17)$$

214 3 Simulation of a Synthetic Virtual Reality and Parameter Field En- 215 sembles

216 The workflow for simulating porous media in the present study proceeded with the
217 generation of a single “synthetic virtual reality” using an object-based simulation method.
218 The synthetic virtual reality acts as the base case for all subsequent simulations. We cre-
219 ated artificial borehole data sets by sampling the synthetic virtual reality. The borehole
220 data sets were used in the generation of ensembles of realizations on which we performed
221 forward flow-and-transport simulations. By comparing the results of the flow-and-transport
222 simulations between model ensembles we can better understand the effects of including
223 or omitting geological concepts and data on solute transport behavior. The methods to
224 generate the parameter fields are described in further detail in this section, and the work-
225 flow is summarized in Figure 1.



226 **Figure 1.** The workflow for generation of field ensembles implemented in the present study.

227 We used three methods of simulating subsurface heterogeneity: an object-based,
228 geology-mimicking simulation package; multiple-point geostatistical methods; and multi-
229 Gaussian simulation approaches. This allowed for the simulation of a suite of model en-
230 sembles. These methods, and those used for solving steady-state groundwater flow and
231 conservative solute transport are described in this section. A single synthetic virtual re-
232 ality was simulated and then the three different methods were each used to generate two

233 ensembles of twenty realizations. Table 1 provides a summary of the model ensembles
 234 generated.

235 **Table 1.** Summary of model ensembles generated.

Model ensemble	Simulation tool	Remarks
Synthetic virtual reality	HyVR ^a	-
Object-based, no conditioning	HyVR ^a	No conditioning
Object-based, soft conditioning	HyVR ^a	Soft conditioning to architectural element table from synthetic virtual reality
MPS, 4×2 data	DeeSse ^b	Object-based training image, conditioned to 4×2 borehole data
MPS, 6×4 data	DeeSse ^b	Object-based training image, conditioned to 6×4 borehole data
Multi-Gaussian, isotropic	GCOSIM3D ^c	Isotropic variogram derived from 6×4 borehole data only, conditioned to 6×4 borehole data
Multi-Gaussian, anisotropic	GCOSIM3D ^c	Anisotropic variogram derived from object-based training image, conditioned to 6×4 borehole data

^a Object-based modeling with the HyVR package [*Bennett et al.*, 2018]

^b Multiple-point geostatistical (MPS) simulation using DeeSse [*Straubhaar*, 2017]

^c Multi-Gaussian simulation using GCOSIM3D [*Gómez-Hernández and Journel*, 1993]

236 The Hydrogeological Virtual Realities (HyVR) simulation package [*Bennett et al.*,
 237 2018] uses object-based methods and a hierarchical modeling framework at different scales.
 238 The largest features considered in the present study are architectural elements: sedimentary
 239 features which range from 10^1 to 10^2 m in lateral extent [*Miall*, 1985]. In the HyVR
 240 package, architectural elements are defined by mean upper and lower elevations, which
 241 are either randomly generated, or can be stipulated by the user. By defining the mean

242 elevation of architectural elements, “soft conditioning” is possible, whereby particular
 243 architectural elements will be generated at certain elevations within the model domain.
 244 Hydrofacies assemblages are structures that occur within architectural elements and have
 245 a coherent spatial arrangement [Bennett *et al.*, 2018]. The HyVR package uses object-
 246 based methods for modeling hydrofacies assemblages (10^0 to 10^2 m in lateral extent).
 247 Hydrofacies assemblages are populated with hydrofacies, which in turn have an inter-
 248 nal microstructure. The HyVR package can also simulate hydraulic anisotropy: each hy-
 249 drofacies is assumed to have a constant anisotropy ratio between the within-bedding and
 250 across-bedding hydraulic conductivity $a = K_{\parallel} / K_{\perp}$. Dividing $K_{\parallel,i}$ by the hydrofacies-
 251 specific anisotropy ratio yields $K_{\perp,i}$.

252 3.1 Synthetic Virtual Reality

253 The synthetic virtual reality mimics Pleistocene braided-river deposits in the Up-
 254 per Rhine valley as described by *Siegenthaler and Huggenberger* [1993]. The main sed-
 255 imentary features (or facies types) observed were: Troughs and trough-fill deposits; hor-
 256izontally bedded gravels; and massive and coarse-grained “brown gravel” beds [*Siegen-
 257 thaler and Huggenberger*, 1993]. For the purposes of simulation using the HyVR algo-
 258 rithm, we have translated these features into two architectural elements: scour-pool fills
 259 within a horizontally bedded background, and brown gravel sheets.

260 The scour-pool fill architectural element consists of truncated ellipsoids within a
 261 background of undifferentiated, horizontally bedded gravels (HG). Scour-pool fills are
 262 often filled with alternating layers of openwork (OW) and bimodal (BM) gravels with
 263 thicknesses of between 0.1 and 0.5 m [*Siegenthaler and Huggenberger*, 1993]. These may
 264 be arranged in bulb-type configurations of nested truncated ellipsoids. As we could not
 265 explicitly resolve such an internal arrangement of hydrofacies in the present study, we
 266 assigned an aggregated OW/BM hydrofacies with locally anisotropic hydraulic conduc-
 267 tivity. We assigned a K_{\parallel} value of 0.01 m s^{-1} [*Jussel et al.*, 1994] and an anisotropic ra-
 268 tio K_{\parallel}/K_{\perp} of 10 [-] to the OW/BM hydrofacies, in which K_{\parallel} and K_{\perp} refer to the hydraulic-
 269 conductivity values within the bedding planes and perpendicular to them, respectively.
 270 The horizontal gravels were assigned a K_{\parallel} value of $1 \times 10^{-4} \text{ m s}^{-1}$ [*Jussel et al.*, 1994] and
 271 an anisotropic ratio of 6 [-], in which the orientation of the bedding is horizontal [*Hu-
 272 ber and Huggenberger*, 2016]. The bulb-type bedding structures are approximated by as-

273 signing azimuth as the angle of paleoflow, and dip as the gradient at the surface of the
 274 truncated ellipsoid geometry (see *Bennett et al.* [2018] for further details).

275 The sheet architectural element mimics brown gravel (BG) features and are mod-
 276 eled as sheet geometries. Brown gravel beds generally do not exhibit strong internal con-
 277 figurations [*Siegenthaler and Huggenberger*, 1993] and therefore no bedding structure is
 278 assigned to this architectural element. The brown gravel architectural elements were as-
 279 signed a K_{\parallel} value of 1×10^{-5} m s⁻¹ [*Jussel et al.*, 1994] and an anisotropy ratio of unity
 280 [-].

281 Microstructure of hydraulic conductivity and porosity within all assigned hydro-
 282 facies is simulated using multi-Gaussian fields generated applying spectral methods [*Di-*
 283 *etrich and Newsam*, 1993]. The mean for each hydrofacies is derived from *Jussel et al.*
 284 [1994, Tab.4]; the geostatistical structure is also derived from that work, with horizon-
 285 tal and vertical correlation lengths set to $\lambda_{hor} = 3$ m and $\lambda_{vert} = 0.3$ m, respectively.
 286 The internal variance of the assigned hydraulic conductivity values $\sigma_{\ln K}^2$ and porosity
 287 values σ_{θ}^2 was set to 1 and 1×10^{-4} for all hydrofacies, respectively; this is consistent with
 288 *Jussel et al.* [1994]. The model domain dimensions were set to $X \times Y \times Z = 200 \times 70$
 289 $\times 10$ m, with grid cell dimensions of $\Delta x \times \Delta y \times \Delta z = 1 \times 1 \times 0.1$ m.

290 **Table 2.** Parameters for the object-based simulation of fluvial aquifers.

Parameter	BG	OW/BM	HG
Within-bedding hydraulic conductivity, K_{\parallel} [m s ⁻¹] ^a	1×10^{-5}	1×10^{-2}	1×10^{-4}
Anisotropy ratio, K_{\parallel}/K_{\perp} [-]	1	10 ^b	6 ^c
Variance of hydraulic conductivity $\sigma_{\ln K_{\parallel}}^2$	1	1	1
Porosity, θ [-] ^a	0.1	0.3	0.2
Variance of porosity σ_{θ}^2	1×10^{-4}	1×10^{-4}	1×10^{-4}
Paleoflow direction range α [°]	-	$[-25, +25]^b$	-
Dip range, ψ [°]	-	$[0, +25]^c$	-

^a*Jussel et al.* [1994].

^b*Bennett et al.* [2017].

^c*Huber and Huggenberger* [2016].

291 **3.1.1 Generation of Conditioning Data from the Synthetic Virtual Re-** 292 **ality**

293 Random-field generators based on multiple-point geostatistics or two-point multi-
294 Gaussian geostatistics can be conditioned to data. Therefore we have generated two sets
295 of “virtual borehole data” from the synthetic virtual reality to assess how additional data
296 impacts the model ensembles. Borehole locations were placed on a regular grid with vary-
297 ing numbers of boreholes in the x - and y -directions. In the x -direction, the boreholes were
298 located at the model inlet and outlet, and at regularly spaced intervals between. In the
299 y -direction, the boreholes were offset from the model boundary by one borehole grid spac-
300 ing. The borehole frequencies for the two data sets were 4×2 and 6×4 , which produced
301 an internal grid spacing of $67 \text{ m} \times 23 \text{ m}$ and $40 \text{ m} \times 14 \text{ m}$ in the horizontal directions, re-
302 spectively. The borehole data sets have the same vertical resolution as the synthetic vir-
303 tual reality. The borehole data were assumed to be error-free.

304 As mentioned previously, the HyVR simulation package can randomly assign the
305 mean elevation of architectural elements during field generation. The resulting output
306 table of mean elevations can then be used as a parameter input for further HyVR sim-
307 ulations, which we refer to as “soft conditioning”. The architectural-element output ta-
308 ble from the simulation of the synthetic virtual reality was retained and used for the soft
309 conditioning of object-based simulations, as described in the next section. The reason-
310 ing behind the chosen soft conditioning is that in practical applications geophysical sur-
311 veys, such as ground-penetrating radar and seismics, may yield structural information
312 on architectural elements but not hydraulic parameters.

313 **3.2 Unconditional Fields using Object-Based Simulation**

314 Object-based simulation methods can replicate characteristics of parameter fields
315 that are commonly observed in nature, such as sharp contact surfaces between features
316 with contrasting hydraulic properties, and the external geometrical boundaries of these
317 features. However, it is typically difficult to condition object-based simulations to data.
318 We are therefore interested in how the variability in the unconditional outputs of object-
319 based simulation methods can affect predictions of mean breakthrough time and plume
320 extent, particularly when compared to the results of a single synthetic virtual reality.

321 Two ensembles of realizations were generated using the object-based HyVR sim-
322 ulation package. Model ensembles are generated using the same HyVR model param-
323 eters as for the synthetic virtual reality, with some small differences. The first model en-
324 semble uses exactly the same input parameters as those used for the generation of the
325 synthetic virtual reality. The second model ensemble also uses HyVR input parameters
326 identical to the synthetic virtual reality, but in addition it has the same configuration
327 of architectural elements (type and mean contact elevation) as the synthetic virtual re-
328 ality. This soft conditioning was achieved by using the architectural-element output ta-
329 ble generated during the synthetic virtual reality simulation. The same distributed pa-
330 rameters were generated for the object-based model ensembles as for the synthetic vir-
331 tual reality.

332 3.3 Conditional Fields using Multiple-Point Geostatistics

333 We used multiple-point geostatistical methods (MPS) conditioned to the virtual
334 borehole data to create two conditional ensembles of parameter fields. The DeeSse al-
335 gorithm [*Straubhaar*, 2017] was used, which implements the direct sampling method of
336 *Mariethoz et al.* [2010]. MPS simulation methods generally require a training image from
337 which geostatistical information can be derived. In the present study, the training im-
338 age was generated with the HyVR simulation package using input parameters identical
339 to those used in the unconditional object-based model ensemble. We directly simulated
340 multivariate fields for the following parameters: hydrofacies, log-hydraulic conductivity,
341 porosity, dip, and azimuth. Hydraulic anisotropy could then be assigned as these val-
342 ues were constant per hydrofacies.

343 Two model ensembles were generated using MPS and conditioned to the two bore-
344 hole data sets (4×2 and 6×4), respectively. In order to make the DeeSse simulations more
345 efficient, the training image generated was smaller than the model simulations, with di-
346 mensions of $\ell_x \times \ell_y \times \ell_z$ of $70 \text{ m} \times 40 \text{ m} \times 10 \text{ m}$. All other HyVR simulation param-
347 eters, including the model grid cell sizes, remained unchanged. The following input pa-
348 rameters were used in the DeeSse simulation: the maximal number of neighboring nodes
349 for all variables was set to 24, the distance thresholds (i.e., fraction of mismatching nodes)
350 were set to 0.03 for all variables, the maximal scan fraction of the training image was
351 0.25, and two levels of Gaussian pyramids were used [*Straubhaar*, 2017, p.32]. All DeeSse
352 input parameters are given in Input File S2 of the Supporting Information.

3.4 Conditional Multi-Gaussian Fields

Multi-Gaussian simulation methods are often used in hydrogeological modeling as they are generally computationally efficient and can be easily conditioned to data. In the present study we generated two model ensembles using the sequential Gaussian co-simulation methods implemented in GCOSIM3D [Gómez-Hernández and Journel, 1993] and conditioned to the virtual borehole data. Log-hydraulic conductivity and porosity parameter fields were simulated for these two model ensembles. We converted K_{\parallel} values from the virtual borehole data sets into isotropic hydraulic conductivity K_{iso} values by taking the geometric mean at each model cell $i(x, y, z)$:

$$K_{iso,i} = \frac{K_{\parallel,i}}{\sqrt{a}} \quad (18)$$

where a is the anisotropy ratio K_{\parallel}/K_{\perp} for that particular hydrofacies.

The first conditional multi-Gaussian ensemble is based on an isotropic geostatistical model fitted to the 6×4 virtual borehole data. We applied normal-score transformation to the empirical distribution of log-hydraulic conductivity of the virtual borehole data. During the geostatistical characterization process we had difficulties fitting three-dimensional anisotropic variograms due to large horizontal distances between the boreholes. In the depositional setting of the synthetic virtual reality, we expected that correlation lengths are longer in the horizontal directions than in the vertical. However, even with relatively high numbers of boreholes (from a practitioner’s perspective), it was not possible to compute the horizontal correlations of the hydraulic parameters as standard fitting resulted in a pure-nugget model indicating that the correlation length was smaller than the borehole spacing. We thus used the well constrained vertical correlation length also in the horizontal direction, resulting in isotropic conductivity fields. Once the ensemble was complete, the simulated normal-score transformed conductivity values were back-transformed to meet the original marginal distribution of the virtual borehole data set.

The second conditional multi-Gaussian model ensemble uses an anisotropic geostatistical model that is derived from the same object-based training image utilized in the multiple-point geostatistical model ensembles. By using a training image to improve the geostatistical characterization, we could reduce the issues related the large horizon-

382 tal distances between virtual boreholes encountered in the previously described model
 383 ensemble. This model ensemble is also conditioned to the 6×4 virtual borehole data. Again,
 384 prior to variogram fitting, log-hydraulic conductivity values from the training image un-
 385 derwent normal-score transformation. The virtual borehole conditioning data was also
 386 transformed using the empirical distribution from the training image. Following com-
 387 pletion of the simulations, the generated fields were back-transformed to meet the marginal
 388 distribution of the training image.

389 Exponential variogram models were manually fitted using the AR2GEMS software
 390 [*AR2Tech*, 2017] and are shown in Table 3. Figures showing the empirical variograms
 391 and variogram models are included in Figures S1 and S2 of the Supporting Information.

392 **Table 3.** Fitted parameters for exponential variogram models derived from borehole data
 393 (isotropic model ensemble) and from an object-based training image (anisotropic model ensem-
 394 ble), respectively.

Parameter	Isotropic			Anisotropic		
	lnK	Porosity	lnK vs. Porosity	lnK	Porosity	lnK vs. Porosity
Sill	1	0.8	0.55	1	0.85	0.55
Range, isotropic [m]	1.6	1.1	2.2	-	-	-
Range, x, y, z [m]	-	-	-	29, 24, 1.5	33, 27, 1.4	45, 33, 1.5

395 4 Numerical Methods for Simulating Flow and Transport

396 4.1 Numerical Methods

397 Steady-state groundwater flow was solved for all generated parameter fields using
 398 MODFLOW 6 [*Langevin et al.*, 2017]. A fixed mean flux \bar{q}_x of 1×10^{-5} m s⁻¹ was applied
 399 at the model inlet and outlet faces. Volumetric discharges Q_i for each inlet and outlet
 400 grid cell i were weighted by the hydraulic conductivity of the model cell K_i in order to
 401 prevent negative inlet discharges or unrealistically high hydraulic gradients in low- K re-
 402 gions of the in- and outlet faces:

$$Q_i = \bar{q}_x \cdot \ell_y \cdot \ell_z \cdot \frac{K_i}{\sum_{i=1}^n K_i} \quad \forall \quad i(x = 0, nx) \quad (19)$$

403 with ℓ_y and ℓ_z the dimensions of the model domain in the y - and z -direction, respectively.
 404 To ensure convergence of the numerical flow solver, a single fixed-head cell of 1 m was
 405 assigned to one grid cell. All other model boundaries were set to no-flow conditions. The
 406 XT3D option [Provost *et al.*, 2017] of MODFLOW 6 was used for handling full hydraulic
 407 conductivity tensors; modeling was facilitated with the FloPy package [Bakker *et al.*, 2016].
 408 The flow simulation models had the same grid discretization as the parameter simula-
 409 tions.

410 We solved advective conservative solute transport was solved using the semi-analytical
 411 particle tracking method of Pollock [1988]. 70,000 particles were initialized on the in-
 412 let face ($x = 0$ m) of each realization, with a grid spacing of 0.1 m in the y, z -directions.
 413 Particle tracking was implemented in MATLAB and performed on the graphical process-
 414 ing unit.

415 We solved steady state conservative advective-dispersive transport using the method
 416 described by Cirpka *et al.* [2015]. The method solves advection along streamlines, and
 417 transverse dispersion is solved using cell-centered Finite Volumes based on Voronoi poly-
 418 gons in the (y, z) -plane. (For details, please refer to Cirpka *et al.* [2015, section 3]). In
 419 the present study, the scheme was amended to allow for variable porosity. We defined
 420 a rectangular source zone at the center of the inlet plane ($x = 0$ m, $y \in [28$ m, 42 m],
 421 $z \in [4$ m, 6 m]); the dimensions of the source zone were $W \times H = 14$ m \times 2 m. The
 422 inflow concentration for streamlines initialized in the source zone was set to one [-], and
 423 to zero [-] for all other streamlines. Table 4 summarizes selected flow and transport model
 424 parameters.

426 5 Results and Discussion

427 5.1 Parameter Field Simulations

428 5.1.1 Parameter Fields

429 Figure 2 depicts log-hydraulic conductivity and hydrofacies for a single realization
 430 each from selected model ensembles (additional parameter fields are depicted in Figure
 431 S3 of the Supporting Information). The synthetic virtual reality (Figure 2, top row) is
 432 dominated by horizontal gravels with inclusions of scour-pool fills. Some laterally exten-
 433 sive but relatively thin brown gravel sheets are present. Bedding structures are only present
 434 in the scour-pool fills, as can be seen in the azimuth and dip parameter fields of the syn-

425

Table 4. Flow and transport model parameters

Parameter	Value
Model domain dimensions $X \times Y \times Z$	$200 \times 70 \times 10$ m
Grid cell dimensions $\Delta x \times \Delta y \times \Delta z$	$1 \times 1 \times 0.1$ m
Particle inlet spacing	0.1 m
Source zone dimensions $W \times H$	14 m \times 2 m
Pore diffusion coefficient D_p	10^{-9} m ² s ⁻¹
Local transverse dispersivity α_t	10^{-3} m

435 thetic virtual reality. The location of the hydrofacies corresponds with differences in hy-
 436 draulic parameters – the scour-pool fills have a higher hydraulic conductivity and poros-
 437 ity than the horizontal gravels, whereas the brown gravel sheets have a lower hydraulic
 438 conductivity and porosity, consistent with a wider range of grain sizes expected to be
 439 in these features.

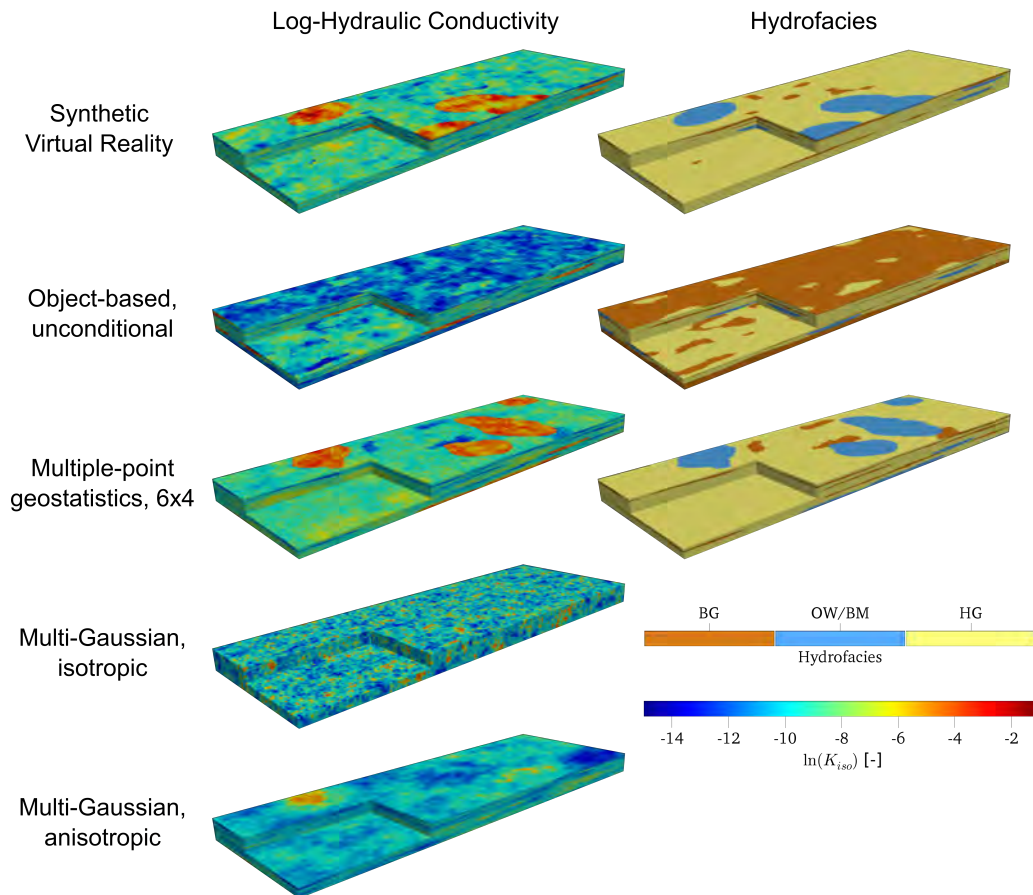
440 The unconditional, object-based realization shown in Figure 2 (second row) has thick
 441 brown gravel sheet hydrofacies at the bottom and top of the model domain. This demon-
 442 strates the random nature of the HyVR simulation process – these thick, low-hydraulic-
 443 conductivity features may strongly influence subsequent flow and transport simulations.

444 The MPS realization conditioned to the 6 \times 4 data set (Figure 2, third row) has cap-
 445 tured the approximate location of the brown gravel sheets; the scour-pool fill external
 446 geometries have been well reproduced by the MPS algorithm, although the individual
 447 geometric centers are somewhat different to those present in the synthetic virtual real-
 448 ity. The DeeSse algorithm was also successful in simulating bedding parameters (Fig-
 449 ure S3, Supporting Information). The dip patterns within the scour-pool fills are con-
 450 sistent with those of the synthetic virtual reality, with the greatest dip occurring at the
 451 sides of the feature. Azimuth values in the scour-pool fills are generally homogeneous
 452 throughout the feature, as they are in the synthetic virtual reality.

453 The multi-Gaussian model ensembles (Figure 2, bottom two rows) only include pa-
 454 rameter fields of log-hydraulic conductivity and porosity. The statistically isotropic multi-
 455 Gaussian fields have short correlation lengths and thus cannot reproduce the laterally

456 extensive features present in the synthetic virtual reality. The statistically anisotropic
 457 multi-Gaussian ensembles show some similarities with the synthetic virtual reality by re-
 458 producing lenses of highly conductive material and also some laterally extensive low-conductivity
 459 zones. However, as expected, the multi-Gaussian simulations cannot reproduce the jux-
 460 taposition of zones of contrasting hydraulic conductivity.

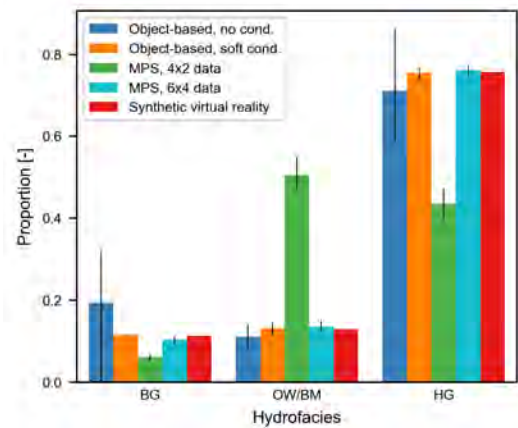
461 The generated parameter fields are available in HDF5 data formats and selected
 462 files are available in VTK rectilinear grid (*.vtr) format – see the Supporting Informa-
 463 tion for further details.



464 **Figure 2.** Log-hydraulic conductivity and hydrofacies parameter fields for example realiza-
 465 tions. The model domain dimensions are $X \times Y \times Z = 200 \times 70 \times 10$ m.

466 **5.1.2 Parameter Distributions**

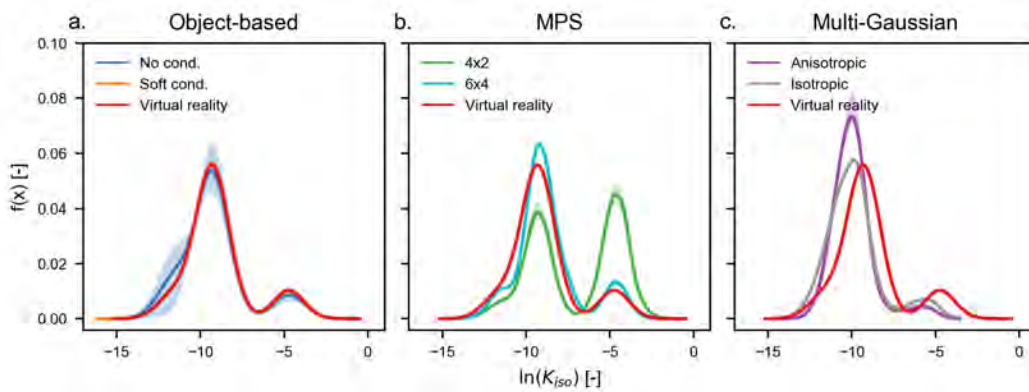
467 The proportion of the hydrofacies BG, OW/BM and HG within the synthetic vir-
 468 tual reality were 21 %, 11 %, and 68 % , respectively. The mean proportions of hydro-
 469 facies in the model ensembles depicted in Figure 3 (excluding the multi-Gaussian ensem-
 470 bles) show that the unconditioned object-based ensemble varies the most and that the
 471 soft conditioning greatly reduced the variance of these proportions in this object-based
 472 ensemble. The unconditioned, object-based ensemble also included realizations where
 473 the BG hydrofacies was absent. The MPS model ensemble conditioned to 4×2 data shows
 474 a much higher proportion of OW/BM hydrofacies than all other model ensembles. With
 475 the additional conditioning data, the MPS ensemble conditioned to 6×4 data has pro-
 476 portions which much more closely mimic those of the synthetic virtual reality. The dis-
 477 crepancy between the MPS model ensembles demonstrates the influence of the training
 478 image on the simulated fields: with more conditioning data, the proportions are closer
 479 to the “true” values of the synthetic virtual reality, whereas with less conditioning data
 480 the proportions are closer to those of the training image.



481 **Figure 3.** Mean proportions of hydrofacies in simulated parameter fields. Error bars denote
 482 5th-95th percentiles.

483 Figure 4 shows the empirical probability density functions of the hydraulic param-
 484 eters for all model ensembles. They mimic the distributions of the hydrofacies in all model
 485 ensembles, as hydraulic conductivity values were assigned according to the correspond-
 486 ing hydrofacies values in each model grid cell. The synthetic virtual reality has a bimodal
 487 distribution of log-hydraulic conductivity $\ln(K_{iso})$, reflecting the OW/BM and horizon-

488 tal sheet-related hydrofacies: this distribution is replicated in the other object-based model
 489 ensembles. The 5th-95th percentile range of the unconditional object-based ensemble dis-
 490 tribution is larger, whereas the soft-conditioned object-based ensemble has a distribu-
 491 tion that is very similar to that of the synthetic virtual reality. The conditional MPS fields
 492 mimic the bimodal distributions of the synthetic virtual reality – with the distribution
 493 of the MPS ensemble conditioned to the 6×4 data being much closer to that of the syn-
 494 thetic virtual reality than the distribution of the MPS ensemble conditioned to 4×2 data,
 495 highlighting the value of additional conditioning data. The multi-Gaussian model en-
 496 semble distributions of hydraulic conductivity reflect the bimodal nature of the synthetic
 497 virtual reality distribution. However, in these model ensembles the modal values of log-
 498 hydraulic conductivity are lower than in the synthetic virtual reality. This is likely due
 499 to the empirical distributions used in the normal-score transformation not capturing all
 500 of the heterogeneity present in the synthetic virtual reality. The 5th to 95th percentile
 501 shading shows that the multi-Gaussian ensemble distributions are relatively constrained.



502 **Figure 4.** Probability distribution functions of log-hydraulic conductivity parameter field
 503 ensembles. The solid line represents the mean value and the shading represents the 5th-95th
 504 percentiles.

505 Table 5 lists summary statistics calculated from the ensemble probability distri-
 506 bution functions for log-hydraulic conductivity and porosity. The mean of the ensem-
 507 ble probability distribution functions for $\ln(K)$ ranges between -9.9 (statistically anisotropic,
 508 multi-Gaussian ensemble) and -7.0 (MPS ensemble conditioned to 4×2 data). The over-
 509 all variance of log-hydraulic conductivity $\sigma_{\ln(K)}^2$ of 4.1 in the synthetic virtual reality is
 510 similar to those of the soft-conditioned, object-based model ensemble and the MPS en-

511 semble conditioned to 6×4 data. The lower frequency of conditioning data in MPS en-
 512 semble conditioned to 4×2 data led to a larger $\sigma_{\ln(K)}^2$ of 7.1. The multi-Gaussian model
 513 ensembles have a smaller $\sigma_{\ln(K)}^2$ values of 2.9 and 2.0 in the ensembles with isotropic and
 514 anisotropic variogram models, respectively.

515 **Table 5.** Summary statistics of ensemble probability distribution functions.

Model ensemble	$\mu_{\ln(K)}$ [-]	$\sigma_{\ln(K)}^2$ [-]	μ_θ [-]	σ_θ^2 [-]
Synthetic virtual reality	-9.0	4.1	0.20	0.0025
Object-based, no condition- ing	-9.3	3.5	0.19	0.0024
Object-based, soft condition- ing	-8.9	4.3	0.20	0.0026
MPS, 4×2 data	-7.0	7.1	0.24	0.0039
MPS, 6×4 data	-8.7	3.9	0.20	0.0025
Multi-Gaussian, isotropic	-9.8	2.9	0.20	0.0017
Multi-Gaussian, anisotropic	-9.9	2.0	0.20	0.0011

516 Porosity probability distribution functions for all model ensembles are trimodal as
 517 they are a weighted sum of three separate hydrofacies distributions. In all model ensem-
 518 bles the mean of the ensemble probability distribution functions ranges between 0.19 and
 519 0.24 [-] and the variance ranges between 0.0014 and 0.0039 [-]. A plot of the probabil-
 520 ity distribution functions for porosity is included in Figure S3 of the Supplementary In-
 521 formation.

522 **5.1.3 Connectivity Based on Minimum Hydraulic Resistance**

523 The connectivity of the simulated parameter fields was analyzed using the mini-
 524 mum hydraulic resistance metric of *Rizzo and de Barros* [2017], here applied between
 525 control planes at the model inlet and outlet (see equation (8)). In the present study, min-
 526 imum hydraulic resistance was calculated using isotropic conductivity fields for all en-
 527 sembles. Hydraulically anisotropic realizations (i.e., object-based, MPS) were geomet-
 528 rically averaged using equation (18).

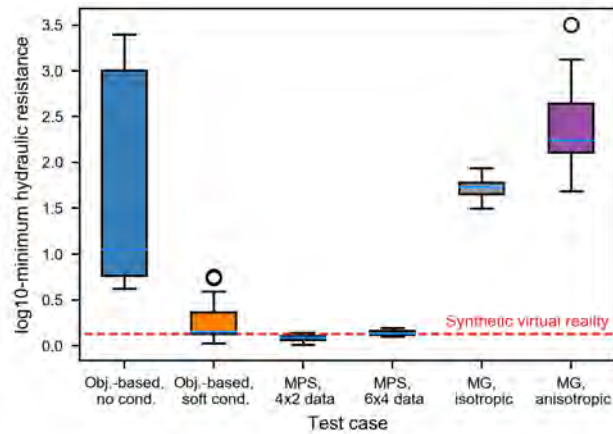
529 Figure 5 shows boxplots of the distribution of \log_{10} -minimum hydraulic resistance
 530 values for all model ensembles, as well as that of the synthetic virtual reality. It is im-
 531 mediately apparent that the unconditional, object-based ensemble is not able to capture
 532 the same connectivity characteristics of the synthetic virtual reality, and varies over a
 533 wide range. The soft conditioning applied to the object-based ensemble both improves
 534 the similarity with the synthetic virtual reality and reduces the range of the ensemble.
 535 The distributions of minimum hydraulic resistance for the MPS model ensemble are well-
 536 constrained and similar to the synthetic virtual reality value. The median value of the
 537 MPS ensemble conditioned to 6×4 boreholes is within 3 % of the synthetic virtual re-
 538 ality value, demonstrating the value of additional conditioning data. In contrast, the con-
 539 ditional multi-Gaussian fields are not able to reproduce the connectivity of the synthetic
 540 virtual reality. The anisotropic multi-Gaussian model ensemble connectivity distribu-
 541 tion has a larger median and wider range than the isotropic ensemble, suggesting that
 542 greater heterogeneity in the least resistance pathways are represented in these simula-
 543 tions.

544 Minimum hydraulic resistance values in model ensembles where large-scale sedi-
 545 mentary features are similar to those of the synthetic virtual reality (soft-conditioned
 546 object-based ensemble, and both MPS ensembles) were much closer to those of the syn-
 547 thetic virtual reality than minimum hydraulic resistance values in model ensembles that
 548 lack the right distinct geological features. Thus, it seems that connectivity is sensitive
 549 to these large-scale features. If they are not reproduced (i.e., unconditional object-based,
 550 and conditional multi-Gaussian ensembles) then the connectivity metrics will be poorly
 551 predicted.

554 **5.2 Groundwater Flow**

555 **5.2.1 Groundwater Velocity Fields**

556 As a measure of variability in specific discharge, we calculated the square root of
 557 the ensemble average of the variance of specific discharge in the three principal direc-
 558 tions ($\bar{\sigma}_{q_x}, \bar{\sigma}_{q_y}, \bar{\sigma}_{q_z}$) normalized by the mean specific discharge in the x -direction \bar{q}_x (Ta-
 559 ble 6). In general, the normalized ensemble standard deviations are similar between all
 560 model ensembles and the synthetic virtual reality. The object-based model ensembles
 561 have values that are closest to those of the synthetic virtual reality. Standard deviations



552 **Figure 5.** Distributions of minimum hydraulic resistance calculated using the method of *Rizzo*
 553 *and de Barros* [2017].

562 for the MPS ensemble with 4×2 data are lower than the synthetic virtual reality; the ad-
 563 ditional data in the 6×4 MPS ensemble seem to have improved the similarity of that en-
 564 semble with the synthetic virtual reality. The statistically isotropic multi-Gaussian field
 565 has the lowest range between the $\bar{\sigma}$ values in the three principal directions, probably be-
 566 cause the correlation lengths are the same in all directions. The additional geological in-
 567 formation included in the statistically anisotropic multi-Gaussian model ensemble brought
 568 the $\bar{\sigma}$ values in the x - and z -directions closer to those of the synthetic virtual reality. In
 569 general, it seems that the variance is controlled by differences between the brown gravel
 570 sheets of lower conductivity and the highly conductive scour-pool features.

572 **5.2.2 Advective Particle Tracks**

573 Figure 6 depicts the intersection of advective particle tracks with control planes per-
 574 pendicular to the mean direction of flow at different travel distances for a single realiza-
 575 tion selected from each model ensemble. The color coding refers to the y -coordinate of
 576 each track in the inlet plane. The advective particle tracks are quickly concentrated in
 577 areas of higher hydraulic conductivity. In general, model ensembles that simulated hy-
 578 drofacies parameter fields (object-based and MPS methods) show particle distributions
 579 that are more concentrated in lenses of high hydraulic conductivity. This contrasts with
 580 the multi-Gaussian simulations where such large hydraulic conductivity contrasts are not
 581 included. The statistically isotropic multi-Gaussian fields show the effect of the isotropic

571

Table 6. Statistical Characteristics of the Velocity Fields

Model ensemble	$\bar{\sigma}_{q_x}/\mu_{q_x}$ [-]	$\bar{\sigma}_{q_y}/\mu_{q_x}$ [-]	$\bar{\sigma}_{q_z}/\mu_{q_x}$ [-]
Synthetic virtual reality	1.9	1.3	0.52
Object-based, no condition- ing	1.8	1.2	0.52
Object-based, soft condition- ing	1.8	1.2	0.50
MPS, 4×2 data	1.5	0.94	0.41
MPS, 6×4 data	1.7	1.1	0.44
Multi-Gaussian, isotropic	1.5	1.1	0.87
Multi-Gaussian, anisotropic	1.8	0.98	0.47

$\bar{\sigma}_{q_i}$: ensemble standard deviation of specific-discharge component in direction i .

μ_{q_x} : mean specific-discharge component in x direction.

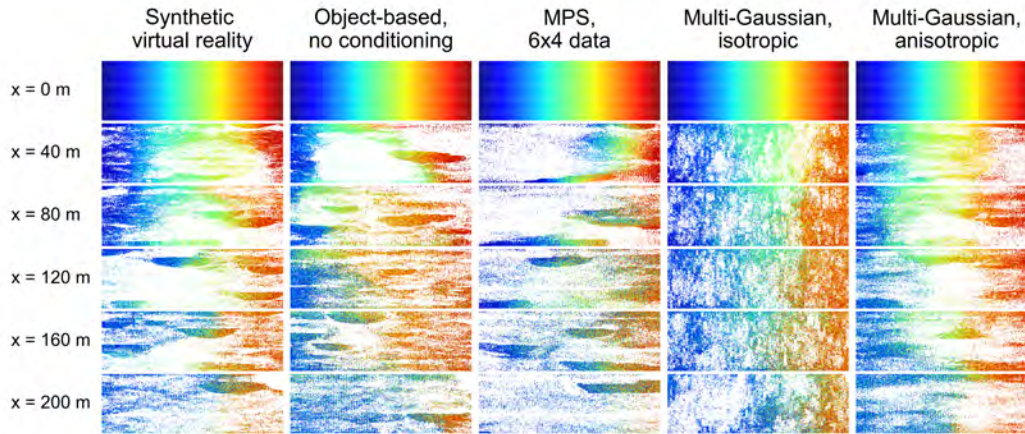
$\mu_{q_x} = 1 \times 10^{-5}$ m s⁻¹ in all model ensembles.

582 geostatistical structure. The particles remain distributed relatively evenly throughout
583 the cross-sections, and intermingling of particle trajectories appears to be low. Conversely,
584 the statistically anisotropic multi-Gaussian fields show some similarity with the hydrofacies-
585 based simulation methods. Lenses of densely concentrated particles also occur in this
586 ensemble, although the lack of distinct hydrofacies boundaries leads to smoothed lateral
587 boundaries of concentrated particle trajectories.

592 **5.3 Solute Transport**

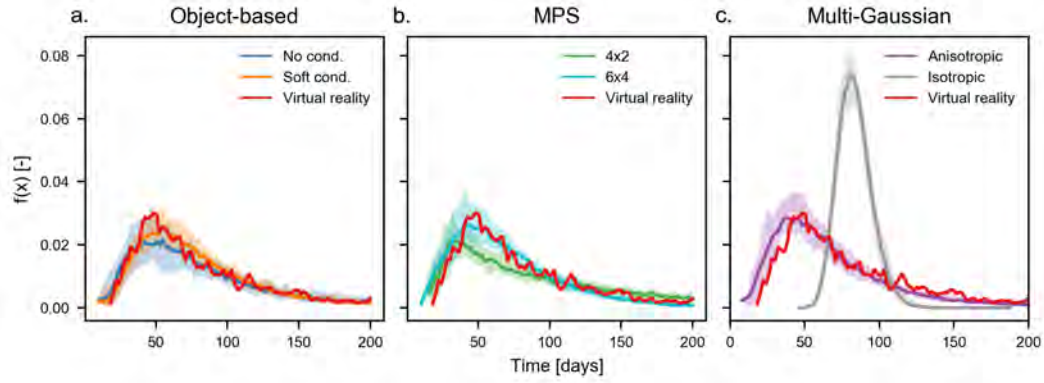
593 **5.3.1 Advective Arrival Time Distributions**

594 Figure 7 shows mean advective arrival time distributions at the model outlet ($x = 200$ m).
595 The object-based model ensembles are similar to the breakthrough curve of the synthetic
596 virtual reality, although they do not match its peak arrival time. Of the two object-based
597 model ensembles, the softly conditioned ensemble appears to resemble the breakthrough
598 curve of the synthetic virtual reality the best. The arrival time distributions for the MPS
599 ensemble conditioned to 4×2 data do not match that of the virtual reality: the peak ar-
600 rival is too early and the tailing is too strong. The distribution for the MPS ensemble



588 **Figure 6.** Advective particle distributions in observation planes perpendicular to the mean
 589 flow direction for single realizations from selected model ensembles. Particle colors denote the
 590 initial y -coordinate value of the particle trajectory. Spatial dimensions of the cross sections:
 591 $70 \text{ m} \times 10 \text{ m}$.

601 conditioned to 6×4 data shows a much better fit to the synthetic virtual reality – here
 602 the peaks occur at a similar time, and the virtual reality breakthrough curve mostly falls
 603 within the 5th-95th percentile range of this ensemble. Despite a somewhat too early first
 604 arrival, these results confirm that additional conditioning data improves the similarity
 605 between the breakthrough curves. The arrival time distributions for the multi-Gaussian
 606 model ensembles do not match that of the synthetic virtual reality so well. In the sta-
 607 tistically isotropic multi-Gaussian conditional ensemble the peak occurs 36 days after
 608 that of the virtual reality and is also much higher and more symmetrical. Conversely the
 609 peak in the statistically anisotropic multi-Gaussian ensemble occurs fifteen days earlier
 610 than the virtual reality. There appears to be a time shift between the breakthrough curves
 611 of the anisotropic multi-Gaussian ensemble and the synthetic virtual reality. In general,
 612 the object-based ensemble with soft conditioning, the MPS ensemble conditioned to 6×4
 613 data, and the anisotropic multi-Gaussian field are all able to predict the advective break-
 614 through behavior of the synthetic virtual reality, despite significant differences in con-
 615 nectivity (see Section 5.1.3).



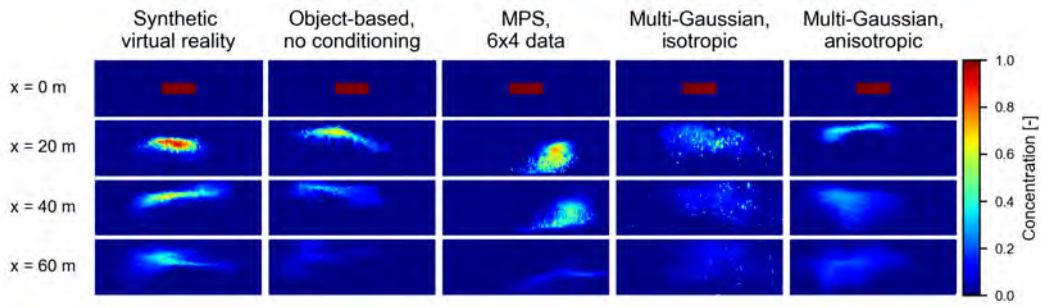
616 **Figure 7.** Advective arrival time distributions at the model outlet ($x=200$ m) for all model
 617 ensembles. Shading denotes 5th-95th percentiles

618 *5.3.2 Steady-State Concentration Distributions*

619 Figure 8 shows concentration distributions of steady-state advective-dispersive trans-
 620 port in cross-sections perpendicular to the mean direction of flow for selected realizations
 621 of the different ensembles. In general, the object-based and MPS model ensembles ex-
 622 hibited similar patterns of concentrations, which contrasts with those of the multi-Gaussian
 623 model ensembles. The concentration distributions for the multi-Gaussian model ensem-
 624 bles tended to be much more diffuse and irregular. Concentration distributions in the
 625 anisotropic multi-Gaussian model ensemble remained much more compact than those
 626 in the isotropic multi-Gaussian model ensemble. Concentration distributions in the present
 627 study were much more irregular than similar distributions reported in *Cirpka et al.* [2015]
 628 and *Bennett et al.* [2017]. This is likely due to the relative difference between the cor-
 629 relation lengths of randomly generated microstructure (3 m horizontal and 0.3 m ver-
 630 tical) and the model grid resolution (1 m horizontal and 0.1 m vertical).

635 *5.3.3 Temporal Moments of Advective-Dispersive Travel Times Distri-* 636 *butions*

637 Temporal moments of advective-dispersive travel time distributions depicted in Fig-
 638 ure 9 generally show good correspondence between mean breakthrough times \bar{t} in the
 639 synthetic virtual reality and all model ensembles. It is clear from panels (a) and (d) that
 640 the unconditioned object-based ensemble shows strong variations, whereas the soft-conditioned,
 641 object-based model ensemble had mean breakthrough times that are match the synthetic

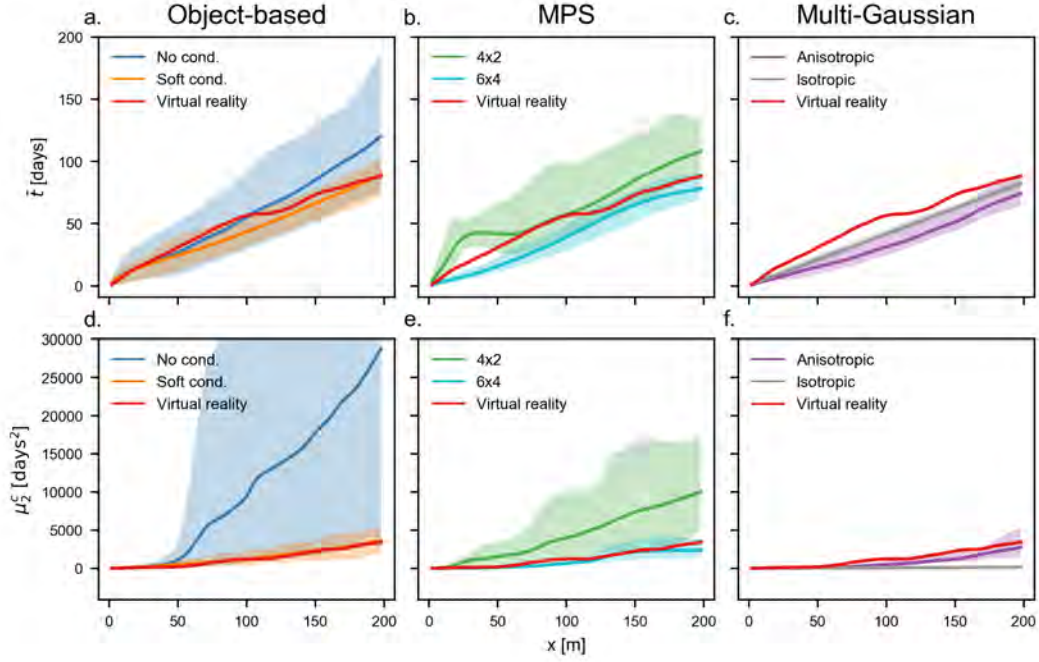


631 **Figure 8.** Steady state concentration distributions in observation planes perpendicular to the
 632 mean flow direction for a single realization from selected model ensembles. Only the first 60 m
 633 of the model domain is displayed as concentration differences beyond this point are generally
 634 difficult to delineate visually. Spatial dimensions of the cross sections: 70 m \times 10 m.

642 virtual reality, particularly when close to the model inlet and outlet. The MPS-generated
 643 ensemble with additional conditioning data shows a better match to the temporal mo-
 644 ments of the synthetic virtual reality. The multi-Gaussian model ensembles display the
 645 least ensemble variance of all model ensembles. The mean breakthrough times of the isotropic
 646 multi-Gaussian ensemble are closer to those of the synthetic virtual reality than the anisotropic
 647 ensemble, whereas the second central moments of the isotropic multi-Gaussian ensem-
 648 ble are completely off target. The similarities between mean breakthrough curves in all
 649 model ensembles and the synthetic virtual reality are imposed by the same mean Eu-
 650 lerian velocity applied to all realizations in all ensembles. Conversely, the second cen-
 651 tral moments σ_T^2 differ between the ensembles as the spread of the breakthrough curves
 652 depends on the Lagrangian velocity covariance function and thus on the spatial config-
 653 uration of the hydraulic conductivity field. The results of second central moments in-
 654 dicate that data conditioning, whether to large-scale features in the object-based ensem-
 655 ble, additional borehole data in the MPS ensemble, or additional geological information
 656 in the form of variogram models for the multi-Gaussian ensemble, can improve estimates
 657 of longitudinal spreading.

660 *5.3.4 Transverse Moments of Steady-State Concentration Distributions*

661 Figure 10 shows the transverse moments of steady-state concentration distributions,
 662 providing a clearer picture of the differences in solute transport between the model en-



658 **Figure 9.** Temporal moments of advective-dispersive arrival time distributions in the longitudi-
 659 nal direction for all model ensembles. Shading denotes 5th-95th percentiles

663 sembles. The mean center of mass (μ_y and μ_z) quantifies the plume center as predicted
 664 by the model ensembles and is an indicator of plume meandering. The second central
 665 moments (σ_y^2 , σ_z^2 , and the mixed moment C_{yz}) describe the spread of the plume about
 666 the center of mass.

667 In the object-based model ensembles, the plume center remains approximately in
 668 the same location in the center of the domain; the interpercentile ranges depicted in Fig-
 669 ure 10 shows that predictions of the center of mass almost extend across the entire model
 670 domain in the y -direction, and across half of the model domain in the z -direction. The
 671 center of mass of the synthetic virtual reality in the y direction is outside of the 5th-95th
 672 percentile range of the object-based ensemble predictions

673 The model ensembles simulated using MPS methods are more congruent with the
 674 synthetic virtual reality plume. The center of mass of the MPS ensemble conditioned to
 675 6×4 follows that of the synthetic virtual reality compared to that of the MPS ensem-
 676 ble conditioned to 4×2 data, demonstrating that the additional conditioning data pro-
 677 vided to the MPS simulation algorithm pays off for predicting plume meandering.

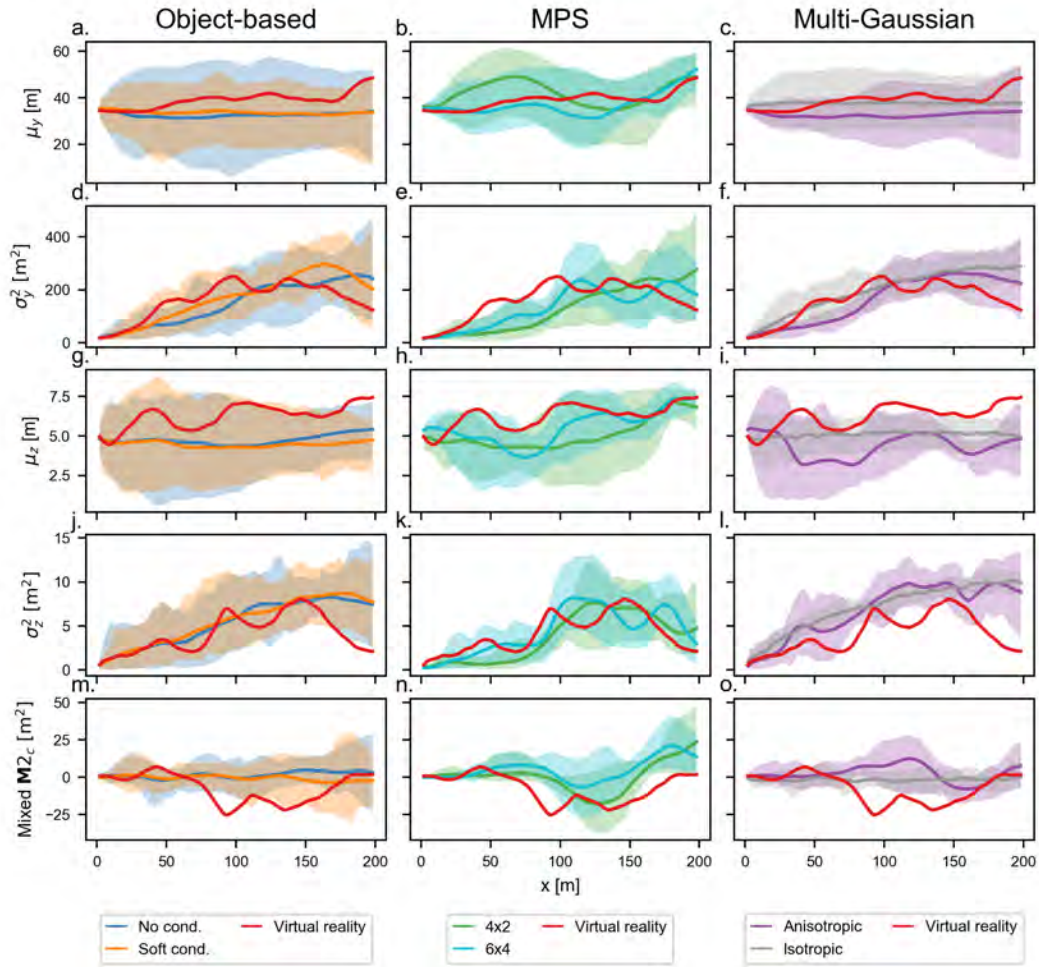
678 The multi-Gaussian ensembles are not so successful in matching the transverse mo-
 679 ments of the synthetic virtual reality. The ensemble center of mass in the statistically
 680 isotropic multi-Gaussian ensemble remains static – here the very short correlation lengths
 681 from the isotropic variogram model are able to “absorb” the conditioning data without
 682 impacting the mean plume behavior. The variance σ_y^2 , σ_z^2 in this model ensemble increases
 683 until it reaches a stable value close to the model outlet. This behavior of the variances
 684 can also be seen in the statistically anisotropic multi-Gaussian ensemble although there
 685 is some fluctuation.

686 To summarize, the results of transverse concentration moments of concentration
 687 distributions show that conditional ensembles generated using the multiple-point geosta-
 688 tistical method are better at predicting the center of mass of the synthetic virtual re-
 689 ality plume than the multi-Gaussian model ensembles. This suggests that the geolog-
 690 ical information provided in the form of the training image is important. It is also clear
 691 that having more conditioning data available will improve the quality of estimation of
 692 plume location and extent.

695 **5.3.5 Plume Dilution**

696 We calculated the flux-weighted dilution indices from the steady-state concentra-
 697 tion distributions using equation (15) and normalized them with by the total volumet-
 698 ric flux across the model inlet plane ($M_Q = E_Q(x)/Q$). Figure 11 depicts the devel-
 699 opment of these values for each model ensemble with distance x . In general, there is good
 700 agreement between the values for all model ensembles and the synthetic virtual reality.
 701 The flux-weighted reactor ratio initially increases only slightly, and takes off at larger
 702 distances. By construction, it must flatten out when reactor ratio approaches unity (im-
 703 plying complete mixing of the solute flux throughout the bounded cross-section) This
 704 is congruent with the behavior observed for the non-stationary anisotropic field reported
 705 in *Cirpka et al.* [2015, fig. 9], albeit over a larger distance due to the shorter correlation
 706 lengths that were used in that study.

707 The flux-weighted dilution indices normalized by the inlet value $E_Q(x)/E_Q(0)$ (not
 708 shown) are generally much higher for all model ensembles than those reported in *Ben-*
 709 *nett et al.* [2017]. This most likely reflects variability in the volumetric flux over the plume-
 710 source area. There is also no discernible difference between the model ensembles which

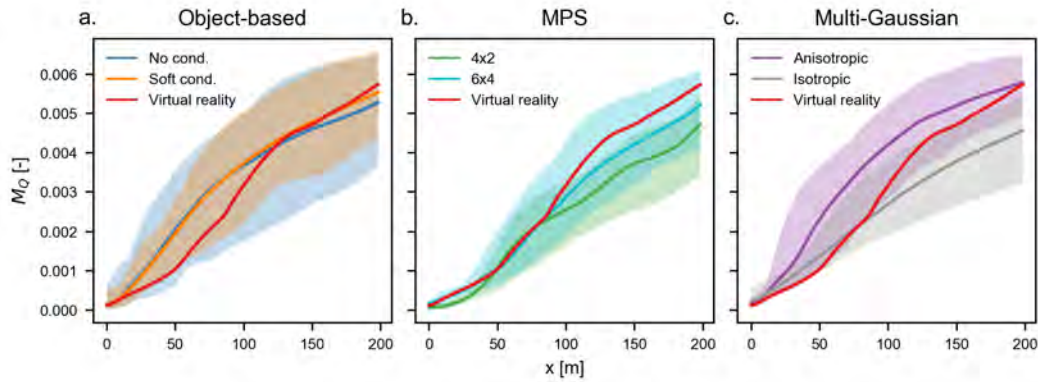


693 **Figure 10.** Transverse moments derived from steady state concentration distributions. Lines
 694 represent ensemble means and shading represents 5th-95th percentiles.

711 included local hydraulic anisotropy (object-based and MPS) and those that were locally
 712 hydraulically isotropic (multi-Gaussian). This lack of difference may be due to the rel-
 713 atively small and infrequent values of dip and azimuth within the generated parameter
 714 fields. Cross-bedded structures, as opposed to the bulb-type dipping features generated
 715 in the present study, are likely to produce very different dilution profiles [cf. *Bennett*
 716 *et al.*, 2017].

719 6 Conclusions

720 In the present study, we have tested the ability of three different subsurface sim-
 721 ulation methods to match the groundwater flow and solute transport behavior of a syn-



717 **Figure 11.** Ensemble means of normalized flux-weighted reactor ratios $M_Q(x) = E_Q(x)/Q$ [-]
 718 for all model ensembles. Shading represents 5th-95th percentiles.

722 thetic virtual reality mimicking realistic geological features of braided-river sediments.
 723 The three methods used (the object-based hydrofacies generator HyVR, the multiple-
 724 point geostatistical simulator DeeSse, and the multi-Gaussian co-simulator GCOSIM3D)
 725 employ different approaches to simulating subsurface properties. It is clear that solely
 726 relying on the object-based methods of the HyVR simulation package will not produce
 727 an ensemble prediction that is close to the virtual reality result because conditioning is
 728 not possible. Conversely, relying solely on two-point geostatistical characterizations of
 729 an aquifer will provide inadequate estimates of the arrival time and extent of a solute
 730 plume, particularly if the horizontal spacing of boreholes is too large to determine hor-
 731 izontal correlation lengths. We have shown that the addition of geological information,
 732 such as training images, to traditional borehole data in conditional MPS and multi-Gaussian
 733 simulations can help to constrain predictions of solute arrival-time distributions and the
 734 extent of a solute plume within a stochastic hydrogeological modeling context.

735 The paucity of detailed hydrogeological characterization studies hampers the de-
 736 velopment of realistic subsurface models for use in hydrogeological research. Such stud-
 737 ies are typically time-consuming and costly, but can provide invaluable information for
 738 numerical modeling efforts. Better uptake in the upload and use of parameter databases
 739 such as WWHYPDA [Comunian and Renard, 2009] by the hydrogeological community,
 740 or opening up access to the large databases of facies data developed in conjunction with
 741 the petroleum industry [e.g., FAKTS, Colombero et al., 2013] could provide rich new
 742 information for constraining parameters in stochastic hydrogeological modeling.

743 A valid criticism of the present study is that we have used the same simulation meth-
 744 ods used for the creation of the synthetic virtual reality as for comparing object-based
 745 methods and for generating training images for MPS simulation methods and anisotropic
 746 variograms for multi-Gaussian simulation. Despite this, we believe the methods and work-
 747 flow used in this study provide a good starting point for further investigation of the ef-
 748 fects of parameter and model uncertainty on groundwater flow and solute transport. The
 749 difficulty of conditioning process-based models such as FLUMY [*MINES ParisTech/ARMINES*,
 750 2017] presents an obstacle for their use as direct inputs for stochastic hydrogeological
 751 modeling. However, a single realization could serve as a more realistic virtual reality than
 752 the object-based training images used in the present study. The challenge is to convert
 753 the stratigraphic outputs of the process-based models into hydraulic parameter fields suit-
 754 able for use in hydrogeological research.

755 **Acknowledgments**

756 This work was funded by the German Research Foundation (DFG) within the Research
 757 Training Group "Integrated Hydrosystem Modelling" (RTG 1829) at the University of
 758 Tübingen. Supporting data for is available at <https://doi.org/10.5281/zenodo.1400484>.
 759 The authors declare no conflicting interests. We are grateful to Julien Straubhaar (Uni-
 760 versity of Neuchâtel) for assistance in running the DeeSse ensemble simulations. We thank
 761 Calogero B. Rizzo and Felipe P.J. de Barros (University of Southern California) for pro-
 762 viding us with the minimum hydraulic resistance executable file. We thank AR2TECH
 763 for providing the AR2GEMS geostatistical software.

764 **References**

- 765 Anderson, M., J. Aiken, E. Webb, and D. Mickelson (1999), Sedimentology and
 766 hydrogeology of two braided stream deposits, *Sedimentary Geology*, 129(3–4),
 767 187–199, doi:10.1016/S0037-0738(99)00015-9.
- 768 AR2Tech (2017), AR2GeMS v1.0b [computer software]. Denver, CO. Available from
 769 <http://www.ar2tech.com/products>.
- 770 Bakker, M., V. Post, C. D. Langevin, J. D. Hughes, J. T. White, J. J. Starn, and
 771 M. N. Fienen (2016), Scripting MODFLOW Model Development Using Python
 772 and FloPy, *Groundwater*, 54(5), 733–739, doi:10.1111/gwat.12413.

- 773 Bayer, P., P. Huggenberger, P. Renard, and A. Comunian (2011), Three-dimensional
774 high resolution fluvio-glacial aquifer analog: Part 1: Field study, *Journal of Hy-*
775 *drology*, *405*(1), 1–9, doi:10.1016/j.jhydrol.2011.03.038.
- 776 Bennett, J., C. P. Haslauer, and O. A. Cirpka (2017), The impact of sedimentary
777 anisotropy on solute mixing in stacked scour-pool structures, *Water Resources*
778 *Research*, *53*(4), 2813–2832, doi:10.1002/2016WR019665.
- 779 Bennett, J. P., C. P. Haslauer, M. Ross, and O. A. Cirpka (2018), An open, object-
780 based framework for generating anisotropy in sedimentary subsurface models,
781 *Groundwater*, doi:10.1111/gwat.12803.
- 782 Bianchi, M., C. Zheng, C. Wilson, G. R. Tick, G. Liu, and S. M. Gorelick
783 (2011), Spatial connectivity in a highly heterogeneous aquifer: From cores
784 to preferential flow paths, *Water Resources Research*, *47*(5), n/a–n/a, doi:
785 10.1029/2009WR008966.
- 786 Chamberlain, T. C. (1890), The method of multiple working hypotheses, *Science*,
787 *15*(366), 92–96, doi:10.1126/science.148.3671.754.
- 788 Cirpka, O. A., and A. J. Valocchi (2016), Debates—Stochastic subsurface hydrology
789 from theory to practice: Does stochastic subsurface hydrology help solving prac-
790 tical problems of contaminant hydrogeology?, *Water Resources Research*, *52*(12),
791 9218–9227, doi:10.1002/2016WR019087.
- 792 Cirpka, O. A., G. Chiogna, M. Rolle, and A. Bellin (2015), Transverse mixing in
793 three-dimensional nonstationary anisotropic heterogeneous porous media, *Water*
794 *Resources Research*, *51*(1), 241–260, doi:10.1002/2014WR015331.
- 795 Colombera, L., N. P. Mountney, and W. D. McCaffrey (2013), A quantitative ap-
796 proach to fluvial facies models: Methods and example results, *Sedimentology*,
797 *60*(6), 1526–1558, doi:10.1111/sed.12050.
- 798 Comunian, A., and P. Renard (2009), Introducing wwhypda: A world-wide collabo-
799 rative hydrogeological parameters database, *Hydrogeology Journal*, *17*(2), 481–489,
800 doi:10.1007/s10040-008-0387-x.
- 801 Dietrich, C. R., and G. N. Newsam (1993), A fast and exact method for multidimensional gaussian stochastic simulations, *Water Resources Research*, *29*(8),
802 2861–2869, doi:10.1029/93WR01070.
- 803
804 Dijkstra, E. W. (1959), A note on two problems in connexion with graphs, *Nu-*
805 *merische mathematik*, *1*(1), 269–271, doi:10.1007/BF01386390.

- 806 Felletti, F., R. Bersezio, and M. Giudici (2006), Geostatistical Simulation and Nu-
807 merical Upscaling, to Model Ground-Water Flow in a Sandy-Gravel, Braided
808 River, Aquifer Analogue, *Journal of Sedimentary Research*, 76(11), 1215–1229,
809 doi:10.2110/jsr.2006.091.
- 810 Fogg, G. E. (1986), Groundwater Flow and Sand Body Interconnectedness in a
811 Thick, Multiple-Aquifer System, *Water Resources Research*, 22(5), 679–694, doi:
812 10.1029/WR022i005p00679.
- 813 Fogg, G. E., and Y. Zhang (2016), Debates-Stochastic subsurface hydrology from
814 theory to practice: A geologic perspective, *Water Resources Research*, doi:
815 10.1002/2016WR019699.
- 816 Gómez-Hernández, J., and X.-H. Wen (1998), To be or not to be multi-Gaussian? A
817 reflection on stochastic hydrogeology, *Advances in Water Resources*, 21(1), 47–61,
818 doi:10.1016/S0309-1708(96)00031-0.
- 819 Gómez-Hernández, J. J., and A. G. Journel (1993), Joint Sequential Simulation of
820 MultiGaussian Fields, in *Geostatistics Tróia '92: Volume 1*, edited by A. Soares,
821 pp. 85–94, Springer Netherlands, Dordrecht, doi:10.1007/978-94-011-1739-5.
- 822 Haslauer, C., P. Guthke, A. Bárdossy, and E. Sudicky (2012), Effects of non-
823 Gaussian copula-based hydraulic conductivity fields on macrodispersion, *Water*
824 *Resources Research*, 48(7), doi:10.1029/2011WR011425.
- 825 Heinz, J., and T. Aigner (2003), Three-dimensional GPR analysis of various Qua-
826 ternary gravel-bed braided river deposits (southwestern Germany), *Geological*
827 *Society, London, Special Publications*, 211(1), 99–110, doi:10.1144/GSL.SP.2001.
828 211.01.09.
- 829 Huber, E., and P. Huggenberger (2016), Subsurface flow mixing in coarse, braided
830 river deposits, *Hydrology and Earth System Sciences*, 20(5), 2035–2046, doi:
831 10.5194/hess-20-2035-2016.
- 832 Jussel, P., F. Stauffer, and T. Dracos (1994), Transport modeling in heterogeneous
833 aquifers: 1. Statistical description and numerical generation of gravel deposits,
834 *Water Resources Research*, 30(6), 1803–1817, doi:10.1029/94WR00162.
- 835 Kerrou, J., P. Renard, H.-J. Hendricks Franssen, and I. Lunati (2008), Issues in
836 characterizing heterogeneity and connectivity in non-multiGaussian media, *Ad-*
837 *vances in Water Resources*, 31(1), 147–159, doi:10.1016/j.advwatres.2007.07.002.

- 838 Kinzelbach, W. (1988), The Random Walk Method in Pollutant Transport Sim-
839 ulation, in *Groundwater Flow and Quality Modelling*, edited by E. Custodio,
840 A. Gurgui, and J. P. L. Ferreira, pp. 227–245, Springer Netherlands, Dordrecht.
- 841 Klingbeil, R., S. Kleineidam, U. Aspriorn, T. Aigner, and G. Teutsch (1999), Re-
842 lating lithofacies to hydrofacies: Outcrop-based hydrogeological characterisation
843 of Quaternary gravel deposits, *Sedimentary Geology*, 129(3-4), 299–310, doi:
844 10.1016/S0037-0738(99)00067-6.
- 845 Langevin, C. D., J. D. Hughes, E. R. Banta, R. G. Niswonger, S. Panday, and A. M.
846 Provost (2017), Documentation for the MODFLOW 6 Groundwater Flow Model,
847 *Tech. Rep. 6-A55*, US Geological Survey, doi:10.3133/tm6A55.
- 848 Linde, N., P. Renard, T. Mukerji, and J. Caers (2015), Geological realism in hy-
849 drogeological and geophysical inverse modeling: A review, *Advances in Water*
850 *Resources*, 86, Part A, 86–101, doi:10.1016/j.advwatres.2015.09.019.
- 851 Mariethoz, G., P. Renard, and J. Straubhaar (2010), The Direct Sampling
852 method to perform multiple-point geostatistical simulations: Performing
853 multiple-points simulations, *Water Resources Research*, 46(11), W11536, doi:
854 10.1029/2008WR007621.
- 855 Miall, A. D. (1985), Architectural-element analysis: A new method of facies anal-
856 ysis applied to fluvial deposits, *Earth-Science Reviews*, 22(4), 261–308, doi:
857 10.1016/0012-8252(85)90001-7.
- 858 MINES ParisTech / ARMINES (2017), FLUMY: Process-based channel-
859 ized reservoir models [computer software]. Paris, France. Available from
860 [http://www.geosciences.mines-paristech.fr/en/organization/presentation-of-the-](http://www.geosciences.mines-paristech.fr/en/organization/presentation-of-the-group-2/main-projects/flumy)
861 [group-2/main-projects/flumy](http://www.geosciences.mines-paristech.fr/en/organization/presentation-of-the-group-2/main-projects/flumy).
- 862 Pirot, G., P. Renard, E. Huber, J. Straubhaar, and P. Huggenberger (2015), In-
863 fluence of conceptual model uncertainty on contaminant transport forecasting
864 in braided river aquifers, *Groundwater flow and transport in aquifers: Insights*
865 *from modeling and characterization at the field scale*, 531, Part 1, 124–141, doi:
866 10.1016/j.jhydrol.2015.07.036.
- 867 Pollock, D. W. (1988), Semianalytical Computation of Path Lines for Finite-
868 Difference Models, *Ground Water*, 26(6), 743–750, doi:10.1111/j.1745-6584.1988.
869 tb00425.x.

- 870 Provost, A. M., C. D. Langevin, and J. D. Hughes (2017), Documentation for the
871 “XT3D” option in the Node Property Flow (NPF) Package of MODFLOW 6,
872 *Report 6-A56*, United States Geological Survey, Reston, VA, doi:10.3133/tm6A56.
- 873 Renard, P., and D. Allard (2013), Connectivity metrics for subsurface flow and
874 transport, *Advances in Water Resources*, *51*, 168–196, doi:10.1016/j.advwatres.
875 2011.12.001.
- 876 Rizzo, C. B., and F. P. J. de Barros (2017), Minimum Hydraulic Resistance and
877 Least Resistance Path in Heterogeneous Porous Media, *Water Resources Research*,
878 *53*(10), 8596–8613, doi:10.1002/2017WR020418.
- 879 Rolle, M., C. Eberhardt, G. Chiogna, O. A. Cirpka, and P. Grathwohl (2009),
880 Enhancement of dilution and transverse reactive mixing in porous media: Ex-
881 periments and model-based interpretation, *Journal of Contaminant Hydrology*,
882 *110*(3-4), 130–142, doi:10.1016/j.jconhyd.2009.10.003.
- 883 Sanchez-Vila, X., and D. Fernández-García (2016), Debates—Stochastic subsur-
884 face hydrology from theory to practice: Why stochastic modeling has not yet
885 permeated into practitioners?, *Water Resources Research*, *52*(12), 9246–9258,
886 doi:10.1002/2016WR019302.
- 887 Scheidegger, A. E. (1961), General theory of dispersion in porous media, *Journal of*
888 *Geophysical Research*, *66*(10), 3273–3278, doi:10.1029/JZ066i010p03273.
- 889 Siegenthaler, C., and P. Huguenberger (1993), Pleistocene Rhine gravel: Deposits
890 of a braided river system with dominant pool preservation, *Geological Society,*
891 *London, Special Publications*, *75*(1), 147–162, doi:10.1144/GSL.SP.1993.075.01.09.
- 892 Straubhaar, J. (2017), DeeSse User’s Guide, *Tech. rep.*, University of Neuchâtel,
893 Neuchâtel, Switzerland.
- 894 Teles, V., F. Delay, and G. de Marsily (2006), Comparison of transport simulations
895 and equivalent dispersion coefficients in heterogeneous media generated by dif-
896 ferent numerical methods: A genesis model and a simple geostatistical sequential
897 Gaussian simulator, *Geosphere*, *2*(5), 275, doi:10.1130/GES00034.1.
- 898 Wen, X.-H., and C.-S. Kung (1993), Stochastic Simulation of Solute Trans-
899 port in Heterogeneous Formations: A Comparison of Parametric and Non-
900 parametric Geostatistical Approaches, *Groundwater*, *31*(6), 953–965, doi:
901 10.1111/j.1745-6584.1993.tb00869.x.

- 902 Zarlenga, A., and A. Fiori (2013), Steady plumes in heterogeneous porous forma-
903 tions: A stochastic Lagrangian approach, *Water Resources Research*, *49*(2), 864–
904 873, doi:10.1002/wrcr.20106.
- 905 Zhang, M., and Y. Zhang (2015), Multiscale solute transport upscaling for a three-
906 dimensional hierarchical porous medium, *Water Resources Research*, *51*(3), 1688–
907 1709, doi:10.1002/2014WR016202.
- 908 Zheng, C., and S. M. Gorelick (2003), Analysis of Solute Transport in Flow Fields
909 Influenced by Preferential Flowpaths at the Decimeter Scale, *Ground Water*,
910 *41*(2), 142–155, doi:10.1111/j.1745-6584.2003.tb02578.x.
- 911 Zheng, C., M. Bianchi, and S. M. Gorelick (2011), Lessons Learned from 25
912 Years of Research at the MADE Site, *Ground Water*, *49*(5), 649–662, doi:
913 10.1111/j.1745-6584.2010.00753.x.

Supporting Information for “A Multi-Model Analysis of Solute Plume Behavior in a Synthetic Braided-River Deposit”

Jeremy P. Bennett ¹, Philippe Renard ², Claus P. Haslauer ¹, and Olaf A. Cirpka ¹

¹Center for Applied Geosciences, University of Tübingen, Hölderlinstr. 12, 72074 Tübingen, Germany.

²Center for Hydrogeology and Geothermics, University of Neuchâtel, Rue Emile-Argand 11, 2000 Neuchâtel, Switzerland.

Contents

1. Figures S1 to S3
2. Input Files S1 to S2

Note: The model ensemble data files (including parameter fields and flow and transport results) and generating codes are available at <https://doi.org/10.5281/zenodo.1400484>.

Figure S1.

Empirical variograms and variogram models for statistically isotropic multi-Gaussian simulations. Note that the data has been transformed using normal scores.

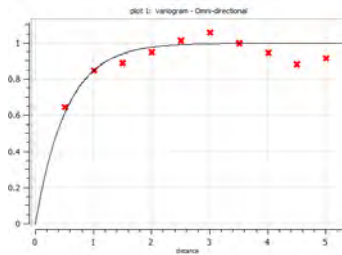


Figure 1: ln geometric hydraulic conductivity.

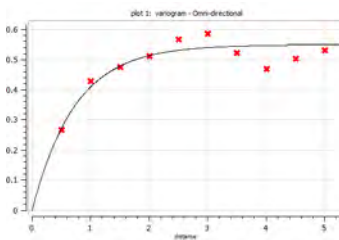


Figure 2: Porosity.

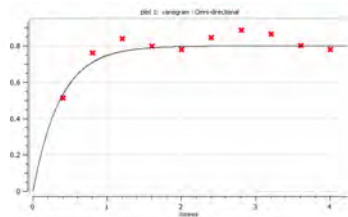


Figure 3: ln geometric hydraulic conductivity & porosity.

Corresponding author: Olaf A. Cirpka, olaf.cirpka@uni-tuebingen.de

Figure S2.

Empirical variograms and variogram models for statistically anisotropic multi-Gaussian simulations. Note that the data has been transformed using normal scores.

A. Log-geometric hydraulic conductivity:

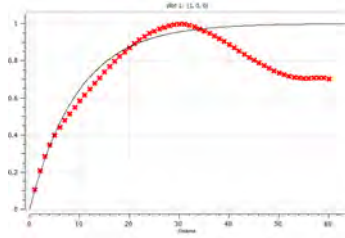


Figure 4: x direction.

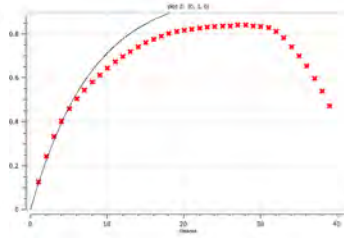


Figure 5: y direction.

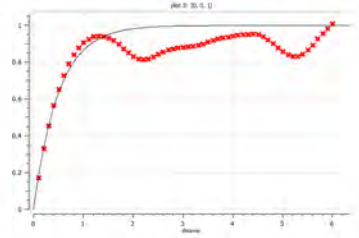


Figure 6: z direction.

B. Porosity:

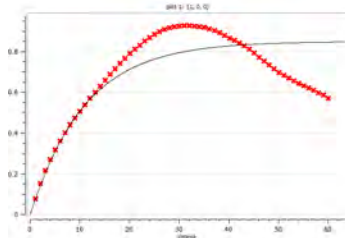


Figure 7: x direction.

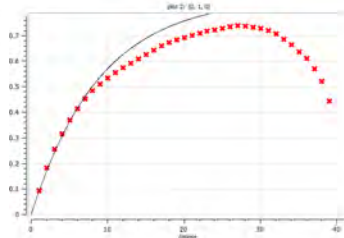


Figure 8: y direction.

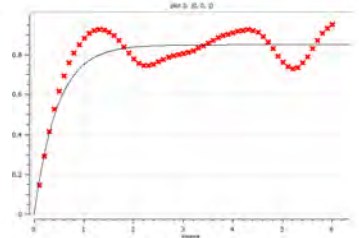


Figure 9: z direction.

C. Log-geometric hydraulic conductivity vs. porosity:

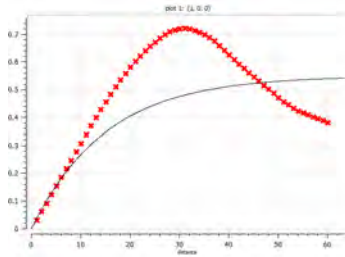


Figure 10: x direction.

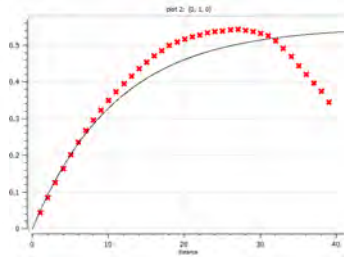


Figure 11: y direction.

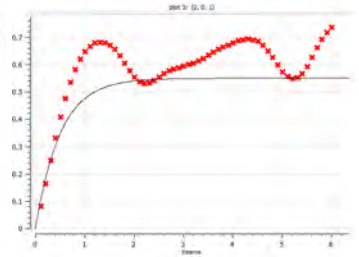


Figure 12: z direction.

Figure S3.

Porosity, dip, and azimuth parameter fields for selected realizations. The model domain dimensions are $X \times Y \times Z = 200 \times 70 \times 10$ m.

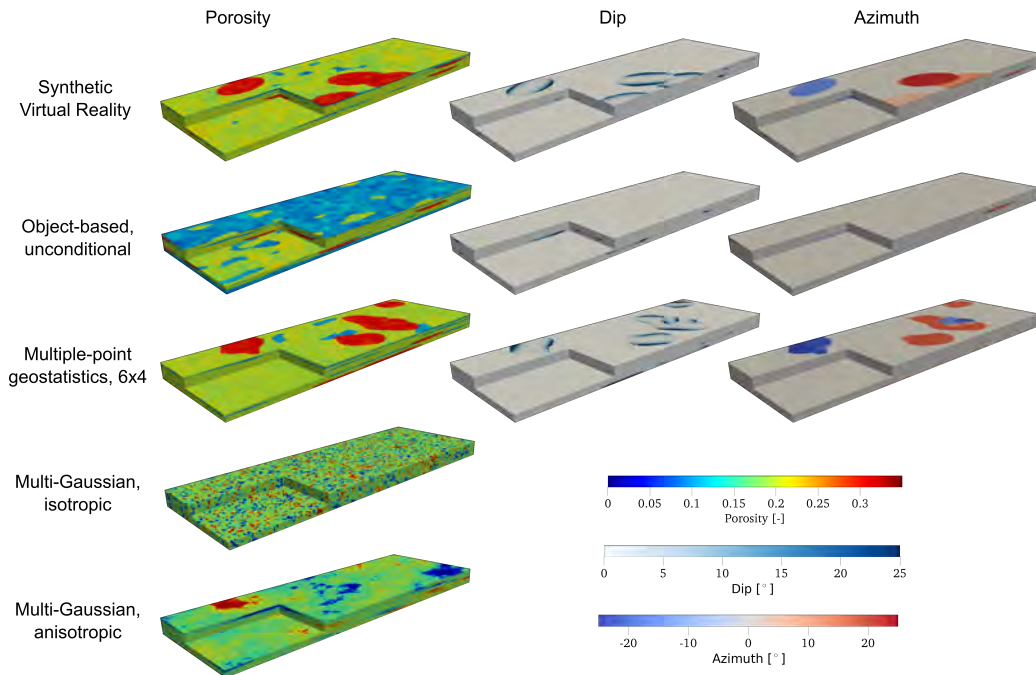
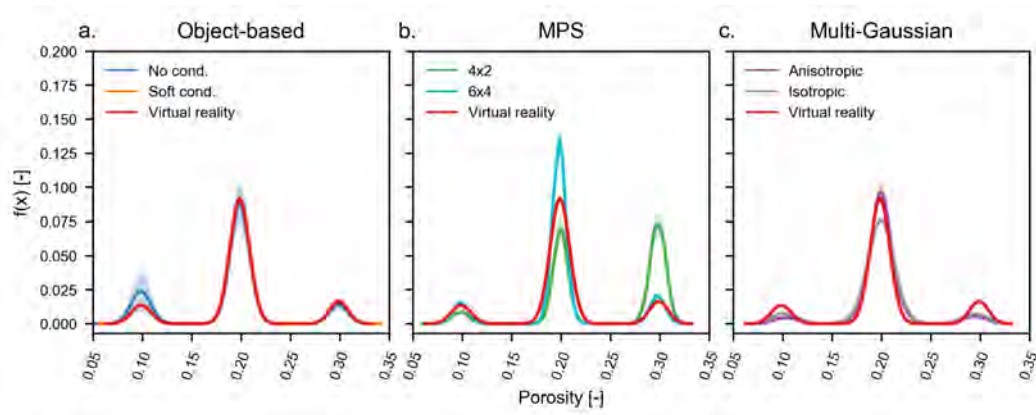


Figure S4.

Probability distribution functions of porosity parameter field ensembles. The solid line represents the mean value and the shading represents the 5-95 percentiles.



Input File S1.

Hydrogeological Virtual Realities (HyVR) simulation package input file for generating the synthetic virtual reality. See *Bennett et al.* [2018] or the HyVR technical documentation (driftingtides.github.io/hyvr/inout.html) for further details.

braid.vr.ini

```
[run]
runname = braid_vr
numsim = 1
dataoutputs = [vtr, h5]
flag_ow = true
anisotropy = true
het = true

[model]
dx = 1
dy = 1
dz = 0.1
lx = 200
ly = 70
lz = 10
periodic = false
hetlev = internal

[strata]
ssm = [braid]
ssm_top = [10]
ssm_contact = random
ssm_contact_model = [0.0,12,6]
ae = [spf, sheet]
ssm_ae = [[spf, sheet]]
ae_prob = [[0.6, 0.4]]
ae_z_mean = [[1.5, 0.5]]
avul_prob = [[0.3]]
avul = [[0.2, 0.4]]
bg = [0, 0, 0]
ae_table = braid_vr_aelu.txt

[spf]
geometry = trunc_ellip
structure = bulb
agg = 0.3
contact = random
contact_model = [0.05,12,6]
el_z = 1e-4
buffer = 0.2
length = 40
width = 25
depth = 1.7
paleoflow = [-25, 25]
dip = [0, 25]
azimuth = [-25, 25]
facies = [1]
dipset_d = 1.5
bulbset_d = 1.5
bg = [2, 0, 0]

[sheet]
geometry = sheet
structure = massive
contact = random
contact_model = [0.05,12,6]
facies = [0]
lens_thickness = -1

[hydraulics]
```

```

flag_gen = true
hydro = [BG, OWBM, HG]
k_h = [1e-5, 1e-2, 1e-4]
sig_y = [1, 1, 1]
n = [0.10, 0.30, 0.20]
sig_n = [1e-4, 1e-4, 1e-4]
ycorlengths = [[3,3,0.3], [3,3,0.3], [3,3,0.3]]
k_ratio = [1, 10, 6]
ncorlengths = [[3,3,0.3], [3,3,0.3], [3,3,0.3]]

[flowtrans]
kw_q_in = 1e-5
flow_tol = 1e-6
flag_2part = false
flag_rw = false
at = 1e-3
dp = 1e-9
flag_sf = false
flag_2paraview = false
flag_plotconcs = false
pt_particle_spacing = 0.1
pt_nxs = 100
flag_pt_printstatus = false

```

Input File S2.

Input file for generating multiple-point geostatistical simulations conditioned to 6×4 borehole data using DeeSse. See *Straubhaar* [2017] for further details.

6x4.in

```

200 70 100
1.0 1.0 0.1
0.0 0.0 0.0
5
poros 1 %.3e
lnK 1 %.3e
fac 1 %.3e
dip 1 %.3e
azim 1 %.3e
OUTPUT_SIM_ONE_FILE_PER_REALIZATION
6x4
// OUTPUT REPORT
//
1
test_report.txt
1
../braid_ti.gslib
0
1
braid_vr_6x4.gslib
0
0
0
-1 //0.05
NORMALIZING_LINEAR
-1.0 -1.0 -1.0
1.0 1.0 1.0
0.0 0.0 0.0
0.0
-1.0 -1.0 -1.0
1.0 1.0 1.0
0.0 0.0 0.0

```

```
0.0
-1.0 -1.0 -1.0
1.0 1.0 1.0
0.0 0.0 0.0
0.0
-1.0 -1.0 -1.0
1.0 1.0 1.0
0.0 0.0 0.0
0.0
-1.0 -1.0 -1.0
1.0 1.0 1.0
0.0 0.0 0.0
0.0
24
24
24
24
24
1.0
1.0
1.0
1.0
1.0
0
0
0
0
0
2
2
0
2
2
1.0
1.0
1.0
1.0
1.0
SIM_ONE_BY_ONE
PATH_RANDOM
0.03
0.03
0.03
0.03
0.03
0
0
0
0
0
0
0
0
0
0
0
0.25
0.0
1
POST_PROCESSING_PARAMETERS_DEFAULT
2
2 2 2
2 2 2
PYRAMID_SIM_HIERARCHICAL_USING_EXPANSION
PYRAMID_ADAPTING_FACTOR_DEFAULT
PYRAMID_ADAPTING_FACTOR_DEFAULT
2
PYRAMID_CONTINUOUS
2
PYRAMID_CONTINUOUS
```

```
2
PYRAMID_CATEGORICAL_AUTO
2
PYRAMID_CONTINUOUS
2
PYRAMID_CONTINUOUS
// SEED NUMBER AND SEED INCREMENT
1234
1
// NUMBER OF REALIZATIONS
20
END
```

References

- Bennett, J. P., C. P. Haslauer, M. Ross, and O. A. Cirpka (2018), An open, object-based framework for generating anisotropy in sedimentary subsurface models, *Groundwater*, doi:10.1111/gwat.12803.
- Straubhaar, J. (2017), DeeSse User's Guide, *Tech. rep.*, University of Neuchâtel, Neuchâtel, Switzerland.

B Technical Documentation

HyVR Documentation

Release 0.2

Jeremy Bennett

Aug 23, 2018

Contents

1	Introduction	2
1.1	Installing the HyVR package	2
1.2	Usage	3
1.3	Source	4
1.4	Requirements	4
1.5	Development	5
1.6	Problems, Bugs, Unclear Documentation	5
2	HyVR Computational methods	5
2.1	Simulation of strata and architectural element contact surfaces	6
2.2	Simulation of hydrofacies assemblages and hydrofacies geometries	6
2.3	Simulation of hydraulic parameters	12
3	HyVR inputs and outputs	13
3.1	The <code>.ini</code> configuration file	13
3.2	Model setup sections	13
3.3	[<code>hydraulics</code>] section	18
3.4	[<code>flowtrans</code>] section	19
3.5	HyVR outputs	19
4	HyVR Example	20
5	Extending HyVR	22
5.1	Adding more geometries	22
5.2	The HyVR wish list	22
6	Troubleshooting	23
6.1	Installation	23

7	Changelog/Bug Fixes	24
7.1	HyVR 0.2.3	24
7.2	HyVR 0.2.2	24
7.3	HyVR 0.2.1	25
7.4	HyVR 0.2	25
	Bibliography	26

1 Introduction

HyVR: Turning your geofantasy into reality!

The Hydrogeological Virtual Reality simulation package (HyVR) is a Python module that helps researchers and practitioners generate subsurface models with multiple scales of heterogeneity that are based on geological concepts. The simulation outputs can then be used to explore groundwater flow and solute transport behaviour. This is facilitated by HyVR outputs in common flow simulation packages' input formats. As each site is unique, HyVR has been designed that users can take the code and extend it to suit their particular simulation needs.

The original motivation for HyVR was the lack of tools for modelling sedimentary deposits that include bedding structure model outputs (i.e., dip and azimuth). Such bedding parameters were required to approximate full hydraulic-conductivity tensors for groundwater flow modelling. HyVR is able to simulate these bedding parameters and generate spatially distributed parameter fields, including full hydraulic-conductivity tensors. More information about HyVR is available in the online [technical documentation](#).

I hope you enjoy using HyVR much more than I enjoyed putting it together! I look forward to seeing what kind of funky fields you created in the course of your work.

HyVR can be attributed by citing the following journal article: Bennett, J. P., Haslauer, C. P., Ross, M., & Cirpka, O. A. (2018). An open, object-based framework for generating anisotropy in sedimentary subsurface models. Groundwater. DOI: [10.1111/gwat.12803](https://doi.org/10.1111/gwat.12803). A preprint version of the article is available [here](#).

1.1 Installing the HyVR package

Installing Python

Windows

If you are using Windows, we recommend installing the [Anaconda distribution](#) of Python 3. This distribution has the majority of dependencies that HyVR requires.

It is also a good idea to install the HyVR package into a [virtual environment](#). Do this by opening a command prompt window and typing the following:

```
conda create --name hyvr_env
```

You need to then activate this environment:

```
conda activate hyvr_env
```

Linux

Depending on your preferences you can either use the Anaconda/Miniconda distribution of python, or the version of your package manager. If you choose the former, follow the same steps as for Windows.

If you choose the latter, you probably already have Python 3 installed. If not, you can install it using your package manager (e.g. `apt` on Ubuntu/Debian).

In any way we recommend using a virtual environment. Non-conda users can use [virtualenvwrapper](#) or [pipenv](#).

Installing HyVR

Once you have activated your virtual environment, you can install HyVR from PyPI using `pip`:

```
pip install hyvr
```

The version on PyPI should always be up to date. If it's not, you can also install HyVR from [github](#):

```
git clone https://github.com/driftingtides/hyvr.git
pip install hyvr
```

Installation from conda-forge will (hopefully) be coming soon.

1.2 Usage

To use HyVR you have to create a configuration file with your settings. You can then run HyVR the following way:

```
(hyvr_env) $ python -m hyvr my_configfile.ini
```

HyVR will then run and store all results in a subdirectory. If no configfile is given, it will run a test case instead:

```
(hyvr_env) $ python -m hyvr
```

If you want to use HyVR in a script, you can import it and use the `run` function:

```
import hyvr
hyvr.run('my_configfile.ini')
```

Examples can be found in the `testcases` directory of the [github repository](#), the general setup and possible options of the config-file are described in the documentation.

1.3 Source

The most current version of HyVR will be available at this [github repository](#); a version will also be available on the [PyPI index](#) which can be installed using `pip`.

1.4 Requirements

Python

HyVR was developed for use with Python 3.4 or greater. It may be possible to use with earlier versions of Python 3, however this has not been tested.

Dependencies

- `scipy = 1.0.0`
- `pandas = 0.21.0`
- `numpy <= 1.13.3`
- `matplotlib <= 2.1.0`
- `flopy == 3.2.9` (optional for modflow output)
- `pyevtk = 1.1.0`
- `h5py` (optional for HDF5 output)

1.5 Development

You can contact the developer(s) of HyVR by [email](#). HyVR is currently being developed by Jeremy Bennett ([website](#)) as part of his doctoral research at the University of Tübingen.


1.6 Problems, Bugs, Unclear Documentation

If you have problems with HyVR have a look at the [troubleshooting](#) section. If this doesn't help, don't hesitate to contact us via email or at github.

If you find that the documentation is unclear, lacking, or wrong, please also contact us.

2 HyVR Computational methods

The first step in the HyVR algorithm is to load the model parameters, as defined in the `*.ini` initialisation file. Major strata contact surfaces are generated first. Architectural element contact surfaces are then simulated within each stratum, either based on input parameters or loaded from a user-defined lookup table of mean contact surface depths. The external and internal geometries of hydrofacies assemblages and associated hydrofacies are then simulated within each architectural element. Finally, microstructure within the features is simulated.



<i>Hierarchical scale</i>	<i>Example feature</i>	<i>Lateral extent</i>
Major strata/ contacts	<ul style="list-style-type: none">◦ Glacial◦ Fluvial	10^2 to 10^4 m
Architectural elements	<ul style="list-style-type: none">◦ Channels◦ Scour-pool fills◦ Gravel and sand bars	10^1 to 10^3 m
Hydrofacies assemblages	<ul style="list-style-type: none">◦ Hydraulically distinct zones	10^0 to 10^2 m
Hydrofacies	<ul style="list-style-type: none">◦ Openwork gravel◦ Sandy silt◦ Massive sand	10^{-1} to 10^1 m
Microstructure	<ul style="list-style-type: none">◦ Hydraulic conductivity◦ Porosity	10^{-3} to 10^{-1} m

Fig. 1: *Hierarchical modeling framework implemented in HyVR.*

Note that in this section model input parameters are denoted in the following manner: parameter-section.parameter.

2.1 Simulation of strata and architectural element contact surfaces

Strata are defined in the input parameter file by their upper mean elevations and the architectural elements that are to be included within them. The upper contact surface is then generated and all model cells between the lower and upper contact surface are assigned to the stratum.

Contact surfaces can either be flat or random. Multi-Gaussian random contact surfaces are generated using the spectral methods outlined by [DN93]. These methods require structural statistical parameters (i.e. mean and variance) for the quantity of interest, and a geostatistical covariance model. We used a Gaussian covariance model in the present study to produce smoothly varying surfaces:

$$R_{ss}(h) = \sigma_s^2 \exp \left[- \left[\frac{\Delta x}{\lambda} \right]^2 \right]$$

where s is the random quantity of interest, σ_s^2 is the variance of s (here elevation), Δx is the distance between the two points, and λ is the correlation length.

Simulation at the architectural element hierarchical level begins once all strata units have been assigned. Architectural elements are defined using a lookup table with the following information:

Architectural element identifier
Mean bottom elevation
Mean top elevation
Architectural element type
Strata identifier

If the architectural element lookup table is not defined before initialising the simulation, then the architectural elements will be simulated based on input parameters defined for each stratum. This starts with the random choice of an architectural element from those defined; the probability of each architectural element being chosen is also defined in the input parameter file. The thickness of the architectural element is then drawn from a random normal distribution that is defined for each stratum in the input parameter file. To account for the erosive nature of many sedimentary environments the algorithm may erode the underlying units: here the ‘avulsion’ thickness $th_{avulsion}$ is subtracted from the bottom and top of the architectural element $z_{AE}^{bot}, z_{AE}^{top}$. Once the architectural element lookup table has been defined, contact surfaces are generated using the same procedure as used for strata contact surfaces. When the architectural element have been generated, the algorithm begins to simulate external hydrofacies assemblage geometries and hydrofacies.

2.2 Simulation of hydrofacies assemblages and hydrofacies geometries

The generation of hydrofacies assemblages and internal hydrofacies occurs stratum- and architectural-element-wise, beginning with the lowest architectural element in the lowest stratum. The simulation of individual hydrofacies assemblages is object-based, with random placement of

features within the architectural element. Object-based methods have been implemented widely in subsurface simulation [JSD94][BHC17] as they are generally computationally efficient and relatively easy to parameterize. The HyVR program approximates hydrofacies assemblages with simple geometric shapes. Currently, three *shapes* are supported: truncated ellipsoids, extruded parabolas, and sheets. Truncated ellipsoids and extruded parabolas are ‘erosive’ hydrofacies assemblages: this means that within the HyVR algorithm they are able to erode underlying units, and therefore the architectural element (and strata) boundaries may be altered during the course of the simulation.

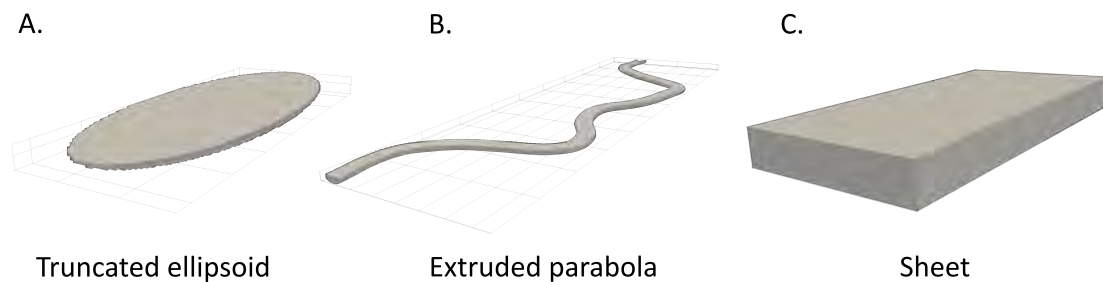


Fig. 2: Geometries implemented in HyVR.

Four properties are assigned to each model grid cell during this simulation step: *ae*, *ha_arr*, *hat_arr*, *facies*, *azimuth*, and *dip*. The *ae* property denotes which architectural element (from `strata.ae`) has been assigned to a model grid cell. The *ha_arr* property is the unique identifier for each individual hydrofacies assemblage generated. *hat_arr* denotes the type of hydrofacies assemblage within the model grid cell is located. The *facies* property denotes which hydrofacies has been assigned to a model grid cell. The *azimuth* κ and *dip* ψ properties are associated with the bedding structure at each model grid cell and denote the angle of the bedding plane from the mean direction of flow and horizontal, respectively.

Truncated ellipsoids

Truncated ellipsoids are generated as a proxy for trough-like features. The method for generating the boundaries of these features has been described previously in [BHC17]. Generation starts at $z_{AEunit}^{bot} + AE_{depth} \cdot \beta$ where AE_{depth} is the depth of the truncated ellipsoid geometry, and β is a buffer term that allows the user to control how much of the underlying unit is eroded. The centre of the truncated ellipsoid (x, y coordinates) and the paleoflow angle α (i.e. major ellipsoid axis orientation) are drawn from a random uniform distribution and the boundary of the truncated ellipsoid is simulated. The *internal structure* of truncated ellipsoids can be defined in the following ways:

- trough-wise homogeneous, with constant azimuth and dip;
- bulb-dip, with azimuth and dip values based on the three-dimensional gradient at the ellipsoid boundary (‘bulb dip’);

- bulb-sets, comprising nested alternating hydrofacies with κ and ψ values generated as for bulb-type;
- dip-sets internal structure, where the features have a constant κ and ψ but the assigned hydrofacies alternate throughout the truncated ellipsoid.

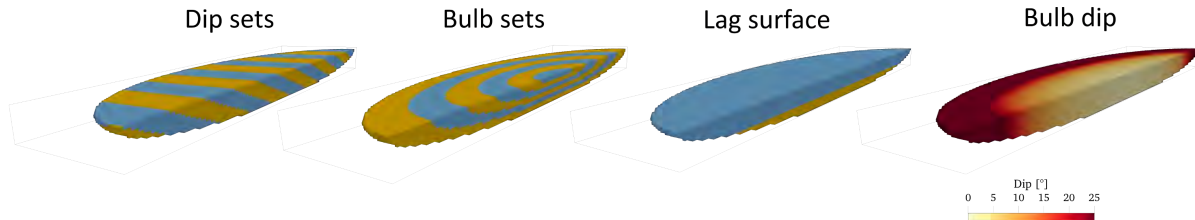


Fig. 3: *Internal structure of truncated ellipsoid hydrofacies assemblages.*

Once a truncated ellipsoid has been generated, an aggradation thickness (`trunc_ellip.agg`) is added to the current simulation elevation z_{sim} and the next assemblage is simulated. This occurs until $z_{sim} = z_{AE}^{top}$.

Bulb dip

Bulb hydrofacies assemblages is simulated by calculating the three-dimensional gradient at the boundary of the truncated ellipsoid and then the angle between the gradient and a horizontal plane. This angle is then compared with a ‘maximum dip angle’ (`dip`) and the smaller of these two values is assigned to all model grid cells within the hydrofacies assemblage with equivalent x, y -coordinates (i.e. column-wise).

Bulb sets

Nested-bulb-like layers are simulated by subdividing the depth of the truncated ellipsoid into a series with a set thickness `trunc_ellip.bulbset_d`. Truncated ellipsoids are simulated consecutively with the same center point and paleoflow α value, starting with the deepest assemblage. With each simulation, a scaling factor is calculated by dividing the new depth with the total depth of the assemblage. This scaling factor is applied to the length and width parameters of the truncated ellipsoid. Each newly generated ellipsoid subsumes the previous. Each nested assemblage represents a constant hydrofacies, however the orientation of these hydrofacies may differ within the entire hydrofacies assemblage, to create bulb-like features that have been reported in the field. The dip of the nested ellipsoids defaults to that determined by the three-dimension gradient at the nested-ellipsoid boundary.

Dip sets

Refer to *dipset section*.

Extruded parabolas

Parabolas extruded along arbitrary curves with variable sinuosity are useful to represent channels. Extruded parabola centerlines in HyVR are parameterized using the disturbed periodic model implemented by [Fer76]:

$$\theta + \frac{2h}{k} \frac{d\theta}{ds} + \frac{1}{k^2} \frac{d^2\theta}{ds^2} = \epsilon(s)$$

with curve direction θ , damping factor $h \in [0, 1]$, $k = 2\pi/\lambda$ is the wavenumber with λ the frequency of the undamped sine wave, and s is the distance along the curve. This model can be approximated using the following second-order autoregressive model described in Equation 15 of [Fer76]:

$$\theta_i - b_1\theta_{i-1} - b_2\theta_i - 2 = \epsilon_i$$

with:

$$b_1 = 2e^{-kh} \cos(k \arcsin(h))$$
$$b_2 = -e^{-2kh}$$

This method was also used by [PBD09] for the simulation of alluvial depositional features. Model grid cells are assigned to the extruded parabola if the following conditions are met:

$$D^2 \leq \frac{w_{ch}^2}{4} - \left[\frac{(z_{ch} - z_{cell}) \cdot \Delta z \cdot w_{ch}}{d_{ch}} \right]^2 \wedge z_{cell} \leq z_{ch}$$

where D^2 is the two-dimensional (x, y) distance from the cell to the extruded parabola centerline, w_{ch} and d_{ch} are the extruded parabola width and depth respectively, z_{ch} and z_{cell} are the elevations of the extruded parabola top and node respectively, and Δz is the model grid cell z dimension. Two-dimensional ‘channel velocities’ \vec{v} are evaluated at the centerline and then interpolated to grid cells using an inverse-distance-weighted interpolation. Azimuth values are calculated by taking the arctangent of the two-dimensional channel velocity at a given point. Dip values of grid cells within the extruded parabola are assigned based on input parameters. If alternating hydrofacies are to be simulated they are constructed by creating planes that are evenly spaced along the extruded parabola centerline.

The HyVR algorithm generates extruded parabolas starting from $z_{AEunit}^{bot} + AE_{depth} \cdot \beta$, as for truncated ellipsoids. However, to account for the multiple extruded parabolas that are often concurrently present in many river systems, multiple extruded parabolas can be generated at each simulation depth (`ext_par.channel_no`). The starting x, y coordinates for the centerlines are drawn from a random uniform distribution such that $x \in [-50, 0]$ and $y \in [0, Y]$. Extruded parabola geometries are then assigned sequentially to the model grid cells; note that in HyVR there is no interaction of extruded parabolas, and subsequent extruded parabolas will supersede (or ‘erode’) those previously generated. Once the predefined number of extruded parabolas stipulated by `ext_par.channel_no` has been simulated a three-dimensional migration vector `ext_par.mig` is added to the extruded parabola centerlines and the extruded parabola assignment to model grid cells begins again. The reuse of the extruded parabola centerline trajectories is more efficient than re-simulating these values at each z_{sim} . This continues until $z_{sim} = z_{seq}^{top}$.

Sheets

Sheets are comparatively simple to generate as they are laterally continuous across the entire model domain (depending on strata boundaries). The internal structure of sheet features may be massive (i.e. without internal structure), or laminations can be generated. In the HyVR algorithm laminations are simulated sequentially by assigning all model grid cells between a specific elevation interval the appropriate hydrofacies codes. Dipping set structures can also be incorporated into these features. Sheets may differ in internal orientation, as specified in the input parameters.

Internal structure

The internal structure of the hydrofacies assemblages is distinguished by hydrofacies. The internal structure of an hydrofacies assemblage may be homogeneous, dipping or ellipsoidal (for truncated ellipsoid only). Additionally, lag surfaces composed of different hydrofacies may be simulated in erosive (i.e. extruded parabola, truncated ellipsoid) hydrofacies assemblage.

Dipset

Architectural elements may be populated with dipping hydrofacies structures. Such structures are generated by creating planes at regular intervals throughout the architectural element, as defined by `element.dipset_d`. In truncated ellipsoids the planes are constructed along the centerline of the element, perpendicular to the paleoflow angle α . In extruded parabola elements, the planes are constructed along the centerline and are perpendicular to $\vec{v}(x)$. The distance from the centre of each model grid cell to all planes is calculated and then the model grid cells between planes are assigned a hydrofacies value.

Lag surfaces

Lag surfaces can be set for erosive hydrofacies assemblages by setting the `element.lag` parameter. This parameter consists of two values:

- The thickness of the lag surface from the element base; and
- The hydrofacies identifier to be assigned.

Lag surfaces cannot have any internal dipping structure.

Alternating hydrofacies

Sedimentary deposits can often exhibit cyclicity in their features; therefore, HyVR allows alternating hydrofacies to be simulated. This is controlled by sequentially assigning hydrofacies

within each hydrofacies assemblage, starting with a hydrofacies randomly selected from those to be simulated in the architectural element (`element.facies`). The hydrofacies which is assigned next is drawn from a subset of hydrofacies specified in the `element.altfacies` input parameter. For each hydrofacies in `element.facies`, a list of alternating hydrofacies (i.e., which hydrofacies can follow the present one) is stipulated. By only specifying one hydrofacies ID in the `element.altfacies`, it guarantees that that ID will be selected. The figure below gives three examples of different input parameters.

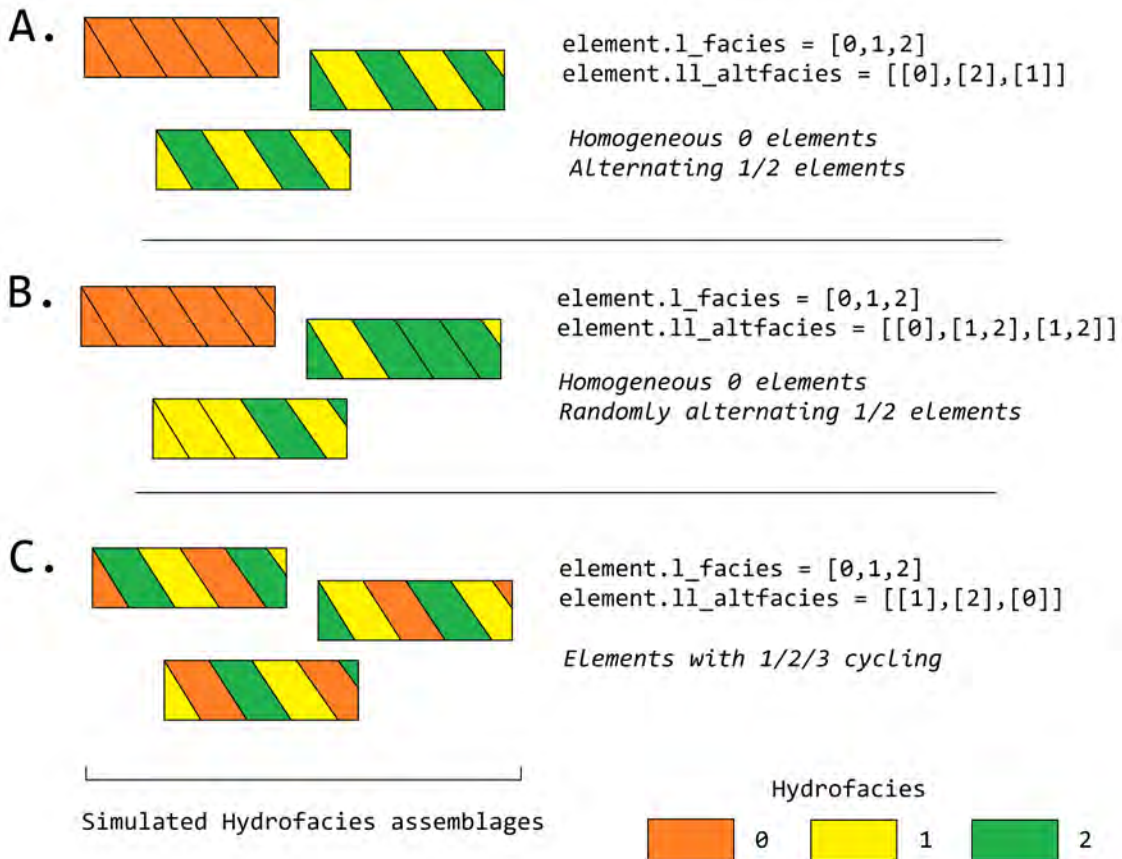


Fig. 4: Variations on alternating hydrofacies in architectural elements

Linear trends

The HyVR algorithm allows for linear trends in geometry sizes with increasing elevation by setting the `element.geo_ztrend` parameter. This parameter comprises a bottom and top factor ξ_{bottom}, ξ_{top} that multiply the usual geometry dimensions. For intermediate elevations the z factor is calculated through a linear interpolation of ξ_{bottom}, ξ_{top} . The parameters of each geometry may be set for each individual architectural element included in the model parameter file.

2.3 Simulation of hydraulic parameters

Hydraulic parameters are simulated once all features have been generated. The distributed hydraulic parameter outputs of HyVR are: the isotropic hydraulic conductivity $K_{iso}(x, y, z)$; porosity $\theta(x, y, z)$; and the full hydraulic conductivity tensor $\mathbf{K}(x, y, z)$, defined for each model grid cell.

Microstructure of hydraulic parameters is first simulated for each individual hydrofacies assemblage (as present in the `mat` storage array) simulated in the previous steps. Spatially varying $\ln(K_{iso})$ and θ fields are generated for each hydrofacies present in an hydrofacies assemblage using spectral methods to simulate random multi-Gaussian fields with an exponential covariance model:

$$R_{ss}(h) = \sigma_s^2 \exp \left[- \left| \frac{\Delta x}{\lambda} \right| \right]$$

An anisotropic ratio is also assigned to each model grid cell according to the hydrofacies present; these ratios are globally constant for each hydrofacies.

Microstructure may also be assigned to model grid cells that are not within hydrofacies assemblage. This background heterogeneity is simulated for each architectural element using values defined for each architectural element type (`element.bg`). Simulation methods are the same as for within-assemblage heterogeneity.

Spatial trends may also be applied once isotropic hydraulic-conductivity values have been assigned to all model grid cells. As for trends in hydrofacies assemblage geometry, trends are assigned using a linearly-interpolated factor ξ_{start}, ξ_{end} in the x - and/or z -directions. The value of each model grid cell is then multiplied by the trend factors.

Hydraulic-conductivity tensors

Full hydraulic-conductivity tensors for each model grid cell are calculated by multiplying the isotropic hydraulic conductivity K^{iso} , with a rotated anisotropy matrix \mathbf{M} :

$$\mathbf{K}_i = K_i^{iso} \mathbf{R}_i \mathbf{M}_i \mathbf{R}_i^T$$

$$\mathbf{R}_i = \begin{bmatrix} \cos(\kappa_i) \cos(\psi_i) & \sin(\kappa_i) & \cos(\kappa_i) \sin(\psi_i) \\ -\sin(\kappa_i) \cos(\psi_i) & \cos(\kappa_i) & -\sin(\kappa_i) \sin(\psi_i) \\ -\sin(\psi_i) & 0 & \cos(\psi_i) \end{bmatrix}$$

Parameters ψ_i and κ_i are the simulated bedding structures (dip and azimuth, respectively). The anisotropy matrix \mathbf{M}_i is diagonal with lateral terms set as equivalent (i.e. $K_{xx} = K_{yy}$). This approach is identical to that of [BHC17]. Once this has been completed, the simulated parameter files are saved and can be used for groundwater flow and solute transport simulations.

3 HyVR inputs and outputs

3.1 The .ini configuration file

The key piece of information required by HyVR is the parameter file. This is an `.ini` configuration file that contains all the parameters required to run a HyVR simulation.

The parameter file is separated into sections denoted by headers surrounded by brackets (e.g. `[section_name]`). Parameters (or keys) and their associated values are then stipulated using the equals sign (e.g. `key = value`). Each key is associated with the section in which it is located. Section and variable names should be in lower case. String values do not require quotation marks in `.ini` files.

In HyVR the following sections are necessary:

- `[run]` - This contains parameters related to the model run.
- `[model]` - This contains details about the model dimensions
- `[strata]` - In this section the strata parameters are set.
- `[*architectural_elements*]` - Each architectural element to be simulated in HyVR is included in its own section. Please see the subsection below for more information.
- `[hydraulics]` - This section includes information for setting the hydraulic properties of simulated features.

An additional section `[flowtrans]` is included in some parameter files - this section included parameters used in groundwater flow and solute transport simulation packages not implemented in HyVR. `.ini` files are readable by a range of programming languages so the user can also store and read flow and transport parameters from the configuration file.

3.2 Model setup sections

`[run]` section

This section contains general sections how the program should be run. It controls where outputs are stored and which kind of output files are generated, what kind of parameters are generated and how many realisations are generated.

HyVR simulations are structured in the following way:

Model -> Run -> Realisation

Typically we assume that the `.ini` file is stored in a model directory:

```
mymodel/  
|-- myconfig.ini
```

When HyVR is run with this parameter file, it will create a run directory. The name of the run directory can be set with the `runname` option, e.g. to `myrun`. HyVR then stores a copy of the `.ini` file inside the run directory under the name `myrun_autogenerated_backup.ini`. If `runname` is not given, the filename of the ini-file without `.ini` will be used. If you are only running one realization, the output of this realization is also stored directly in this directory:

```
mymodel/
|-- myconfig.ini
|-- myrun/
|   |-- myrun_autogenerated_backup.ini
|   |-- myrun_hyvr.dat
|   |-- myrun_hyvr.vtk
|   |...
```

If you are running multiple realizations, HyVR creates a subdirectory for each realization output:

```
mymodel/
|-- myconfig.ini
|-- myrun/
|   |-- myrun_autogenerated_backup.ini
|   |-- real_001/
|       |-- myrun_real_001_hyvr.dat
|       |-- myrun_real_001_hyvr.vtk
|   |-- real_002/
|       |-- myrun_real_002_hyvr.dat
|       |-- myrun_real_002_hyvr.vtk
|   |...
```

ATTENTION: If the name of the ini-file ends with `_autogenerated_backup.ini` we assume the file was created automatically and is already in the run directory. In this case the model directory will default to the directory above the directory of the ini-file and the run directory will be the directory of the ini-file. Also, if the `runname` is not given in the ini-file, the part before `_autogenerated_backup.ini` will be chosen as `runname`.

Example: If you run the file `myrun_autogenerated_backup.ini` in the example above, the run directory will be `myrun` and the `runname` will default to `myrun` if it is not given.

For every run, HyVR needs to have a empty run directory. This can either be accomplished by changing the `runname` in the config file, or you can either run HyVR with the `--overwrite` option or add `flag_ow=1` in the config file to automatically remove the old run directory.

ATTENTION: Setting `flag_ow=1` or using `--overwrite` will delete everything from the run directory before running HyVR.

The following settings are possible in the run section:

- `runname`: (*optional*) Name of the model simulation run. Defaults to the name of the ini-file without the last for characters (`.ini`)

- `numsim`: (*optional, default: 1*) Number of realisations to be generated.
- `dataoutputs`: (*optional*) List of simulation output data formats (see *Model outputs*), e.g. `[vtk, mat, py]`
- `modeloutputs`: (*optional*) List of simulation output formats for model input (see *Model outputs*), e.g. `[mf, hgs]`
- `flag_ow`: (*optional, default: true*) Whether to overwrite previous model results. If `true` (*default*) and the run directory already exists, all previous content in the run directory is deleted. If `false`, HyVR will check if the directory already exists and will ask you to change the runname in case it exists.
- `anisotropy`: (*optional, default: true*) Generate anisotropy parameters?
- `het`: (*optional, default: true*) Generate heterogeneity?

[model] section

- `dx, dy, dz`: (*required/optional*) Model grid cell dimensions. If `dy` or `dz` are not given, `dx` will be used instead.
- `lx, ly, lz`: (*required*) Model domain dimensions.
- `periodic`: (*optional, default: false*) Periodic model domain? (Sheets/truncated ellipsoids only)
- `display`: (*optional, default: false*) ‘Display’-type simulation? If this flag is set to `true`, the simulated architectural elements are centred in the model domain so they can be viewed easily.
- `hetlev`: (*required*) Hierarchical level at which heterogeneity should be simulated. Can be `ae`, `facies` or `internal`

[strata] section

- `ssm`: (*required*) List of sequence names. This should be a list of strings.
- `ssm_top`: (*required*) List of mean strata contact elevations. This should be a list of floats of the same length as `ssm`.
- `ssm_contact_model`: (*required*) Statistical parameters for strata contact model. This can either be a list of floats of length 3, e.g. `[0.05, 6, 6]`, or a list of the same length as `ssm` of lists of floats of length 3, e.g. `[[0.05, 6, 6], [0.05, 5, 4], ...]`
- `ssm_contact`: (*optional, default: flat*) Contact surface type, either `flat`, `random`, or `user`
- `ae_table`: (*optional*) Relative filepath (starting from the `modedir`) for a architectural element lookup table.

- `ae`: List of architectural elements. This is a list of strings, which are the names of the [`*architectural_elements*`] sections below.
- `ssm_ae`: (*required*) Which architectural elements are in each stratum. This should be a list of lists of strings. The outer list must have the same length as `ssm`, the inner list can be of variable length. The elements of the inner lists must be strings from `ae`.
- `ae_prob`: (*required*) Probability of an architectural element occurring. This must be a list of lists of floats with the same shape as `ssm_ae`.
- `ae_z_mean`: (*required*) Mean thickness of architectural element unit. This must be a list of lists of floats with the same shape as `ssm_ae`.
- `avul_prob`: (*required*) Probability of avulsion. List of floats with the same length as `ssm`.
- `avul`: (*required*) Avulsion depth range. List of lists of floats. The outer list must have the same length as `ssm`, the inner lists must be of length 2 and are the start and end point of the depth range.
- `bg`: (*optional*) Background parameters for unassigned cells in the architectural elements. This should be three float values: facies, azimuth, and dip background values.

[`element`] sections for architectural elements

Sections that describe architectural elements are entitled with an identifying name (e.g. [`sparse_scour`]). Note that section names should not include spaces. The first parameter to be set is the `geometry`. The current implementation of HyVR includes three geometries: truncated ellipsoids (`trunc_ellip`), channels (`channel`), and sheets (`sheet`).

Unless otherwise noted, ranges (`r_`) represent the lower and upper limits of uniform distributions from which values are randomly generated.

General [`*element`] parameters

- `geometry`: (*required*) Geometry of hydrofacies assemblages within architectural element, either `trunc_ellip`, `ext_par`, or `sheet`
- `structure`: (*required*) Internal structure of hydrofacies assemblages. This can be `massive` or `dip` and also `bulb`, `bulb_l`, or `random` for truncated ellipsoids.
- `contact`: (*required*) Type of bedding contact between element units. Either `flat` or `random`.
- `contact_model` (*required*) Statistical parameters for bedding contact model. This should be a list of floats of length 3.
- `facies`: (*required*) Hydrofacies included in hydrofacies assemblage. These are indices referring to [`hydraulics`].`hydro` (starting from 0).

- `altfacies`: (*optional*) Alternating facies specification. This is a list of lists where the outer list has the same length as `facies`.
- `bg`: (*optional*) Background parameters for unassigned cells in the architectural element. This should be three float values: facies, azimuth, and dip background values.
- `geo_ztrend`: (*optional*) Linear trend in geometry sizes with elevation. Given as a percentage change multiplier in mean value from bottom to top of domain, i.e. $[\lambda_{bottom}, \lambda_{top}]$
- `k_ztrend`: (*optional*) Linear trend in isotropic hydraulic conductivity from bottom to top of domain $[\xi_{bottom}, \xi_{top}]$
- `k_xtrend`: (*optional*) Linear trend in isotropic hydraulic conductivity from model inlet to outlet $[\xi_{inlet}, \xi_{outlet}]$
- `n_ztrend`: (*optional*) Linear trend in porosity from bottom to top of domain $[\xi_{bottom}, \xi_{top}]$
- `n_xtrend`: (*optional*) Linear trend in porosity from model inlet to outlet $[\xi_{inlet}, \xi_{outlet}]$

Erosive element-specific parameters (truncated_ellipsoid, extruded parabola)

- `agg`: (*required*) Aggradation thickness added between each generation elevation.
- `buffer`: (*optional*) Buffer to reduce erosion of underlying units (see *methods*).
- `dipset_d`: (*optional*) Thickness of dipping internal structures.
- `migrate`: (*optional*) Lateral migration of ellipsoid centrepoints drawn from a random normal distribution, given as mean and variance in x and y directions $[\Delta x, \sigma_{\Delta x}^2, \Delta y, \sigma_{\Delta y}^2]$.
- `lag`: (*optional*) Parameters for lag surface [*lag thickness, hydrofacies ID*]
- `dip`: (*required*) Range of the uniform distribution from which the dip will be randomly drawn.

Truncated ellipsoid parameters

- `el_z`: (*required*) Number of elements to be simulated per simulation elevation and layer area
- `length, width, depth`: (*required*) Mean geometry of truncated ellipsoids
- `paleoflow`: (*required*) Range of the uniform distribution from which the paleoflow orientation will be randomly drawn.
- `azimuth`: (*required*) Range of the uniform distribution from which the azimuth will be randomly drawn.
- `bulbset_d`: (*optional*) Thickness of nested-bulb structures at the maximum depth of the truncated ellipsoid.

- `te_xyz`: (*optional*) List of 3D coordinated for manually setting the centrepoint of truncated ellipsoids. This should be a list of lists. The inner lists must have length 3.

Extruded parabola parameters

- `width, depth`: (*required*) Mean geometry of channel
- `h`: (*required*) Extruded parabola centreline curve shape parameter
- `k`: (*required*) Extruded parabola centreline curve shape wave number
- `ds`: (*required*) Distance between centreline points along trajectory
- `eps_factor`: (*required*) Variance of random fluctuations of channel centreline.
- `channel_no`: (*required*) Number of Extruded parabolas to generate at each elevation
- `dipset_d`: (*required*) Thickness of dipping internal structures.

Sheet parameters

- `lens_thickness` - Thickness of individual sheets. If set to `-1` then no individual sheets are generated within each sheet architectural element unit.

3.3 [hydraulics] section

The input parameters in this section are associated with the simulation of hydraulic parameters. It is also possible to only simulate the geometries of architectural elements and hydrofacies if required.

- `gen`: (*optional, default: true*) Generate hydraulic parameters (i.e. hydraulic conductivity)?
- `hydro`: (*required*) List of hydrofacies codes
- `k_h`: Mean horizontal hydraulic conductivity. This must be either a float if it is the same for all hydrofacies, or a list of the same length as `hydro`.
- `sig_y` - Variance of log hydraulic conductivity. This must be either a float if it is the same for all hydrofacies, or a list of the same length as `hydro`.
- `ycorlengths`: (*required*) Default correlation lengths for $\log(K_{iso})$ in each hydrofacies in x, y, z -directions. This can be either a single float, if it's the same in all directions for all hydrofacies, a list of floats of length 3 if it's the same for all hydrofacies, or a list of lists of floats, where the outer list has the same length as `hydro` and the inner lists have length 3
- `k_ratio`: (*required*) List of perpendicular anisotropy ratios (i.e. $\frac{K_h}{K_v}$) or single value if it's the same for all hydrofacies.
- `n`: (*required*) List of mean porosity values or single value if it's the same for all hydrofacies.

- `sig_n`: (*required*) Variance of porosity values. List of floats or single float if it's the same for all hydrofacies.
- `ncorlengths`: (*required*) Default correlation lengths for porosity in each hydrofacies in x, y, z -directions This can be either a single float, if it's the same in all directions for all hydrofacies, a list of floats of length 3 if it's the same for all hydrofacies, or a list of lists of floats, where the outer list has the same length as `hydro` and the inner lists have length 3

3.4 [flowtrans] section

This section contains parameters to be used for groundwater flow and solute transport simulations. This allows all input parameters for field generation and subsequent modelling to be stored in the same `.ini` file.

- `hin`: (*required*) boundary condition (head in). List of 3 floats
- `hout`: (*required*) boundary condition (head out). List of 3 floats

3.5 HyVR outputs

Parameter field outputs

Model outputs include three-dimensional fields with values at each model grid cell for the following parameters:

- **Strata** `ssm` - strata identifier
- **Architectural element** `ae` - architectural element identifier
- **Hydrofacies assemblage** `ha` - Unique identifiers for each hydrofacies assemblage generated
- **Hydrofacies assemblage type** `hat` - Type of hydrofacies assemblage generated
- **Hydrofacies** `fac` - Type of hydrofacies
- **Isotropic hydraulic conductivity** `k_iso`
- **Dip** `dip` - bedding parameter
- **Azimuth** `azim` - bedding parameter
- **Anisotropy ratio** `ani_rat`
- **Porosity** `poros`
- **Full hydraulic conductivity tensor** `ktensors` - based on isotropic hydraulic conductivity, dip, azimuth and anisotropy ratio (*methods*)

Output formats

HyVR has a number model outputs that can be set in the input parameter file. A copy of the `ini` model parameter file is saved in the model directory automatically. The following data output files include model outputs as three-dimensional arrays:

- `dat` : Python 'pickle' file - this is a native Python format that can be loaded into Python using `hyvr.utils.load_pickle()`.
- `mat` : MATLAB file
- `vtr` : VTK rectilinear grid file - this can be opened in ParaView for improved three-dimensional visualisation.
- `h5` : HDF5 format
- `npz` : Numpy compressed format

HyVR can also create files that can be used as model inputs for some flow and transport modelling packages. These currently include:

- `mf` : MODFLOW-2005 - `bas`, `dis`, `lpf`, `nam`, `oc`, and `pcg` model input files. Provided suitable flow and transport parameters are set in the `[flowtrans]` section of the input parameter file, this simulation can be executed.
- `mf6` : MODFLOW 6 - `dis`, `nam`, and `npf` model input files. A complete set of MODFLOW 6 input files cannot be generated in HyVR at this stage.
- `hgs` : HydroGeoSphere - K tensors and porosity at each grid node.

Note that these model inputs can only have regular model grids. They have not been tested for use in the above-named packages.

4 HyVR Example

Two examples are provided with the HyVR simulation module: the MADE site example (`made.ini`), mimicking the MADE site in Columbus, Mississippi, and a test case with user-defined architectural element mean contact surface elevations (`test_lu.ini`).

The MADE site example is described in more detail in the following article in *Groundwater*: Bennett, J. P., Haslauer, C. P., Ross, M., & Cirpka, O. A. (2018). An open, object-based framework for generating anisotropy in sedimentary subsurface models. *Groundwater*. DOI:10.1111/gwat.12803. A preprint version of the article is available [here](#).

The **parameter file** can be found on [github](#).

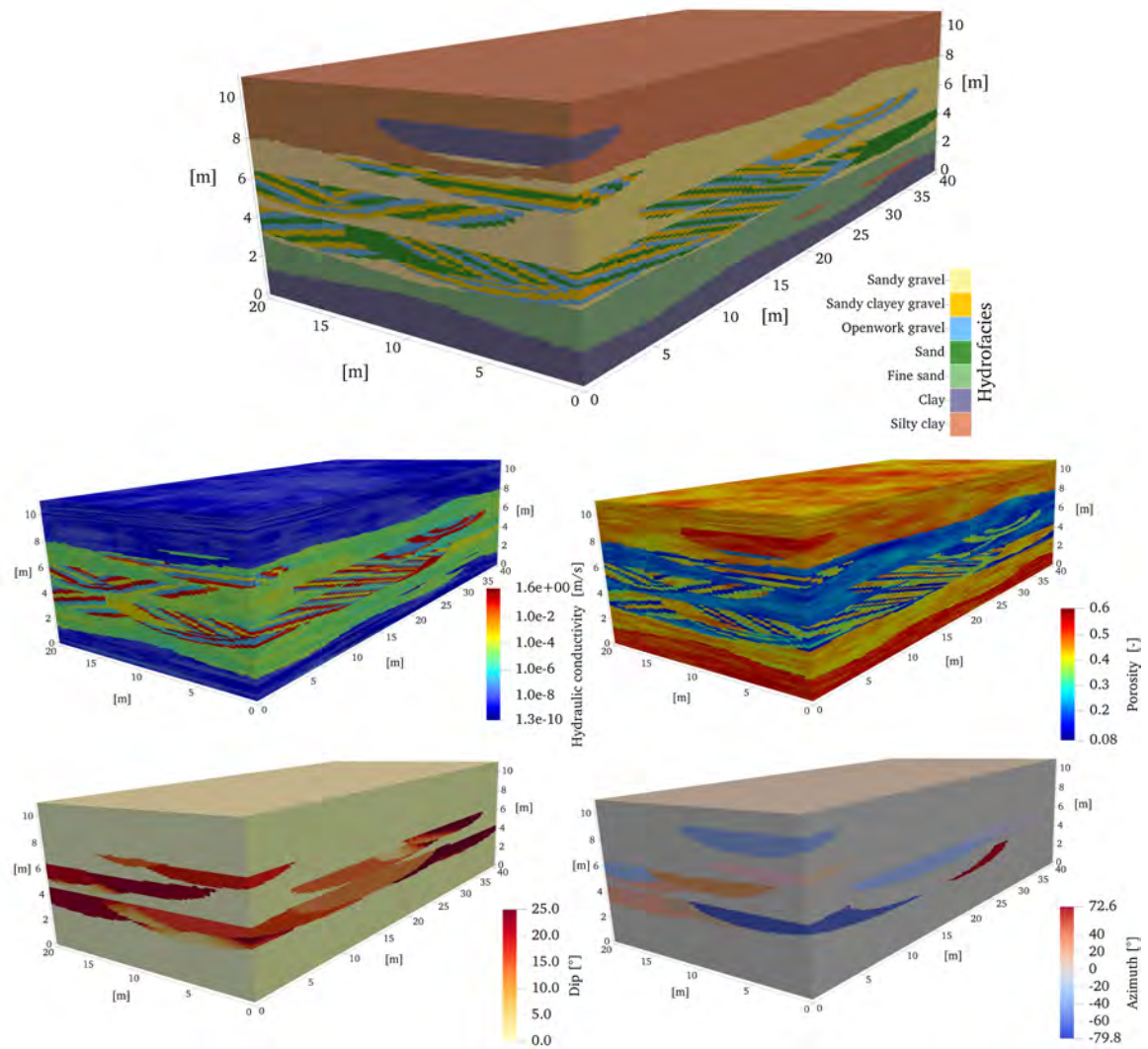


Fig. 5: Example field mimicking the MADE site, generated using HyVR.

5 Extending HyVR

The HyVR package is a work in progress. It has been implemented in Python in order to make it accessible for researchers, easily customisable, and hopefully somewhat easy to extend to suit the needs of future research. In this section I have included some tips on ways to extend the HyVR source code.

5.1 Adding more geometries

HyVR has been set up in such a way to facilitate the implementation of additional hydrofacies assemblage geometries.

In order to generate new types of geometries a new function needs to be written in the `hyvr` module that will be called from `hyvr.run()` where individual architectural elements and hydrofacies are simulated (around line 288 of `hyvr.run()` - search for `ADD_NEW GEOMETRIES HERE`).

Any new geometry function needs to return a `count` integer value (for keeping track of individual hydrofacies assemblage identifiers) and a `props` dictionary containing the following properties:

- `ha_array` (numpy array) - hydrofacies assemblages
- `hat_array` (numpy array) - types of hydrofacies assemblage
- `azim` (numpy array) - azimuth
- `dip` (numpy array) - dip
- `fac` (numpy array) - hydrofacies

When adding geometries, we suggest reviewing the code for the existing geometries to see how it is currently implemented. This should provide a reasonable idea of how to put a new geometry together.

5.2 The HyVR wish list

Any modelling project will have ‘areas for growth’ (as opposed to weaknesses). I have identified some things that I would like HyVR to have, but that are outside of the scope of my PhD research (and funds...). Perhaps you have the time and need to complete these yourself?

- Some level of conditioning, or improved interfacing with multiple-point geostatistical packages.
- Interaction of extruded parabolas, as well as more complex/realistic configurations of channel deposits (e.g. point bars).

- Utilities for deriving HyVR simulation parameters from transitional probability geostatistics.
- Simulation of chemofacies.

6 Troubleshooting

This section contains problems we encountered during testing and how we solved them. It might or might not help you. If you have problems that are not listed here, don't hesitate to contact us either via opening an issue in the github repository or via email. If you had problems that are not listed here but you solved them yourself, let us know anyway so we can either fix it or add the solution here.

6.1 Installation

```
ModuleNotFoundError: No module named 'numpy'

-----

Command "python setup.py egg_info" failed with error code 1 in <some_
↳path>/flopy/
```

This happens because in order to install flopy you need to have numpy installed first. Just install numpy and try again. In newer versions flopy will be an optional dependency, so this should not happen anymore.

```
ImportError: libtk8.6.so: cannot open shared object file: No such file_
↳or directory
```

On Linux this can be fixed by installing the package tk using your distribution's package manager. Depending on your distribution, this might be called tk-devel, tkinter, tk-dev, tk, python-tk or maybe another variation. A google search could be helpful.

```
Failed building wheel for hyvr
...
<very long command containing the words 'compile' and 'install'>
```

This happens if there's only a source distribution on PyPI and you don't have access to a compiler. Contact us if this happens and we'll try to upload a pre-built binary.

7 Changelog/Bug Fixes

7.1 HyVR 0.2.3

Release Date: 19 July 2018

Contributors

- Jeremy Bennett
- Samuel Scherrer

Changes

- Improvements to file/directory handling, including separation of parameter file parsing and directory setup.
- New name for back-up parameter files.
- Flopy is now an optional dependency.
- Virtual boreholes can now be sampled on grids defined by number of boreholes in x,y-directions, or by a specific grid spacing.
- Journal article references added.

7.2 HyVR 0.2.2

Release Date: 12 June 2018

Contributors

- Jeremy Bennett
- Samuel Scherrer

Changes

- Removed `hyvr.utils.to_vtk` function.
- HyVR now uses Flopy 3.2.9, and incorporates more of that package's features.
- Some changes to MODFLOW 6 utilities.

- HyVR can now be installed from PyPI using pip
- Improvements to h5 I/O.
- Improvements to `hyvr.utils.virtual_boreholes` function

7.3 HyVR 0.2.1

Release Date: 9 May 2018

Contributors

- Jeremy Bennett
- Samuel Scherrer
- Emilio Sanchez

Changes

- Fixed bug in parsing of boolean options: previously all existing boolean options were parsed as `True`
- Outputs for ParaView `.vtr` files are now specified with `vtr` instead of `vtk` as in previous versions.
- Some small changes to the testcase parameter file examples.
- Trends in porosity microstructure are now working.
- Architectural element lookup tables can now be saved to text files following simulation.
- Addition of `virtual_boreholes` function to `HyVR.utils` module. This can be used for generating borehole data from HyVR simulations.
- Some improvements to creation of MODFLOW 6 input files, including linear hydraulic head initial condition.
- Added testing functions.

7.4 HyVR 0.2

Release Date: April 2018

Contributors

- Jeremy Bennett
- Samuel Scherrer

Changes

- First Release

References

- [BHC17] Jeremy Bennett, Claus P. Haslauer, and Olaf A. Cirpka. The impact of sedimentary anisotropy on solute mixing in stacked scour-pool structures. *Water Resources Research*, 53(4):2813–2832, April 2017. doi:[10.1002/2016WR019665](https://doi.org/10.1002/2016WR019665).
- [DN93] C. R. Dietrich and G. N. Newsam. A fast and exact method for multidimensional gaussian stochastic simulations. *Water Resources Research*, 29(8):2861–2869, August 1993. doi:[10.1029/93WR01070](https://doi.org/10.1029/93WR01070).
- [Fer76] R. I. Ferguson. Disturbed periodic model for river meanders. *Earth Surface Processes*, 1(4):337–347, October 1976. doi:[10.1002/esp.3290010403](https://doi.org/10.1002/esp.3290010403).
- [JSD94] Peter Jussel, Fritz Stauffer, and Themistocles Dracos. Transport modeling in heterogeneous aquifers: 1. Statistical description and numerical generation of gravel deposits. *Water Resources Research*, 30(6):1803–1817, June 1994. doi:[10.1029/94WR00162](https://doi.org/10.1029/94WR00162).
- [PBD09] M.J. Pyrcz, J.B. Boisvert, and C.V. Deutsch. ALLUVSIM: A program for event-based stochastic modeling of fluvial depositional systems. *Computers & Geosciences*, 35(8):1671–1685, August 2009. doi:[10.1016/j.cageo.2008.09.012](https://doi.org/10.1016/j.cageo.2008.09.012).